

Differential single-top-quark cross sections in t channel at 8 and 13 TeV with the CMS detector

Doctoral dissertation presented by
Matthias Komm
in fulfilment of the requirements for the degree of Doctor in Sciences

Thesis support committee

Prof. Vincent Lemaitre (Chair)	UCL, Belgium
Dr. Andrea Giammanco (Advisor)	UCL, Belgium
Prof. Freya Blekman	VUB, Belgium
Prof. Fabio Maltoni (Secretary)	UCL, Belgium
PD Dr. Andreas Meyer	DESY & KIT, Germany

Contents

Introduction	7
Unit convention	8
1 The standard model of particle physics	9
1.1 Particle content	9
1.2 Quantum field theory	11
1.3 Electroweak interactions and Higgs mechanism	12
1.4 Strong interactions	17
1.5 Observables	20
1.6 Open questions	21
2 The top quark	23
2.1 Decay and W boson polarization	24
2.2 Pair production	26
2.3 Single-top-quark production	27
2.4 Polarization in t -channel single-top-quark production	29
2.5 Flavor schemes	32
2.6 Anomalous couplings	33
2.7 Selection of experimental results	36
3 Experimental setup	41
3.1 Large Hadron Collider	41
3.1.1 Accelerator complex	42
3.1.2 Overview of experiments	43
3.2 CMS experiment	44
3.2.1 Solenoid magnet	45
3.2.2 Inner tracking system	46
3.2.3 Electromagnetic calorimeter	47
3.2.4 Hadron calorimeter	48
3.2.5 Muon system	50
3.2.6 Data acquisition	51
4 Event reconstruction	53
4.1 Track reconstruction	53
4.1.1 Muon tracks	55

4.1.2	Electron tracks	56
4.2	Vertex reconstruction	56
4.3	Particle flow	57
4.4	Muons	58
4.5	Electrons	60
4.6	Jets	61
4.7	b-tagging	63
4.8	Missing transverse energy	66
4.9	Luminosity	67
4.10	Summary of corrections	68
5	Analysis techniques	69
5.1	Event generation	69
5.2	Top quark reconstruction	72
5.3	Boosted Decision Trees	74
5.4	Template-based fitting	77
5.5	Parton and particle level observables	79
5.6	Unfolding	82
6	Measurement of single-top-quark polarization in t channel at 8 TeV	87
6.1	Outline of analysis strategy	87
6.2	Event selection and simulated samples	88
6.3	Training of Boosted Decision Trees	90
6.4	Background modeling	96
6.5	Background estimation	99
6.6	Validation	102
6.7	Signal-enriched region	103
6.8	Unfolding and asymmetry estimation	104
6.9	Statistical evaluation	107
6.10	Results	110
6.11	Limits on anomalous couplings	111
7	Measurement of differential single-top-quark cross sections at 13 TeV	115
7.1	Outline of analysis strategy	115
7.2	Event selection and simulated samples	116
7.3	Background modeling	119
7.4	BDT training	123
7.5	Signal extraction	125
7.6	Validation	130
7.7	Unfolding	130
7.8	Statistical evaluation	133
7.9	Results	135

8 Prospects for differential t-channel measurements at 13 TeV	137
8.1 Setup	137
8.2 New BDT discriminant	141
8.3 Signal extraction	142
8.4 Particle level selection	143
8.5 Unfolding and results	146
8.6 Summary of improvements	147
Conclusion	151
Acknowledgments	153
Acronyms	155
References	159

Introduction

"But I don't want to go among mad people," Alice remarked. "Oh, you can't help that," said the Cat: "we're all mad here. I'm mad. You're mad." "How do you know I'm mad?" said Alice. "You must be," said the Cat, "or you wouldn't have come here."

— Lewis Carroll, Alice in Wonderland

The standard model of particle physics is a very successful theory in describing electroweak and strong interactions between point-like, fundamental particles. Its predictions are constantly challenged with experimental data but so far no significant deviations have been confirmed.

The heaviest known elementary particle is the top quark whose mass is close to a tungsten atom. It was discovered in 1995 by the CDF and DØ experiments at the Tevatron (Fermilab, USA) through its production process via strong interactions leading to top quark/antiquark pairs. An experimentally more elusive production mode of top quarks predicted by the standard model occurs via electroweak interactions resulting in events containing only single top quarks. The detection of such events is more challenging due to the larger occurrence of background events mimicking its signature. It took 14 more years until the production of single top quarks was finally observed in 2009 by the CDF and DØ experiments as well. Since the start of the physics program at the LHC (CERN, Switzerland) in 2009, the production of single top quarks can be studied for the first time in great detail using an unprecedented quantity of proton-proton collision events.

Single-top-quark events offer a unique opportunity to measure the properties of the electroweak theory and to test its predictions in the presence of such a heavy particle. For instance, measurements of the inclusive cross section of single-top-quark production allow to infer the modulus of the Cabibbo-Kobayashi-Maskawa (CKM) matrix element V_{tb} whose value is a free parameter of the standard model. Measurements of differential cross section on the other hand yield in-deep tests of the electroweak production mechanisms and of its coupling structure which in case of deviations may also provide hints towards physics beyond the standard model.

In this thesis, the production of single top quarks via t channel is investigated. Measurements of differential cross sections based on proton-proton collision data at center-of-mass energies of 8 and 13 TeV with the CMS experiment are presented.

In 8 TeV data the top quark polarization angle is studied, defined as the angle between the lepton from the top quark decay and the spectator quark in the top quark rest frame. The top quark spin asymmetry, a quantity related to the top quark polarization, is extracted from the differential cross section. The asymmetry allows to test the coupling structure of the involved interactions. In the standard model a vector – axial vector (V-A) coupling structure is predicted which permits only left-handed top quarks or

right-handed top antiquarks to interact with a W boson and a bottom quark. Hence, one expects that single top quarks in t channel are produced with a high degree of polarization. On the other hand, a potential depolarization may occur through new physics beyond the standard model. In effective field theory their influence can be recast into anomalous couplings for which limits are derived using the measured spin asymmetry. Events containing single muons or electrons together with two or three jets are analyzed in this measurement. Two boosted decision trees are trained to define a signal-enriched region from which the differential cross section is inferred from data through a regularized unfolding procedure.

In the second part, an early measurement of differential cross sections as a function of the top quark transverse momentum and rapidity is presented using the first data recorded at a center-of-mass energy of 13 TeV with the CMS experiment. For this, the analysis strategy of the top quark polarization measurement has been significantly extended. The new strategy involves the estimation of the amount of signal events as a function of the unfolding observables from data through multiple maximum-likelihood fits. The resulting differential cross sections are compared to the predictions by various event generator programs.

The thesis is organized as follows. First a general introduction to the standard model is given in Ch. 1. The phenomenology of the top quark, its properties and production mechanisms, relevant for this thesis, are introduced in Ch. 2 with a particular emphasis on the electroweak coupling structure. The experimental setup consisting of the LHC accelerator and the CMS experiment is outlined in Ch. 3 which is followed by a detailed description of the reconstruction of physics objects for analyses in Ch. 4. In Ch. 5 the employed analysis techniques are elaborated. The performed differential cross section measurements at 8 and 13 TeV are detailed in Ch. 6 and Ch. 7 respectively. Before the thesis is concluded, improvements for future differential single-top-quark measurements are investigated in Ch. 8.

Unit convention

The “natural units” of particle physics are used throughout this thesis unless it is explicitly stated otherwise. These differ from the SI units and are derived by defining the natural constants as:

- speed of light: $c \equiv 1$;
- Planck constant: $\hbar \equiv 1$;
- electric permittivity: $\epsilon_0 \equiv 1$;
- Boltzmann constant: $k_B \equiv 1$.

This changes the units of the following quantities amongst others:

- length: $[m] \mapsto [eV^{-1}]$;
- time: $[s] \mapsto [eV^{-1}]$;
- mass: $[kg] \mapsto [eV]$;
- energy: $[J] \mapsto [eV]$;
- temperature: $[K] \mapsto [eV]$.

1.

Chapter

The standard model of particle physics

An overview of the standard model of particle physics (SM) is given in the following. First, the fundamental particles and their properties are introduced. Then, the electroweak and strong interactions are detailed. This includes a brief description of the electroweak symmetry breaking mechanism which generates particle masses through interactions with the Higgs field. After sketching the calculation of observables in perturbation theory, the chapter is concluded by highlighting some open questions of the SM.

The standard model of particle physics (SM) describes the interactions between fundamental particles. It is based on quantum field theory (QFT) which allows to predict observables of particle interactions. Exemplary observables are production cross sections and decay rates of particles which can be calculated within its framework. The validity of the SM is constantly challenged by comparing its predictions to experimental data. No significant deviations have been found so far that would hint towards physics beyond the standard model (BSM).

1.1. Particle content

Fundamental particles are defined as objects for which experiments have not revealed an internal structure. Hence, such particles are considered as point-like. They can be grouped by their spin into fermions with half-integer and bosons with integer spin. All fundamental fermions of the SM have a spin of $1/2$. The fermions can be further divided into leptons and quarks where only the latter can participate in strong interactions. Tables 1.1 and 1.2 list the leptons and quarks respectively. Each column is called a generation. It encapsulates an isospin pair whose components are therefore also referred to as up- or down-type respectively. It is unknown why there are exactly three lepton and three quark generations. Atoms which form ordinary matter consist only of particles from the first generation. These are electrons, protons, and neutrons, where the latter two are bound states of uud quarks and udd quarks respectively.

For the masses of the neutrinos, only upper limits CL are known. Those are derived by combining measurements of beta decay spectra with results from neutrino oscillation experiments. When the SM was constructed in the mid 1970s, neutrinos were assumed to be massless. However, the observation of neutrino oscillations requires that at least two neutrino generations have non-zero masses [2].

The bosons of the SM are listed in Tab. 1.3. They are connected to fundamental interactions by requiring invariance of the Lagrangian density under certain gauge group transformations as demonstrated later in this chapter. With the exception of the Higgs

Table 1.1. The leptons of the SM. The particle masses are taken from Ref. [1]. Uncertainties on the measured masses are omitted because the precision is beyond the sub permille level. For the neutrino masses only upper exclusion limits (CLs) are given.

	1. generation	2. generation	3. generation
Name	electron neutrino (ν_e)	muon neutrino (ν_μ)	tau neutrino (ν_τ)
Mass	< 225 eV (95% CL)	< 0.19 MeV (90% CL)	< 18.2 MeV (95% CL)
Electric charge	0	0	0
Name	electron (e^-)	muon (μ^-)	tau (τ^-)
Mass	511.0 keV	105.66 MeV	1.776 GeV
Electric charge	-1	-1	-1

Table 1.2. The quarks of the SM. The u,d,s,c, and b quark masses are reported in the $\overline{\text{MS}}$ mass scheme [1]. For the top quark the pole mass is quoted instead as measured in Ref. [3].

	1. generation	2. generation	3. generation
Name	up (u)	charm (c)	top (t)
Mass	$2.2^{+0.6}_{-0.4}$ MeV	1.27 ± 0.03 GeV	172.44 ± 0.49 GeV
Electric charge	2/3	2/3	2/3
Name	down (d)	strange (s)	bottom (b)
Mass	$4.7^{+0.5}_{-0.4}$ MeV	96^{+8}_{-4} MeV	$4.18^{+0.04}_{-0.03}$ GeV
Electric charge	-1/3	-1/3	-1/3

boson, all other bosons carry a spin of 1. The Higgs boson is the only scalar fundamental particle (spin 0) of the SM. For a long time, it was a purely hypothetical particle. In July 2012, the ATLAS [4] and CMS [5] collaborations independently reported the observation of a Higgs-like particle. Further investigations whether this new particle exhibits the expected interactions with other particles revealed that it is consistent with the SM Higgs boson [6]. This discovery completed the SM and thus gave further confidence into its theoretical foundation.

For each fundamental particle there exists a charge-conjugated partner called antiparticle. Other properties such as mass and spin are identical. The photon, Z boson, and Higgs boson are their own antiparticle. It is still under investigation if the neutrino is its own antiparticle. Fermions with such a property are called Majorana particles [8]. Experimentally, this can be probed in double beta decays where in the case of Majorana neutrinos the decay can occur as $n\bar{n} \rightarrow p\bar{p} + e^-e^-$ without emitting two additional neutrinos. However, this scenario seems to be disfavored by recent results as reviewed in Ref. [9].

Table 1.3. The bosons of the SM. The Z and W boson masses are taken from Ref. [1]. The uncertainties on their masses are omitted because the precision is beyond the sub permille level. The Higgs boson mass is taken from Ref. [7].

Name	Mass	Associated interaction	Gauge group
Photon (γ)	0	Electromagnetism	$U(1)$
Z boson	91.19 GeV	Weak interaction	$SU(2)$
W boson	80.39 GeV		
Higgs boson (H)	125.09 ± 0.24 GeV	Yukawa interaction	$SU(2) \otimes U(1)$
8 gluons (g)	0	Strong interaction	$SU(3)$

1.2. Quantum field theory

In the framework of QFT particles are described as excitation modes of quantized fields. This is referred to as “canonical” or “second” quantization which allows to describe the dynamics of many-particle systems^(*). Field operators can be decomposed as

$$\psi(x) = \sum_i^N u_i(x) a_i, \quad \psi^\dagger(x) = \sum_i^N u_i^\dagger(x) a_i^\dagger, \quad (1.1.)$$

where $u_i(x)$ denotes the ordinary wave function of a single particle and a_i^\dagger (a_i) its creation (annihilation) operator, respectively. As in classical mechanics the action of a system is calculated as

$$S = \int L dt = \iint \mathcal{L} d^3x dt = \int \mathcal{L} d^4x, \quad (1.2.)$$

where \mathcal{L} denotes the Lagrangian density. For example, a system of free fermions is described by the Dirac Lagrangian density,

$$\mathcal{L}_{\text{Dirac}} = \bar{\psi}(i\gamma^\mu \partial_\mu - m)\psi \quad (1.3.)$$

using the definitions $\partial_\mu \equiv \partial/\partial x_\mu$ with $\mu \in \{0\dots3\}$ and $\bar{\psi} \equiv \psi^\dagger \gamma^0$, where γ_μ denote the Dirac matrices^(**). The principle of least action, $\delta S = 0$, that is satisfied by the Euler-Lagrange equation yields the equation of motion as

$$\frac{\partial \mathcal{L}}{\partial \bar{\psi}} - \frac{\partial}{\partial_\mu} \left(\frac{\partial \mathcal{L}}{\partial (\partial_\mu \bar{\psi})} \right) = (i\gamma^\mu \partial_\mu - m)\psi = 0. \quad (1.4.)$$

Assuming $\psi \propto e^{-ip^\mu x_\mu}$ leads to the well-known energy-momentum relation

$$0 = (-i\gamma^\mu \partial_\mu - m)^* \cdot (-i\gamma^\nu \partial_\nu - m)\psi \quad (1.5a.)$$

$$= (\partial^\mu \partial_\mu + m^2)\psi \quad (\text{Klein-Gordon equation}) \quad (1.5b.)$$

^(*) An alternative quantization can be achieved via path integrals.

^(**) Multiple representations are possible. The matrices need to satisfy a Clifford algebra with the anticommutation relation: $\{\gamma^\mu, \gamma^\nu\} = \gamma^\mu \gamma^\nu + \gamma^\nu \gamma^\mu = 2g^{\mu\nu}$.

$$\Rightarrow (-p^\mu p_\mu + m^2) = 0. \quad (1.5c.)$$

Interactions between particles are introduced in the SM by requiring local invariance of the Lagrangian density for certain groups of gauge transformations. This concept is briefly demonstrated in the following where the requirement of local invariance under a U(1) transformation leads to quantum electrodynamics (QED).

Applying the gauge transformation

$$\psi(x) \mapsto \psi'(x) = \psi(x) \cdot e^{-iq\cdot\alpha(x)}, \quad (1.6.)$$

on Eq. 1.3 yields

$$\mathcal{L}(\psi, \partial_\mu \psi) \mapsto \mathcal{L}(\psi', \partial_\mu \psi') = \bar{\psi} \left(i\gamma^\mu \partial_\mu + q\gamma^\mu \partial_\mu \alpha(x) - m \right) \psi \neq \mathcal{L}(\psi, \partial_\mu \psi), \quad (1.7.)$$

where the arbitrary phase $\alpha(x)$ is a function of the local space-time coordinate x . The invariance $\mathcal{L}(\psi, \partial_\mu \psi) = \mathcal{L}(\psi', \partial_\mu \psi')$ is restored by adding a bosonic spin-1 field $A_\mu(x)$ to the Lagrangian density which interacts with ψ and transforms under Eq. 1.6 as

$$A_\mu(x) \mapsto A'_\mu(x) = A_\mu(x) - \partial_\mu \alpha(x). \quad (1.8.)$$

In summary, this procedure results in a Lagrangian density containing the following terms

$$\mathcal{L} = \bar{\psi} (i\gamma^\mu \partial_\mu - m) \psi \quad (\text{fermion propagator}) \quad (1.9a.)$$

$$+ q \bar{\psi} \gamma^\mu \psi A_\mu \quad (\text{interaction}) \quad (1.9b.)$$

$$- \frac{1}{4} (\partial_\mu A_\nu - \partial_\nu A_\mu)^2 \quad (\text{boson propagator}) \quad (1.9c.)$$

where the gauge-invariant boson propagator describing the dynamics of a free A_μ field has been added as well. The introduced interaction (Eq. 1.9b) which is required to ensure the invariance under the U(1) transformation (Eq. 1.6) can be identified as electromagnetic interaction between a fermion described by the field ψ with electric charge q and a spin-1 particle, the photon, described by the field A_μ . The photon is predicted to be massless since adding a term of the form $m_A^2 A^\mu A_\mu$ would violate the invariance.

Other interactions of the SM are connected to local gauge transformations as well (see Tab. 1.3) and can thus be introduced through similar procedures. A common property of the generated interactions follows from the Noether theorem which states that a conserved current exists for each differentiable symmetry of the action. Hence the charge associated to each gauge group is conserved. This is however already the case for a global transformation which does not depend on the space-time coordinate. The invariance even under a local gauge transformations is a puzzling feature of the theory.

1.3. Electroweak interactions and Higgs mechanism

Electromagnetic and weak interactions can be unified using a $U(1) \otimes SU(2)$ gauge group. A complication arises from the fact that the W and Z bosons, mediators of the weak interaction, are massive. The masses of these particles have to be introduced

in a different way if the concept of local gauge invariance should continue to hold. Experimentally, the UA1 and UA2 experiments at the CERN SPS proton-antiproton collider measured their masses for the first time [10–13] while the existence of weakly-interacting charged and neutral currents was already known from beta decay and bubble chamber experiments [14].

Another feature of weak interactions is that parity is not conserved but instead maximally violated. This property manifests itself in a dependence of the interaction on the spin orientation of a particle with respect to its momentum. Experimentally, the Wu experiment [15] discovered the violation of parity in $^{60}_{27}\text{Co} \rightarrow ^{60}_{28}\text{Ni} + e^- \bar{\nu}_e \gamma\gamma$ decays by analyzing the direction of the escaping electron with respect to the polarization of the cobalt probe through an external magnetic field. In the electroweak theory fermion fields are decomposed into chiral eigenstates to account for the violation of parity using the projections

$$\psi_L \equiv P_L \psi = \frac{1}{2} (1 - \gamma_5) \psi, \quad \psi_R \equiv P_R \psi = \frac{1}{2} (1 + \gamma_5) \psi \quad (1.10.)$$

with $\gamma_5 = i\gamma_0\gamma_1\gamma_2\gamma_3$ ^(*) where ψ_L (ψ_R) is called a “left-handed” (“right-handed”) fermion respectively. For massless particles Eq. 1.3 decouples into two independent equations for ψ_L and ψ_R . The chirality (eigenvalue of γ_5) is then equal to the Lorentz-invariant helicity

$$H = \frac{\vec{p} \cdot \vec{s}}{|\vec{p}|}, \quad (1.11.)$$

which denotes whether the spin \vec{s} of a particle is aligned along ($H = +1$) or against ($H = -1$) the momentum. For massive particles however Eq. 1.3 cannot be decomposed since chirality is not Lorentz-invariant.

In the Glashow-Weinberg-Salam model [16–18] fermion fields are split into left-handed doublet fields

$$\vec{E}_L = \left\{ \begin{pmatrix} \nu_{e,L} \\ e_L^- \end{pmatrix}, \begin{pmatrix} \nu_{\mu,L} \\ \mu_L^- \end{pmatrix}, \begin{pmatrix} \nu_{\tau,L} \\ \tau_L^- \end{pmatrix} \right\}, \quad \vec{Q}_L = \left\{ \begin{pmatrix} u_L \\ d_L \end{pmatrix}, \begin{pmatrix} c_L \\ s_L \end{pmatrix}, \begin{pmatrix} t_L \\ b_L \end{pmatrix} \right\} \quad (1.12.)$$

and right-handed singlet fields

$$\vec{e}_R = \{e_R^-, \mu_R^-, \tau_R^-\}, \quad \vec{u}_R = \{u_R, c_R, t_R\}, \quad \vec{d}_R = \{d_R, s_R, b_R\} \quad (1.13.)$$

of the SU(2) group. Right-handed neutrinos do not participate in any interactions described by the SM. The gauge transformation of the combined U(1) \otimes SU(2) group is

$$\psi(x) \mapsto \psi'(x) = \psi(x) \cdot \underbrace{e^{-\frac{1}{2}ig\vec{\alpha}(x)\cdot\vec{\omega}}}_{\text{SU}(2)} \cdot \underbrace{e^{-\frac{1}{2}ig'\beta(x)}}_{\text{U}(1)}, \quad (1.14.)$$

where ω_a ($a \in \{1,2,3\}$) denote the Pauli matrices and g, g' the corresponding conserved charges. This leads to four boson fields, W^a and B , that interact with the fermions. In

^(*) The matrix γ_5 has the following properties: $(\gamma_5)^\dagger = \gamma_5$; $(\gamma_5)^2 = I_{4 \times 4}$; $\gamma_5 \gamma_\mu + \gamma_\mu \gamma_5 = 0$.

analogy to Eq. 1.9b one obtains the electroweak (EWK) interactions

$$\begin{aligned}\mathcal{L}_{\text{EWK int.}} &= \sum_i^{\text{doublets}} \bar{\psi}_L^i \gamma^\mu \left(\frac{1}{2} g \vec{W}_\mu \cdot \vec{\omega} + \frac{1}{2} g' B_\mu \right) \psi_L^i \\ &+ \sum_j^{\text{singlets}} \bar{\psi}_R^j \gamma^\mu \left(\frac{1}{2} g' B_\mu \right) \psi_R^j + \text{h.c.}\end{aligned}\quad (1.15.)$$

where the summations are implied over the fermion doublet and singlet fields. A fermion mass term $m_f \bar{\psi}_f \psi_f = m_f (\bar{\psi}_{f,L} \psi_{f,R} + \bar{\psi}_{f,R} \psi_{f,L})$ cannot be added to the Lagrangian density since it violates the invariance under the SU(2) transformation. This is solved by the Englert-Brout-Higgs-Guralnik-Hagen-Kibble-mechanism [19–22] which introduces mass terms not only for fermions but also for the gauge bosons through the concept of “symmetry breaking”. For this, a new scalar SU(2) doublet field $\phi = (\phi^+, \phi^0)^{(*)}$, invariant under Eq. 1.14, is added to the Lagrangian density which interacts with the gauge bosons as

$$\mathcal{L}_\phi = (D_\mu \phi)^\dagger (D^\mu \phi) - V(\phi) \quad (1.16\text{a.})$$

$$D^\mu \phi = (\partial^\mu - \frac{1}{2} i g \vec{W}^\mu \cdot \vec{\omega} - \frac{1}{2} i g' B^\mu) \phi. \quad (1.16\text{b.})$$

In addition ϕ has a potential

$$V(\phi) = -\mu^2 \phi^\dagger \phi + \frac{1}{2} \lambda (\phi^\dagger \phi)^2 \quad (1.17.)$$

in the form of a “Mexican hat” as shown in Fig. 1.1 that leads to a non-zero vacuum expectation value (VEV) for ϕ for $\mu^2 > 0$ of

$$\phi_0 = \sqrt{\frac{\mu^2}{2\lambda}} \equiv \frac{v}{\sqrt{2}}. \quad (1.18.)$$

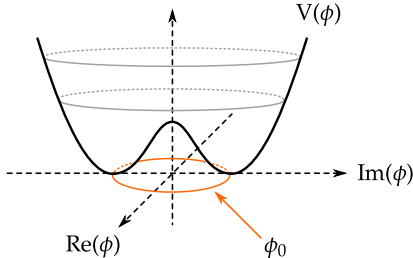


Figure 1.1. || The “Mexican hat” potential of the Higgs field ϕ with a non-zero vacuum expectation value (VEV) ϕ_0 that leads to symmetry breaking.

One says that this shifted VEV “breaks” the SU(2) symmetry when parameterizing ϕ around the minimum of $V(\phi)$ as

(*) ϕ^+ annihilates positively charge scalar particles / creates antiparticles with negative charge;
 ϕ^0 annihilates neutral particles / creates neutral antiparticles.

$$\phi(x) \Big|_{\phi_0} = \frac{1}{\sqrt{2}} \begin{pmatrix} 0 \\ v + H(x) \end{pmatrix} \cdot \exp \left(-i \frac{\vec{\theta}(x) \cdot \vec{\omega}}{2v} \right), \quad (1.19.)$$

where $\vec{\theta}$ denotes three so-called “Goldstone” bosons and H the Higgs boson. In fact, the symmetry still exists but is “hidden”. A SU(2) transformation called “unitary gauge” can be performed such that $\vec{\theta}$ vanishes. One says that these three Goldstone bosons and their degrees of freedom are “eaten” by the W and Z bosons to become massive. Hence, through the extra degrees of freedom they can also have a longitudinal polarization after symmetry breaking. The parametrization of ϕ is chosen such that it leaves the minimum invariant under the U(1) subgroup transformation

$$\psi(x) \mapsto \psi'(x) = \psi(x) \cdot e^{-\frac{1}{2}ig\alpha_3(x)\cdot\omega_3} \cdot e^{-\frac{1}{2}ig'\beta(x)}. \quad (1.20.)$$

Inserting Eq. 1.19 into Eq. 1.16a yields amongst others the following Lagrangian densities capturing the non-interacting terms:

$$\mathcal{L}_{\text{Higgs boson}} = \frac{1}{2}(\partial_\mu H^\dagger)(\partial^\mu H) - \lambda^2 v^2 H^2 \quad (1.21a.)$$

$$\begin{aligned} \mathcal{L}_{W_1, W_2 \text{ bosons}} = & -\frac{1}{4}(W_{1,\mu\nu}W_1^{\mu\nu} + W_{2,\mu\nu}W_2^{\mu\nu}) \\ & + \frac{1}{8}g^2 v^2 (W_{1,\mu}W_1^\mu + W_{2,\mu}W_2^\mu) \end{aligned} \quad (1.21b.)$$

$$\begin{aligned} \mathcal{L}_{W_3, B \text{ bosons}} = & -\frac{1}{4}(B_{\mu\nu}B^{\mu\nu} + W_{3,\mu\nu}W_3^{\mu\nu}) \\ & + \frac{1}{8}v^2(gW_{3,\mu} - g'B_\mu)(gW_3^\mu - g'B^\mu). \end{aligned} \quad (1.21c.)$$

The first term (Eq. 1.21a) describes the free scalar Higgs boson with mass $m_H = \lambda v$. Next, the W_1 and W_2 fields in Eq. 1.21b can be identified as a particle/antiparticle pair $W^\pm = (W_1 \mp iW_2)/\sqrt{2}$ with mass $m_W = \frac{1}{2}gv$. Lastly, the fields W_3 and B in Eq. 1.21c appear to be in a mixed-mass state. By performing a rotation of the couplings

$$\begin{pmatrix} Z \\ A \end{pmatrix} = \begin{pmatrix} \cos\theta_W & -\sin\theta_W \\ \sin\theta_W & \cos\theta_W \end{pmatrix} \begin{pmatrix} W_3 \\ B \end{pmatrix}, \quad \cos\theta_W = \frac{g}{\sqrt{g^2+g'^2}}, \quad (1.22.)$$

where θ_W is called the “weak-mixing” or “Weinberg” angle, another massive boson, the Z boson, with mass $m_Z = v\sqrt{g^2+g'^2}/2$ and a massless boson A_μ , the photon, can be identified. The angle is determined as $\sin^2\theta_W \approx 0.23$ [1] through the couplings g and g' . Equation 1.16a also yields the relation $\rho \equiv m_W^2/(m_Z^2 \cdot \cos\theta_W^2) = 1$ which is commonly referred to as the “custodial symmetry”. Rewriting the covariant derivative of Eq. 1.16b into these mass eigenstates yields

$$\begin{aligned} D_\mu = & \partial_\mu + i\frac{g}{\sqrt{2}} \cdot (W_\mu^+ T^+ + W_\mu^- T^-) \\ & - i\frac{g^2 T_3 - g'^2 Y}{\sqrt{g^2+g'^2}} \cdot Z_\mu - i\frac{g'g(T_3 + Y)}{\sqrt{g^2+g'^2}} \cdot A_\mu, \end{aligned} \quad (1.23.)$$

where Y denotes the U(1) so-called “hyper” charge, T_3 the weak isospin (eigenvalue

of ω_3), and T^\pm the ladder operators for increasing or lowering T_3 . From the coupling to the photon one can read off the electric coupling constant to be

$$e = \frac{g' g}{\sqrt{g^2 + g'^2}}, \quad (1.24.)$$

which is measured as $\alpha_{\text{EM}} = e^2/(4\pi) \approx 1/137$ [1] and the corresponding electric charge to be $Q = T_3 + Y$ which is invariant under Eq. 1.20 and thus conserved. For the weak coupling constant one finds the relation $e = g \cdot \sin\theta_W$ which yields $\alpha_W = \alpha_{\text{EM}}/\sin^2\theta_W \approx 0.032$. The value of the VEV can be estimated from muon lifetime measurements (e.g. Ref. [23]) through the Fermi coupling constant, G_F , as

$$\frac{G_F}{\sqrt{2}} \approx \frac{g^2}{8m_W^2} = \frac{1}{2v^2} \quad \Rightarrow \quad v = (\sqrt{2} G_F)^{-1/2} \approx 246 \text{ GeV}. \quad (1.25.)$$

A consequence of electroweak symmetry breaking is the prediction of the Higgs boson. Its mass is not predicted by the SM since it is a function of the free parameter λ which required to consider multiple mass hypotheses in searches for the Higgs boson. Almost fifty years after its prediction the Higgs boson was finally discovered in July 2012 independently by the ATLAS [4] and CMS [5] collaborations and thus completed the electroweak theory.

By introducing gauge-invariant Yukawa interactions between the fermions and the Higgs field as

$$\mathcal{L}_{\text{Yukawa lepton int.}} = - \sum_i \lambda_e^{ij} \cdot \bar{E}_L^i \phi \cdot e_R^j + \text{h.c.}, \quad (1.26a.)$$

$$\mathcal{L}_{\text{Yukawa quark int.}} = - \sum_{i,j} \lambda_d^{ij} \cdot \bar{Q}_L^i \phi \cdot d_R^j - \sum_{i,j,k} \lambda_u^{ik} \cdot \bar{Q}_L^i \epsilon^{ij} \phi^j \cdot u_R^k + \text{h.c.}, \quad (1.26b.)$$

where λ_X^{ij} denote the coupling strengths and ϵ^{ij} an antisymmetric matrix, fermion mass terms are generated as well. After the symmetry breaking mass terms for the electron, muon and tau lepton of

$$\mathcal{L}_{\text{Yukawa lepton int.}} \supset - \underbrace{\frac{\lambda_e v}{\sqrt{2}}}_{\equiv m_e} \bar{e}_L e_R - \underbrace{\frac{\lambda_\mu v}{\sqrt{2}}}_{\equiv m_\mu} \bar{\mu}_L \mu_R - \underbrace{\frac{\lambda_\tau v}{\sqrt{2}}}_{\equiv m_\tau} \bar{\tau}_L \tau_R + \text{h.c.} \quad (1.27.)$$

can be identified. The quarks can be disentangled from their mixed-mass state through a rotation of the fields

$$u_L^i \mapsto U_u^{ij} u_L^j, \quad d_L^i \mapsto U_d^{ij} d_L^j, \quad (1.28.)$$

which allows to write the Lagrangian density in the quark mass eigenstates. In particular, using Eqs. 1.15 and 1.23, this yields the interaction terms

$$\mathcal{L}_{\text{Wif int.}} = i \frac{g}{2\sqrt{2}} \sum_i \left(\bar{\nu}_i (\gamma^\mu - \gamma^\mu \gamma^5) W_\mu^+ \ell_i^- + \ell_i^+ (\gamma^\mu - \gamma^\mu \gamma^5) W_\mu^- \nu_i \right)$$

$$+ i \frac{g}{2\sqrt{2}} \sum_{ij} \left(V_{ij} \bar{u}_i (\gamma^\mu - \gamma^\mu \gamma^5) W_\mu^+ d_j + V_{ij}^\dagger \bar{d}_i (\gamma^\mu - \gamma^\mu \gamma^5) W_\mu^- u_j \right) \quad (1.29.)$$

between the W bosons and fermions where $V_{ij} = (U_u^\dagger U_d)_{ij}$ denotes the Cabibbo-Kobayashi-Maskawa (CKM) matrix. Its elements are free parameters of the SM and have to be measured experimentally. A global fit using a multitude of measurements [1] while assuming unitarity for the three quark generations yields

$$\begin{aligned} V_{\text{CKM}} &= \begin{pmatrix} |V_{ud}| & |V_{us}| & |V_{ub}| \\ |V_{cd}| & |V_{cs}| & |V_{cb}| \\ |V_{td}| & |V_{ts}| & |V_{tb}| \end{pmatrix} \\ &= \begin{pmatrix} 0.9743 \pm 0.0001 & 0.2250 \pm 0.0005 & 0.0036 \pm 0.0001 \\ 0.2249 \pm 0.0005 & 0.9735 \pm 0.0001 & 0.0411 \pm 0.0013 \\ 0.0088 \pm 0.0003 & 0.0403 \pm 0.0013 & 0.9992 \pm 0.0001 \end{pmatrix}. \end{aligned} \quad (1.30.)$$

The coupling structure, $\gamma_\mu - \gamma_\mu \gamma_5$, between W bosons and the fermions is referred to as a vector – axial vector (V-A) structure because of its spatial transformation properties. Axial vectors do not switch sign under parity transformation unlike normal spatial vectors^(*). This allows only left-handed fermions or right-handed antifermions to couple to W bosons as observed by the Wu experiment.

1.4. Strong interactions

The theory of quantum chromodynamics (QCD) describes the strong interaction between quarks and gluons. It is connected to a SU(3) gauge group with the Lagrangian density

$$\mathcal{L}_{\text{QCD}} = \bar{\psi} i \gamma^\mu (\partial_\mu - i g_s \vec{G}_\mu \cdot \vec{\lambda}) \psi - \frac{1}{4} \vec{G}_{\mu\nu} \vec{G}^{\mu\nu}, \quad \psi = \begin{pmatrix} \psi_{\text{red}} \\ \psi_{\text{green}} \\ \psi_{\text{blue}} \end{pmatrix}, \quad (1.31.)$$

which is invariant under the local gauge transformation

$$\psi(x) \mapsto \psi'(x) = \psi(x) \cdot e^{-i g_s \vec{\alpha}(x) \cdot \vec{\lambda}}. \quad (1.32.)$$

The fields \vec{G}_μ describe eight gluons which represent the massless gauge bosons of the group. The conserved charge of the group is called “color” (red, green, blue) which is equal in strength for all charges. The generators λ_a ($a \in \{1 \dots 8\}$) obey the relation $[\lambda_a, \lambda_b] = i f_{abc} \lambda^c$ with the antisymmetric structure constant f_{abc} . A common representation of $\vec{\lambda}$ is given by the Gell-Mann matrices. The non-abelian group structure leads to gluon self-interactions through the gluon field strength tensor

$$G_{\mu\nu}^a = \partial_\mu G_\nu^a - \partial_\nu G_\mu^a + g_s f^{abc} G_{\mu,b} G_{\nu,c}. \quad (1.33.)$$

^(*) A typical example of an axial vector (also known as pseudovector) is the angular momentum $\vec{L} = \vec{r} \times \vec{p}$.

No free quarks can exist in nature because of a phenomenon called “color-confinement”. The QCD potential between two quarks can be approximated as a “Coulomb-plus-linear” potential [24]

$$V(r) \approx -\frac{4 \cdot \alpha_s}{3r} + k \cdot r, \quad \alpha_s = \frac{g_s^2}{4\pi}, \quad (1.34.)$$

where a linear term dominates at large distances r or equivalently small exchanged energies. The factor k can be understood as a “gluon-spring” tension similar to that of a harmonic oscillator. New quark/antiquark pairs can be created from the vacuum if the gluon field energy exceeds the mass of the new pair. This can lead to a cascade of particles emerging from the gluon field at sufficiently large energies which bind “free” quarks into color-neutral singlets called hadrons. Such a process is referred to as hadronization. In experiments the momentum of a quark or gluon candidate is therefore inferred by clustering collimated particles into jets.

Hadrons can be either mesons which consist of quark-antiquark pairs ($q\bar{q}$) or baryons consisting of quark triplets (qqq). These constituents of a hadron are referred to as “valence quarks”. Common mesons are the pions π^+ ($u\bar{d}$), π^0 ($(u\bar{u} - d\bar{d})/\sqrt{2}$), kaons K^+ ($u\bar{s}$), K^0 ($d\bar{s}$) and J/Ψ ($c\bar{c}$). Typical baryons are the proton (uud), the neutron (udd), and Λ^0 (uds). The baryon number, $B \equiv N(\text{baryons}) - N(\text{antibaryons})$, is conserved in interactions. Hence, the proton is stable and cannot decay because it is the lightest baryon. In 2003, a new bound state containing four quarks has been observed by the Belle experiment [25] at KEK, Japan. The LHCb experiment at the LHC, CERN confirmed this observation in 2013 [26] followed by the discovery of more so-called “tetraquark” candidates [27, 28] and even “pentaquarks” forming a bound state of five quarks [29].

Besides the valence quarks, virtual quarks (so-called “sea quarks”) and gluons are considered constituents of a hadron as well. This whole group of particles is commonly referred to as partons. In hadron collision experiments at a sufficiently high momentum transfer, one can approximate all partons as free which allows to treat hadron-hadron scattering as a single parton-parton interaction instead [30]. The momentum of a parton is expressed in terms of the fraction of the hadron momentum $\vec{p}_{\text{parton}} = x \vec{p}_{\text{hadron}}$, where x is also referred to as “Björken scaling variable” [31]. Then, the probability of finding two parton flavors f_i with momentum fraction x_i interacting at an energy scale μ_F in a hadron-hadron collision is given by the parton distribution function (PDF) as $\text{PDF}(x_1, f_1, \mu_F) \cdot \text{PDF}(x_2, f_2, \mu_F)$. The PDFs are normalized such that

$$\sum_f^{\text{partons}} \int_0^1 dx \ x \cdot \text{PDF}(x, \mu_F, f) = 1 \quad (1.35.)$$

yields the total momentum of the hadron. The scale μ_F is called “factorization scale” below which non-perturbative low energy effects such as soft gluon emissions have been absorbed into the PDF. Measuring the PDFs at scale μ_F , one can extrapolate them to any other scale by solving the DGLAP^(*) equation [32–34]. A review of common PDF sets which are currently used in descriptions of LHC collisions can be found in

^(*) Named after the authors: Dokshitzer, Gribov, Lipatow, Altarelli, and Parisi.

Ref. [35]. There are various groups estimating PDF sets from fits to experimental data using different approaches; e.g. CTEQ, MMHT (formerly MSTW), ABM, HERAPDF, and NNPDF. Exemplary distributions taken from the NNPDF group (version 3.0), using the LHAPDF library [36], are shown in Fig. 1.2 for $\mu_F = 10$ GeV and $\mu_F = 100$ GeV. More information on this PDF set can be found in Ref. [37]. At a momentum fraction of $x \approx 0.2$ one can observe an excess of the up and down quark distributions as expected from the valence quark composition of the proton. These vanish at low momentum fractions at which the contributions from virtual sea quarks and gluons dominate.

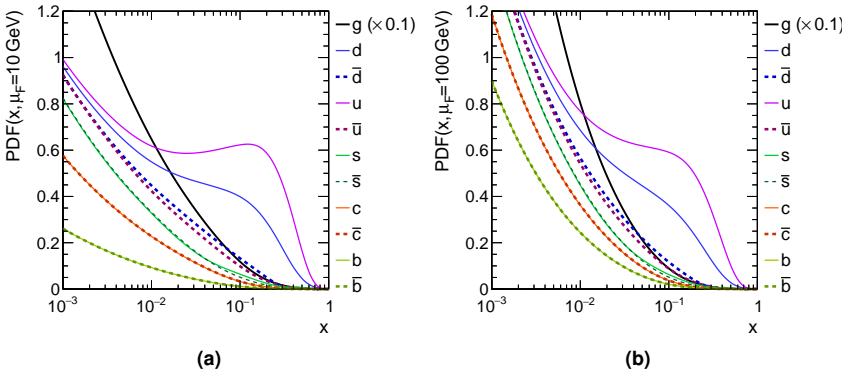


Figure 1.2. || NNPDF 3.0 NNLO PDF set in 5 flavor scheme for $\alpha_s(m_Z) = 0.118$ and factorization scales of (a) 10 GeV and (b) 100 GeV. The gluon PDF has been scaled down by a factor of 0.1.

At high energies, quantum fluctuations lead to divergences. In order to let a theory still describe the experimental energy regime, physical quantities are redefined at the so-called “renormalization scale” μ_R . This leads amongst others to a “running” behavior of the coupling constants as a function of μ_R . Beyond this scale, high energy effects such as loop corrections to propagators (“self-energy”) are absorbed in the physical quantities through a renormalization of the fields. In particular, the running behavior of the strong coupling constant is found to be

$$\alpha_s(\mu_R) = \frac{\alpha_s(\mu_0^2)}{1 + \alpha_s(\mu_0^2) \cdot \frac{33 - 2 \cdot n_f}{12\pi} \cdot \ln\left(\frac{|\mu_R^2|}{\mu_0^2}\right)}, \quad (1.36.)$$

where n_f denotes the number of quarks and μ_0 is a reference scale where the coupling is known from measurements, e.g. $\mu_0 = m_Z$. The current world average of the strong coupling constant at the Z boson mass is estimated to be $\alpha_s(m_Z) = 0.1181 \pm 0.0011$ [1].

Quarks can be treated as “asymptotically free” since the strong coupling decreases towards larger energies. On the other hand, following the behavior of $\alpha_s(\mu_R^2)$ to lower energies, a limit $\Lambda_{\text{QCD}} \approx 200$ MeV is found at which α_s becomes even larger than one. Below such energies, perturbative calculations of observables can no longer be performed (see Sec. 1.5).

1.5. Observables

A particle scattering process or decay is fully characterized by the initial and final state particles as well as the interactions between them. Typical experimental observables are inclusive and differential cross sections as well as decay rates which can be calculated using perturbation theory. The cornerstone of such a calculation is the scattering matrix (S-matrix) which describes the transition probability of a system from an initial to a final multiparticle state as $|\langle i | \mathcal{S} | f \rangle|^2$. In the Heisenberg picture the S-matrix is given by the Dyson series

$$\begin{aligned}\mathcal{S} &= T \left[\exp \left(-i \int d^4x \mathcal{H}_{\text{int}}(t) \right) \right] \\ &= \sum_{n=0}^{\infty} \frac{(-i)^n}{n!} \int_{-\infty}^{\infty} d^4x_1 \dots \int_{-\infty}^{\infty} d^4x_n T \left[\mathcal{H}_{\text{int}}(t_1) \dots \mathcal{H}_{\text{int}}(t_n) \right],\end{aligned}\quad (1.37.)$$

where particle interactions are described within the non-free part of the Hamiltonian density $\mathcal{H}_{\text{int}} = \mathcal{H} - \mathcal{H}_{\text{free}}$. The operator T ensures that products of $\mathcal{H}_{\text{int}}(t_i)$ are ordered by time. The transition amplitude from an initial to a final multiparticle state with particles $\psi_i^{\text{in/out}}$ respectively is then given by

$$\mathcal{A}_{\text{in} \rightarrow \text{out}} = \langle \psi_1^{\text{out}} \dots \psi_{N'}^{\text{out}} | \mathcal{S} | \psi_1^{\text{in}} \dots \psi_N^{\text{in}} \rangle \quad (1.38.)$$

$$= \underbrace{\langle \psi_1^{\text{out}} \dots \psi_{N'}^{\text{out}} | \psi_1^{\text{in}} \dots \psi_N^{\text{in}} \rangle}_{\text{no interaction}} + i\mathcal{M}(2\pi)^4 \delta^4(\sum p_i^{\text{in}} - \sum p_j^{\text{out}}) \quad (1.39.)$$

where the matrix element (ME), denoted \mathcal{M} , captures the interaction terms at all orders of the perturbative series. If $\mathcal{H}_{\text{int}} > 1$ the series does not converge and one says the problem is not solvable perturbatively. For instance, the ground states of hadrons can not be calculated perturbatively because of the running of the strong coupling constant. An alternative approach based on lattice gauge theory allowed to solve this problem [38].

For a scattering process, given a flux $L = \rho v$ of incoming particles with density ρ and velocity v , the cross section σ is defined as the number of interactions per unit density ($\rho = 1$). It is usually denoted in the unit ‘‘barn’’ [b] which is defined as $1 \text{ b} \equiv 10^{-28} \text{ m}^2$. The number of interaction events per time is given by $dN/dt = L\sigma$. The flux L is commonly referred to as luminosity. In the case of hadron-hadron collisions the total cross section can be calculated from the partonic cross section $\sigma(f_i f_j \rightarrow X)$ for a given process as

$$\sigma(pp \rightarrow X) = \sum_{i,j} \iint dx_1 dx_2 \text{PDF}(x_1, f_i) \text{PDF}(x_2, f_j) \sigma(f_i f_j \rightarrow X), \quad (1.40.)$$

where additional summations and integrations over the PDFs are required to account for the individual contributions per incoming parton flavor f_i and momentum fraction x_i .

Cross sections can be written in terms of the number of interaction vertices contributing to \mathcal{M} originating from elements of the perturbative series (Eq. 1.37). This allows to expand them as a power series in terms of the coupling constant α as

$$\sigma = \sigma_{\text{LO}} \cdot \left(1 + \left(\frac{\alpha}{2\pi} \right) \cdot \sigma_1 + \left(\frac{\alpha}{2\pi} \right)^2 \cdot \sigma_2 + \left(\frac{\alpha}{2\pi} \right)^3 \cdot \sigma_3 + \dots \right). \quad (1.41.)$$

Depending at which term the series is cut off one speaks of leading order (LO), next-to-leading order (NLO), or next-to-next-to-leading order (NNLO) accuracy in α . In general, it is desirable to calculate observables beyond LO. Predictions including higher order corrections tend to be less affected by theoretical uncertainties which originate from a variation of the chosen renormalization and factorization scales^(*).

The optical theorem, which can be derived from the unitarity of the S-matrix ($S^\dagger S = 1$), states that the imaginary part of a forward scattering amplitude $\mathcal{M}(i \rightarrow f)$ is directly related to the total scattering amplitude of producing all possible intermediate particles $\sum_X \mathcal{M}^\dagger(i/f \rightarrow X)$ from the initial or final state. Since a total cross section is at least as big as the single forward scattering cross section one finds that the matrix elements \mathcal{M} are bound and cannot be arbitrary large. Nonetheless, a theory may describe experimental data well but violate the unitarity bound at higher energies. Such a case would hint towards a new physics model which restores unitarity by introducing new particles or interactions above the experimentally probable energy regime. This is called ultraviolet (UV) completion. Hence, a unitarity-violating theory may just reflect the low energy limit of an unknown UV-complete theory. Exemplary, the $W^+ W^- \rightarrow W^+ W^-$ scattering amplitude would grow as $\mathcal{M} \sim s/m_W^2$ if there is no Higgs boson and eventually violate unitarity at $\sqrt{s} \approx 1$ TeV.

1.6. Open questions

The SM is believed to be not the final theory describing fundamental interactions. In the following some of its problems are briefly outlined.

Gravity The SM cannot describe gravitational interactions. The mediator of gravity, the graviton, would have to be a spin 2 boson which however leads non-renormalizable divergences. At energy scales reached by colliders, it is fine nonetheless to ignore gravitational interactions since those become only comparable in strength to the electroweak and strong interactions at the Planck scale which is $\mathcal{O}(10^{18}$ GeV) if there are no extra dimensions.

Naturalness A large correction to the bare Higgs boson mass originates from top quark loops via Yukawa interactions. Those need to be absorbed by the physical Higgs mass through renormalization. The resulting mass can be written as $m_H^2 \approx (m_H^{\text{bare}})^2 + \lambda_t^2 \mu^2 / (16\pi^2)$. If the SM is valid up to the Planck scale it would require an extraordinary fine-tuning of the bare Higgs mass in order to cancel this large correction. Such a coincidence is considered to be not very “natural”.

Dark matter and dark energy Cosmological observations of rotation speeds of galaxies, mapping of matter distributions through micro-lensing, and acoustic oscillations in the cosmic microwave background suggest that there exists a yet unidentified kind of matter, called “dark matter”. An even more puzzling building block of the universe which is missing from the SM is dark energy. It is a crucial ingredient to describe the expansion of the universe.

^(*) Partonic LO cross sections (without loops) can only be monotonous functions of μ_R since $\sigma \propto \alpha(\mu_R)$. Hence an uncertainty due to a scale variation can be even considered meaningless.

2.

Chapter

The top quark

A theoretical introduction to the top quark, its properties and production mechanisms, is given in this chapter. A feature of the top quark is that its spin orientation is preserved in decays due to an interplay between its high mass and electroweak interactions which allows to study the coupling structure of various processes. In particular, aspects of the production of single top quarks in t channel via W boson exchange are detailed. Furthermore, BSM production mechanisms, detectable through an alteration of the Wtb coupling structure, are discussed which can be characterized using effective field theory. The chapter is concluded with a discussion of recent experimental results.

The top quark is the heaviest known fundamental particle so far. Its high mass of $m_t = 172.44 \pm 0.49$ GeV [3] is close to the minimum of the Higgs potential. From Eq. 1.26b one obtains

$$\mathcal{L}_{\text{top-Yukawa int.}} = -\frac{\lambda_t v}{\sqrt{2}} \cdot \bar{t}_L t_R - \frac{\lambda_t}{\sqrt{2}} \cdot H \bar{t}_L t_R + \text{h.c.}, \quad (2.1.)$$

which yields a Yukawa coupling strength of

$$|\lambda_t| = \frac{\sqrt{2} m_t}{v} = 0.991 \pm 0.003. \quad (2.2.)$$

All other Yukawa couplings in the SM are however of the order $\mathcal{O}(10^{-2})$ instead. The top quark may therefore play an important role in understanding the mechanisms of electroweak symmetry breaking itself. Furthermore, top quarks are excellent probes to search for BSM physics. For example, many extensions of the SM predict additional W' and Z' bosons which are heavier versions of their SM counterparts and can decay into top quarks. Other BSM models can have an extended Higgs sector including additional neutral and charged Higgs bosons which may couple to top quarks predominantly due to its high mass (see Ref. [39] and references therein).

Historically, the top quark was discovered in 1995 by the CDF [40] and DØ [41] collaborations at the Tevatron collider at Fermilab using proton-antiproton collision data. They observed the production of top quark-antiquark pairs which occurs through strong interactions. Already before the direct observation of this process an attempt to explain CP-violation by introducing the CKM matrix and hence postulating a third quark generation [42] which was followed by the discovery of the bottom quark [43,44] hinted strongly towards the top quark's existence. Another milestone in top quark research was the observation of single-top-quark production which occurs through electroweak interactions only. This process was discovered in 2009 at the Tevatron collider as well [45,46]. The lower cross section together with the overwhelming back-

ground necessitated the use of sophisticated analysis techniques such as multivariate classifiers and the matrix element method [47].

With the start of the physics program at the LHC in 2009, the production mechanisms of top quarks can be probed with unprecedented precision. This thesis focuses on the electroweak production of single top quarks at center-of-mass energies of 8 TeV and 13 TeV.

2.1. Decay and W boson polarization

The top quark decays into a W boson and a b quark almost exclusively due to the CKM matrix element V_{tb} which is found experimentally to be $V_{tb} \gg V_{ts}, V_{td}$ and close to 1 (see Eq. 1.30). The decay via electroweak interactions is favored since $m_W < m_{\text{top}}$ and thus the W boson can be on-shell. This leads to a very short lifetime of only $1/\Gamma_t \approx 5 \cdot 10^{-25}$ s [1] which does not allow the formation of bound states involving top quarks [48]. Furthermore, the lifetime is even shorter than the typical hadronization timescale of $1/\Lambda_{\text{QCD}} \approx 10^{-23}$ s. Hence, soft gluons cannot radiate from the top quark before it decays which keeps its spin coherent. The top quark spin orientation can be inferred from the angular distributions of its decay products since electroweak interactions via W boson exchange feature a V-A coupling structure. This offers the possibility to study the polarization of top quarks from angular distributions in various processes. For such studies, a spin axis has to be chosen along which the top quark spin is quantized.

In the leptonic top quark decay chain $t \rightarrow b\ell\nu$ the polarization states of the W boson can be investigated independent of the production process [49]. The top quark decay width is decomposed into

$$\frac{d\Gamma}{\Gamma \cdot d \cos \theta_W^*} = \frac{3}{8} (1 - \cos \theta_W^*)^2 F_L + \frac{3}{8} (1 + \cos \theta_W^*)^2 F_R + \frac{3}{4} \sin^2 \theta_W^* F_0, \quad (2.3.)$$

where F_L , F_R , and F_0 denote the left-, right-handed, and longitudinal polarization fractions of the W boson respectively. They are dimensionless form factors and normalized as $F_L + F_R + F_0 = 1$. The angle

$$\cos \theta_W^* = \frac{\vec{s}_W \cdot \vec{p}_\ell^{(W)}}{|\vec{s}_W| \cdot |\vec{p}_\ell^{(W)}|} \quad (2.4.)$$

is taken between the lepton momentum $\vec{p}_\ell^{(W)}$ in the W boson rest frame and a spin quantization axis \vec{s}_W . A common choice is the helicity basis where the reversed top quark momentum in the W boson rest frame $\vec{s}_W = -\vec{p}_t^{(W)}$ is used to quantize the spin of the W boson^(*). Figure 2.1a shows the Feynman diagram of leptonic top quark decays involving two electroweak vertices, Wtb and $W\ell\nu$, which feature both a V-A coupling structure. The polarization angle in the helicity basis is shown in Fig. 2.1b where the top quark decay chain is drawn in the W boson rest frame.

Potential scenarios of spin orientations at the Wtb vertex are presented in Fig. 2.2 for longitudinal ($H = 0$), left-handed ($H = -1$), and right-handed ($H = +1$) W bosons in

^(*) There are multiple equivalent definitions in literature for the helicity basis: $\vec{s}_W = -\vec{p}_t^{(W)} = \vec{p}_W^{(t)} = \vec{p}_b^{(W)}$. It should be noted that multiple sequential boosts into various rest frames are Lorentz-invariant but can induce unwanted rotations.

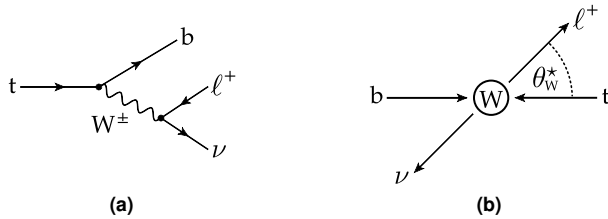


Figure 2.1. | Decay of the top quark through W boson exchange: (a) Feynman diagram; (b) helicity angle in W boson rest frame.

the top quark rest frame. In the last scenario the conservation of angular momentum forces the b quark to be right-handed. This is however suppressed by the electroweak V-A coupling structure leading to a nearly vanishing probability at LO. It would vanish entirely for massless b quarks since then the b quark helicity would be equal to its chirality [50]. The expected distributions per helicity state as a function of $\cos\theta_W^*$ are shown in Fig. 2.3 together with the NNLO SM expectation of $F_L = 0.311 \pm 0.005$, $F_R = 0.0017 \pm 0.0001$, and $F_0 = 0.687 \pm 0.005$ [51]. The non-zero but small right-handed helicity fraction arises from the non-zero mass of the b quark and from the considered corrections beyond LO to the vertices.

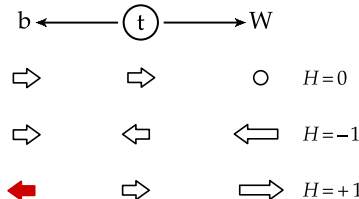


Figure 2.2. | Scenarios of spin orientations at the Wtb vertex in the top quark rest frame. The right-handed W boson helicity ($H = +1$) is suppressed by the electroweak V-A coupling structure which does not allow the right-handed b quark (marked in red) to interact.

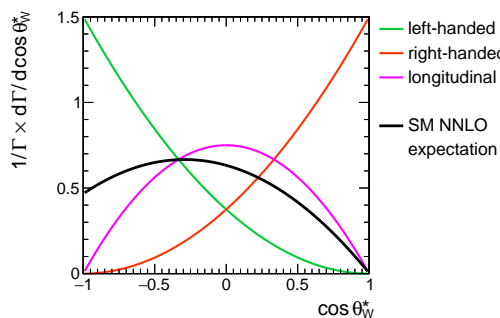


Figure 2.3. | Distributions of the helicity angle for various W boson helicity scenarios. The SM expectation at NNLO is taken from Ref. [51].

For a general analysis of the top quark spin one introduces the so-called “spin-analyzing power”, $\alpha_X \in [-1; 1]$, of the decay product $X = \ell, \nu, W, b$ [49]. It denotes

the fraction of instances when the top quark spin is aligned along the momentum of the spin analyzer in the top quark rest frame. The calculated spin-analyzing powers at LO and NLO in the SM are listed in Tab. 2.1. Additionally, the spin-analyzing powers for $X = q/q'$ for $W \rightarrow qq'$ decays are provided where q (q') denotes all up-type (down-type) quarks respectively. However, studying the top quark spin in those decays is experimentally very challenging since the original quark flavor of a jet and its origin in case of additional final state radiation are difficult to infer. The spin-analyzing powers flip their sign $\alpha_X = -\alpha_{\bar{X}}$ in the case of top antiquark decays for the corresponding particle or antiparticle. This holds also in BSM scenarios inducing CP-violation in the top quark sector.

Table 2.1. | Spin-analyzing power per top quark decay product. The values are taken from Ref. [49] and references therein.

Decay product X	spin-analyzing power α_X	
	LO	NLO
ℓ^+	1.00	0.998
ν	-0.32	-0.33
\bar{q}' (down-type)	1.00	0.93
q (up-type)	-0.32	-0.31
b	-0.41	-0.39
W^+	0.41	0.39

The charged lepton is a nearly perfect spin analyzer for studying the top quark polarization. Its spin-analyzing power is even larger than that of its mother particle, the W boson, due to constructive (destructive) interference of the longitudinal and left-handed W boson helicity states in cases when the lepton is aligned (antialigned) with the top quark spin, respectively [50]. Simplified sketches of various spin orientations for longitudinal and left-handed W boson helicities are shown in Fig. 2.4 demonstrating that the momentum of the charged antilepton in the top quark rest frame tends to be aligned along the top quark spin. Scenarios with antialigned lepton momentum with respect to the top quark spin (Figs. 2.4b and 2.4d) are suppressed by the V-A coupling structure which does not allow right-handed particles or left-handed antiparticles to interact. Similar diagrams with reversed spin orientations are expected for top antiquarks.

2.2. Pair production

The dominant mechanism producing top quarks at hadron colliders is top quark pair production through strong interactions via gluon ($gg \rightarrow t\bar{t}$) or quark fusion ($q\bar{q} \rightarrow t\bar{t}$). Figure 2.5 shows the corresponding Feynman diagrams at LO. Especially the production channel via gluon fusion leads to a large cross section at the LHC compared to the Tevatron because of the steeply increasing gluon PDF towards smaller momentum fractions. The $gg \rightarrow t\bar{t}$ channel contributes approximately 80–90% to the total $t\bar{t}$ production cross section in the LHC center-of-mass energy regime of 7–14 TeV [1]. The theoretical $t\bar{t}$ cross sections in pp collisions at center-of-mass energies of 8 and 13 TeV, relevant for

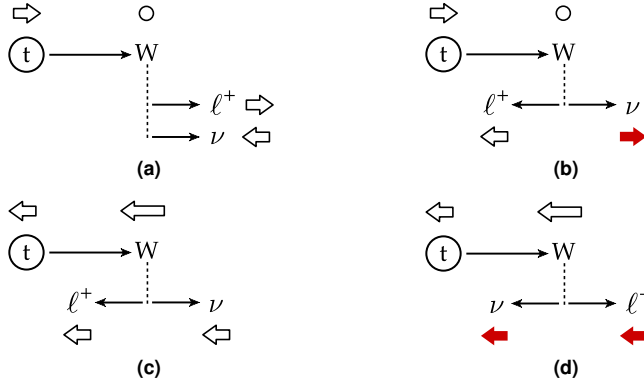


Figure 2.4. | Sketches of various spin orientations in top quark decays for (a,b) longitudinal and (c,d) left-handed W boson helicities. Suppressed spin orientations are marked in red.

this thesis are listed in Tab. 2.2. Those have been calculated at NNLO+NNLL accuracy using the `Top++ 2.0` program [52,53] assuming a top quark mass of 172.5 GeV. The PDF uncertainty includes also the uncertainty on α_s .

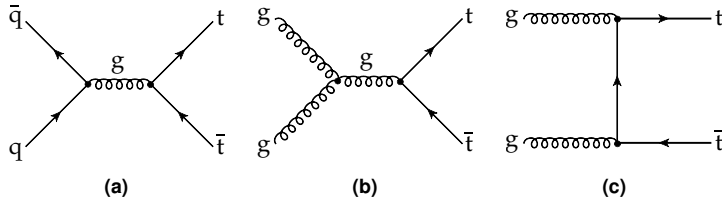


Figure 2.5. | Feynman diagrams of $t\bar{t}$ production at LO: (a) quark fusion; (b,c) gluon fusion.

Table 2.2. | Top quark pair production cross sections per center-of-mass energy.

Center-of-mass energy	Cross section
8 TeV	$252.9^{+6.4}_{-8.6}$ (scale) ± 11.7 (PDF) pb
13 TeV	$831.8^{+19.8}_{-29.2}$ (scale) ± 35.6 (PDF) pb

2.3. Single-top-quark production

Besides producing top quarks in pairs single top quarks can be produced through electroweak interactions as well. At LO one can categorize the production into three main channels depending on the exchanged W boson and its virtuality, $Q^2 = -p_\mu p^\mu$. The corresponding Feynman diagrams are presented in Fig. 2.6. Overall, the single-top-quark cross sections are smaller than for pair production due to the electroweak coupling strength $\alpha_W < \alpha_s$. Additionally, the requirement of sea quarks (b, \bar{q}) in the initial states whose PDFs increase less steeply at low momentum fractions compared to the gluon PDF suppresses the cross sections further (see Fig. 1.2).

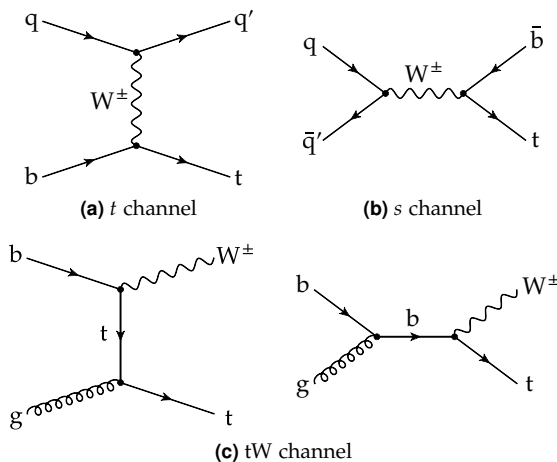


Figure 2.6. | Feynman diagrams of electroweak single-top-quark production at LO in the 5 flavor scheme.

t channel The production via *t*-channel (Fig. 2.6a) has the highest single-top-quark cross section in pp collisions. The virtuality of the W boson is found to be $Q^2 > 0$ and hence it is said to be “space-like”. A characteristic feature of this mode is the production of an additional spectator quark (q') which recoils against the W boson and tends therefore to be scattered fairly forward in the CMS detector ($|\eta| \sim 3$). In this production mode top quarks are produced roughly twice more often than top antiquarks which is a consequence of the up-over-down valence quark composition of the proton. Hence the production ratio, $\sigma(t)/\sigma(\bar{t})$, is sensitive to the PDF of the proton. The ratio depends however on the center-of-mass energy since at higher energies lower momentum fractions are probed at which contributions from the valence quarks become less dominant.

s channel Amongst the three main single-top-quark production channels the one with the smallest cross section is the s channel (Fig. 2.6b). This is because of the “time-like” W boson ($Q^2 < 0$) which has to have a large virtuality to produce the heavier top quark. In various BSM scenarios however the cross section of this process is expected to increase due to new heavy particles such as W' or charged Higgs bosons which may even be produced on their mass shell, $p_\mu p^\mu - m^2 = 0$, and hence occur as a resonance.

tW The third mode is the production of a single top quark in association with a W boson (Fig. 2.6c) where the latter can be produced on-shell $Q^2 = -m_W^2$. It is commonly referred to as “tW channel”. This process interferes at NLO with t̄t production which complicates its definition. In the diagram removal (DR) scheme diagrams with two resonant top quarks are subtracted from the common amplitude whereas in the diagram subtraction (DS) scheme the contribution from t̄t is locally removed from the cross section [54, 55]. The difference between both schemes lies in the treatment of the interference term which is kept in the DS but removed in the DR. A new approach has been developed where the t̄t and tW

production and the inference between them are combined into a process with a $W^+W^-b\bar{b} + X$ final state [56] whose simulation is currently being studied [57].

The theoretical cross sections of the three single-top-quark production modes in pp collisions for center-of-mass energies of 8 and 13 TeV, relevant for this thesis, are listed in Tab. 2.3. These have been calculated at NLO in QCD with the HATHOR v2.1 program [58, 59] using a top quark mass of $m_t = 172.5$ GeV while setting the factorization and renormalization scales to $\mu_R = \mu_F = m_t$. The PDF uncertainty includes also the uncertainty on α_s .

Table 2.3. || Single-top-quark cross sections per production mode and center-of-mass energy.

Mode	Cross section / center-of-mass energy	
	8 TeV	13 TeV
t channel	$84.7^{+2.6}_{-1.7}$ (scale) ± 2.8 (PDF) pb	$217.0^{+6.6}_{-4.6}$ (scale) ± 6.2 (PDF) pb
tW channel	22.4 ± 0.6 (scale) ± 1.4 (PDF) pb	71.7 ± 1.8 (scale) ± 3.4 (PDF) pb
s channel	$5.24^{+0.15}_{-0.12}$ (scale) ± 0.16 (PDF) pb	$10.32^{+0.29}_{-0.24}$ (scale) ± 0.27 (PDF) pb

Measurements of single-top-quark cross sections allow to extract a limit on the CKM matrix element V_{tb} . If one assumes $|V_{td}|^2 + |V_{ts}|^2 \ll |V_{tb}|^2$ then the $t \rightarrow bW$ branching ratio can be approximated as

$$\mathcal{B}(t \rightarrow bW) = \frac{|V_{tb}|^2}{\underbrace{|V_{td}|^2 + |V_{ts}|^2 + |V_{tb}|^2}_{\ll |V_{tb}|^2}} \approx 100\%. \quad (2.5.)$$

Hence, the cross section is independent of the top quark decay vertex and therefore directly proportional to $|f_L \cdot V_{tb}|^2$. The form factor f_L is introduced to absorb potential contributions from BSM physics that modify the left-handed coupling strength. It is $f_L^{SM} = 1$ in the SM. A measured single-top-quark cross section can then be used to extract the value of $|f_L V_{tb}|$ as

$$|f_L V_{tb}| = \sqrt{\frac{\sigma_{\text{measured}}}{\sigma_{\text{theory}}}}. \quad (2.6.)$$

It should be noted that for this interpretation of single-top-quark cross sections no assumptions on the number of quark generations and subsequently no unitarity of the CKM matrix is required.

2.4. Polarization in t -channel single-top-quark production

The SM predicts that top quarks are produced highly polarized via t channel since there are only electroweak interactions with a V-A coupling structure involved at LO [50]. New BSM physics models may however lead to a depolarization by altering the coupling structure effectively through new production vertices and/or higher order corrections. The differential cross section as a function of the polarization angle can be parametrized as

$$\frac{d\sigma}{\sigma \cdot d \cos \theta_X^*} = \frac{1}{2} \left(1 + P_t \cdot \alpha_X \cdot \cos \theta_X^* \right), \quad (2.7.)$$

where P_t denotes the polarization along a given axis and α_X the spin-analyzing power with respect to the decay product X . The polarization angle

$$\cos \theta_X^* = \frac{\vec{s}_t \cdot \vec{p}_X^{(t)}}{|\vec{s}_t| \cdot |\vec{p}_X^{(t)}|} \quad (2.8.)$$

is calculated between the spin analyzer X in the top quark rest frame and a suitable spin quantization axis \vec{s}_t . A potential spin axis is given in the helicity basis where the top quark momentum in the partonic center-of-mass system is chosen, $\vec{s}_t^{\text{hel.}} = \vec{p}_t^{(tq)}$. However, this system cannot be reconstructed unambiguously beyond LO when additional initial state radiation (ISR) or final state radiation (FSR) occurs. An alternative axis is motivated in Fig. 2.7 where exemplary spin orientations in the top quark rest frame for t -channel production and decay are sketched. There exists a symmetry between the down-type spectator quark on the production side (q') and the charged antilepton on the decay side (ℓ^+) leading to a correlation between their momentum directions and the intermediate top quark spin. This suggests to take the spectator quark momentum in the top quark rest frame as the spin quantization axis, $\vec{s}_t = \vec{p}_q^{(t)}$. At LO, this axis would coincide with the axis in helicity basis since the top quark and the spectator quark are back-to-back in the center-of-mass system [60]. A high degree of polarization can therefore be expected when quantizing the top quark spin along the spectator quark momentum. This is further motivated by the fact that the charged lepton is a nearly perfect spin analyzer and thus the down-type spectator quark is a good spin analyzer as well because of the depicted symmetry. Higher-order corrections however dilute this symmetry somewhat as also expected from Tab. 2.1 where a slightly lower spin-analyzing power for the down-type quark compared to the charge lepton is expected at NLO.

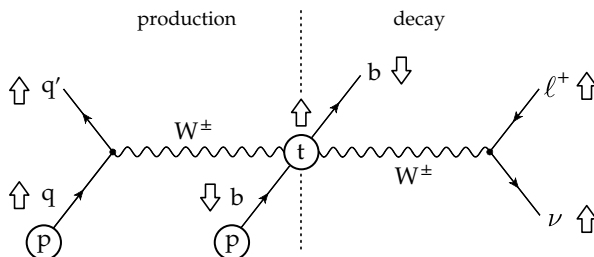


Figure 2.7. || Sketch of spin orientations in t -channel single-top-quark production and decay. The figure has been inspired from Ref. [60].

A crucial ingredient which is however missing in this argumentation is the fact that the spectator quark has to be of down-type flavor for obtaining a high polarization. This is true in about 80% for t -channel top quark production but only in 31% of all cases for top antiquark production. In such events the down-type quark is found with a probability of 69% in the initial state instead. However, the spectator quark is only mildly deflected after recoiling against the W boson. It is therefore still sufficiently

close to the direction of the down-type quark momentum which results in a high degree of polarization nonetheless [50].

The expect degrees of polarization for the top quark and top antiquark have been calculated at 7 TeV and are listed in Tab. 2.4 at LO and NLO accuracy. The combined polarization for top quark and antiquark is obtained using a weighted sum with the corresponding cross sections as weights^(*). At 8 TeV, a similar polarization of $|P_{t+\bar{t}}^{8 \text{ TeV}}| = 0.88$ is expected using simulated events from the NLO generator PowHeg [61].

Table 2.4. | Expected polarizations of top quarks and top antiquarks in t -channel single-top-quark production at 7 TeV. The values are taken from Ref. [60].

	$P_t^{7 \text{ TeV}}$	$P_{\bar{t}}^{7 \text{ TeV}}$	$ P_{t+\bar{t}}^{7 \text{ TeV}} $
LO	0.99	-0.93	0.95
NLO	0.91	-0.86	0.88

The high polarization of the top quark along the spectator quark momentum allows also to extend the W boson polarization with two additional axes. Figure 2.8 shows the construction procedure. The top quark spin is approximated by the spectator quark momentum. Then the normal and transverse axes are defined as

$$\vec{N} = \vec{p}_{q'}^{(t)} \times \vec{p}_W^{(t)} \quad (\text{normal axis}), \quad (2.9a.)$$

$$\vec{T} = \vec{p}_W^{(t)} \times \vec{N} \quad (\text{transverse axis}). \quad (2.9b.)$$

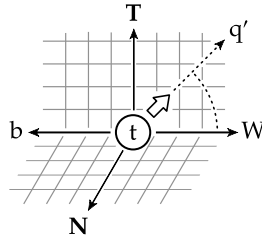


Figure 2.8. | Extended W boson polarization axes in t -channel single-top-quark production and decay: N = normal axis; T = transverse axis.

The differential cross sections as a function of the polarization angles with respect to these new axes take the same functional form as in Eq. 2.3. However, the corresponding polarization fractions $F_L^{N,T}$, $F_0^{N,T}$, and $F_R^{N,T}$ are probing different aspects of the coupling structure. In particular, the left- and right-handed polarization along \vec{N} are sensitive to potential CP-violation [49]. Since the top quark is not fully polarized along the

^(*) The expected single-top-quark cross sections at 7 TeV are $\sigma(t) = 41.8_{-1.5}^{+1.8}$ pb and $\sigma(\bar{t}) = 22.0_{-1.2}^{+1.3}$ pb. These are calculated with the same setup as used for Tab. 2.3

spectator quark momentum, the polarization fractions are modified as

$$\tilde{F}_R^{N,T} = \frac{1+P_t}{2} \cdot F_R^{N,T} + \frac{1-P_t}{2} \cdot F_L^{N,T}, \quad (2.10a.)$$

$$\tilde{F}_L^{N,T} = \frac{1+P_t}{2} \cdot F_L^{N,T} + \frac{1-P_t}{2} \cdot F_R^{N,T}, \quad (2.10b.)$$

$$\tilde{F}_0^{N,T} = F_0^{N,T}. \quad (2.10c.)$$

2.5. Flavor schemes

In single-top-quark production via t channel a b quark is required in the initial state. There are two approaches called 4 and 5 flavor scheme (FS) to treat initial state b quarks in theoretical calculations. They differ in the number of quark flavors considered within the PDF of the proton. Figure 2.9 shows a representative Feynman diagram where in the 4 FS the b quark originates from gluon splitting and is not part of the PDF. On the other hand this splitting is resumed into the PDF in the 5 FS instead.

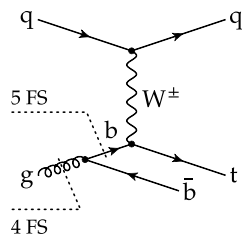


Figure 2.9. | Feynman diagram at LO for t -channel single-top-quark production in 4 and 5 FS. The dashed lines denote where the partonic initial state begins.

Since the b quark mass of $m_b \approx 4.2$ GeV is higher than the mass of the proton ($m_p \approx 1$ GeV) the 4 FS seems more natural at first glance. The b quark is treated as a heavy quark state that decouples completely from the α_s and PDF evolutions through renormalization and the DGLAP equation, respectively. However, this approach results in terms proportional to $\log(Q^2/m_b^2)$ arising from the intermediate b quark propagator which may prohibit the convergence of perturbative calculations at high momentum transfers Q . In this case, such terms together with the $g \rightarrow b\bar{b}$ splitting function can be absorbed into a PDF for the b quark instead which yields the 5 FS [62].

Both schemes are valid approaches for calculating observables. The difference between them at fixed order lies in their dependence on the energy scale at which a process is described. The predictions by both schemes will thus converge if calculated at sufficiently high orders. This is demonstrated in Fig. 2.10a where the t -channel single-top-quark cross section at 14 TeV as a function of the renormalization and factorization scale is depicted. The dashed curves show the LO predictions in 4 and 5 FS respectively which are far apart. Their opposite behavior originates from the running of coupling constant α_s in the 4 FS versus the scale dependence of the b quark PDF in the 5 FS as depicted in Fig. 2.10b. Both approach the NLO prediction only at low (large) scales for 4 FS (5 FS) respectively. On the other hand, the NLO predictions start to converge already at a scale choice of about $\mu_R = \mu_F = m_t/2$ for this process.

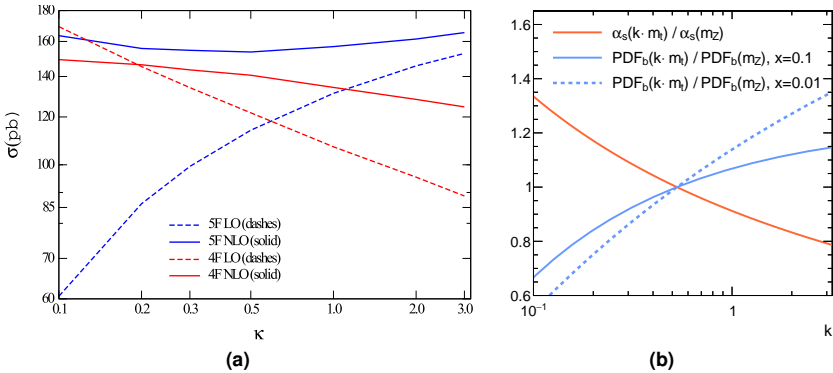


Figure 2.10. In (a): single-top-quark cross section in t channel for top quarks at 14 TeV as a function of the renormalization and factorization scale $\kappa = \mu/m_t$. The cross sections have been calculated in 4 and 5 FS at LO and NLO. The figure is taken from Ref. [62]. In (b): the relative dependence of the strong coupling constant and the b quark PDF (NNPDF3.0) on the scale κ with respect to their values at the Z boson mass.

Fixed-order predictions of differential cross sections are also sensitive to the flavor scheme choice. Ratios of the 4 FS over the 5 FS t -channel cross sections at NLO as a function of the transverse momentum and pseudo rapidity with respect to the top quark and spectator jet are shown in Fig. 2.11. The differences between both schemes are found to be around the 10 % level [63]. In particular, the top quark p_T displays here an almost linear increasing ratio.

2.6. Anomalous couplings

Direct searches for BSM physics can be viewed as a top-down approach. The starting point is marked by a well-defined and usually UV-complete BSM theory. Experimentally, one is then interested to detect additional events originating from a new process within such a theory. Exemplary models are the minimal super symmetric standard model (MSSM) (reviewed in Ref. [64]) or the two Higgs doublet model (2HDM) [65]. Since no signal has been found yet it may be that the energy scale at which a BSM process becomes significant is not accessible in direct searches. Nonetheless, potential new particles or interactions will contribute higher-order corrections to processes within the SM already at low energies. An example of such a process is the rare $B_s^0 \rightarrow \mu^+ \mu^-$ decay [66] which can be altered by contributions from e.g. the MSSM. This motivates a model-independent bottom-up approach where observables of the SM are measured with great precision and compared to their expectation. Any deviations can then be interpreted within multiple new theories.

The idea of a bottom-up approach is depicted in Fig. 2.12 for some exemplary UV-complete theory contributing to single-top-quark production through a new heavy scalar particle χ . If the new particle has a sufficiently high mass it would not be possible to observe it as a new resonance in s channel. However, the shown production of single top quarks would be altered through additional contributions from this new process. At energies $q \ll m_\chi$ it would mimic a 4-fermion contact interaction with a

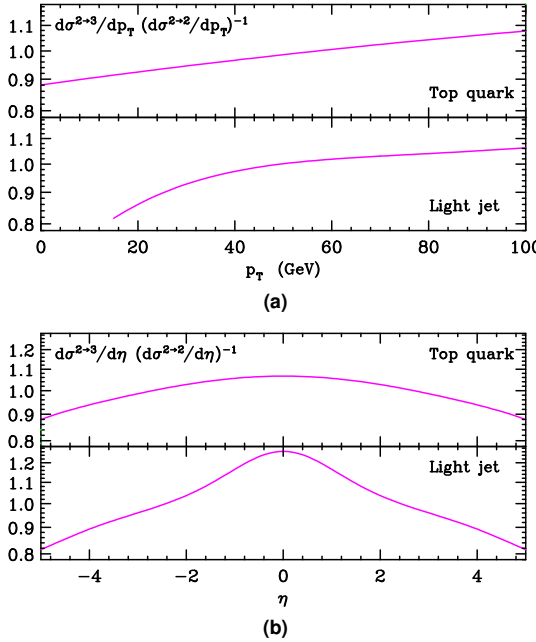


Figure 2.11. || Ratio of 4 FS ($\sigma^{2 \rightarrow 3}$) over 5 FS ($\sigma^{2 \rightarrow 2}$) differential NLO single-top-quark cross sections in t channel for top quarks at 14 TeV as a function of (a) the transverse momentum and (b) the pseudo rapidity of the top quark and light (spectator) jet. The figures are taken from Ref. [63]

simple scalar coupling structure. The SM+BSM inclusive cross section of this process may still correspond to the one expected from the SM alone by fine-tuning the SM and BSM couplings correspondingly. However, since this new process has a scalar coupling structure it manifests itself as a deviation from the expected V-A coupling structure of the SM. Differential cross section measurements and related observables like the top quark polarization can then be used to probe for such anomalous couplings at the production vertex.

Such deviations from the SM coupling structure can be characterized in the framework of effective field theories (EFTs) in a model-independent manner. Those can be derived using an operator product expansion (OPE) as first proposed in Ref. [67]. Here, products of operators are expanded as

$$O_1(x_1) \dots O_n(x_n) = \sum_i c_{1\dots n}^i(x_1, \dots x_n) \cdot O_i^{\text{eff}}(x_n), \quad (2.11.)$$

where O_i^{eff} denote effective operators and c^i are the so-called Wilson coefficients. The expansion is applicable if $x_{1\dots n-1}$ are close to x_n , i.e. only the low energy limit of a UV-complete theory is relevant. Otherwise, unitarity can be violated if the energy scale of a process within the EFT approaches the scale of the concrete BSM theory as discussed in Sec. 1.5. In the example above this would be the case when the momentum transfer q approaches m_χ at which the EFT approach becomes invalid.

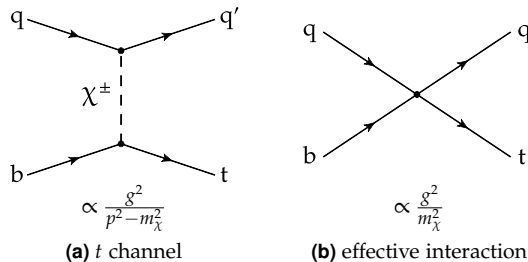


Figure 2.12. | Feynman diagram of potential BSM physics contributing to single-top-quark production via flavor-changing neutral current interaction. At low energies $p \ll m_\chi$ the propagator in (a) can be approximated as an anomalous 4-fermion coupling as shown in (b).

One can extend the Lagrangian of the SM, which contains only operators up to dimension-four, into an effective one as

$$\mathcal{L}^{\text{eff}} = \mathcal{L}_{(4)}^{\text{SM}} + \frac{1}{\Lambda} \sum_i c_i^{(5)} O_i^{(5)} + \frac{1}{\Lambda^2} \sum_i c_i^{(6)} O_i^{(6)} + \mathcal{O}\left(\frac{O^{(7)}}{\Lambda^3}\right), \quad (2.12.)$$

where new effective operators of dimension-five and -six have been added. Those are however suppressed by inverse powers of the new physics scale Λ . This approach leads to 59 independent operators of dimension-six when requiring gauge invariance and baryon number conservation [68]. The only operator of dimension-five is

$$\mathcal{L}_{(5)}^{\text{eff.}} = \frac{1}{\Lambda} c_{vv}^{ij} \left(E_{L,i}^c \tilde{\phi} \right) \left(E_{L,j} \tilde{\phi} \right) + \text{h.c.}, \quad \tilde{\phi}_i = \epsilon_{ij} \phi_j \quad (2.13.)$$

which can be used to introduce neutrino masses and mixing after electroweak symmetry breaking^(*). Only a subset of operators are relevant in the top quark sector [69]. In particular, the following operators contribute to the Wtb vertex

$$\mathcal{L}_{\text{Wtb}}^{\text{eff.}} = \mathcal{L}_{\text{Wtb}}^{\text{SM}} + \frac{1}{\Lambda^2} \left(c_{\phi q}^{33} O_{\phi q}^{33} + c_{\phi \phi}^{33} O_{\phi \phi}^{33} + c_{dW}^{33} O_{dW}^{33} + c_{uW}^{33} O_{uW}^{33} \right) + \text{h.c.}, \quad (2.14a.)$$

$$O_{\phi q}^{33} = i \left(\phi^\dagger \omega_a D_\mu \phi \right) \left(\bar{Q}_L^3 \gamma^\mu \omega^a Q_L^3 \right), \quad O_{\phi \phi}^{33} = i \left(\tilde{\phi}^\dagger D_\mu \phi \right) \left(\bar{u}_R^3 \gamma^\mu d_R^3 \right), \quad (2.14b.)$$

$$O_{dW}^{33} = \left(\overline{Q}_L^3 \sigma^{\mu\nu} \omega_a d_R^3 \right) \phi W_{\mu\nu}^a, \quad O_{uW}^{33} = \left(\overline{Q}_L^3 \sigma^{\mu\nu} \omega_a u_R^3 \right) \tilde{\phi} W_{\mu\nu}^a, \quad (2.14c.)$$

where D_μ denotes the covariant derivative (Eq. 1.16b) and the quark field indices refer to the third generation following the notation of Eqs. 1.12 and 1.13. Anomalous couplings can be introduced after electroweak symmetry breaking which absorb all constant terms including $c_i v^2 / (2\Lambda^2)$. One obtains

$$\mathcal{L}_{Wtb}^{\text{eff.}} = -\frac{g}{\sqrt{2}} \bar{b} \gamma^\mu (V_L P_L + V_R P_R) t W_\mu^-$$

^(*) This assumes Majorana neutrinos. The coefficients $c^{ij}v^2/(2\Lambda)$ after symmetry breaking can be interpreted as mass mixing matrix for neutrinos similar to the CKM matrix for quarks. The superscript c stands for charge conjugation.

$$-\frac{g}{\sqrt{2}} \bar{b} \frac{i\sigma^{\mu\nu} q_\nu}{m_W} (g_L P_L + g_R P_R) t W_\mu^- + \text{h.c.}, \quad (2.15.)$$

where $V_{L,R}$ and $g_{L,R}$ denote the vector- and tensor-like anomalous couplings respectively. In the SM (Eq. 1.29) there exists only a vector-like, left-handed coupling $V_L = V_{tb}$ whereas the other couplings vanish $V_R = g_L = g_R = 0$.

Another effective operator relevant for single-top-quark production is O_{qW}^{ij} which is however not associated to the effective Wtb interaction (Eq. 2.14). Its contribution can be mostly absorbed by the other operators as

$$\begin{aligned} \mathcal{L}_{qW} &= \frac{1}{\Lambda^2} c_{qW}^{ij} O_{qW}^{ij} = \frac{1}{\Lambda^2} c_{qW}^{ij} \left(\bar{Q}_{L,i} \gamma^\mu \omega_a D^\nu Q_{L,j} \right) W_{\mu\nu}^a + \text{h.c.} \\ &\supset (\text{terms } \propto \mathcal{L}_{Wtb}^{\text{eff.}}) + \frac{g \text{Re}(c_{qW})}{\Lambda^2} (\bar{b} \gamma^\mu P_L t) (\bar{q} \gamma_\mu P_L q') + \text{h.c.}, \end{aligned} \quad (2.16.)$$

where however a four-fermion contact interaction term remains [70]. This interaction does not contribute to top quark production and decays via a Wtb vertex directly which is why it is usually not added to Eqs. 2.14 and 2.15. However, the four-fermion vertex cannot be neglected when studying in particular single-top-quark production. Here, it can contribute a $udbt$ vertex (similar to Fig. 2.12b) as an addition to the $Wud+Wtb$ vertices which e.g. occurs in the production via t channel.

To investigate the presence of anomalous couplings in experimental data, various (pseudo) observables are proposed in literature [49, 71, 72]. A few of them are the inclusive single-top-quark cross sections, the W boson helicity fractions (Sec. 2.1), and the top quark polarization in t channel (Sec. 2.4).

2.7. Selection of experimental results

To conclude this chapter, a selection of experimental results in the top quark sector are presented. An overview of inclusive $t\bar{t}$ cross section measurements at center-of-mass energies of 5, 7, 8, and 13 TeV are shown in Fig. 2.13a and compared to the theoretical NNLO+NNLL prediction. Measurements of inclusive single-top-quark production in t , tW , and s channel at 7, 8, and 13 TeV are summarized and compared to the theoretical NLO predictions in Fig. 2.13b. These cross section measurements can be used to determine the absolute value of the CKM matrix element V_{tb} as detailed in Sec. 2.3. The results are presented in Fig. 2.14. The currently most precise estimation of V_{tb} stems from a combination of t -channel single-top-quark cross section measurements at 7 and 8 TeV by CMS resulting in $|f_L V_{tb}| = 0.998 \pm 0.038(\text{exp}) \pm 0.016(\text{theo})$. This yields a limit of $|V_{tb}| > 0.92$ at 95% CL when assuming $f_L = 1$ and $|V_{tb}| < 1$.

The results from measurements of the W boson helicity fractions are presented in Fig. 2.15 and compared to their NNLO prediction. These have been mostly obtained by analyzing top quark decays in $t\bar{t}$ events. However, one measurement uses decays of top quarks from t -channel single-top-quark production yielding a comparable precision [74].

Overall, the various measurements presented here show a good agreement with the SM prediction. Since no deviation is observed, limits on the anomalous couplings can be derived. Global fits of the anomalous couplings are however a complicated and

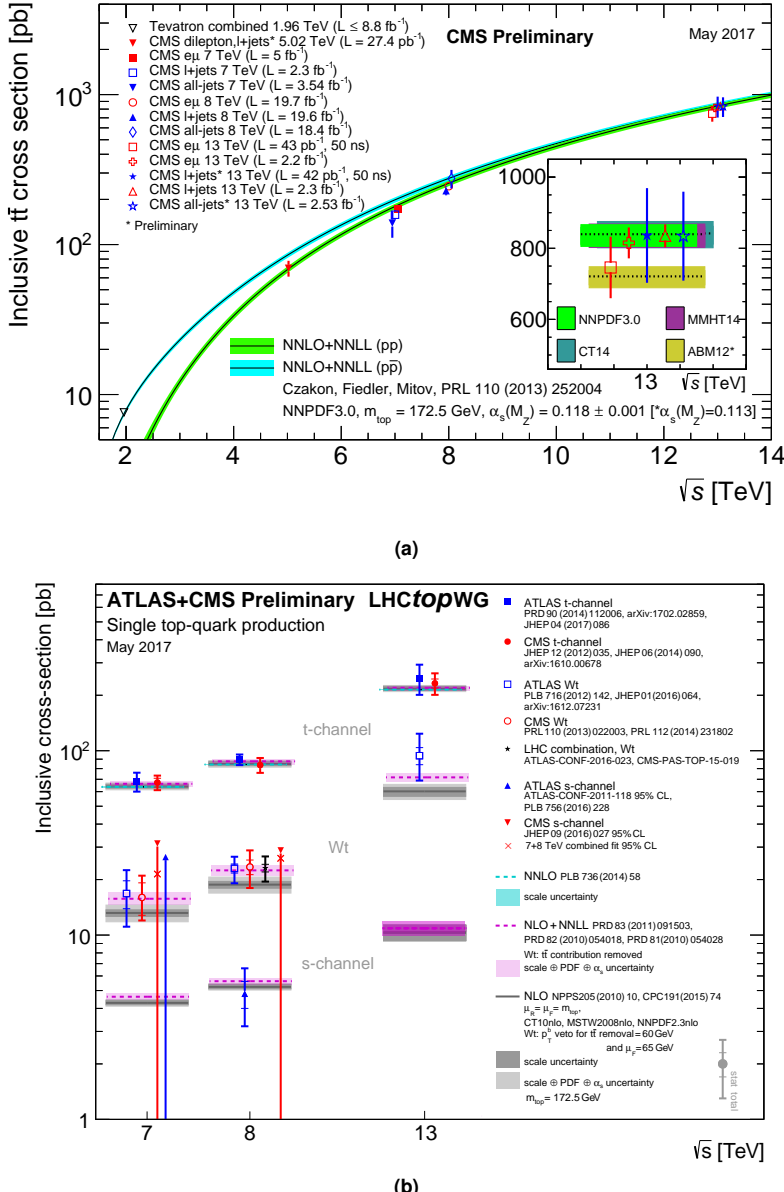


Figure 2.13. || Overview of inclusive (a) $t\bar{t}$ and (b) single-top-quark cross section measurements by the ATLAS and CMS collaborations at various center-of-mass energies. The figures are taken from the TopLHC working group [73].

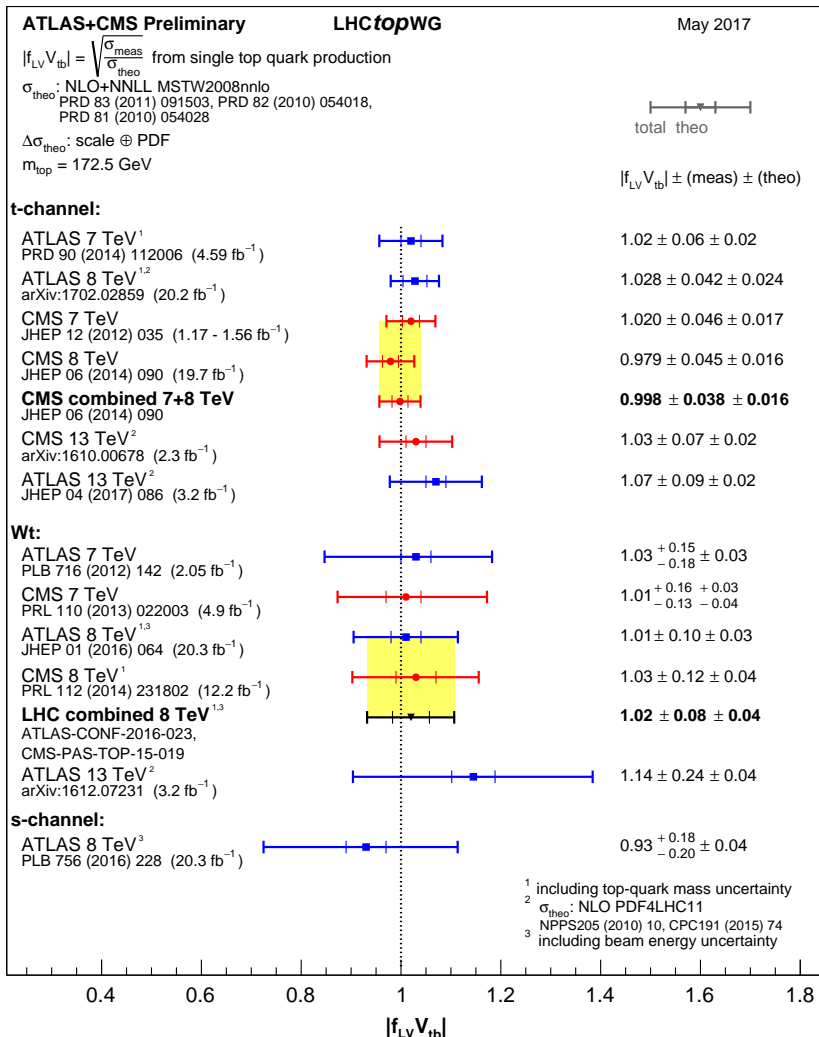


Figure 2.14. Estimations of the CKM matrix element V_{tb} from single-top-quark cross section measurements. The figure is taken from the TopLHC working group [73].

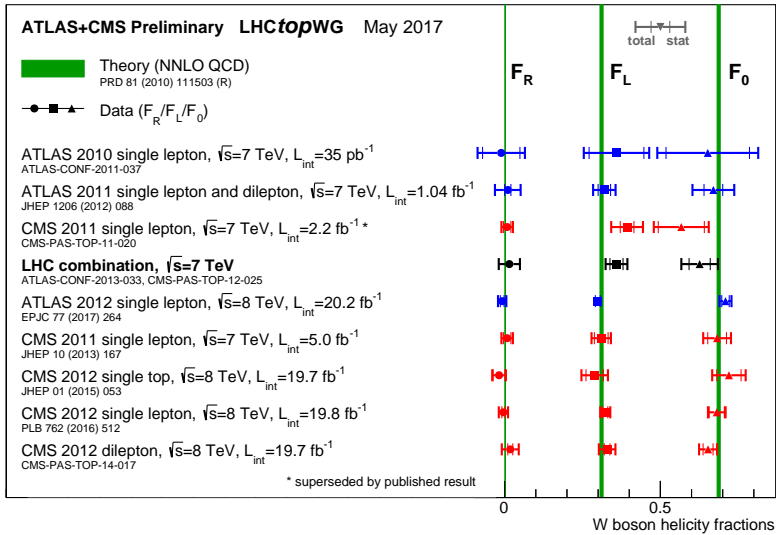


Figure 2.15. | Overview of W boson helicity fraction measurements. The figure is taken from the TopLHC working group [73].

computing-intense undertaking. Given a certain point in the coupling hyperspace, multiple observables need to be computed and compared to the results from various measurements while accounting for statistical and systematic uncertainties. A sophisticated fitting framework called TopFitter has been recently developed [75]. The estimated couplings strength per operator contributing to single-top-quark production obtained from various measurements at the LHC and the Tevatron are shown in Fig. 2.16. The results are found to be consistent with the SM expectation where those operators vanish.

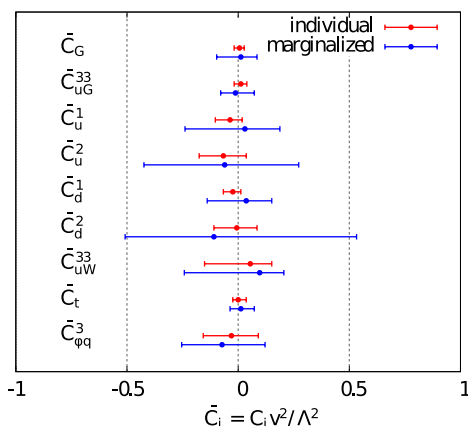


Figure 2.16. | Coupling strength per operator contributing to single-top-quark production. Shown are 95% confidence intervals. The Wilson coefficient C_t contains all contributions from four-fermion interactions. The figure is taken from Ref. [75].

3.

Chapter

Experimental setup

The measurements within this thesis are based on proton-proton (pp) collision data recorded with the CMS detector in 2012, 2015, and 2016 at center-of-mass energies of 8 and 13 TeV. In this chapter the experimental setup is described. First, an overview of the LHC, its preaccelerator chain and the experiments at the LHC is given. Then, the CMS detector and its major components are detailed which are: the solenoid magnet, the inner tracking system, the electromagnetic and hadronic calorimeters, and the muon system. The chapter is concluded with a brief overview of the event trigger and data acquisition systems of the CMS experiment.

3.1. Large Hadron Collider

The Large Hadron Collider (LHC) is a 26.7 km long accelerator and storage ring for protons and heavy ions located at the European Organization for Nuclear Research (CERN) in the vicinity of Geneva, Switzerland [76]. It was constructed between 1998–2008 in the existing tunnel of the former Large Electron-Positron Collider (LEP) which lies 45–170 m below the surface of Switzerland and France. The LHC ring features two beam pipes which can be separately filled with up to 2808 countercycling bunches per pipe with a bunch spacing of 25 ns. The two beams can be focused to cross each other at four interaction points (IPs). The design allows to accelerate protons with a momentum of 450 GeV at injection to up to 7 TeV yielding a maximum center-of-mass energy of 14 TeV in collisions.

The beams are bent by 1232 dipole cryostats that host both beam pipes and corresponding dipole magnets within a cold mass in a twin-bore design. The cold mass itself is placed in a vacuum vessel for thermal insulation. The magnet coils consist of niobium-titanium (NbTi) cables which are cooled down to 1.9 K using superfluid helium. At this temperature, the NbTi alloy is superconducting. This allows to produce the required dipole field strength ranging from 0.54 T at injection to up to 8.33 T at the maximum beam energy for sustaining a closed beam orbit. Such high magnetic fields cannot be achieved with normal conductors due to magnetic saturation which is why the coils have to be superconducting. At maximum field a current of 11850 A is required. In addition to the dipole magnets about 3800 single aperture and 1000 twin aperture magnets are installed. Quadrupole magnets keep the beam particles focused around the nominal orbit. Further, non-linear corrections to the orbit are applied using sextu-, octu-, and decapoles. Special quadrupole triplets at each side of the four IPs focus the beams for collision. The envelope of the particle trajectories with respect to the nominal beam orbit is described by the betatron function which can be approximated around the IPs as

$$\beta(x) \approx \beta^* + \frac{x^2}{\beta^*}, \quad (3.1.)$$

where x denotes the distance to the focal point. In design the beams can be squeezed to $\beta^* = 0.55$ m at two high luminosity IPs. The transverse beam size at the IPs can be calculated as $r = \sqrt{\epsilon_n \cdot \beta^* / \gamma} \approx 17 \mu\text{m}$ for $\gamma = E_p / m_p = 7000$, where ϵ_n denotes the normalized beam emittance. The emittance is a measure of the phase space area occupied by the particles within the beam which is constant in a closed system following Liouville's theorem. For the LHC it cannot be larger than $\epsilon_n > 3.75 \mu\text{m} \cdot \text{rad}$ in order not to loose significant amounts of the beam intensity in the LHC arcs where $\beta(x)$ is the largest.

For acceleration and longitudinal focusing of the bunches, a system of eight superconducting cavities per beam with a resonance frequency of 400.8 MHz are installed. This matches the 35 640 harmonic mode of the beam revolution frequency of $f_{\text{rev}} = 11245$ Hz. The cavity system yields an energy gain per turn of 485 keV which results in an acceleration time of about 20 min from injection to the maximum beam energy.

The expected luminosity at the IPs can be calculated from the introduced machine and beam parameters as

$$L = \frac{N_p^2 n_b f_{\text{rev}}}{4\pi d_{x,y}^2} \cdot F, \quad F = \frac{1}{\sqrt{1 + (\theta \cdot d_z)^2 / (2d_{x,y})^2}}, \quad (3.2.)$$

where N_p denotes the number of protons per bunch and n_b the number of colliding bunches. The design proton population per bunch is $N_p = 1.15 \cdot 10^{11}$. The factor F accounts for a reduction in luminosity due to a slight tilting of the beams by the crossing angle θ . In 2016, the design luminosity of $10^{34} \text{ cm}^{-2}\text{s}^{-1}$ was surpassed through various new developments [77]. In detail these were a decreased transverse emittance, a smaller longitudinal bunch size, a better focusing at the IPs down to $\beta^* = 0.4$ cm, and a smaller crossing angle compared to the design values which resulted in a peak luminosity of about $1.5 \cdot 10^{34} \text{ cm}^{-2}\text{s}^{-1}$ at the IPs of the ATLAS and CMS experiments. An overview of the peak luminosities per day in pp collisions recorded by the CMS experiment from 2010–2016 is shown in Fig. 3.1. In Run 1 (2010–2012) the LHC produced pp collisions at center-of-mass energies of 7 and 8 TeV. After the first long shutdown (LS1) the center-of-mass energy was raised to 13 TeV for Run 2 which commenced in 2015.

During a bunch crossing multiple proton-proton interactions can occur which are referred to as pileup (PU). Their number on average is proportional to the luminosity times the total inelastic pp cross section. In 2012, an average of 21 pileup interactions has been observed in 8 TeV pp collisions at the IP of CMS. This increased in 2016 due to the higher luminosity and cross section at 13 TeV to about 27 interactions on average.

3.1.1. Accelerator complex

An overview of the accelerator complex at CERN is given in Fig. 3.2 which includes the systems for filling the LHC with bunches of protons or lead ions.

The production sequence of proton bunches for the LHC is as follows. In the linear

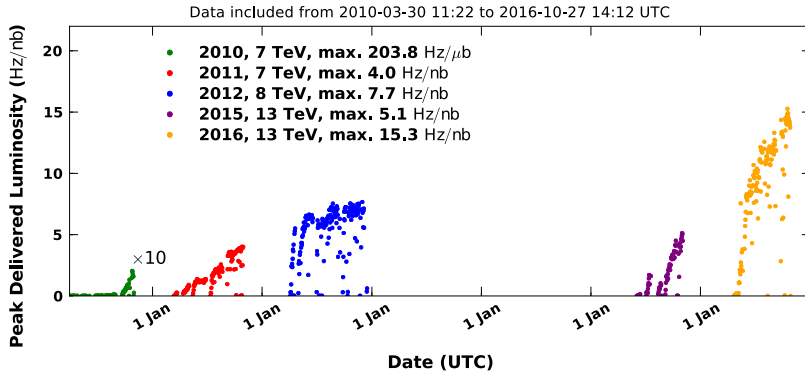


Figure 3.1. Peak luminosity in proton-proton collision data per day as measured with the CMS experiment. The figure is taken from the public luminosity result web page of CMS [78]. The design luminosity corresponds to $10 \text{ Hz/nb} = 10^{34} \text{ cm}^{-2}\text{s}^{-1}$.

accelerator “Linac 2” hydrogen atoms are stripped of their electron through an electric field. The remaining protons are accelerated to a momentum of 50 MeV and injected into the Proton Synchrotron Booster (PSB). It consists of four vertically separated beam pipes which allow multi-turn injections to increase the bunch intensity which however also increases the transverse emittance [80]. After accelerating the protons to 1.4 GeV, the beams are injected into the Proton Synchrotron (PS). Here the required bunch spacing of 25 ns is formed. The standard procedure was to use only six bunches from two PSB cycles and split them first by three, accelerate them to 25 GeV, and then split each again by two twice to produce in total 72 bunches with the required spacing [81]. A new scheme called batch compression merging and splitting scheme (BCMS) was introduced in July, 2016. It utilizes all eight bunches from two PSB cycles which are first narrowed and then combined to four followed by the same splitting and acceleration procedure as before resulting in 48 bunches with a higher intensity and a lower transverse emittance [82]. After the PSB the proton bunches are injected into the Super Proton Synchrotron (SPS) and accelerated up to the LHC injection energy of 450 GeV.

3.1.2. Overview of experiments

Various particle detectors are installed at the LHC to record the outcome of proton-proton or heavy ion collisions. Four major detectors are directly located at the four IPs. Two general purpose detectors are located at two high luminosity IPs. These are the ATLAS [83] and CMS [84] experiments which have both a wide physics program ranging from precision measurements of the SM to searches for various kinds of new physics like extra dimensions, dark matter particles or SUSY. Despite similar goals the technical realization of the two experiments is different. The ATLAS detector is of cylindrical shape around the beam pipe with a length of 44 m and a diameter of 25 m. It consists of an inner tracking detector, a liquid argon electromagnetic calorimeter, a hadronic calorimeter, and a muon spectrometer with full 2π coverage in the azimuthal angle. A detailed description of the CMS detector is given below in Sec. 3.2. The two other major detectors are the ALICE [85] and LHCb [86] experiments which

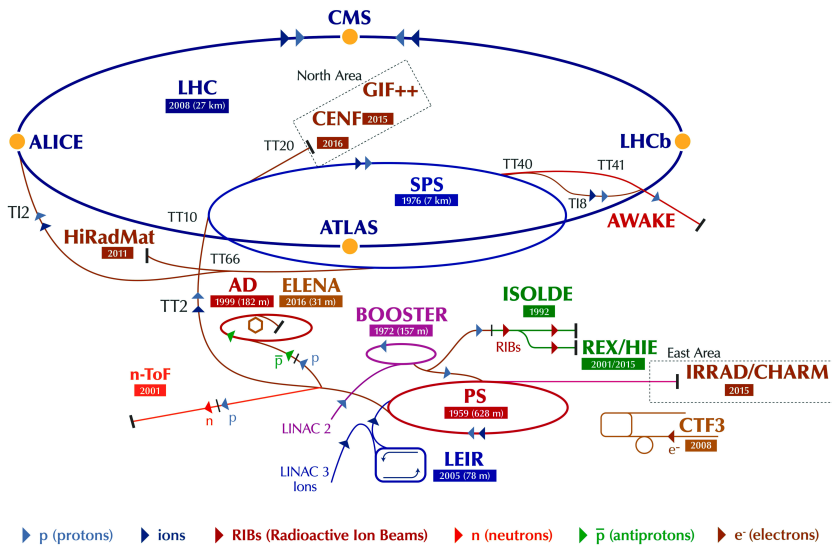


Figure 3.2. || The accelerator complex at CERN. The figure is taken from Ref. [79].

are more specialized. Their luminosity is intentionally leveled down by displacing the beams slightly at their IPs [87]. The lower luminosity is required to reduce the number of pileup interactions and to prevent damage to the detectors through radiation. The ALICE experiment focuses on heavy ion collisions in which the properties of quark-gluon plasma can be studied. The goals of the LHCb experiment are precision measurements of CP-violating processes and searches for rare decays of B hadrons amongst others.

In addition, three smaller experiments, LHCf [88], TOTEM [89], and MoEDAL [90], have been installed at the LHC using certain fractions of the scattered particles from the IPs of the ATLAS, CMS, and LHCb detectors, respectively.

3.2. CMS experiment

The CMS (Compact Muon Solenoid) experiment is a multipurpose particle detector whose goal is to record $p\bar{p}$ and heavy ion collisions at high luminosities. It consists of a superconducting solenoid and multiple subdetectors as shown in Fig. 3.3 to track, reconstruct, and identify particles which traverse the detector each bunch crossing.

The detector is shaped cylindrically by layers in the barrel region and endcap disks in the forward regions around the beam pipe. It has an overall length of 21.6 m and a diameter of 14.6 m with a total weight of approximately 12 500 tons. A right-handed coordinate system has been established whose center is located at the nominal IP. It is oriented such that the y-axis points upwards, the x-axis points inwards to the center of the LHC ring, and the z-axis points counterclockwise along the beam pipe. The azimuthal angle ϕ is defined in the transverse plane, spanned by the x- and y-axes, which lies perpendicular to the beam pipe. In this plane, the radius is defined as $r = \sqrt{x^2 + y^2}$ which measures the distance to the z-axis. For a particle originating from

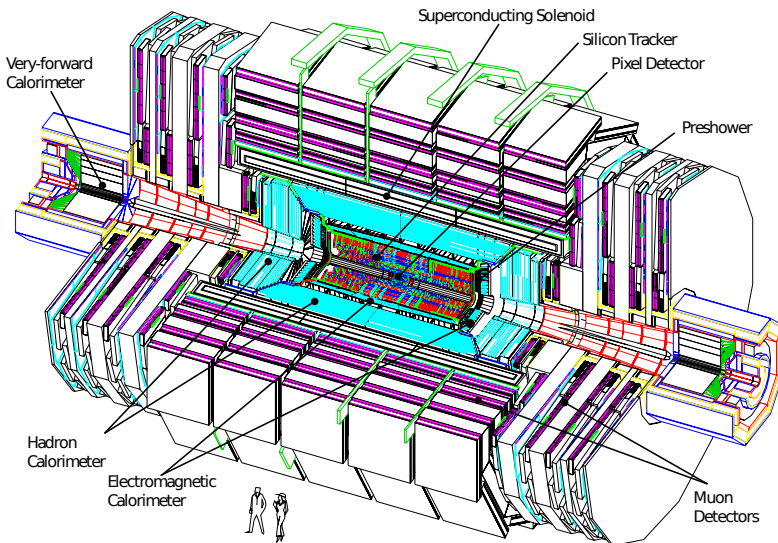


Figure 3.3. | Overview of the CMS subcomponents. The figure is taken from Ref. [84].

the center with an energy E and momentum p_z along the z-axis one defines its rapidity as

$$y = \frac{1}{2} \ln \left(\frac{E + p_z}{E - p_z} \right). \quad (3.3.)$$

The advantage of the rapidity over the usage of the angle θ measured from the z-axis is that differences of rapidities are invariant under Lorentz-boosts. Furthermore, in the case of a massless particle, the rapidity is equal to the pseudorapidity

$$\eta = \text{artanh} \left(\frac{p_z}{|\vec{p}|} \right) = -\ln \left[\tan \left(\frac{\theta}{2} \right) \right]. \quad (3.4.)$$

In the following, the components of CMS are briefly described and their purpose is motivated. Further information can be found in Refs. [84, 91].

3.2.1. Solenoid magnet

The solenoid magnet is a central part of the CMS detector. It enables momentum measurements of charged particles by analyzing their curved trajectories with the inner tracking system. Additionally, the muon system located in the outer return flux of the magnetic field allows to measure the momenta of muons originating from the IP a second time. The design of CMS was particularly motivated to achieve a good resolution of muon momenta and dimuon mass spectra which are key ingredients when searching for new resonances like the at that time undiscovered Higgs boson [92].

The magnet consists of four layers of superconducting NbTi cables. It is placed in a cold mass within a vacuum tank which is cooled down to 4.7 K using liquid helium.

To guide the return flux of the magnetic field, a large iron yoke has been installed. It consists of five 12-sided barrel wheels in three layers with a length of 11 m and six endcap disks. In design the solenoid is capable of producing a homogeneous magnetic field of up to 4 T in its inner free bore which has a diameter of 6 m and a length of 12.5 m. However, the magnet has been operated with a reduced current of 18164 A so far yielding a slightly lower field of 3.8 T [93].

3.2.2. Inner tracking system

The inner tracking system is located closest to the beam pipe and has a total length of 5.8 m with a diameter of 2.5 m. It is used to find trajectories of charged particles which are bent by the magnetic field. Their momentum, charge, and point of origin is estimated in the track reconstruction.

At design luminosity approximately 1000 particles traverse the tracking system per bunch crossing on average. This yields a hit rate density of about 1 MHz/mm^2 at an inner radius of 4 cm which is reduces to 3 kHz/mm^2 at the outer edge of the tracker. The tracker modules are based on doped silicon semiconductors which are operated in reverse mode to detect the traversing of charged particles through ionization. This technology allows for modules with a sufficiently high granularity and a fast response time that are also able to operate in such high radiation environments.

The system consists of various parts with different module types as shown in Fig 3.4. In total it covers a pseudorapidity range of $|\eta| < 2.5$. Pixel modules are located next to the beam pipe where the particle flux is particularly high. They are installed in three barrel layers (BPX) at radii of 4.4, 7.3, and 10.3 cm, and in two endcap disks (FPX) per side. A pixel module has a cell size of $100 \times 150 \mu\text{m}^2$ which allows a two-dimensional local hit position measurements. Local positions are transformed into three-dimensional global positions by accounting for the surface orientation of each module. The channel occupancy of the pixel subdetector, which is defined as the fraction of active readout channels, has been measured in data and ranges between 0.002–0.02% only [94]. This facilitates the search for particles trajectories in recorded hit patterns by starting from the precise hits on the pixel modules.

Silicon strip modules are installed in the other parts of the inner tracking system. They are organized in four inner barrel layers (TIB) at radii of 20–50 cm; six outer barrel layers (TOB) at radii of 55–116 cm; three inner endcap disks (TID); and nine outer endcap disks (TEC). In the barrel, the strip directions on each module are aligned along the z-axis with a strip-to-strip distance that varies between 80–183 μm . In the endcap disks, the modules are wedge-shaped with their strips running along the radial axis whose distance ranges between 100–184 μm . They are cooled down and operated below -10°C to counteract the heat produced by the electronics and to improve their lifetime. The strips allow to measure a local one-dimensional hit position perpendicular to their direction. However, a few layers and disks contain double-sided strip modules as indicated in Fig. 3.4 which are tilted by an angle of 0.1 rad with respect to each other. Those modules allow to reconstruct 2D hits by matching two 1D hits from both sides together.

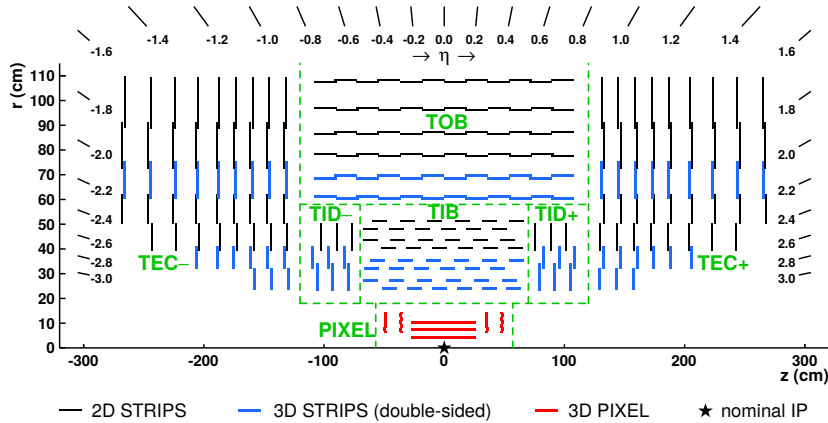


Figure 3.4. | Overview of the CMS tracking system. The figure is taken from Ref. [94].

3.2.3. Electromagnetic calorimeter

The electromagnetic calorimeter (ECAL) encloses the inner tracker and covers a pseudorapidity range of $|\eta| < 3$. It consists of scintillating lead tungstate (PbWO_4) crystals to detect electromagnetic showers originating from charged or neutral particles (especially photons and electrons) in the crystals. In particular, the capability of detecting a diphoton resonance from Higgs boson decays has been one of its design goals.

An overview of the ECAL layout is displayed in Fig. 3.5. In total 61 200 crystals in the shape of a truncated pyramid are installed in the barrel and 7 324 in each of the two endcaps. The barrel crystals have a length of 23 cm and a rectangular front cross section of $22 \times 22 \text{ mm}^2$. In the endcaps the crystals have a similar shape with a length of 22 cm and a front cross section of $28.62 \times 28.62 \text{ mm}^2$. The crystals are slightly tilted such that no particle originating from the nominal IP can pass the ECAL through a crack between the crystals within its acceptance.

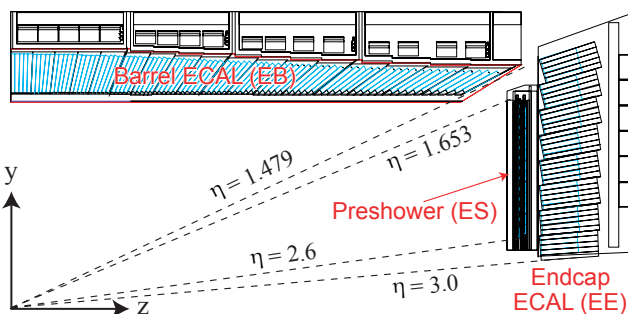


Figure 3.5. | Overview of the CMS electromagnetic calorimeter system. The figure is taken from Ref. [91].

The crystal material was chosen for its high density of 8.28 g/cm^3 , short radiation length of 0.89 cm , and radiation hardness. In addition, the spatial extension of an

electromagnetic shower inside the crystals, the so-called Molière radius, amounts to only 2.2 cm which yields a good position resolution and shower separation. The crystals emit about 4.5 photoelectrons per MeV with a wavelength of 420–430 nm. About 80% of the light is emitted within 25 ns after an electromagnetic shower occurred. In the barrel the signal of the collected photons is amplified by avalanche photodetectors (APDs) whereas in the endcaps vacuum photodiodes (VPTs) are used instead which are specifically designed to operate also in the axial magnetic field. The energy resolution of the crystals has been measured in electron beams for energies $20 < E < 250$ GeV [95]. It can be parameterized as

$$\left(\frac{\sigma}{E}\right)^2 = \underbrace{\left(\frac{2.8\%}{\sqrt{E/\text{GeV}}}\right)^2}_{\text{stochastic}} + \underbrace{\left(\frac{0.12}{E/\text{GeV}}\right)^2}_{\text{noise}} + \underbrace{(0.30)^2}_{\text{constant}} \quad (3.5.)$$

which yields for example a resolution of 0.43 GeV at an electron energy of 100 GeV.

In front of the two ECAL endcaps the preshower detector (ES) is located which covers a pseudo rapidity range of $1.652 < |\eta| < 2.6$. It consists of two layers of lead radiators to initiate electromagnetic showers with a layer of silicon strip sensors after each radiator for measuring the transverse profile of a shower. This allows to identify neutral pions and improves the identification and position measurement of electrons and photons.

3.2.4. Hadron calorimeter

The hadron calorimeter (HCAL) is a sampling calorimeter and organized in four parts as shown in Fig. 3.6. It covers a pseudorapidity range of $|\eta| < 5$ in total. Its function is to initiate and detect hadronic showers from particles such as protons, neutrons, kaons, and pions which allows to measure their position and energy. Furthermore, it helps to determine the transverse momentum imbalance of an event since the only remaining particles from a collision that are not stopped by the HCAL are neutrinos and muons where the latter are however identified and measured in the muon system as discussed later in Sec. 3.2.5.

The central hadron calorimeter, consisting of a barrel (HB) and two endcap (HE) regions, is located directly after the ECAL and extends up to the solenoid. The HB covers a pseudorapidity range of $|\eta| < 1.3$. It consists of brass absorber plates in 14 layers oriented along the z-axis with a thickness of 50.5 mm (first eight) and 56.5 mm (last six), respectively. For structural support two additional layers of 40 mm and 50.5 mm thick steel absorber plates are installed at its inner and outer rim respectively. Between the absorbers 72 azimuthal wedges of plastic scintillators in 17 layers with a thickness of 3.7 mm or 9 mm are installed where each covers a segment of $\Delta\eta \times \Delta\phi = 0.087 \times 0.087$. Their emitted light is optically added per tower and guided through wavelength shifting (WLS) fibers to hybrid photodiodes (HPDs) located at the end of the HB structure. The HB has a depth of 5.8 interaction lengths at $\eta = 0$ which increases with pseudorapidity and amounts to 10.4 interaction lengths at $|\eta| = 1.3$.

The same design of alternating brass absorbers (79 mm thick) with 17 scintillator layers in between and WLS fibers for readout is utilized in the HE. It covers a pseudorapidity range of $1.3 < |\eta| < 3$ and has a depths of about 10 interaction lengths. Its granularity

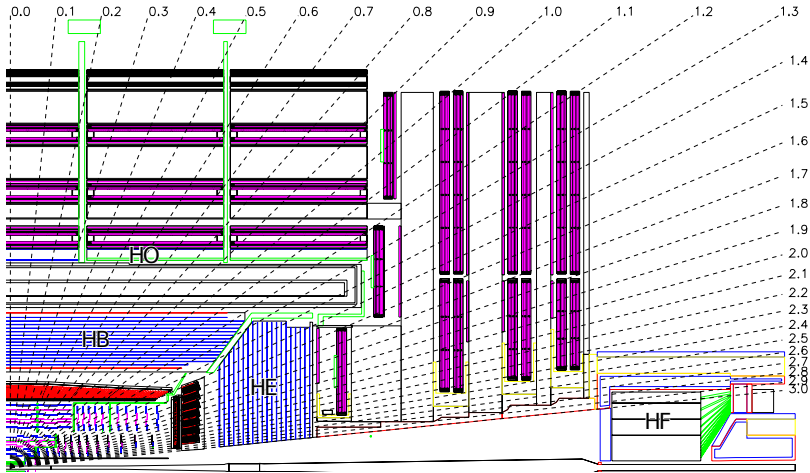


Figure 3.6. || Overview of the CMS hadronic calorimeter system. The figure is taken from Ref. [84].

increases from $\Delta\eta \times \Delta\phi = 0.087 \times 0.087$ to 0.17×0.17 for $|\eta| > 1.6$.

To contain hadronic showers in the barrel region further, an additional calorimeter, the hadron outer calorimeter (HO), is placed directly at the outside of the solenoid utilizing it as absorber. It consists of one or two layers of scintillators, depending on the pseudorapidity, which match the granularity of the HB. This extends the depths of the combined HB+HE+HO system to an overall minimum of 11.8 interaction length with the exception of the HB-HE transition region ($|\eta| \sim 1.3$).

An additional calorimeter system, the hadron forward calorimeter (HF), is located 11.2 m away from the IP at both sides where it covers a pseudorapidity range of $3 < |\eta| < 5.2$. The HF is of particular importance for this thesis since the signature of t -channel single-top-quark events features a characteristic forward jet that is often detected within its acceptance. For the HF a different detector technology was chosen to withstand the expected higher levels of radiation of about 1 MGy/a occurring in the forward region. It uses quartz fibers to detect Cherenkov light from the electromagnetic component of a shower. The fibers are oriented along the z-axis and placed in grooves within steel plates which act as absorbers. The fibers are arranged to achieve a granularity of $\Delta\eta \times \Delta\phi = 0.175 \times 0.175$. Only half of the fibers extend over the complete HF depth of 165 cm which corresponds to 10 interaction lengths. The other half starts at a depth of 22 cm instead. Since electromagnetic showers are typically shorter than hadronic ones the two shower types can be disentangled from each other by comparing the separated readouts from the long and short fibers. The produced Cherenkov light is guided to photomultiplier tubes (PMTs) located behind a shield of 40 cm steel and polyethylene slabs which protects them from the high radiation.

The energy response of the HCAL modules has been measured in pion beams with energies of $20 < E < 300$ GeV [96]. This results in

$$\left(\frac{\sigma_{\text{HB+HE}}}{E} \right)^2 = \left(\frac{115\%}{\sqrt{E/\text{GeV}}} \right)^2 + (5.5\%)^2 \quad (3.6.)$$

for the combined HB+HE system which is found in agreement with simulation. For the HF resolutions of

$$\left(\frac{\sigma_{\text{HF}}}{E_e}\right)^2 = \left(\frac{198\%}{\sqrt{E/\text{GeV}}}\right)^2 + (9\%)^2, \quad \left(\frac{\sigma_{\text{HF}}}{E_\pi}\right)^2 = \left(\frac{280\%}{\sqrt{E/\text{GeV}}}\right)^2 + (11\%)^2 \quad (3.7.)$$

have been measured in electron and pion test beams respectively [97].

3.2.5. Muon system

A major design goal of CMS is the precise and robust detection of muons to achieve a good dimuon mass resolution (1% at 100 GeV) and charge determination over a wide muon momentum range of up to 1 TeV and beyond. Muons are a key ingredient to detect signatures of various SM processes and beyond as for example in Higgs bosons studies where their decay to four muons via intermediate Z bosons is analyzed. In particular, events containing a single muon amongst others that may stem from the decay of a single top quark are analyzed in this thesis.

The muon system is located at the outside of the CMS detector within the gaps of the iron yoke. It consists of three types of gaseous detectors. Muons passing through the gas will ionize it. A strong electric field pulls the freed electrons then to wires and the resulting electric pulse is read out. The choice of the gas mixture together with the electric field strength lets the drifting electrons ionize the gas further close to the wire which amplifies the pulse. An overview of the muon system is provided in Fig. 3.7. Drift tubes (DTs) are installed in the barrel ($|\eta| < 1.2$) where the muon flux is relatively low. In the endcaps ($0.9 < |\eta| < 2.4$) cathode strip chambers (CSCs) are used which can operate in the higher muon flux environment and in the inhomogeneous magnetic field. In addition, resistive plate chambers (RPCs) are installed in the barrel and endcaps as a complementary system with a coverage of $|\eta| < 1.6$.

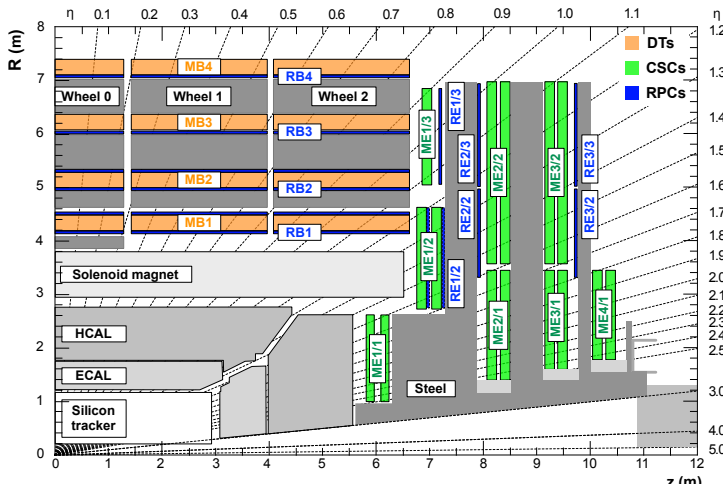


Figure 3.7. || Overview of the CMS muon system by the end of LHC Run 1. The figure is taken from Ref. [98].

The DTs consist of nearly rectangular cells with a cross section of $42 \times 13 \text{ mm}^2$ in which a $50 \mu\text{m}$ thick and 2.4 m long gold-plated steel wire is spanned through the center. The cells are filled with a gas mixture of 85% Ar and 15% CO₂ which yields an amplification of 10^5 and a drift time of about 380 ns for a maximum drift length of 21 mm. The DTs are organized in four layers which form an independent gas-tight super layer unit. A DT chamber consists of three (or two) super layers where the wires in the first and last layers are oriented along the z-axis and the wires in the middle layer are oriented orthogonal along the ϕ direction. Four layers of DTs chambers are placed in the barrel region with 60 chambers in each of the inner three layers and 70 in the outer one which amounts to about 172 000 wires in total.

In the endcaps trapezoidal-shaped CSCs are installed in four disks per side. Each disk consists of 18 or 36 chambers which are slightly overlapping to ensure full azimuthal coverage. The CSCs are multiwire proportional chambers where each consists of seven radially-oriented cathode strips glued on 12.7 mm-thick panels. Their pitch changes radially from 8.4 mm to 16 mm at the outside. Six azimuthally-oriented wires are placed in the gas gaps between the panels with a width of 9.5 mm. A gas mixture of 40% Ar, 50% CO₂, and 10% CF₄ is used which yields a gain of about 7×10^4 at a voltage of 3.6 kV. Since the first inner CSCs (labeled ME1/1) are located inside the solenoid a slightly different design with tilted wires by 29° was chosen to compensate for the Lorentz drift in the magnetic field. The fourth CSC disk labeled ME4/2 (not present in Fig. 3.7) has been installed after Run 1 which adds an additional redundancy for muons within $1.2 < |\eta| < 1.8$ [99].

The muon system is completed by RPCs in the barrel and endcaps. These are gaseous parallel-plate detectors with two gaps of 2 mm width each. They provide a much shorter time resolution than the DTs and CSCs of about 1 ns. Hence, they are used to associate a muon signal to the corresponding LHC bunch crossing. In the barrel six layers of RPCs are installed with their strips oriented along the z-axis. Their pitch varies per layer such that an azimuthal granularity of $5/16^\circ$ is achieved. In the endcaps four RPC disks are installed with radially oriented strips. A fourth endcap disk was added after Run 1 as well [100].

3.2.6. Data acquisition

The CMS trigger and data acquisition system [101, 102] deals with the individual readouts of the various subdetector front-end systems. It associates them to an event and finally transmits a file of multiple events to the CERN computing cluster for storage. A two-staged event triggering system is employed whose aim is to reduce the high data rate and to select only events for storage of certain physics interest. The event rate from the bunch crossing frequency of 40 MHz is reduced to about 100 kHz after the first stage, the level 1 (L1) trigger, and then to less than 1 kHz after the final high level trigger (HLT) system.

The data acquisition starts at the subdetector systems where the individual channel readouts are stored continuously in pipelined buffers at a rate of 40 MHz. The L1 trigger system analyzes only the readout of the calorimeter and muon systems per bunch crossing to reach a decision within a maximum latency of 3.2 μs . It consists of field-programmable gate arrays (FPGAs) which enable a flexible adaptation of the

system to potential varying conditions and needs. The regional (RCT) and global calorimeter trigger systems (GCT) attempt to locate electron, photon, jet, and τ -jet candidates from coarsely segmented ECAL and HCAL readouts. Additional pieces of information like the missing transverse energy and number of jets are also determined. The global muon trigger system (GMT) attempts to find muon candidates by using local information from the independent DT, CSC, and RPC trigger systems. In addition, a muon is considered isolated if the hadronic activity in its vicinity (provided by the GCT) is below a certain threshold. The final L1 decision is taken by the global trigger (GT) based on the candidates found by the GCT and GMT systems.

After a positive L1 decision is received the individual readout fragments with a size of up to 8 kB are transferred via optical links to readout units (RUs) by front end drivers (FEDs) where multiple fragments are merged. Event builder units (BUs) pick up the fragments via a high speed, Infiniband-based switching network from the RUs and assemble the events. The HLT system then reads the assembled events from the BUs via an Ethernet network. Its triggering rules are part of the standard CMS software (CMSSW [91]) which is invoked on a special computing farm called filter units (FUs). Starting from L1 candidates, the complete readout of an event is subjected to a sequence of reconstruction and filtering steps to reach a HLT decision. One output file is created per CMSSW process, HLT stream, and luminosity section where the latter corresponds to a period of about 23 s. Streams and files of selected events are merged in two steps on the FUs and BUs before they are transferred to the CERN computing center for full reconstruction.

4.

Chapter

Event reconstruction

The reconstruction of basic analysis objects within an event is described in this chapter. A key ingredient in the event reconstruction of CMS is the particle flow (PF) algorithm. It creates particle candidates by combining various subdetector information for a global event interpretation which improves the identification, spatial resolution, and energy measurement of particles. The focus of this chapter is set on the reconstruction and performance of muons, electrons, jets, and the missing transverse energy in 8 and 13 TeV pp collision data which are used to study single-top-quark production in this thesis. The chapter is concluded with a summary of corrections to enhance the agreement between data and simulation.

The event reconstruction attempts to build and identify basic analysis objects from the raw detector data. In CMS, basic objects are charged-particle tracks, vertices, charged leptons, photons, and jet candidates. During the reconstruction, additional information such as the missing transverse energy, \cancel{E}_T , and the likelihood of jets to originate from the hadronization of b quarks (“b-tagging”) is determined. Since tau leptons have not been utilized and photons are not relevant in the presented studies of t -channel single-top-quark production, a description of their reconstruction and performance is omitted here yet details can be found in Refs. [103, 104].

4.1. Track reconstruction

The reconstruction of tracks from the readout of the inner tracking system consists of a local and a global reconstruction step. In the local reconstruction, hits from charge distributions on the pixel and strip modules are formed. Then, in the global reconstruction, trajectory candidates are first seeded and then sequentially built from the inside out. Finally, a helix track is fitted through the associated hits per trajectory candidate to estimate the particle’s momentum and charge through its curvature in the magnetic solenoid field. An overview of the local and global reconstruction is given in the following. Further information can be found in Ref. [94].

Different algorithms are used to determine the local positions of two-dimensional (one-dimensional) hits from the distributions of charge deposits on the pixel (strip) modules, respectively. The pixel hit positions are estimated first with a fast algorithm whose outcome is used in the trajectory seeding and building stage only. The algorithm projects the 2D charge distributions onto each axis and estimates the positions from the charges at the edges of each charge cluster while accounting for their Lorentz-drift within the modules. During the track-fit stage, the optimal pixel hit positions are estimated by comparing the charge distributions against the expectations from simulated templates for various track incident angles [105]. In the barrel layers, a pixel hit resolution of 9.4 μm in $r\text{-}\phi$ and between 21–45 μm along the z-axis depending on

the incident angle is achieved [94].

For reconstructing hits on the strip modules, charge clusters are formed if the channel readout of adjacent strips is sufficiently above their individual noise levels. The hit position is then calculated as a charge-weighted average over a cluster while correcting for the Lorentz drift and potential inefficiencies which occur at the edges of a module. The hit resolution depends on the size of a cluster and on the strip-to-strip distance of the modules (Sec. 3.2.2). It ranges roughly between 10–30 μm (10–50 μm) for the TIB (TOB) modules, respectively [94].

After the formation of hits, the reconstruction of tracks is performed in multiple passes, called iterations, over the obtained pixel and strip hit collections to reduce the combinatorial complexity. Each iteration consists of the same algorithmic steps—seeding, trajectory finding, track fitting, and selection—but is configured differently. The first iterations attempt to reconstruct only simple tracks which originate close to the interaction region and have a sufficiently large transverse momentum. The hits belonging to successfully reconstructed tracks passing certain quality criteria are then masked in subsequent iterations to reduce the number of hit combinations in the seeding and trajectory finding stages. Later iterations focus on reconstructing displaced or low momentum tracks which may not originate from the interaction region using the remaining hits. Figure 4.1 shows the efficiency times acceptance for successfully reconstructing a track^(*) in simulation, broken down per iteration, as a function of its transverse momentum or displacement.

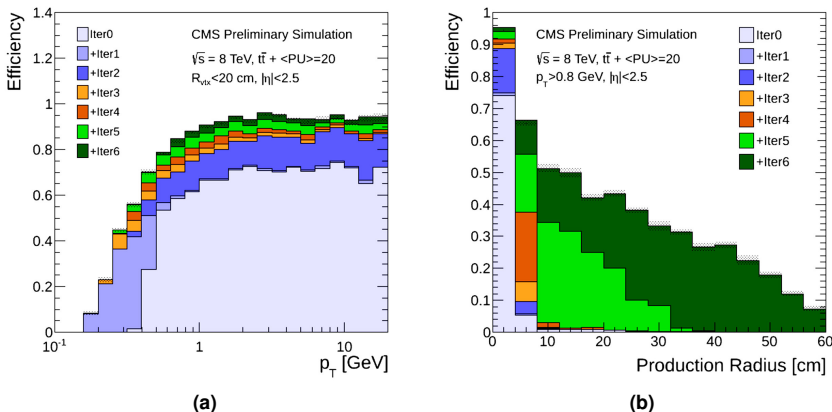


Figure 4.1. | The efficiency times acceptance of successfully reconstructing a track in simulation per tracking iteration as a function of (a) the transverse momentum and (b) the transverse displacement. The figures are taken from Ref. [106].

Each iteration commences by forming a trajectory seed from a hit doublet or triplet where only certain combinations of tracker layers are allowed depending on the iteration. First iterations utilize mostly 3D hits on the pixel layers for seeding since their low channel occupancy results in less ambiguity and a higher efficiency for close-by

^(*) Tracks are reconstructed “successfully” if at least 75% of their hits can be associated to a simulated particle.

tracks. Late iterations use hits from the strips modules instead where the spatial track density is low. Here, 3D matched hits are utilized mostly for seeding which stem from double-sided strip modules but also hits from mono layers are allowed. Seed candidates have to fulfill certain quality criteria like a minimal transverse momentum and compatibility with either the beam spot or a preliminary reconstructed vertex depending on the iteration before they are passed to the trajectory finding stage.

Each seed contains enough information to perform a first estimate of the track parameters. Then an algorithm called combinatorial track finder (CTF) extrapolates the estimated trajectory to find additional hits on subsequent layers which are compatible with a particle track hypothesis. The CTF algorithm is based on the Kalman filter (KF) technique [107–109] which describes how to update the track parameters and their uncertainties iteratively after adding a hit to the trajectory candidate. If multiple compatible hits are found on a layer, the trajectory is cloned for each of them. If no compatible hit can be found on a layer a ghost hit is created instead.

The hits per trajectory are then passed to a KF-based helix fit to estimate the track parameters without utilizing the initial estimate from the seed. In addition, the fit accounts for material effects and the inhomogeneous magnetic field. The fitted tracks have to pass a quality selection to reduce the amount of fake tracks before they are considered in physics analyses. The criteria reflect the seed requirements and depend additionally on the total number of fitted 2D/3D hits, the χ^2/ndof of the fit, the amount of ghost hits, and the amount of shared hits with other tracks amongst others.

The tracking efficiency for isolated muon tracks with $1 < p_T < 100$ GeV is found to be above 99% over the full tracker acceptance since their trajectories are only disturbed by energy loss through ionization and Coulomb scattering. The trajectories of charged hadrons like pions are additionally affected by nuclear interactions, especially at low momenta ($p_T < 700$ MeV), which results in efficiencies between 80–95% [94]. For electrons, a special tracking is performed on top of the standard one (described in Sec. 4.1.2) which attempts to recover cases where the electron loses large amounts of energy via bremsstrahlung. In parts of the 2016 collision data the overall tracking efficiency decreased by about 2–6% at high instantaneous luminosities of 10–12 Hz/nb due to a charge saturation effect on the readout chips leading to missing hits. This has been recovered by adjusting the voltage which controls the charge drain speed of the tracker modules. For already collected data, the effect has been mitigated offline while any residual loss of efficiency is known and accounted for through dedicated scale factors.

4.1.1. Muon tracks

The track reconstruction for muons begins with the local reconstruction of hits in the three muon systems [91]. The positions of hits in the DT system are reconstructed by first forming independent segments in $r\text{-}\phi$ and $r\text{-}z$ through a combination of pattern recognition and linear fitting steps which are then combined in a second step. For the CSCs, independent 2D hits are reconstructed at wire–strip intersections in each of the six layers which are then combined into a track segment through a linear fit. Hits in the RPC modules are built from clusters of active strips where their positions are taken as the center of gravity of the cluster’s area.

Standalone muon tracks are reconstructed from hits in the muon system only without using the inner tracker. The muon tracking starts by generating seeds from linear fits through hits in the DT and CSC systems. Then, KF-based track fits are performed taking as starting point the seeds while also utilizing the hits in the RPC system. In addition, the resulting track is constrained to be close to the beam spot which improves the momentum resolution. A global muon track is reconstructed by extrapolating the standalone muon track inwards to define a region of interest inside the inner tracking system. Starting from trajectory seeds inside this region, a global muon trajectory is built and fitted which employs also compatible hits from the inner tracker.

4.1.2. Electron tracks

In CMS, an electron radiates more than 70% of its energy with a probability of 35% in the inner tracker through bremsstrahlung before reaching the ECAL. This leads to an increasingly curved electron trajectory in the magnetic field as a function of its flight distance. The standard tracking is suboptimal for reconstructing such trajectories because the employed Kalman filtering assumes that the energy loss is Gaussian-distributed. Therefore, a different filtering algorithm the so-called Gaussian sum filter (GSF) [110] is used in the electron tracking reconstruction instead.

Trajectory seeds for the GSF tracking are constructed in two ways. The first method creates ECAL-driven seeds by forming super clusters of ECAL crystals with a size of 0.09 in η but ± 0.3 rad azimuthally to capture electrons together with their potentially radiated photons [111]. The second method tries to identify electron tracks inside the standard track collection which are typically marked by either a poor fit quality if the energy loss was large or by its compatibility with an ECAL cluster otherwise. The resulting seeds from the two methods are selected to initiate the GSF tracking. In its core, the algorithm book-keeps a set of trajectories which are subjected to the standard KF-based tracking algorithm. However, different Gaussian distributions are assumed for the energy loss per trajectory while their sum is an approximation of the Bethe-Heitler formula per hit describing the probability of energy loss for electrons via bremsstrahlung. After extrapolating a trajectory set to a new layer, incompatible trajectories are removed or merged with similar ones to limit the exponential growth to a maximum of 12 trajectories per set. The final electron track is estimated by using the summed Gaussian distributions as uncertainties per hit in the track fit.

The electron reconstruction efficiency has been measured in 8 TeV pp collision data to be better than 93% for electrons with an ECAL super cluster energy of $E_T > 20$ GeV [112]. A tracking efficiency of about 96% is obtained for electrons with $E_T > 25$ GeV in 13 TeV pp collision data [113].

4.2. Vertex reconstruction

The vertex reconstruction tries to locate points of pp interactions which are identified by sets of close-by charged-particle tracks in the interaction region. In analyses, the association of tracks to vertices allows to separate tracks belonging to the hard scattering from additional tracks which originate from pileup interactions instead.

The first step in the vertex reconstruction encompasses the forming clusters of spatially-close tracks. For this, tracks which are close to the beam spot are selected and supplied

to a deterministic annealing (DA) algorithm [114]. It is based on a statistical mechanics model where each track reflects a microstate. The association of a track to a vertex candidate is floating and controlled by a probability denoted p_i in the following. A quantity

$$F = -T \sum_i^{\text{tracks}} p_i \cdot \left(\sum_j^{\text{vertices}} \rho_j \cdot \exp \left[-\frac{(z_i^{\text{track}} - z_j^{\text{vertex}})^2}{(T \cdot \sigma_{z,i}^2)} \right] \right), \quad (4.1.)$$

which is an analog of the free energy in a thermodynamical model, is monitored while decreasing the corresponding temperature T of the system. Here, z_i are the track/vertex positions, σ_i denotes the uncertainty of the track positions, and ρ_k is an additional weight to treat overlapping vertices effectively. A protovertex is split in two nearby ones if a minimum of the free energy is reached. The decrease of temperature is stopped when a trade-off between the expected spatial vertex resolution and the probability of splitting a proper vertex falsely is reached.

Finally, the optimal vertex positions are estimated through an adaptive vertex fit [115] per cluster of tracks. The obtained vertices are referred to as “primary vertices” since they mark the point of a pp interaction and are therefore lined up along the z-axis. The vertices are ordered by the summed p_T^2 of their associated tracks where the leading vertex is assigned to mark the hard interaction of interest while the others are treated as pileup interactions. In 2016 pp collision data, the primary vertex resolution is measured as $\sigma_z \leq 19 \mu\text{m}$ and $\sigma_{x,y} \leq 14 \mu\text{m}$ for vertices whose summed p_T of associated tracks exceeds 100 GeV [116].

4.3. Particle flow

A central element in the standard event reconstruction of CMS is the particle flow (PF) algorithm [117, 118]. It aims at reconstructing global particle candidates like electrons, muons, photons, and charged and neutral hadrons in an event by tracing the flow of particles through the various subdetectors. The combination of the individual subdetector information leads to an improved spatial resolution, energy measurement, and type identification of particles while avoiding double counting.

The PF-based reconstruction of particles consists of an algorithm to link information from several subdetectors together. The linked elements can be charged-particle tracks from the inner tracking system, calorimeter clusters from the ECAL or HCAL, and muon tracks. The algorithm starts by extrapolating reconstructed charged-particle tracks from the inner tracking system into the calorimeter systems. In the ECAL, the trajectories are extended to the expected depth of the shower maximum of an electron candidate whereas in the HCAL, the trajectories are extrapolated up to one interaction length. A link is created if a trajectory is located inside the boundaries of a compatible ECAL or HCAL cell cluster within uncertainties. Photon candidates, which could have been emitted tangentially from electron tracks, are also created by extrapolating straight tracks from intersections of the electron track with the tracker layers to compatible ECAL cells. For neutral particle candidates links between calorimeter clusters are formed. Here, the algorithm starts with ECAL clusters for which a good resolution is expected due to their high granularity and extrapolates them to potential HCAL

clusters which has a coarser granularity. Links are also created from the ES to clusters in the coarser ECAL endcaps. A link between a tracker track and the muon system is created if the described track reconstruction of a global muon (Sec. 4.1.1) yields an acceptable goodness-of-fit.

Identification of particles is performed by exploiting the different types of information from the linked blocks. First, global PF muons are identified if their momenta are compatible with the corresponding tracker-only track momenta. Next, PF electrons are identified through the GSF tracking together with potential photons from bremsstrahlung. A PF charged hadron candidate is created for each of the remaining PF candidates that have a charged-particle track linked to it. Finally, the amount of neutral energy is determined by subtracting the charged particle energy fraction from the calibrated energy of the linked calorimeter clusters. This procedure yields PF photon and PF neutral hadron candidates depending on the excess of neutral energy in the ECAL and HCAL clusters respectively. Outside the acceptance of the inner tracking system ($|\eta| > 2.4$), no information on the particle's charge is available. Thus, only a simplified identification is performed by constructing either hadronic or electromagnetic PF candidates only. In a pseudorapidity range of $2.4 < |\eta| < 3$, such candidates are formed from ECAL/HCAL clusters, whereas in $3 < |\eta| < 5$ the difference between the readouts of the long and short fibers of the HF calorimeter allows to discriminate between these two types.

The achieved improvement in spatial and energy resolution through the PF algorithm is demonstrated exemplary for jets in Fig. 4.2. In particular, the energy resolution at low momenta is significantly improved compared to jets clustered from calorimeter cells only since the jet energy estimation in the PF algorithm exploits also the measured momenta of charged-particle tracks from the inner tracking system.

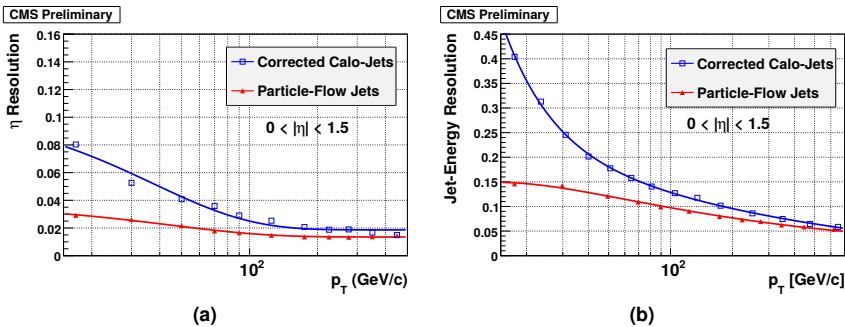


Figure 4.2. | Comparison of simulated calorimeter and particle flow jet performances: (a) spatial resolution in η ; (b) energy resolution. The figures are taken from Ref. [118].

4.4. Muons

Identification of muon candidates for physics analyses is performed by requiring additional selection criteria. A detailed study of muon identification with 7 TeV pp collision data can be found in Ref. [119]. Throughout the analyses within this thesis, muon candidates have to fulfill identification criteria which correspond to a “tight”

working point yielding most genuine muons while rejecting falsely reconstructed ones. In the following, the criteria and performance of muon identification employed in the analysis of 8 TeV and 13 TeV pp collision data within this thesis are briefly discussed. Detailed reports on their performance can be found in Ref. [120, 121].

The muon identification criteria are as follows. The global muon fit is required to include at least one valid hit in the muon chambers for which in addition at least two muon segments in two muon stations are present. Only muon tracks for which the global track fit yields a goodness-of-fit of $\chi^2/\text{ndof} < 10$ are selected. The motivation behind these criteria is to reject fake muons from hadron showers that are not contained by the HCAL and reach the muon system (so-called “punch-throughs”). To suppress the decay of muons in flight, the muon track needs to consist of at least one pixel hit. Additionally, a minimum number of five hits in the tracker is required. A selection on the minimal distance of the muon track to the primary vertex of $d_{x,y} < 2$ mm and $d_z < 5$ mm is applied to reject cosmic muons and muons stemming from PU interactions. A comparison of muon identification efficiencies for data and simulation is presented in Fig. 4.3. These have been estimated using the tag-and-probe method for which $Z \rightarrow \mu^+ \mu^-$ events are selected where one muon is required to pass the identification criteria (“tag”). It is then measured in how many instances the other muon fulfills the identification criteria as well (“probe”) to infer the efficiency. The efficiency is found to be mostly between 95–100% with the exception of two dips at $0.2 < |\eta| < 0.3$ which occur due to a crack between the wheels of the DT system. Overall, a fair agreement between data and simulation is observed. The residual differences are corrected in simulation by applying (p_T, η)-dependent scale factors ($\epsilon_{\text{data}}/\epsilon_{\text{MC}}$) to simulated events.

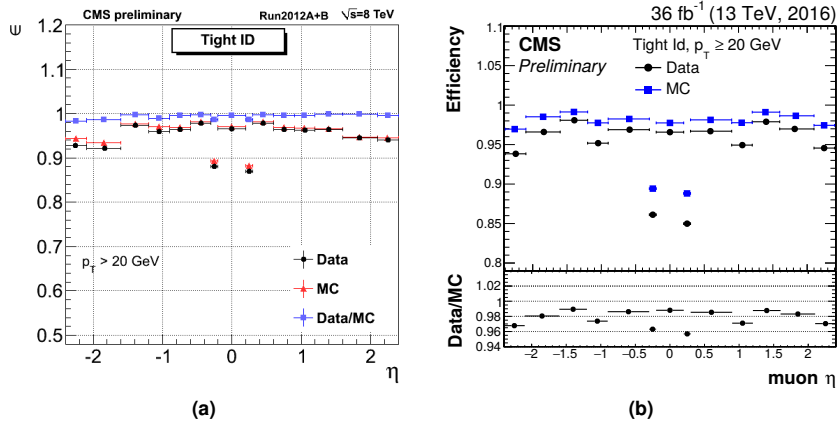


Figure 4.3. | Comparison of muon identification efficiencies in data and simulation as a function of the pseudorapidity of the muon for analyses at (a) 8 TeV and (b) 13 TeV. The figures are taken from Refs. [120, 121].

Muon candidates in the analyses of single-top-quark production within this thesis are required to be spatially isolated from EM and hadronic activity in addition to the tight identification criteria. The relative $\Delta\beta$ -based (“delta-beta”) isolation for muons is defined as

$$I_{\text{rel.}}^{\mu} = \frac{I_{\text{ch.-had.}} + \max(0, I_{\gamma} + I_{\text{neut.-had.}} - \beta \cdot I_{\text{PU}})}{p_{\text{T}}^{\mu}}, \quad \beta = \frac{1}{2}, \quad (4.2.)$$

where $I_{\text{ch.-had.}}$, I_{γ} , and $I_{\text{neut.-had.}}$ denote the summed transverse energies of charged hadrons, photons, and neutral hadrons respectively within $\Delta R = \sqrt{\Delta\eta^2 + \Delta\phi^2} < 0.4$ around a muon candidate. The term I_{PU} is used to correct the amount of considered neutral energy. It denotes the summed transverse energies of charged-particle tracks within $\Delta R < 0.4$ that are associated to pileup vertices. Hence, the applied correction $\beta \cdot I_{\text{PU}}$ can be interpreted as an estimate of the amount of neutral energy from pileup interactions within I_{γ} and $I_{\text{neut.-had.}}$. The chosen value for β is motivated by assuming equal production rates for the (π^+, π^0, π^-) isospin triplet leading to a ratio of $1/2$ for the production of neutral pions over charged ones.

4.5. Electrons

Similar to muon candidates, electron candidates are required to pass certain identification criteria as well. Studies of the electron reconstruction and identification performances in 8 TeV and 13 TeV pp collision data can be found in Refs. [112, 113]. The “tight” identification criteria, employed in this thesis, are elaborated briefly in the following.

A PF electron candidate with a GSF track is required. Candidates within the ECAL barrel-endcap transition region of $1.4442 < |\eta| < 1.5660$ are ignored. The electron track has to have a hit on the innermost tracker layer which prevents the selection of electrons from potential photon conversions ($\gamma \rightarrow e^+ e^-$). An explicit photon conversion veto is applied by testing if a pair of electron tracks originates from a common displaced vertex. Further selection criteria are combined into a multivariate identification discriminant. It is based on various input observables like the GSF track quality, the ECAL cluster shapes, their energy distribution, and the agreement between the independent cluster energy and track energy estimates. For 13 TeV data, the discriminant is replaced by a simplified cut-based version where multiple fine-tuned selections on similar observables are applied. A comparison of the efficiency of electron identification in 8 TeV data and simulation, estimated from $Z \rightarrow e^+ e^-$ events using the tag-and-probe method, is shown in Fig. 4.4. For transverse momenta above 30 GeV the identification reaches efficiencies of $\approx 95\%$. The small differences between data and simulation are corrected by dedicated scale factors as well, similar to the treatment of muon identification efficiencies (Sec. 4.4).

An electron candidate is also required to be isolated from other EM or hadronic activity in its vicinity. The relative $A_{\text{eff.}}^{\rho}$ -based (“effective area”) isolation for electrons is defined as

$$I_{\text{rel.}}^e = \frac{I_{\text{ch.-had.}} + \max(0, I_{\gamma} + I_{\text{neut.-had.}} - \rho \cdot A_{\text{eff.}}(\eta_{\text{SC}}))}{p_{\text{T}}^e}, \quad (4.3.)$$

where the transverse energies I_X per particle type X are summed in a cone of $\Delta R < 0.3$ around the electron candidate. The amount of neutral energy is corrected by the effective area $A_{\text{eff.}}$ times the median of the transverse energy density ρ calculated

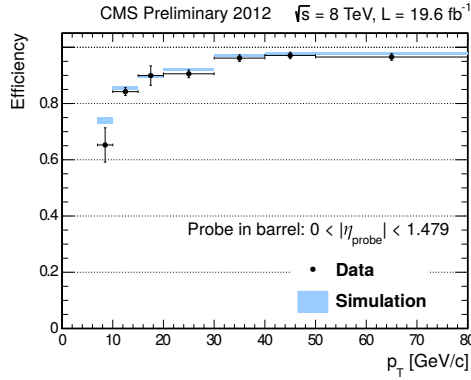


Figure 4.4. | Comparison of the electron identification efficiency in data and simulation as a function of its transverse momentum. The figure is taken from Ref. [122].

in $\delta\eta \times \delta\phi$ from charged-particle tracks that are associated to pileup vertices. The effective area is estimated from simulation and denotes the expected amount of neutral energy from pileup interactions per ρ within the isolation cone as a function of the pseudorapidity of the associated ECAL supercluster. The general idea behind the A_{eff}^ρ -based isolation for electrons is motivated by a proposed pileup subtraction method for jets which is detailed in Ref. [123].

4.6. Jets

Jets are clustered from PF candidates with the exclusion of charged hadrons that are associated to pileup vertices. This procedure is referred to as charged hadron subtraction (CHS) technique [124]. In addition, preselected isolated muons or electrons can be excluded from the jet clustering as well to prevent double counting of their momenta. For example, when studying the decay $t \rightarrow b\mu\nu$ a selected muon candidate should be prevented from being clustered into the b jet as well. This approach has been chosen in the reconstruction of 8 TeV data, whereas in analyses of 13 TeV data a minimal ΔR distance between the final leptons and jets for analysis is required instead. Jets are clustered using the iterative anti- k_T algorithm [125]. In its initial step all candidates are considered to be so-called ‘protojets’. At each iteration step the two distances

$$d_{ij} = \min \left(\frac{1}{p_{T,i}^2}, \frac{1}{p_{T,j}^2} \right) \cdot \frac{\sqrt{\Delta\eta_{ij}^2 + \Delta\phi_{ij}^2}}{R^2}, \quad d_i = \frac{1}{p_{T,i}^2}, \quad (4.4.)$$

are calculated for protojets i and j . If d_{ij} is the smallest distance between two protojets in an iteration, they are merged and their 4-momenta are summed. If otherwise d_i is found to be the smallest distance, the corresponding protojet is promoted to a final jet and ignored in subsequent steps. The parameter R controls the cone size of the resulting jets. In 8 TeV data, jets are clustered with $R = 0.5$ which was lowered to $R = 0.4$ in the reconstruction of 13 TeV data since the objects are more boosted due to the higher energy resulting into a smaller cone size.

In this thesis a “loose” jet identification is applied. The criteria are motivated by the fact that a proper jet, stemming from the hadronization of a quark or gluon, consists of a multitude of PF particles and types. The exact criteria are somewhat adjusted from one data taking period to the next. A jet should consist of more than one constituent and the neutral hadron and neutral EM energy fractions should be both less than 99%. In addition, for jets that fall within the tracker acceptance ($|\eta| < 2.4$) at least one constituent has to be a charged hadron and the charged EM fraction is required to be less than 99% amongst others. The identification efficiencies are found to be very close to 100% for both data and simulation.

In data and simulation the energies of reconstructed jets are found to deviate from the energies of corresponding jets clustered from the hadronization products of true partons from simulation due to non-linear subdetector responses and efficiencies. Therefore a series of jet energy corrections (JECs) are applied to relate the reconstructed energy to the true jet energy on average. The applied corrections are briefly outlined in the following whereas a detailed discussion can be found in Ref. [126]. The JECs are multiplicative factors for rescaling the 4-momenta of jets. Multiple levels of corrections are applied to data and simulation sequentially. First, the offset correction removes the dependence of the jet energy response on the additional pileup activity within an event. It is based on the jet area method [123]. The correction factors are derived by comparing the jet responses in simulated events with and without pileup events overlaid. The next level of corrections aims to obtain a uniform energy response which is independent of the transverse momentum and pseudorapidity of a jet. The corrections are derived from simulated events by matching reconstructed jets to close-by true particle jets and comparing their momenta. Lastly, residual differences between data and simulation are corrected by comparing the p_T balance in various types of events (multijet, Z+jets, γ +jets) where one jet is restricted to be within the barrel region ($|\eta| < 1.3$) to provide a reference. The total and individual uncertainties from the various corrections are shown in Fig. 4.5 for 8 TeV and 13 TeV data. At 8 TeV, the uncertainty is found to be mostly around 1% and only approaches 2% for forwards jets ($|\eta| > 3$) with low transverse momenta of $p_T \approx 30$ GeV, whereas larger uncertainties of 3–5% are found at 13 TeV for jets with a transverse momentum of 30 GeV and above. The optional jet flavor corrections shown in the plots have not been applied in the measurements within this thesis.

In addition to rescaling the jet energy, the jet energy resolution (JER) is corrected for simulated jets to mimic the spread in p_T as observed in data. Exemplary relative resolutions in terms of $p_T^{\text{reco.}}/p_T^{\text{true}}$ in 8 TeV simulation are presented in Fig. 4.6a for various pileup scenarios. Two methods are used to rescale the reconstructed 4-momentum which are chosen whether or not a jet can be matched to a true jet in simulation. The factors are defined as

$$c_{\text{matched}} = 1 + \frac{p_T^{\text{reco.}} - p_T^{\text{true}}}{p_T^{\text{reco.}}} \cdot (s_{\text{JER}} - 1), \quad (4.5a.)$$

$$c_{\text{unmatched}} = 1 + N(0, \sigma_{\text{JER}}) \cdot \sqrt{\max(s_{\text{JER}}^2 - 1, 0)}, \quad (4.5b.)$$

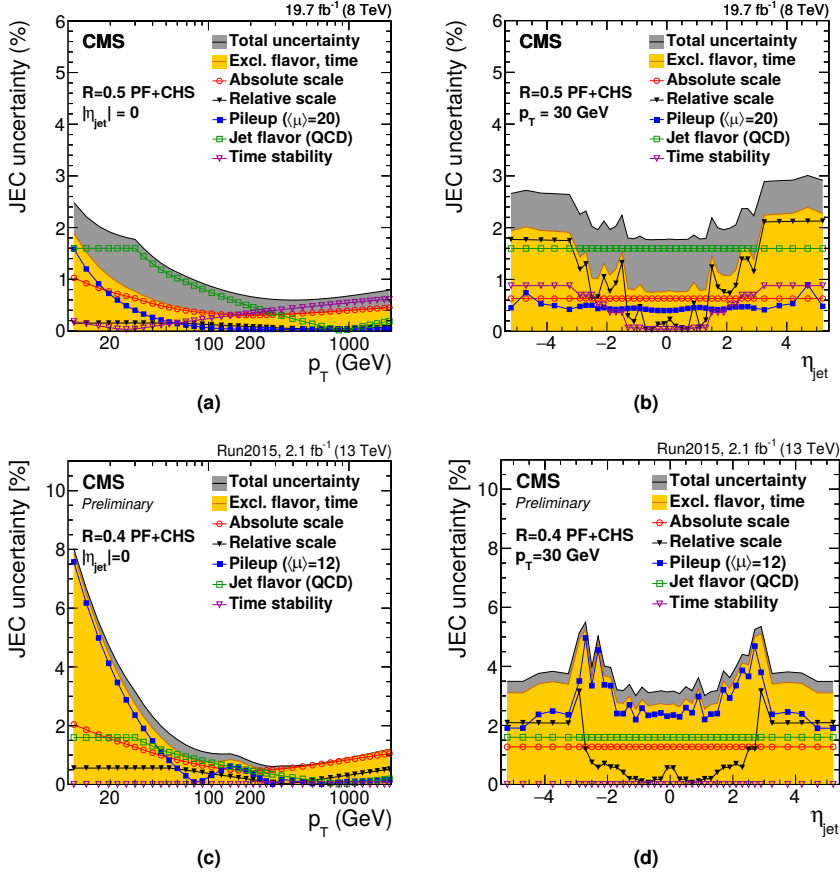


Figure 4.5. | Uncertainty on the jet energy corrections as a function of (left column) the transverse momentum and (right column) the pseudorapidity for center-of-masss energies of (top row) 8 TeV and (bottom row) 13 TeV. The figures are taken from Refs. [126, 127].

where σ_{JER} denotes the relative resolution in simulation and s_{JER} η -dependent resolution scale factors. The latter are determined from data by analyzing the p_T balance in dijet or γ +jets events. Exemplary scale factors, obtained from 8 TeV data, are shown in Fig. 4.6b. Similar scale factors are obtained from 13 TeV data as well [127]. A random smearing of the jet energy is performed instead in cases where it cannot be matched to a true jet using Eq. 4.5b. Here, $N(0, \sigma_{\text{JER}})$ denotes a sampled value from a normal distribution centered at zero with standard deviation σ_{JER} .

4.7. b-tagging

The identification of jets that stem from the hadronization of b quarks, so-called “b-tagging”, is a crucial ingredient in studies of top quark production. It provides discrimination power to single out jets which can be related to b quarks as expected in top quark decays.

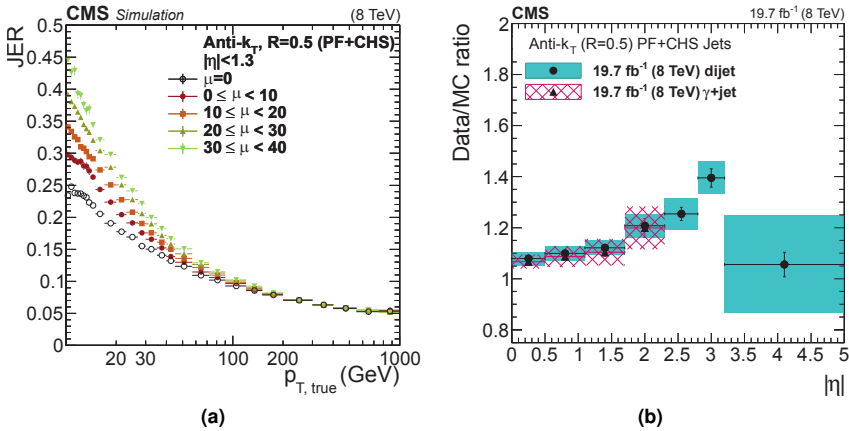


Figure 4.6. | Jet p_T -resolution correction: (a) relative spread in $p_T^{\text{reco.}}/p_T^{\text{true}}$ for different pileup scenarios as a function of the true jet momentum in simulation; (b) resolution scale factors derived from 8 TeV data. The figures are taken from Ref. [126].

Multiple algorithms have been developed within CMS to perform b-tagging [128, 129] for jets that fall within the pseudorapidity acceptance of the tracker. A common feature of most algorithms is the identification of a secondary vertex which is reconstructed from displaced tracks within a jet. The general idea is illustrated in Fig. 4.7. After hadronization, a final state b quark is encapsulated into a B meson (e.g. B^\pm , B_0 , B_s) which can then travel a measurable distance away from the primary vertex before decaying due to its relatively long lifetime. For example, a B^\pm meson, which has a mean lifetime of about 1.6 ps [1], can travel distances of roughly 4–9 mm for momenta of 40–100 GeV on average before decaying.

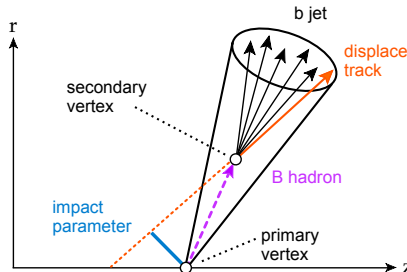


Figure 4.7. | Sketch of the production of displaced tracks in b jets through the displaced decay of a B hadron.

After reconstruction, secondary vertices are subjected to pass certain quality criteria to enhance their purity with respect to the B meson hypothesis. These are based on the amount of shared tracks with the primary vertex, the invariant vertex mass to reject kaon decays, and the direction of tracks with respect to the jet axis. In this thesis, b-tagging algorithms based on multivariate discriminators are employed. These combine multiple properties of the secondary vertex, tracks, and impact parameters amongst

others into a powerful discriminant. The training of the discriminator also covers scenarios where no secondary vertex has been reconstructed within a jet. In such cases, the compatibility of tracks with the primary vertex is condensed into the discriminant. A comparison of the performance of various *b*-tagging algorithms employed within CMS is presented in Fig. 4.8. It shows the misidentification probability of falsely tagging charm and light (*g,u,d,s*) quarks as a function of the efficiency to identify true *b* jets in simulation.

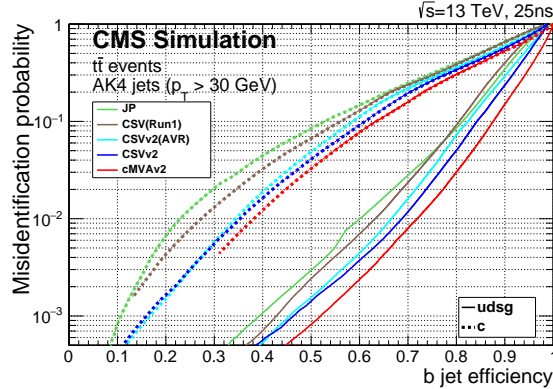


Figure 4.8. | Comparison of various *b*-tagging algorithms in simulation. The indicated version 2 refers to the algorithms in Run 2. The figure is taken from Ref. [129].

The combined secondary vertex (CSV) (Run 1) algorithm is employed in the 8 TeV and first 13 TeV (CSV version 2) analyses within this thesis. At their tight working points, a *b*-tagging efficiency of approximately 50% with a misidentification probability of only 0.1% is achieved. A new algorithm, called combined MVA (cMVA), is utilized in the analysis of 13 TeV data recorded in 2016. It combines the output of various other *b*-tagging algorithms which includes also the CSV discriminant. Additionally, the results of MVA discriminators trained to identify low- p_T electrons or muons inside a jet for *b*-tagging are taken as inputs as well. The final cMVA discriminant exhibits an improved rejection of charm and light quark jets compared to the other algorithms as shown in Fig. 4.8 [129].

The *b*-tagging efficiency in simulation typically deviates somewhat from the one observed in data. This is corrected by applying efficiency scale factors $\epsilon_b^{\text{data}} / \epsilon_b^{\text{sim}}$ to simulation which are derived from data. Multiple methods are used to measure the scale factors in either multijet data events, which are enriched with heavy-flavored jets by requiring close-by muons, or in events with two leptons and two jets yielding a $t\bar{t}$ -enriched sample [130]. A weight is calculated for each simulated jet based on the ratio of probabilities between simulation and data that the jet was tagged, i.e. its *b*-tagging discriminator value is past a working point. For multiple working points the weight can be expressed as

$$w_{\text{jet}} = \frac{p_{\text{data}}(\text{jet} \mid W_i < d^{\text{jet}} < W_{i+1})}{p_{\text{sim.}}(\text{jet} \mid W_i < d^{\text{jet}} < W_{i+1})} = \frac{s_i^{\text{jet}} \cdot \epsilon_i^{\text{jet}} - s_{i+1}^{\text{jet}} \cdot \epsilon_{i+1}^{\text{jet}}}{\epsilon_i^{\text{jet}} - \epsilon_{i+1}^{\text{jet}}}, \quad (4.6.)$$

where d^{jet} denotes the value of the b-tagging discriminant, W_i the working points $i = 0 \dots N$, ϵ_i the efficiency measured in simulation, and s_i the corresponding scale factors. In this equation, the scale factors and efficiencies for untagged jets ($i = 0$) are set to $s_0 = \epsilon_0 = 1$ whereas the efficiency of passing the highest working point W_N is set to $\epsilon_{N+1} = 0$. An event is reweighted by the multiplied weights from all jets passing the selection. The efficiencies and scale factors themselves depend on the reconstructed jet p_T , η and flavor, where the latter is determined from the decay and hadronization history of a matched true jet. In case no true jet can be matched (e.g. the reconstructed jet is driven by PF candidates from pileup interactions) a light flavored quark (g,u,d,s) is assumed as its origin.

4.8. Missing transverse energy

The missing transverse momentum, \vec{p}_T , and energy, E_T , is calculated from the momentum imbalance of the summed PF candidate momenta as

$$E_T = |\vec{p}_T|, \quad \vec{p}_T = \begin{pmatrix} p_x \\ p_y \end{pmatrix} = - \sum_i^{\text{PF cand.}} \vec{p}_{T,i}. \quad (4.7.)$$

In analyses it can be used to infer the summed transverse momenta of produced neutrinos which escape the CMS detector without being detected due to their very low interaction probability. In this thesis one neutrino is expected to be produced in signal events stemming from the decay of a single top quark which can lead to significant missing transverse energy of about $\langle E_T \rangle \approx 50$ GeV on average. The p_z component cannot be calculated from the momentum imbalance since the boost along the z-axis of an event, determined by the initial parton momentum fractions x_i , cannot be reconstructed.

The E_T scale is improved by propagating the corrected energy for PF candidates which are clustered into jets to the missing transverse momentum. Only jets with a p_T of at least 10 GeV (15 GeV) are considered for which energy calibrations are measured in 8 TeV (13 TeV) data respectively. The correction can be expressed as

$$\vec{p}_T^{\text{corr.}} = - \sum_i^{\text{jets}} \vec{p}_{T,i}^{\text{corr.}} - \sum_i^{\text{unclustered}} \vec{p}_{T,i}^{\text{raw}} \quad (4.8a.)$$

$$= \vec{p}_T^{\text{raw}} - \sum_i^{\text{jets}} \left(\vec{p}_{T,i}^{\text{full JEC}} - \vec{p}_{T,i}^{\text{PU-only}} \right), \quad (4.8b.)$$

where $\vec{p}_{T,i}^{\text{PU-only}}$ denotes the transverse jet momentum after applying only the first level of energy corrections which deals with the contribution from pileup. The resulting improvement is demonstrated in Fig. 4.9. It shows the parallel component of the missing momentum vector u_{\parallel} along the direction of a reconstructed Z boson or photon \vec{q}_T in a ratio over the recoil momentum. After propagating the applied jet energy corrections to \vec{p}_T , the energy scale of its parallel component is reconstructed well within 3% or better for recoil momenta above 50 GeV. At low momenta, contributions from unclustered PF candidates dominate which results in a degradation of the energy scale.

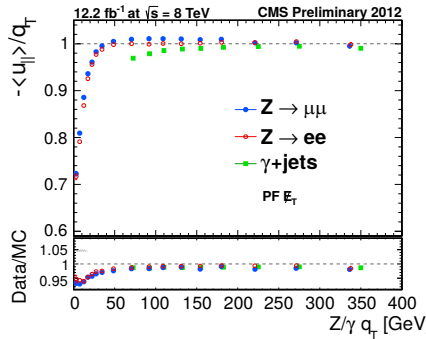


Figure 4.9. | The average \vec{p}_T component parallel to the recoiling Z/γ boson as a function of the boson's momentum. The figure is taken from Ref. [131].

In 8 TeV data and simulation an additional correction is applied to decrease the influence of pileup on the \cancel{E}_T scale. Since typical inelastic pp interactions do not produce any prompt neutrinos, pileup events will only lead to a smearing of the \cancel{E}_T due to the finite detector response for measuring neutral particle momenta. This can be mitigated by subtracting the amount of charged and neutral energy associated to pileup vertices where the latter is estimated from the amount of charged hadron activity.

4.9. Luminosity

The luminosity delivered by the LHC during collisions at the CMS interaction point is determined by measuring certain process rates with so-called luminometers. These are the pixel detector, the HF calorimeter, and the pixel luminosity telescope [132] amongst others. The instantaneous luminosity is then calculated from the recorded process rate R of the luminometer as

$$L \cdot dt = \frac{R \cdot dt}{\sigma_{\text{fid}}} , \quad (4.9.)$$

where $\sigma_{\text{fid}} = \sigma \cdot A$ is the fiducial cross section observed within the luminometer acceptance A . The fiducial cross section is estimated from so-called van der Meer (VdM) scans during which the proton beams are first separated and then gradually crossed with each other. By fitting the rate as a function of the beam separation in such scans an absolute calibration of the luminometers is obtained. The most precise luminosity estimations for the data analyzed in this thesis are obtained with the pixel cluster counting method [133–135]. Here, the rate is defined as the number of pixel clusters reconstructed in the second and third pixel barrel layers per bunch crossing. This luminometer profits from the low channel occupancy of the pixel detector which results in a linear dependency between the cluster rate and the instantaneous luminosity even in high pileup events with many particle tracks.

From the measured luminosity the distribution of the number of pileup interactions in data can be inferred. For simulated samples a predefined distribution is assumed instead according which the hard scattering event is overlaid with additional minimum bias events. Thus, a reweighting of simulated events has to be performed to match

the corresponding distribution of PU interactions in data. The average number of PU interactions is estimated in data per luminosity section using $\langle N_{\text{PU}} \rangle = \sigma_{\text{pp}} \cdot L$ where σ_{pp} denotes the total inelastic pp cross section. An event weight is then derived from the ratio of the distributions of PU interactions in data and simulation. The inelastic cross section has been measured in 13 TeV pp collisions as 71.3 ± 3.5 mb [136]. However, a better agreement between data and simulation is obtained for pileup sensitive observables such as the number of primary vertices or the median of the transverse energy density, ρ , with a slightly lower cross section of 69 mb.

4.10. Summary of corrections

Several corrections have been introduced throughout this chapter to improve the agreement between data and simulation. The corrections are also considered sources of systematic uncertainties in the presented analyses within this thesis. A summary of the corrections and associated uncertainties is provided in the following.

Lepton selection The efficiencies for selecting isolated muons or electrons which pass dedicated tight identification criteria are corrected through data-to-simulation scale factors. In addition, the analyzed data events have been recorded using single muon or electron triggers whose efficiencies in simulation are also corrected to match the ones observed in data. The applied lepton scale factors are varied independently within one standard deviation of their measured uncertainties to assess the systematic impact on the measurements.

Jet energy scale and resolution The momenta of reconstructed jets in data and simulation are corrected to relate to the expected true jet energy derived from the hadronization products of partons in simulation. Residual corrections and a smearing procedure are applied to match the overall scale and resolution of the jet energy in data. The corrections are also propagated to the \cancel{E}_T which improves its energy response as well. The systematic uncertainties arising from the measured energy and resolutions scale factors are estimated by varying them within their uncertainties and repeating the measurements with recalibrated jets and \cancel{E}_T .

Unclustered energy The momentum of PF candidates which are not clustered into jets is varied to estimate the uncertainty due their uncalibrated contributions to the missing transverse energy.

B-tagging Scale factors are applied in simulation to match the performance of the employed b-tagging algorithm in data. The systematic uncertainties are assessed for b and c jets by varying their scale factors simultaneously while the scale factor for mistagging g,u,d,s jets is varied independently.

Pileup The impact of pileup is estimated by varying the inelastic pp cross section by $\pm 5\%$ which changes the estimated distribution of true pileup interactions in data. The corresponding reweighting factors are rederived and applied to simulation.

5.

Chapter

Analysis techniques

The techniques and toolset to perform the measurements within this thesis are introduced. The chapter is organized to follow the common steps of the performed analyses. First, the generation of simulated events is introduced. Then, the reconstruction of top quark candidates in data and simulated events is described. An introduction to boosted decision trees (BDTs) is given which yield powerful discriminants for separating signal and background events further after the event selection. Then, the estimation of the amount of signal and background events in data through template-based maximum-likelihood (ML) fits is elaborated. To compare the results with theoretical predictions, observables at parton and particle level are defined whose distributions are inferred from data through unfolding in the measurements. Lastly, the unfolding problem is investigated and a regularized unfolding technique is detailed.

5.1. Event generation

To compare reconstructed data with theoretical predictions, samples of simulated collision events are generated and passed through a simulation of the CMS detector and an emulation of its readout. For the analyses, the standard so-called “Full Simulation” package [137, 138] is employed for performing the detector simulation. It is based on the Geant4 toolkit [139] which allows a detailed simulation of the interactions of particles with the detector material. A faster alternative, the so-called “Fast Simulation” package [140, 141], exists within CMS as well but it has not been utilized within this thesis.

The generation of events begins with the matrix elements (MEs) of a hard scattering process of interest. Monte-Carlo (MC) methods are used for sampling the corresponding cross section integral. The advantage of MC-based methods is that the variance of their result decreases as $\propto 1/n$ independently of the integral’s dimensionality, where n is the number of samples. This makes MC methods particular efficient for calculating cross sections from matrix elements (MEs) compared to quadrature-based methods (e.g. Simpson’s rule, Newton-Cotes). A common method to integrate a ME for a given process is the VEGAS algorithm (see e.g. Ref. [142]). It is based on importance sampling where the cross section integral is sampled not uniformly but along an adaptive density function instead. The resulting sample of events reflects the probability distribution of a process over its final state phase space. A reweighting is typically performed in addition such that all events contribute the same probability, i.e. they carry the same absolute weight.

After obtaining a sample of events from the hard interaction, a parton shower (PS) program simulates the hadronization of final state partons into hadrons which may then also decay further afterwards. In addition, radiation of soft gluons or quarks from

initial or final state partons is simulated as well which is referred to as initial state radiation (ISR) or final state radiation (FSR) respectively. Furthermore, contributions from soft secondary interactions, the so-called underlying event, and color reconnection effects are taken into account by PS simulations as well. A sketch of an exemplary pp collision event after hadronization is shown in Fig. 5.1 where various parts of the event simulation are highlighted.

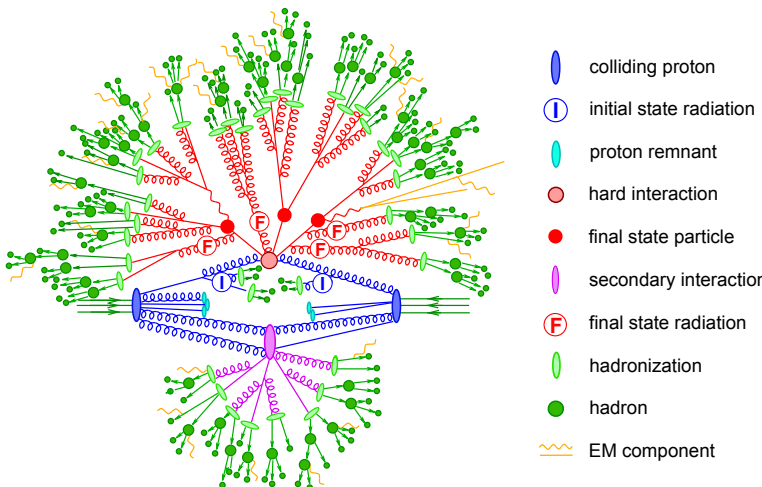


Figure 5.1. | A sketch of a generated event from the simulation of the hard interaction and subsequent hadronization through a parton shower. The figure is taken from Ref. [143].

PS simulations are based on Altarelli-Parisi splitting functions [34] which allow to calculate the probability that a soft parton splits into two others as $q \rightarrow q\bar{q}$, $g \rightarrow q\bar{q}$, or $g \rightarrow gg$. It is convenient to calculate the “survival” probability, the so-called Sudakov factor, that a parton does not split between two energy scales. The emission of soft partons leads to a complication during the PS simulation since such emissions could be double-counted if the upstream simulation of the hard interaction may have produced a similar soft emission already. The problem of double-counting occurs due to the fact that the phase spaces, where an event generator and a subsequent PS program simulate their products in, are overlapping. This is avoided by applying a dedicated ME-to-PS matching scheme which consists of a method to assign additional emissions exclusively to either the ME or the PS simulation depending on the event kinematics. Thus both simulation phase spaces become orthogonal to each other. Further information on parton shower simulation and matching algorithms can be sought in Refs. [143, 144].

A brief overview of the employed programs used for event generation and subsequent parton showering for t -channel single-top-quark production is given in the following.

MadGraph5_aMC@NLO The MadGraph5_aMC@NLO program [145] is a merge of the LO MadGraph generator [146] and the aMC@NLO program (first showcased in Ref. [147]) into a common framework. It supports the generation of samples at LO or NLO accuracy together with a dedicated matching to parton showers using the MLM [148] or MC@NLO [149] schemes respectively. The latter matching scheme produces a

certain fraction of events with negative weights (depending on the process) which originate from a subtraction of amplitudes containing additional emissions from the NLO matrix element to prevent double-counting. The `MadGraph5_aMC@NLO` framework is also capable of producing multiple samples with additional final state partons at ME level that can be merged into a combined sample. The overlap with the PS simulation between the exclusive samples is removed through the MLM [144] or FxFx [150] merging schemes.

Powheg The POWHEG box (versions 1,2) [151] is a program that contains predefined implementations of various processes such as t -channel single-top-quark production at NLO [152]. It applies the so-called POWHEG method [153] for ME-to-PS matching in which the hardest radiation generated from the ME has priority over subsequent PS emissions to remove the overlap with the PS simulation. A small fraction of negatively weighted events may be generated as well in phase space regions where NLO calculations are not feasible.

CompHEP The CompHEP program (version 4.5) [154] can perform calculations of cross sections from Lagrangian densities at LO. In addition, generation of events is also possible such as single-top-quark production [155]. Here, an approximation is used by combining events from the $2 \rightarrow 2$ and $2 \rightarrow 3$ processes which reproduces NLO corrections in an effective way.

Tauola Event generators can be interfaced with the Tauola library [156,157] which is specialized for simulating leptonic and hadronic decays of tau leptons with high accuracy. It accounts for spin polarization effects while the radiation of photons from QED corrections in also included by incorporating the Photos library [158].

MadSpin The generation of events from processes involving the production and decay of resonances is a computational-intensive task especially at NLO. In the narrow width approximation, where a resonant particle is taken to be on-shell, the production and decay amplitude factorizes which allows to perform the simulation of the production and decay of heavy resonances like top quarks or Higgs bosons in separate steps to reduce the complexity. The MadSpin program [159] extends this approach by also accounting for off-shell effects through a partial reweighting of events. In addition, spin correlations effects between production and decay products are taken into account as well.

Pythia The Pythia program (versions 6,8) [160,161] can generate events of various processes at LO. However, in the analyses only its PS simulation is used which can be interfaced with other LO and NLO event generators to perform subsequent parton showering, hadronization, and the simulation of the underlying event. The Pythia program employs a phenomenological model for simulating hadronization in which one-dimensional strings^(*) interconnect the partons to reflect the color field. Additional partons are created through string branching which leads finally to the formation of color-neutral singlets.

Herwig++ The Herwig program [162,163] is an NLO event generator that can also perform a standalone PS simulation which can be interfaced with various other event generators as well. Similar to the usage of Pythia in this thesis, only its PS

^(*) The string model is motivated by the fact that the spatial form of a dipole color field does not extend radially like an EM field but is instead squeezed to a tube-like form.

algorithm is employed for sample generation in the analyses. Its hadronization algorithm is based on a model in which color-connected quarks are spatially kept together in clusters [164]. This is motivated by the concept of “preconfinement” for colored particles [165]. If the mass of a cluster is sufficiently high it can decay into lighter clusters with a certain probability. In the final simulation step, a cluster decays then into hadrons according to its quark content.

5.2. Top quark reconstruction

In the presented analyses, a top quark candidate is reconstructed in data and simulated events from selected analysis objects under the assumption of t -channel signal top quark production. Assuming that the top quark decayed leptonically as $t \rightarrow bW \rightarrow b\ell\nu$ in selected events, its energy and momentum is calculated by summing the 4-momenta of a selected lepton candidate (muon or electron), a b -tagged jet, and a neutrino candidate. The neutrino candidate itself is reconstructed from the missing transverse momentum and the lepton momentum by imposing a W boson mass constraint of

$$\begin{aligned} m_W^2 &= (80.4 \text{ GeV})^2 = \left(\begin{pmatrix} E_W \\ \vec{p}_W \end{pmatrix} \right)^2 \stackrel{!}{=} \left[\left(\begin{pmatrix} E_\ell \\ \vec{p}_\ell \end{pmatrix} + \begin{pmatrix} E_\nu \\ \vec{p}_\nu \end{pmatrix} \right) \right]^2 \\ &= \underbrace{m_\ell^2 + m_\nu^2}_{\approx 0} + 2 \cdot E_\ell E_\nu - 2 \cdot \begin{pmatrix} p_{\ell,x} \\ p_{\ell,y} \\ p_{\ell,z} \end{pmatrix} \cdot \begin{pmatrix} p_{\nu,T} \cdot \cos\phi_\nu \\ p_{\nu,T} \cdot \sin\phi_\nu \\ p_{\nu,z} \end{pmatrix}, \end{aligned} \quad (5.1.)$$

where the lepton and neutrino are approximated as massless. One can then solve for the unknown $p_{\nu,z}$ -component of the neutrino momentum while setting $\vec{p}_{\nu,T}$ to the missing transverse momentum \vec{p}_T . After rearranging Eq. 5.1 one obtains the quadratic equation

$$0 = p_{\nu,z}^2 - \frac{2\xi p_{\ell,z}}{E_\ell^2 - p_{\ell,z}^2} \cdot p_{\nu,z} - \frac{\xi^2 - E_\ell^2 p_{\nu,T}^2}{E_\ell^2 - p_{\ell,z}^2}, \quad \xi = \frac{m_W^2}{2} + p_{\nu,T} p_{\ell,T} \cdot \cos(\phi_\ell - \phi_\nu), \quad (5.2.)$$

which possesses the solutions

$$p_{\nu,z}^{1,2} = \frac{1}{E_\ell^2 - p_{\ell,z}^2} \left[\xi \cdot p_{\ell,z} \pm E_\ell \sqrt{\underbrace{\xi^2 - p_{\nu,T}^2 (E_\ell^2 - p_{\ell,z}^2)}_{\equiv \kappa}} \right]. \quad (5.3.)$$

A detailed derivation of this result can be found in Ref. [166]. In simulated t -channel single-top-quark events this procedure leads to two real solutions in about 65% of all selected events. In Fig. 5.2 the difference of both real solutions with respect to the true neutrino p_z at parton level is shown. The plot demonstrates that choosing the solution which has the smallest absolute $|p_{\nu,z}|$ value yields on average the solution which is significantly closer to the true neutrino p_z .

Complex solutions are obtained if the radicand κ in Eq. 5.3 becomes negative. This happens in about 35% for selected signal events. Such solutions occur mostly due to the finite E_T resolution whereas negligence of off-shell W bosons and the resolution

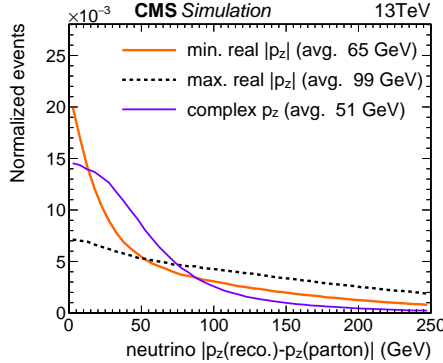


Figure 5.2. || Difference between the reconstructed neutrino p_z and the neutrino p_z at parton level for events with two real solutions (distinguished by their $|p_z|$ value) and for events with complex solutions where the imaginary part is ignored in t -channel single-top-quark production.

of the lepton momentum are found to be minor effects. The imaginary part of the solutions is removed by requiring that the discriminant vanishes

$$0 \stackrel{!}{=} \kappa^2 = \xi^2 - p_{\nu,T}^2 (E_\ell^2 - p_{\ell,z}^2) \quad (5.4a.)$$

$$\Rightarrow p_{\nu,z} = \frac{\xi \cdot p_{\ell,z}}{E_\ell^2 - p_{\ell,z}^2}, \quad (5.4b.)$$

which is equivalent to setting the transverse mass m_T to the W boson mass itself as

$$\begin{aligned} m_W^2 &\stackrel{!}{=} m_T^2 = (p_{\ell,T} + p_{\nu,T})^2 - (p_{\ell,x} + p_{\nu,x})^2 - (p_{\ell,y} + p_{\nu,y})^2 \\ &\approx 2 p_{\ell,T} p_{\nu,T} \cdot (1 - \cos(\phi_\ell - \phi_\nu)). \end{aligned} \quad (5.5.)$$

This is achieved by varying the $p_{\nu,x}$ and $p_{\nu,y}$ components simultaneously such that they satisfy Eq. 5.4a. The $(p_{\nu,x}, p_{\nu,y})$ -pair which additionally minimizes the distance $|\vec{p}_{\nu,T} - \vec{p}_T|$ with respect to the measured missing transverse momentum vector is then taken as the result. Figure 5.2 shows that after removing the imaginary part (Eq. 5.4b) the $p_{\nu,z}$ solution is on average closer to the true neutrino $p_{\nu,z}$ momentum compared to cases with real solutions. This can be explained as follows. Initially $m_T > m_W$ is found in cases of complex solutions which is then modified to $m_T = m_W$ by ignoring the imaginary part and applying the minimization procedure as described above. One can therefore argue that this represents a correction of the missing transverse momentum which is mismeasured in signal events and thus led to the initial problem of obtaining complex solutions when solving Eq. 5.3.

After finding a solution for the unknown neutrino p_z component, a top quark candidate can be constructed. For simulated signal events, a comparison of the resulting shapes of the reconstructed top quark mass and pseudorapidity for the two neutrino solution cases is presented in Fig 5.3. For events with initial complex solutions the reconstruction procedure yields a top quark candidate with an improved mass resolution compared

to events with real solutions. Similarly, the pseudorapidity of the top quark candidate demonstrates an improved reproduction of the corresponding shape at parton level as well.

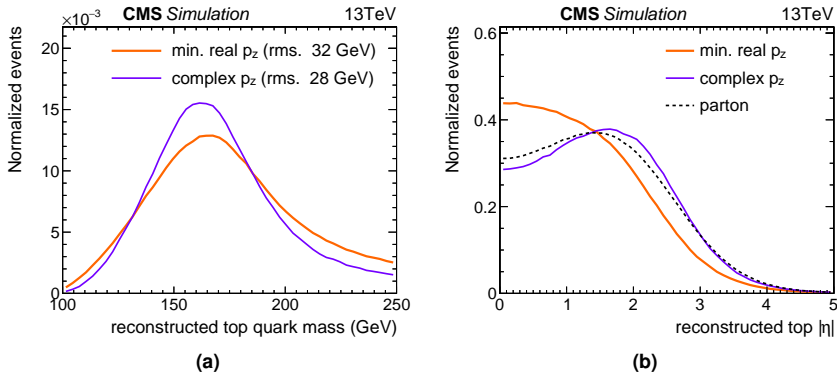


Figure 5.3. | Differences in shape for the reconstructed top quark (a) mass and (b) pseudorapidity for cases with real neutrino p_z solutions (where the one with the smallest $|p_z|$ is picked) or with initially complex solutions for simulated events of t -channel single-top-quark production.

5.3. Boosted Decision Trees

After selecting events with one isolated lepton, two jets (where one is b-tagged), and significant \cancel{E}_T or $m_T(W)$, the majority of events does not stem from t -channel single-top-quark production but from background processes instead which mimic its signature. The ratios of the signal-over-background (S/B) yields amount to about 13% and 14% in cross section measurements at 8 and 13 TeV, respectively [167, 168]. Most of the background events stem from $W+jets$, $t\bar{t}$, and multijet production whereas contributions from single-top-quark production in tW and s channel, Z/γ^*+jets , and diboson production are found to be less than 10% in 8 and 13 TeV data after the event selection. The small S/B ratios motivate the usage of multivariate analysis (MVA) techniques to separate signal and background events further. In this thesis, boosted decision trees (BDTs) are employed for event classification as implemented in the TMVA framework [169]. They are based on a set of decision trees where each yields a binary output depending on whether an event is signal- or background-like. Their training and how the outputs of single decision trees are combined into a powerful one-dimensional discriminant are described in the following.

An exemplary decision tree is presented in Fig. 5.4. It consists of sequential selections on observables x_i which are applied on events such that the leaf nodes contain either a majority of signal or background contributions. Such trees are constructed by using samples of simulated events for which the desired classification is a priori known (“supervised learning”).

The optimal selection per node is found by analyzing the separation between signal and background distributions for various observables and corresponding working points C_i . In the analyses, the separation is measured as the cross entropy

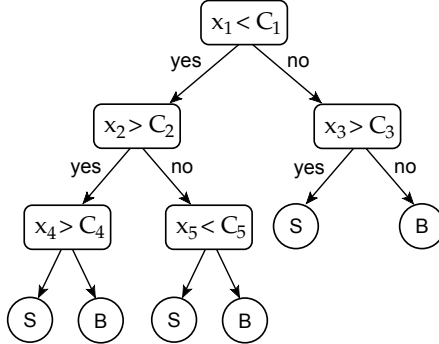


Figure 5.4. | A sketch of an exemplary decision tree.

$$H = -p \cdot \ln(p) - (1-p) \cdot \ln(1-p), \quad p_i = \frac{\int_{C_i}^{\infty} N_{\text{sig.}}(x_i) dx_i}{\int_{C_i}^{\infty} N_{\text{sig.}}(x_i) + N_{\text{bkg.}}(x_i) dx_i}, \quad (5.6.)$$

where p_i denotes the achieved purity of a selection $x_i > C_i$ per node i . Other common measures of separation in literature are the misclassification error or the so-called “Gini” index [170]. The measures are constructed to be symmetric when swapping the signal and background classes since obtaining a high purity background leaf is of equal importance for classification. A node is not split further if it contains less than a predefined minimum number of events which ensures that the decisions of all nodes and the binary output per leaf are statistically significant. This also mitigates a potential “overtraining” of a decision tree that occurs when statistical fluctuations are learned instead of the underlying physical distributions due to the finite statistics of the training sample.

Additional caution is required when training decision trees with a sample that contains a fraction of negatively weighted events (e.g. generated with MadGraph5_aMC@NLO). In such cases a tree may be trained incorrectly if a significant fraction of negatively weighted events are selected in one of the nodes which are not canceled by sufficient amounts of positively weighted ones. The distributions of observables which are scanned to find the optimal node splitting can contain regions with negative yields that are unphysical. To prevent such cases the minimum number of events per node can be increased further beyond the statistical motivated threshold. In addition, the scanned working points per observable can be preset which prevents that a decision becomes sensitive to events close to a selection border. Specifically, in the employed TMVA framework one can configure that only a certain number of equidistantly-spaced working points are scanned per observable.

Single decision trees can still be affected by statistical fluctuation leading to misclassification errors when evaluated on a statistically-independent test sample. This is mitigated by training multiple decision trees with binary outputs $h_i \in \{-1, 1\}$ which are then combined into a pseudo-continuous discriminant via a majority vote

$$M(\vec{x}) = \sum_i^{N_{\text{trees}}} w_i \cdot h_i(\vec{x}; \vec{C}_i), \quad (5.7.)$$

where each decision tree output is multiplied by a weight w_i . Apart from mitigating overtraining this procedure has further advantages. It has been demonstrated in literature that the output of a majority vote can yield a classifier with high accuracy, a so-called “strong learner”, even when all single decision trees possess only a low accuracy. In fact, it is even sufficient if the accuracy of single trees is just slightly better than random guessing [171, 172]. Therefore, the individual decision trees can be kept very shallow, i.e. they have only a low number of layers which also improves their robustness against overtraining. A strong learner can be obtained nonetheless by adjusting the weights in the majority vote according to the individual accuracy per tree. Usually a “boosting” procedure prescribes the training cycle of decision trees and how the corresponding weights have to be set.

The two boosting procedures employed in this thesis are the AdaBoost [173] (short for “adaptive boosting”) and the GradientBoost [174] algorithms. In the AdaBoost algorithm, decision trees are trained iteratively. At each step, a single decision tree is trained and the misclassified events are identified. Their weight is then increased in the training of subsequent trees by the boosting weight

$$\alpha_{n+1} = \left(\frac{1 - \epsilon_n}{\epsilon_n} \right)^\beta, \quad (5.8.)$$

where ϵ_i denotes the misclassification error of the current tree n and β is a configurable learning rate. The corresponding weights in Eq. 5.7 are then given by $w_i = \ln \alpha_i$. Typically, a slow learning rate of $\beta \leq 0.5$ is chosen to allow for more boosting steps. It can be shown that the AdaBoost algorithm is equivalent to the minimization of the exponential loss function $L(M, y) = \exp(-M(\vec{x}) \cdot y)$ where y denotes the true classification of events [169]. If the loss function is instead changed to

$$L(M, y) = \ln \left(1 + e^{-2 M(\vec{x}) \cdot y} \right) \quad (5.9.)$$

the GradientBoost algorithm is obtained instead. Its loss function is more robust in the presence of outliers and noise events for which the AdaBoost algorithm may degrade. In the GradientBoost algorithm the loss function is iteratively minimized with respect to the weights and decision tree parameters in M using the method of gradient descent. During the minimization the output of the majority vote will gradually tend towards y because misclassified events result in large gradients of the loss function. Similar to the AdaBoost algorithm, an increased performance is obtained when decreasing the learning rate that controls the boosting weights which is called “shrinkage” here. Both boosting algorithms have been tested to validate their performances with respect to each other. Only negligible differences in their discrimination power have been found when trained on the classification problems considered in this thesis.

The discrimination power of a BDT is assessed by analyzing the receiver operating characteristic (ROC) curve. Exemplary ROC curves are presented in Fig. 5.5 for separating t -channel single-top-quark events against $W+jets$ and $t\bar{t}$ background events at 13 TeV. The area-under-curve (AUC) value denotes the area under the ROC curve with respect to random guessing. Its ranges from 0% in case of no discrimination power to up to 50% in the case that both event classes are fully separated in the analyzed

distribution. In the figure, the ROC curves of a trained BDT is compared to the pseudorapidity of the untagged light jet and to the reconstructed top quark mass. An AUC of about 32% is achieved with the trained BDT which outperforms the other two typical event observables for separating t -channel events from background processes. The exact setup of the BDT shown here will be discussed later in Sec. 7.4 together with the corresponding analysis.

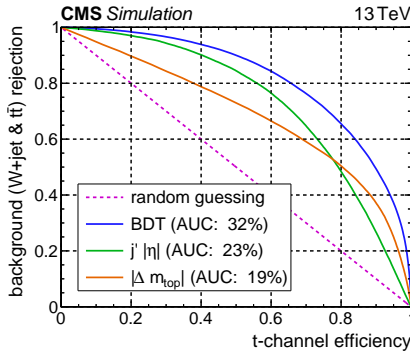


Figure 5.5. Comparison of ROC curves for separating t -channel single-top-quark events from background events ($W+jets$ and $t\bar{t}$ samples mixed according to their cross section) using: random guessing; a trained BDT discriminant; the pseudorapidity of the untagged light jet (j'); the difference between the reconstructed top quark mass and the nominal top quark mass, $|\Delta m_{\text{top}}| = |m_{\text{top}}^{\text{reco.}} - 172.5 \text{ GeV}|$.

5.4. Template-based fitting

The amounts of signal and background events in data are estimated through template-based maximum-likelihood (ML) fits. For an observable to be fitted, histograms act as templates which reflect the expected distributions of events per process. One can express the likelihood that the observed distribution in data is a realization of the expectation as

$$\mathcal{L}_{\text{Poi.}} = \prod_i^{\text{bins}} \frac{p_i^{d_i} \cdot e^{-p_i}}{d_i!}, \quad p_i = \beta^{(\text{sig.})} \cdot T_i^{(\text{sig.})} + \sum_j^{\text{bkgs.}} \beta^{(j)} \cdot T_i^{(j)}, \quad (5.10.)$$

where the amount of data events d_i per bin i is modeled as a Poisson distribution with the expected event yield p_i as mean. The expected yields per bin are obtained by summing the signal and background templates $T_i^{(X)}$. The normalization of the templates can be modified through scale factors $\beta^{(X)}$. These are then estimated from data by maximizing the likelihood. The signal scale factor is also referred to as signal “strength” whereas the background scale factors are sometimes called nuisance parameters because their result is of less importance. Technically, the theta framework [175] is employed for template-based fitting in this thesis where the negative logarithm of the likelihood

$$-\ln \left(\mathcal{L}_{\text{Poi.}}(\vec{\beta}) \right) = - \sum_i^{\text{bins}} \left[d_i \ln p_i(\vec{\beta}) - p_i(\vec{\beta}) \right] + \text{const.} \quad (5.11.)$$

is minimized instead for convenience and numerical stability. Such fits perform best when the templates feature different shapes in the fitted observable, i.e. the individual contribution to the summed expectation differs per template and additionally varies across the fitted bins.

An estimated scale factor can be directly translated into a cross section since the templates are normalized to their expected SM cross sections multiplied with the integrated luminosity of data. One obtains

$$\hat{\sigma}_{\text{sig.}} = \frac{\hat{N}_{\text{sig.}}}{A \cdot \epsilon \cdot \int L}, \quad \hat{N}_{\text{sig.}} = \hat{\beta}_{\text{sig.}} \cdot N_{\text{exp.}} = \hat{\beta}_{\text{sig.}} \cdot \underbrace{\sigma_{\text{SM}} \cdot \int L}_{\text{norm.}} \cdot \overbrace{A \cdot \epsilon}^{\text{sel./reco.}}, \\ = \hat{\beta}_{\text{sig.}} \cdot \sigma_{\text{SM}}, \quad (5.12.)$$

where A denotes the acceptance and ϵ the efficiency of the event selection and reconstruction which are estimated through the simulated samples. This includes also any applied corrections of the selection efficiency as summarized in Sec. 4.10. In fits, additional constraints are typically applied for the background scale factors by adding log-normal priors to the likelihood as

$$-\ln(L_{\text{total}}) = -\ln(L_{\text{Poi.}}(\vec{\beta})) + \sum_j^{\text{bkgs.}} \frac{1}{2} \cdot \left(\frac{\ln \beta^{(j)}}{\delta^{(j)}} \right)^2. \quad (5.13.)$$

The additional constraints with uncertainties $\pm\delta$ reflect a priori beliefs of the background contributions in the analysis phase space where the fit is carried out. They are motivated by the fact that the selected analysis phase space is usually not optimized to measure the background yields very precisely. Log-normal distributions are explicitly preferred over Gaussian distributions for implementing these constraints because they are not biased when requiring that the scale factors have to be strictly positive. For Gaussian distributions on the other hand, such a truncation would shift their mean which can then bias the fit result.

Extra uncertainties have to be considered in the fit to account for the limited accuracy of the expected event yields per bin since the fitted templates are usually derived from samples of simulated events with finite statistics. A method proposed by R. Barlow and C. Beeston [176], commonly called Barlow-Beeston method, introduces additional nuisance parameters v_{ij} per bin i and process j which modify the predicted yields as $p'_i = \sum_j v_{ij} \cdot p_{ij}$ while adding additional constraints to the likelihood which reflect the uncertainties due to the finite MC statistics. This approach however increases the complexity of the fit due to the plethora of new nuisance parameters which have to be estimated in addition to the signal and background scale factors. The number of Barlow-Beeston parameters is reduced in the “Barlow-Beeston-lite” method [177] where the uncertainties per bin are grouped and described by only a single nuisance parameter. A further, technical simplification can be achieved when using numerical minimization algorithms for fitting. Here, it is computationally advantageous to only maximize the likelihood with respect to the scale factors while profiling the Barlow-Beeston parameters per bin in each step in-situ. This approach is also implemented in

the employed theta framework. One should note that such an approach can however result in discontinuous jumps of the likelihood. Certain minimization algorithms (e.g. Minuit [178]) may therefore not converge properly since the Hessian matrix is not positive-definite near such discontinuities. Therefore, the minimization in theta is explicitly set to a simple iterative Newton algorithm.

5.5. Parton and particle level observables

Cross sections can be measured not only inclusively but also differentially in intervals of an observable. Such measurements allow to perform in-depth comparisons of data with theoretical predictions and to assess the modeling of event generators. Furthermore, some differential cross sections can be sensitive to the coupling structure of a certain process as detailed in Ch. 2 and can thus be used to extract pseudo observables like the top quark spin asymmetry which is sensitive to the polarization of single top quarks produced in t channel. However, to perform a proper comparison of differential cross sections, observables of interest have to be well-defined, and identical across event generators and in analytical calculations. There are two “levels”—parton and particle level—at which physics objects of a process and related observables are typically defined.

The “parton level” encompasses the intermediate and final state particles within Feynman diagrams of a given process while not distinguishing between different initial states. In event generators, these partonic particles are produced in the hard interaction before hadronization. An exemplary event of t -channel single-top-quark production at parton level as produced by the POWHEG event generator is shown in Fig 5.6.

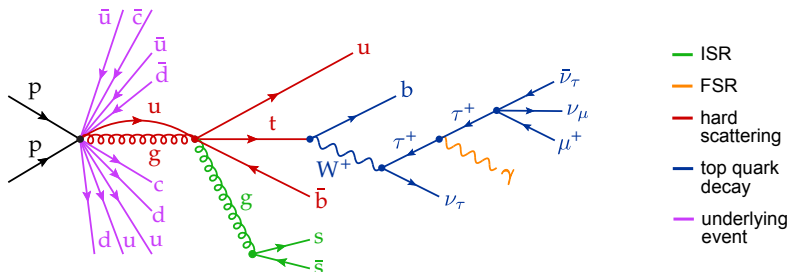


Figure 5.6. Production and decay of an exemplary t -channel single-top-quark event in 4 FS at parton level as produced by POWHEGv2 interfaced with MadSpin and Pythia8. Some intermediate state particles and vertices are not stored by the generator. Copies of particles reflecting the exclusion or inclusion of boosts induced by QCD/QED radiations have been omitted.

Some intermediate particles and vertices are not provided by the generator for simplicity but also due to the quantum nature of a process. Since events are generated to follow the probability of the squared sum of various matrix elements contributing to a certain process, one can usually not associate a generated event to only one specific Feynman diagram with absolute certainty. Nonetheless, various intermediate and final particles are stored unambiguously in the event record and can thus be used to define

also related observables at parton level. This is detailed in the following for t -channel single-top-quark production.

Prompt charged leptons These are charged leptons that are associated to the hard interaction and originate from the decay of a Higgs, Z or W boson. They are thus distinguished from leptons produced in hadron decays. In t -channel single-top-quark production, about 15% of the prompt muons or electrons from the top quark decay stem from an intermediate prompt tau lepton as it is for example also shown in Fig. 5.6. This fraction depends on the p_T of the muon or electron which is depicted in Fig. 5.7. It reduces to about 6% when requiring events with an electron or muon in the final state that has a transverse momentum of at least 20 GeV.

Prompt neutrinos Neutrinos are also required to be prompt and are thus associated to the hard interaction while not stemming from hadron decays. In the case of leptonically decaying tau leptons, a prompt pseudo-neutrino is defined by summing the 4-momenta of both neutrinos occurring in the decay.

Top quark The partonic top quark is required to be on-shell and to stem from the hard interaction. Some generators store multiple top quark copies in the event record which reflect different levels of the event generation process. For the analyses the top quark after accounting for QCD/QED radiations and the intrinsic k_T of the initial state partons is taken since it carries the most physical momentum.

Spectator quark The spectator quark occurring in t -channel single-top-quark production is required to be produced in association with the single top quark, i.e. they share common ancestors as depicted in Fig. 5.6. Furthermore, the spectator quark has to be a light flavored quark (u, d, s, c) to distinguish it from a potential second b quark occurring in 4 FS production. At NLO, the production of additional light quarks through ISR can lead to an ambiguity here. In such cases, the quark which balances best the top quark momentum in the transverse plane is chosen.

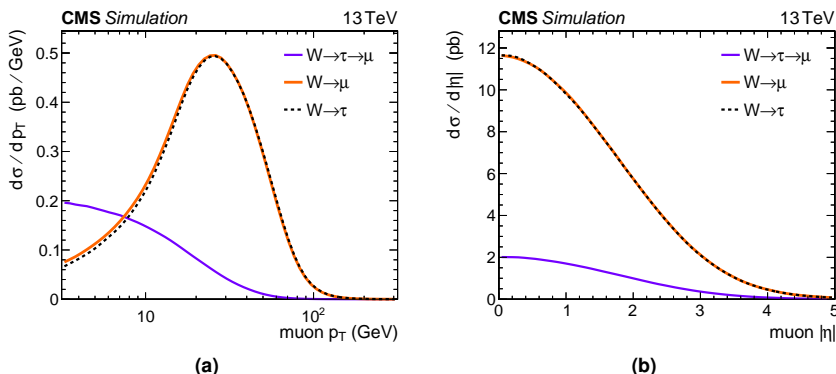


Figure 5.7. || Distributions of the (a) transverse momentum and (b) pseudorapidity of the final state lepton produced in t -channel single-top-quark production at 13 TeV. The lines represent various decays of W bosons into either muons/taus directly or via intermediate tau decays. The distributions have been generated using POWHEGv2 interfaced with MadSpin and Pythia8.

The polarization angle of the top quark can be calculated from the defined objects at parton level for t -channel single-top-quark events. A comparison of its shape for the various W boson decay chains to muons or tau leptons is presented in Fig. 5.8. The $\cos\theta_\mu^*$ shape is distorted when requiring events for which the lepton momentum is above a certain threshold. This results into a drop of the distribution at $\cos\theta_\mu^* \rightarrow 1$ which is demonstrated in Fig. 5.8b where the polarization angle is shown for events with $p_T(\mu) > 20$ GeV only.

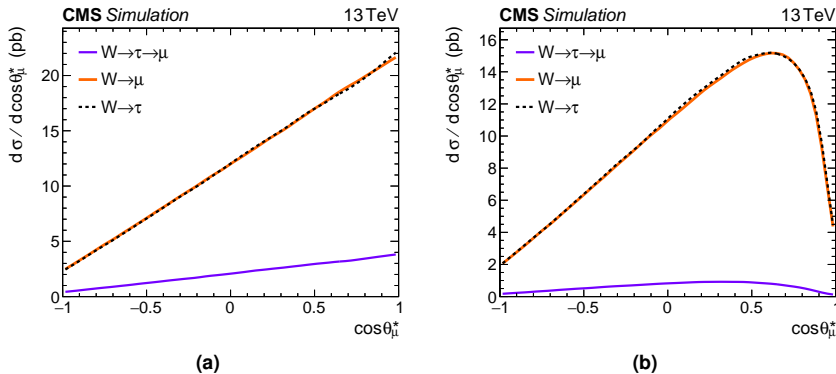


Figure 5.8. | Distributions of the polarization angle for t -channel single-top-quark production at 13 TeV: (a) inclusive distribution; (b) only events with $p_T(\mu) > 20$ GeV. The lines represent various decays of W bosons into either muons/taus directly or indirectly via intermediate tau decays. The distributions have been generated using POWHEGv2 interfaced with MadSpin and Pythia8.

Another level at which observables can be defined is the “particle level”. Here, an event selection similar to the one at reconstruction level is applied on the generated particles after hadronization. This allows to report results close to the “fiducial” phase space of the detector. The advantage is that an extrapolation into the inclusive phase space as it is intrinsically performed for parton level measurements (e.g. inclusive cross sections) is not required. A sketch of parton and particle level objects for t -channel single-top-quark production and their correspondence is depicted in Fig. 5.9. Objects at particle level are defined by using only the final particles produced by event generators and subsequent parton showers which have a mean lifetime of more than 30 ps and are therefore considered to be stable. Final state quarks and gluons appear as jets after hadronization which consist of hadrons and non-prompt leptons. Prompt charged leptons may radiate photons which are accounted for by clustering them with close-by photons. These are then referred to as “dressed” leptons. The performed clustering yields a universal treatment of QCD/QED radiations without relying on information about intermediate particles in the decay chain which can be ambiguous at parton level; especially for the definition of the spectator quark in the case of FSR as for example demonstrated in Fig. 5.9. Detailed definitions of the analysis objects at particle level used in this thesis are given in the following.

Dressed leptons Photons which do not stem from hadron decays are clustered with prompt muons or electrons if they are within $\Delta R = \sqrt{\Delta\eta^2 + \Delta\phi^2} < 0.1$. A dressed

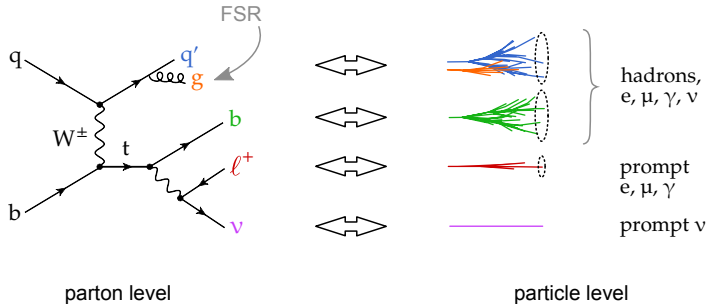


Figure 5.9. | A sketch of parton and particle level objects and their correspondence for t -channel single-top-quark production. An additional gluon has been added as an exemplary final state radiation.

lepton consists of exactly one charged lepton and any number of potentially close-by photons.

Neutrinos The 4-momenta of all prompt neutrinos are summed to define the missing transverse energy. To improve the agreement with the neutrino candidate at reconstruction level, the same algorithm as described in Sec. 5.2 is applied at particle level using a dressed lepton here to solve for the neutrino p_z component.

Jets Jet are clustered from stable particles excluding all neutrinos and the particles used to define the dressed leptons. The anti- k_T algorithm with a distance of $R=0.4$ is employed at 13 TeV copying the jet size at reconstruction level. The “ghost” b-tagging method [179] where jets are tagged by using B-hadrons with rescaled momentum will not be utilized here since its high efficiency is found to disagree with the performance of the tagging algorithm at reconstruction level. More details about these findings will be discussed in Ch. 8.

Pseudo top quark A pseudo top quark is reconstructed by combining the 4-momenta of a dressed lepton, a neutrino candidate, and a jet. Since the ghost b-tagging method is not utilized, the jet which yields a top quark mass that is closest to 172.5 GeV is chosen in the pseudo top quark reconstruction.

After applying a suitable selection on the particle level objects, the fiducial cross section can be obtained by modifying Eq. 5.12 as

$$\sigma_{\text{sig.}}^{\text{fid.}} = \frac{N_{\text{sig.}} \cdot A_{\text{fid.}}}{A_{\text{reco.}} \cdot \epsilon_{\text{reco.}} \cdot \int L} = \sigma_{\text{sig.}}^{\text{inc.}} \cdot A_{\text{fid.}}, \quad (5.14.)$$

where $A_{\text{fid.}}$ denotes the acceptance of events in the fiducial phase space. Similar to the acceptance and efficiency of the event selection at reconstruction level, it can be estimated from a sample of simulated signal events as $A_{\text{fid.}} = N_{\text{fid.}} / N_{\text{total}}$.

5.6. Unfolding

Distributions of reconstructed data events are typically distorted due to the finite resolution and acceptance and reconstruction inefficiencies of the detector with respect to their counterpart at parton or particle level. The idea of unfolding in HEP is to “revert” these effects. An unfolded distribution can then be easily compared to the

expectations from theory or to equivalent measurements. In general, a reconstructed distribution $f(y)$ of interest can be related to its true distribution $g(x)$ (i.e. at parton or particle level) as

$$\underbrace{f(y)}_{\text{reco.}} = \int \underbrace{A(y)\epsilon(y)R(y,x)}_{\text{detector}} \cdot \underbrace{g(x)}_{\text{true}} dx, \quad (5.15.)$$

by folding $g(x)$ with the detector response $R(y,x)$ and accounting for the acceptance of the event selection $A(y)$ and the reconstruction efficiency $\epsilon(y)$. Mathematically, Eq. 5.15 is called a Fredholm equation of first kind. Unfolding is then a procedure to estimate the true distribution given $f(y)$ from data while $A(y)$, $\epsilon(y)$, and $R(y,x)$ are typically taken from simulation.

Equation 5.15 can be discretized and written as a matrix equation

$$\vec{y} = \tilde{\mathcal{R}} \cdot \vec{x}, \quad \tilde{\mathcal{R}} = \mathcal{A} \cdot \mathcal{E} \cdot \mathcal{R}, \quad (5.16.)$$

where the continuous distributions are converted into vectors (histograms) and the response, acceptance, and efficiency functions are described by matrices (two-dimensional histograms). Elements of the response matrix \mathcal{R}_{ij} can be interpreted as the transition probability $p_{i \rightarrow j}$ that an event in bin i at truth level is measured in bin j by the detector for a given observable. Attempting to solve Eq. 5.16 for \vec{x} through a simple inversion of the response matrix reveals that the unfolding problem is actually ill-posed. A simple inversion can result in unstable solutions with large variances and significant anticorrelations between bins. Figure 5.10 demonstrates this for a simple model which is defined as

$$g(x) = \frac{1}{2} + A \cdot x, \quad A = 0.44 \quad (5.17a.)$$

$$R(y,x) \propto \exp\left(\frac{1}{2} \cdot \frac{(x-y)^2}{\sigma^2}\right), \quad \sigma = 0.15. \quad (5.17b.)$$

Here, a distribution g , similar to the expected distribution of the top-quark polarization angle at parton level, has been folded with a simple Gaussian smearing function R . When unfolding by inverting the response matrix, a small deviation (dash-orange line) from the folded distribution (violet markers) results into an unphysical, oscillating solution due to the introduced anticorrelations.

The origin of these oscillations can be investigated by performing a singular value decomposition (SVD) of Eq. 5.16. The SVD is a generalization of the eigendecomposition that allows to decompose even non-quadratic matrices as

$$\vec{x} = (\tilde{\mathcal{R}})^{-1} \vec{y} = (\mathcal{U} \cdot \underbrace{\mathcal{S}}_{\text{diagonal}} \cdot \mathcal{V})^{-1} \vec{y} = \mathcal{V}^{-1} \cdot \begin{pmatrix} \frac{1}{s_{11}} & 0 \\ 0 & \ddots & \frac{1}{s_{nn}} \end{pmatrix} \cdot \mathcal{U}^{-1} \vec{y}, \quad (5.18.)$$

where \mathcal{U} and \mathcal{V} contain the so-called left- and right-singular vectors, respectively. The matrix \mathcal{S} has only non-zero elements s_{ii} on its diagonal which are also referred to as singular values. Typically, they are ordered as $s_{ii} > s_{i+1,i+1}$ while the singular vectors are normalized to 1. The vectors are orthogonal to each other and can be interpreted

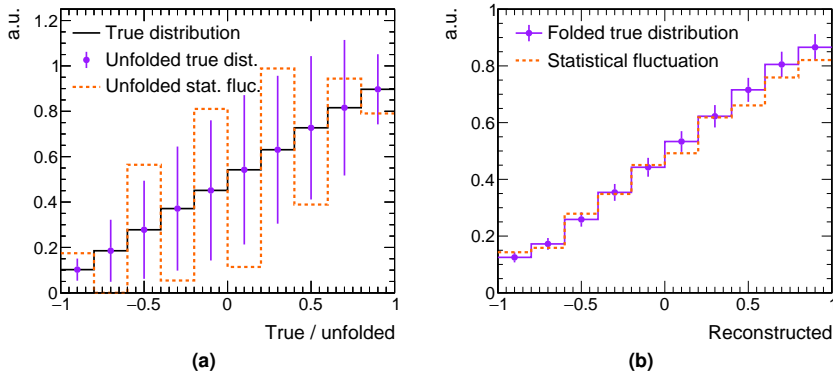


Figure 5.10. Exemplary unfolding of a distribution using a simple inversion of the response matrix: (a) true distribution with overlaid unfolding results; (b) the true distribution after folding and a sample of a corresponding statistical fluctuation.

as modes of the measured distribution. When a singular value is small, the unfolded distribution becomes unstable since the corresponding mode in the reconstructed distribution is unphysically amplified by a factor $1/s_{ii}$ through the inversion.

Various regularization procedures have been proposed to mitigate this problem. The most straightforward regularization scheme is employed in the “SVD unfolding” algorithm [180]. It modifies the response matrix as

$$\left(\mathcal{R}^{\text{reg.}}[\tau] \right)^{-1}_{ij} = \sum_k^{\tau} \mathcal{V}_{ik}^{-1} \cdot \left(\frac{1}{s_{kk}} \right) \cdot \mathcal{U}_{kj}^{-1}, \quad (5.19.)$$

where the regularization parameter τ controls a cutoff that keeps only singular values with indices $k \leq \tau < n$ during the inversion. Thus, higher order modes in the reconstructed distribution leading to oscillating solutions are ignored. A more sophisticated unfolding method can be derived from the Tikhonov regularization scheme [181]. The unfolding problem (Eq. 5.16) is rewritten as a minimization of the loss function

$$L(\vec{x}) = \|\vec{y} - \tilde{\mathcal{R}} \cdot \vec{x}\|^2 + \|\Gamma \cdot \vec{x}\|^2, \quad \Rightarrow \quad \frac{\partial L}{\partial x_i} = 0, \quad (5.20.)$$

where a suitable matrix Γ is added to suppress unphysical solutions. In this thesis unfolding is performed using the TUnfold package [182] which employs a similar regularization scheme. Its loss function is given by

$$L_{\text{TUnfold}}(\vec{x}, \lambda | \tau) = \sum_i \sum_j \left(y_i - (\tilde{\mathcal{R}} \cdot \vec{x})_i \right) \cdot \mathcal{C}_{y,ij}^{-1} \cdot \left(y_j - (\tilde{\mathcal{R}} \cdot \vec{x})_j \right) \quad (5.21a.)$$

$$+ \tau^2 \cdot \left(\Gamma \cdot (\vec{x} - \vec{x}_0) \right)^2 \quad (5.21b.)$$

$$+ \lambda \cdot \sum_i \left(y_i - \mathcal{A}_{ii} \mathcal{E}_{ii} x_i \right). \quad (5.21c.)$$

The matrix \mathcal{C} in Eq. 5.21a describes the covariances between the bins in the recon-

structed distribution. For uncorrelated data bins it is a diagonal matrix with entries $\mathcal{C}_{ii} = y_{ii}$ assuming Poisson uncertainties. The Tikhonov regularization scheme is applied through the penalty term in Eq. 5.21b. Solutions with large fluctuations are suppressed through the matrix Γ which approximates numerically the second derivatives per bin of the resulting distribution as

$$\frac{d^2g(x)}{dx^2} \approx \frac{g(x-h) - 2g(x) + g(x+h)}{h^2}, \Rightarrow \Gamma = \begin{pmatrix} 1 & -2 & 1 & 0 & 0 \\ 0 & 1 & -2 & 1 & 0 \\ \dots & \dots & \dots & \dots & \dots \\ 0 & 0 & 1 & -2 & 1 \end{pmatrix}. \quad (5.22.)$$

The regularization strength is controlled via the parameter τ and needs to be optimized as detailed below. The vector \vec{x}_0 allows to bias the calculation of the second derivatives. It is usually set to the expectation from theory. This way, the regularization vanishes when unfolding the expectation from theory for closure tests since $(\Gamma(\vec{x}_{\text{exp.}} - \vec{x}_0))^2 = 0$. Thus, the result is bias-free even for heavily curved expectations, e.g. like the p_T spectra of particles. An alternative procedure to achieve this is by reweighting \vec{y} such that $x'_i = x_i / x_i^{\text{exp.}}$ which lets the regularization vanish as well when unfolding the expectation since $\Gamma \vec{x}'_{\text{exp.}} = 0$. The last part of the loss function, Eq. 5.21c, attempts to match the overall normalization of the solution by accounting for the acceptance and reconstruction efficiencies per bin. It is minimized independently with respect to the Lagrange parameter λ .

Finding a suitable regularization strength is of crucial importance. If the applied amount of regularization is too weak, the unfolding becomes unregulated and thus leads to unphysical solutions with an oscillating behavior. On the other hand, if the regularization is too strong, the solution will be biased towards a solution with minimum curvature. In this case, the solution might tend towards the expectation from theory since it is always a solution with vanishing curvature when a bias vector or the described reweighting is applied. A method to analyze the unfolding behavior in detail is to monitor the induced bin-by-bin correlations as a function of the regularization strength. The covariance matrix of the unfolded spectrum is given by propagation of uncertainty as

$$\mathcal{C}_x[\tau] = J \cdot \mathcal{C}_y \cdot J^T = \tilde{\mathcal{R}}_{\text{reg.}}^{-1}[\tau] \cdot \mathcal{C}_y \cdot (\tilde{\mathcal{R}}_{\text{reg.}}^{-1}[\tau])^T, \quad (5.23.)$$

where J denotes the Jacobian matrix which is equal to the regularized and inverted response matrix as obtained through the minimization of Eq. 5.21. This allows to calculate the averaged correlations between the unfolded bins as

$$\bar{\rho}_j[\tau] \equiv \frac{1}{n-j-1} \sum_i^{n-j-1} \rho_{i,i+j}[\tau], \quad \rho_{i,j}[\tau] = \frac{\mathcal{C}_{x,ij}[\tau]}{\sqrt{\mathcal{C}_{x,ii}[\tau] \cdot \mathcal{C}_{x,jj}[\tau]}}. \quad (5.24.)$$

They are presented in Fig. 5.11a for the model defined in Eq. 5.17 as a function of the regularization strength. This so-called “subway plot”^(*) shows three different regions in τ to classify the various solutions. The region on the left contains solutions where

^(*) Subway plots have been developed in my Master’s thesis [183].

$\bar{\rho}_1 < 0$ which indicates large anticorrelations between directly adjacent bins. These anticorrelations lead to an oscillating behavior as demonstrated in Fig. 5.10a since the regularization too weak. On the right side the averaged correlation between adjacent bins is found to be $\bar{\rho}_1 > 0$. This however indicates that the applied regularization is too strong because the solutions are biased towards a solution with minimal curvature. In the intermediate region between both extremes, solutions with vanishing correlations can be found. However, this does not occur at the same regularization strength for all monitored correlations. Thus, one cannot choose the regularization strength in such a way that a correlation-free result is obtained. In the analyses, the regularization strength is set to the minimum of the average global correlation coefficient

$$\rho_i^{\text{global}}[\tau] = \sqrt{1 - \frac{1}{\mathcal{C}_{x,ii}[\tau] \cdot (\mathcal{C}_x^{-1}[\tau])_{ii}}} \quad (5.25.)$$

which results into a suitable trade-off with minimal correlation across the unfolded spectrum. Its value as a function of the regularization strength is indicated in Fig. 5.11a by the black solid curve. The resulting regularized spectrum is shown in Fig. 5.11b which does not exhibit the oscillating behavior as shown in Fig. 5.10a above. Furthermore, the regularization has stabilized the result against small deviations as indicated by the reduced variances.

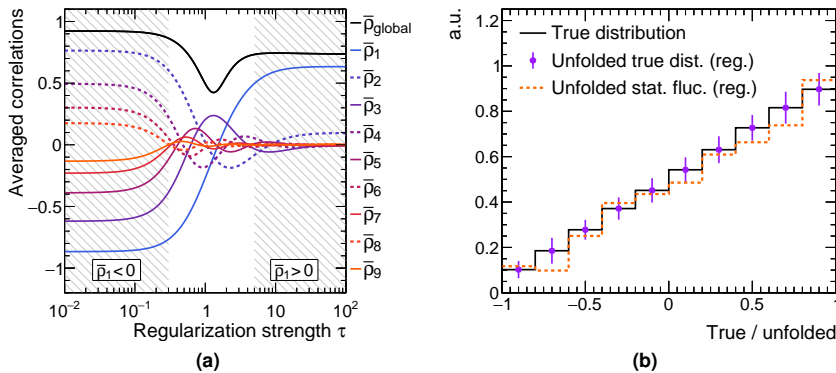


Figure 5.11. || Regularized unfolding using the TUnfold package: (a) the average bin-by-bin correlations (Eqs. 5.24 and 5.25) as a function of the regularization strength; (b) the resulting spectrum when choosing the regularization at the minimum of the averaged global correlation.

In conclusion, unfolding is an ill-posed problem which requires regularization to obtain meaningful results that are stable against statistical fluctuations. The TUnfold package regularizes the response matrix by suppressing solutions with large curvatures. However, this procedure induces bin-by-bin correlations as a function of the regularization strength. The correlations are kept small by adjusting the regularization strength to the minimum of the average global correlation coefficient.

6.

Chapter

Measurement of single-top-quark polarization in t channel at 8 TeV

A first measurement of the top quark spin asymmetry in t channel single-top-quark production, sensitive to the top quark polarization, is presented. Proton-proton collision data at a center-of-mass energy of 8 TeV have been analyzed corresponding to about 20 fb^{-1} . Events with an isolated muon are selected together with two or three jets for the final measurement. Events containing an isolated electron and jets have been studied as well as a cross check. Two boosted decision trees (BDTs) are trained for separating signal from background events further. Their discriminants are used to define a signal-enriched region from which the normalized differential cross section at parton level is inferred as a function of the angle between the lepton and the spectator quark in the top quark rest frame. From the differential cross section a spin asymmetry of $0.26 \pm 0.03 \text{ (stat)} \pm 0.10 \text{ (syst)}$ is obtained through a linear fit. The result is found to be compatible within 2.0 standard deviations with the expected SM spin asymmetry of 0.44. The result has been published in Ref. [61]. In a further step, the derivation of limits on anomalous electroweak top quark couplings arising from dimension-six effective operators is illustrated by combining the measured spin asymmetry with other measurements sensitive to the coupling structure.

6.1. Outline of analysis strategy

An overview of the strategy to measure the top quark spin asymmetry and to derive limits on anomalous couplings is given in the following. After selecting events with an isolated muon or electron and two or three jets, two BDTs are employed. The first one, labeled $\text{BDT}_{\text{multi.}}$, is trained to reject events with fake leptons stemming from multijet production. The shape of multijet events is modeled by a template obtained from data in a sideband region for which the lepton isolation is inverted. Then, a two-component ML fit to the $\text{BDT}_{\text{multi.}}$ discriminant is performed to estimate the amount of multijet contamination after the event selection. The second BDT, $\text{BDT}_{t\text{-ch.}}$, is trained to separate signal from $W+jets$ and $t\bar{t}$ events. Another ML fit to data using the distribution of its discriminant is performed to estimate the individual amounts of signal and background contributions. By applying an optimized selection on each of the two BDT discriminants, a signal-enriched phase space is obtained with a S/B ratio of about 90%. The shape of the polarization angle, $\cos\theta_\mu^*$, of data in this phase space is unfolded to parton level after subtracting the remaining background contributions. This is repeated for each source of systematic uncertainty to estimate their impact on the measurement. An overall larger impact of systematic uncertainties is observed in the electron channel compared to the muon channel rendering its standalone result much less significant. Furthermore, shortcomings in the modeling of the data-driven multijet

template have been identified in the electron channel as well. The final measurement is therefore performed in the muon channel only.

The differential cross section as a function of the polarization angle is estimated and the spin asymmetry is obtained through a linear fit to its shape. In a further step, the TopFit program [184] is used to derive limits on anomalous electroweak top quark couplings by combining the measured spin asymmetry with an inclusive cross section measurement of t -channel single-top-quark production and a measurement of the W boson helicity fractions in $t\bar{t}$ events.

6.2. Event selection and simulated samples

Proton-proton collision data at $\sqrt{s} = 8$ TeV are analyzed corresponding to 19.7 fb^{-1} recorded with the CMS experiment in 2012. Events are triggered on the presence of a single muon candidate. The employed single muon trigger requires an isolated muon candidate with $p_T > 24 \text{ GeV}$ within a pseudorapidity range of $|\eta| < 2.1$. For analysis, events have to contain one muon candidate with $p_T > 26 \text{ GeV}$ within $|\eta| < 2.1$ that passes tight identification requirements. To suppress fake leptons from multijet production, the muon candidate is required to be isolated with a relative $\Delta\beta$ -based isolation of $I_{\text{rel.}}^{\mu} < 12\%$ within a cone of $\Delta R < 0.4$. Events containing additional muons ($p_T > 10 \text{ GeV}$, $|\eta| < 2.5$, $I_{\text{rel.}}^{\mu} < 20\%$) or electrons ($p_T > 20 \text{ GeV}$, $|\eta| < 2.5$, $I_{\text{rel.}}^e < 15\%$) which pass corresponding loose identification criteria are rejected to suppress contributions from $Z/\gamma^* + \text{jets}$ and $t\bar{t}$ production with dileptonic decay.

Events containing single electrons are investigated as well but are not utilized in the final measurement. For their study a single electron trigger is employed which requires an electron candidate with $p_T > 27 \text{ GeV}$ within $|\eta| < 2.5$ that has to fulfill some additional quality criteria which yield a selection efficiency of 80% for prompt electrons. Single electron events for analysis have to contain one electron candidate with $p_T > 30 \text{ GeV}$ within $|\eta| < 2.5$ where however the ECAL barrel-endcap transition region is excluded. In addition, the electron candidate has to fulfill tight MVA-based identification criteria. Furthermore, a relative $A_{\text{eff.}}^{\rho}$ -based isolation of $I_{\text{rel.}}^e < 10\%$ in a cone of $\Delta R < 0.3$ is required. Events containing additional muons or electrons are vetoed using the same criteria as applied in the muon channel.

Jets are clustered from PF candidates with the anti- k_T algorithm using a distance parameter of $R = 0.5$ while applying the CHS technique [124] to mitigate the influence by pileup. PF candidates belonging to preselected muon or electron candidates that are loosely isolated are not clustered into jets to prevent double counting. In addition, jets that are within $\Delta R < 0.3$ to the selected tight lepton are ignored in the analysis. The reconstructed jet energy in data and simulation and the energy resolution in simulation are calibrated through dedicated JEC and JER scale factors. Events which contain two or three jets with $p_T > 40 \text{ GeV}$ within $|\eta| < 4.5$ in addition to a tight lepton that pass loose identification criteria are considered for analysis. B-tagging of jets is performed with the MVA-based CSV algorithm [128]. B-tagged jets are restricted to $|\eta| < 2.4$ since the algorithm operates only within the acceptance of the inner tracking system. In simulation an efficiency of about 50% for tagging true b jets with a mistagging rate of 0.1% for other jets (from u,d,s quarks and gluons) is found at the employed tight working point of the algorithm. In simulation the b-tagging efficiency is reweighted

through scale factors to match the one measured in data. More details about the analysis objects, identification, and corrections are described in Ch. 4.

After the selection, events are categorized into signal and control regions per muon and electron channel. The regions are labeled as “ $Nj Mt$ ” where N denotes the number of selected jets and M the subset of jets which are also b-tagged. Control regions dominated by either $W+jets$ ($2j0t$) or $t\bar{t}$ ($3j1t, 3j2t$) production are defined besides the signal region ($2j1t$) as indicated in Fig. 6.1. The analysis was developed by validating the background modeling and optimizing the strategy with data in the control regions only. During this process, distributions of data in the signal region have not been used which is commonly referred to as “blinding”. After the strategy is fixed the final measurement was conducted by unblinding the signal region while refraining from any further optimizations. Thus, the blinding procedure prevents a result-driven tuning of the analysis strategy which may otherwise bias the measurement.

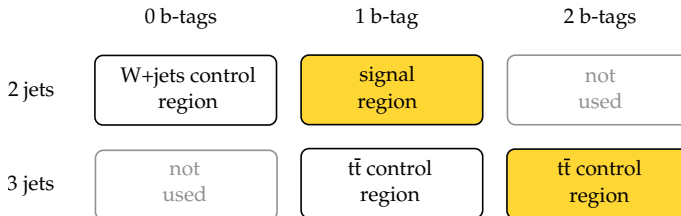


Figure 6.1. | Categorization of events depending on number of selected jets, number of b-tags, and the signal BDT discriminant. The shaded regions are employed in a template-based ML fit as described in Sec. 6.5 for estimating the signal and background yields.

Various samples of simulated events for signal and background processes are generated. The default t -channel single-top-quark sample is generated in 5 FS using the POWHEG generator interfaced with Pythia 6 for parton showering and Tauola to simulate the decay of tau leptons. For comparisons, two alternative signal samples are generated. One utilizes the aMC@NLO generator interfaced with Pythia 8 in 4 FS while the other employs the CompHEP generator interfaced with Pythia 6. A set of special samples with anomalous Wtb couplings is generated as well using the CompHEP generator to perform a cross check of the analysis with pseudo data. Samples containing single-top-quark events produced via tW and s channel are generated with POWHEG interfaced with Pythia 6 and Tauola. The major background processes, $W+jets$, Z/γ^*+jets , and $t\bar{t}$, are generated with the MadGraph generator interfaced with Pythia 6 and Tauola as well. Samples with up to three ($t\bar{t}$) or four ($W+jets, Z/\gamma^*+jets$) additional partons at ME level are merged together using the MLM procedure. For $W+jets$ production, an alternative sample generated with the Sherpa generator [185] is employed for validation purposes. In this thesis, $W+jets$ events are categorized based on their jet flavor content. Events with at least one heavy-quark-flavored jet from the hadronization of either c , or b quarks are abbreviated as “ $W+HF$ ” while events with only light-quark-flavored jets (g,u,d,s) are labeled “ $W+LF$ ” instead. Diboson production (WW, WZ, ZZ) is simulated with Pythia 6 and found to be only a minor background. The theoretical SM cross sections used to normalize these samples are listed in Tab. 6.1. Throughout this chapter signal and background templates are presented after they have been scaled to the result of a

binned ML fit to data (Sec. 6.5) while additional corrections to the simulated W+jets and tt> events (Sec. 6.4) have been applied as well to improve their modeling unless it is explicitly stated otherwise.

Table 6.1. || Theoretical cross sections at 8 TeV used to normalize the simulated samples.

Process	Cross section	Accuracy
t channel	$87.2^{+2.6}_{-1.8}$ pb	approx. NNLO [186]
s channel	5.55 ± 0.22 pb	approx. NNLO [186]
tW channel	22.2 ± 1.5 pb	approx. NNLO [186]
$t\bar{t}$	253^{+15}_{-16} pb	NNLO (using Top++ 2.0 [52])
$W \rightarrow \ell\nu + \text{jets}$	12234^{+422}_{-416} pb	NNLO (using FEWZ [187])
$Z/\gamma^* \rightarrow \ell^+\ell^-$, $m_{\ell\ell} > 50$ GeV	1177 ± 39 pb	NNLO (using FEWZ [187])
$W^+ W^-$	54.8 ± 3.0 pb	NLO (using MCFM 5.8 [188])
$W^\pm Z/\gamma^*$, $m_{\ell\ell} > 12$ GeV	33.2 ± 2.7 pb	NLO (using MCFM 5.8 [188])
$Z/\gamma^* Z/\gamma^*$, $m_{\ell\ell} > 40$ GeV	8.1 ± 0.4 pb	NLO (using MCFM 5.8 [188])

Contributions from fake leptons produced in multijet events that survive the event selection are not simulated but estimated from data through the following procedure. The shape of multijet events per channel is extracted from a sideband region for which the isolation of the lepton is inverted in the event selection as $I_{\text{rel}}^{\mu} > 20\%$ and $I_{\text{rel}}^e > 15\%$ for the muon and electron candidate respectively. The resulting distribution of data after subtracting the remaining contamination by other processes serves as a template to model the shape of multijet production. The amount of multijet events in signal and control regions is estimated by fitting the extracted template to data which is described later in Sec. 6.5. For illustration the distribution of the transverse W boson mass in the 2j1t sideband region of the muon channel is shown in Fig. 6.2a. The contribution of other processes in the sideband regions amounts to a contamination of only 9% (2%) in muon (electron) channel respectively. The resulting multijet template after its yield has been estimated from data in the 2j1t region of the muon channel is presented in Fig. 6.2b. A good description of the unknown multijet shape in the 2j1t region is obtained with the employed data-driven procedure.

Distributions of the reconstructed top quark mass in muon and electron channel are presented in Fig. 6.3 after the event selection and the estimation of multijet events have been performed. In control regions containing no or more than one b-tagged jet, the jet with the highest value of the CSV discriminant is associated to the top quark decay to calculate the top quark mass. The presented distributions demonstrate that data is well described by the simulated event samples and the data-driven multijet templates in control and signal regions of both channels.

6.3. Training of Boosted Decision Trees

Two BDTs are trained in this analysis whose output is utilized two-fold, i.e. for estimating the amount of signal and background events in data and to obtain a signal-enriched phase space for unfolding. The first BDT, labeled BDT_{multi.}, is trained to

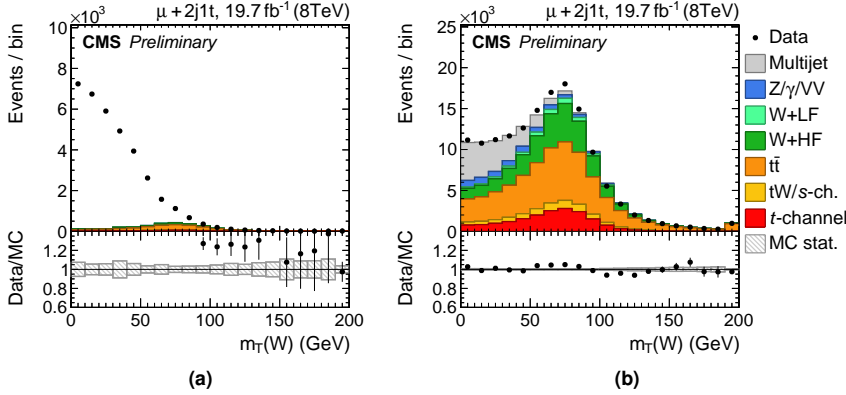


Figure 6.2. | Distributions of the transverse W boson mass in muon channel: (a) antiisolated sideband region for extracting the multijet template; (b) resulting distribution in the 2j1t region after scaling the extracted template to the result of a ML fit to data.

reject background events stemming from multijet production. In its training simulated t -channel single-top-quark events are set as signal whereas data events in the sideband region, from which the multijet template is extracted, are set as background. The GradientBoost procedure is chosen with a relatively low shrinkage of 10%. The number of single decision trees is restricted to 50 while each tree is kept shallow with a maximum depth of two. The minimum node size is set to 250 events and the number of scanned working points per node is restricted to 200. These settings are not optimized to yield the best discrimination power but instead are motivated to protect well against overtraining. Overtraining is a particular concern here since the used data events in the training may not reflect the actual distribution of multijet events in the signal region in great detail. Multiple BDT candidates are trained to assess which set of input observables yields the best rejection of multijet events with the final discriminant. In addition, input observables which are found to be correlated with the polarization angle or with other input observables are excluded from the training. This optimization results in the following list of input observables:

- the reconstructed invariant mass of the top quark candidate;
- the transverse mass of the W boson candidate, $m_T(W)$, before solving for the unknown neutrino p_z component since this modifies \vec{p}_T in the case of complex solutions;
- the missing transverse energy, E_T ;
- the transverse momentum of the untagged spectator jet (j');
- the event isotropy which is defined as $(s_{\max} - s_{\min})/s_{\max}$ with $s = \sum_i^{\ell, \text{jets}} |\vec{n} \cdot \vec{p}_i|$ where the unit vector $\vec{n} = (\cos\phi, \sin\phi, 0)$ is chosen in the transverse plane such that it either maximizes or minimizes s .

The BDT is trained on events in the 2j1t region only while the resulting discriminator is evaluated in control regions as well. Distributions of $m_T(W)$, the spectator jet p_T , and the event isotropy are presented in Fig. 6.4. Other input observables are shown in Figs. 6.2 and 6.3 above. Distributions of the resulting BDT discriminants in electron

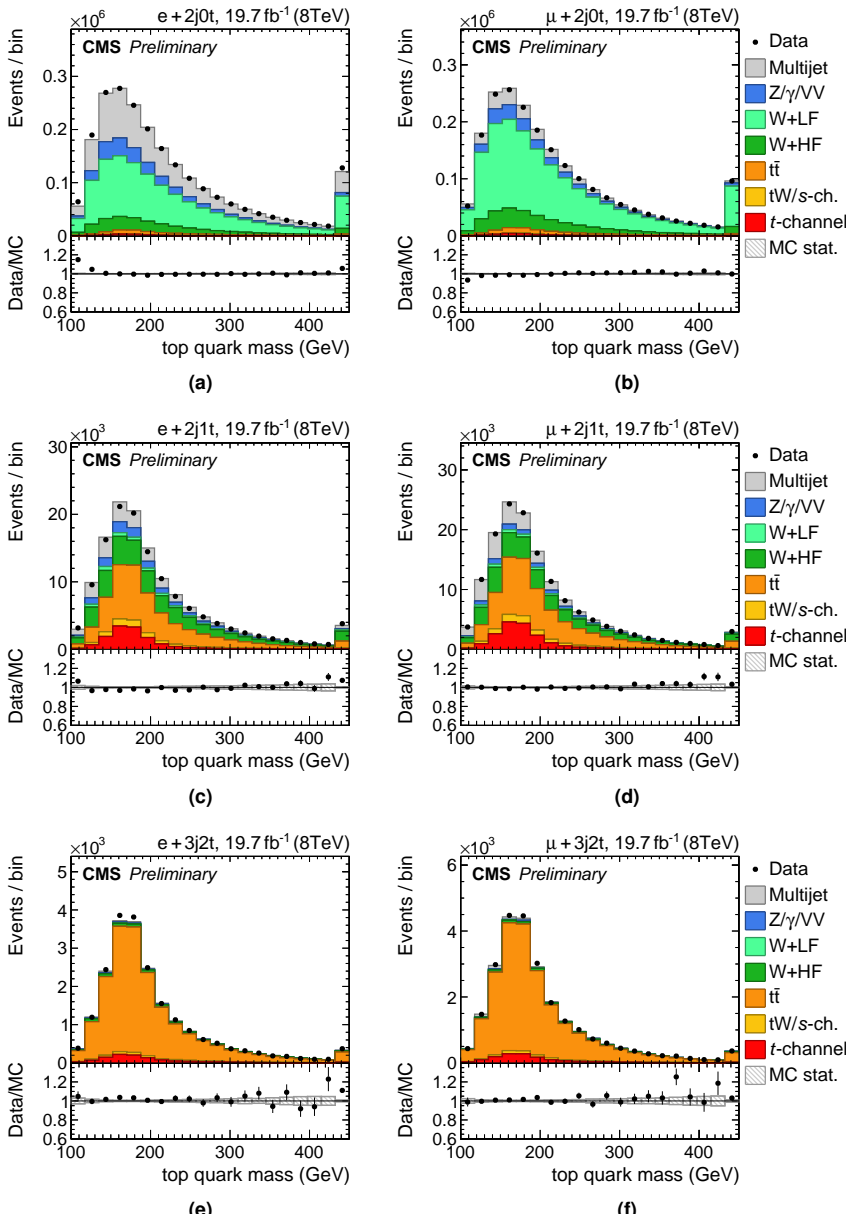


Figure 6.3. | Distributions of the reconstructed top quark mass in (left column) electron and (right column) muon channel. Top row: 2j0t $W+jets$ control region; middle row: 2j1t region; bottom row: 3j1t $t\bar{t}$ control region. The top quark p_T reweighting (Sec. 6.4) is exceptionally not applied here.

and muon channel are shown Figs. 6.6a and 6.6b respectively. A fair agreement is observed between data and simulation in the distributions of the input observables and for the resulting discriminant.

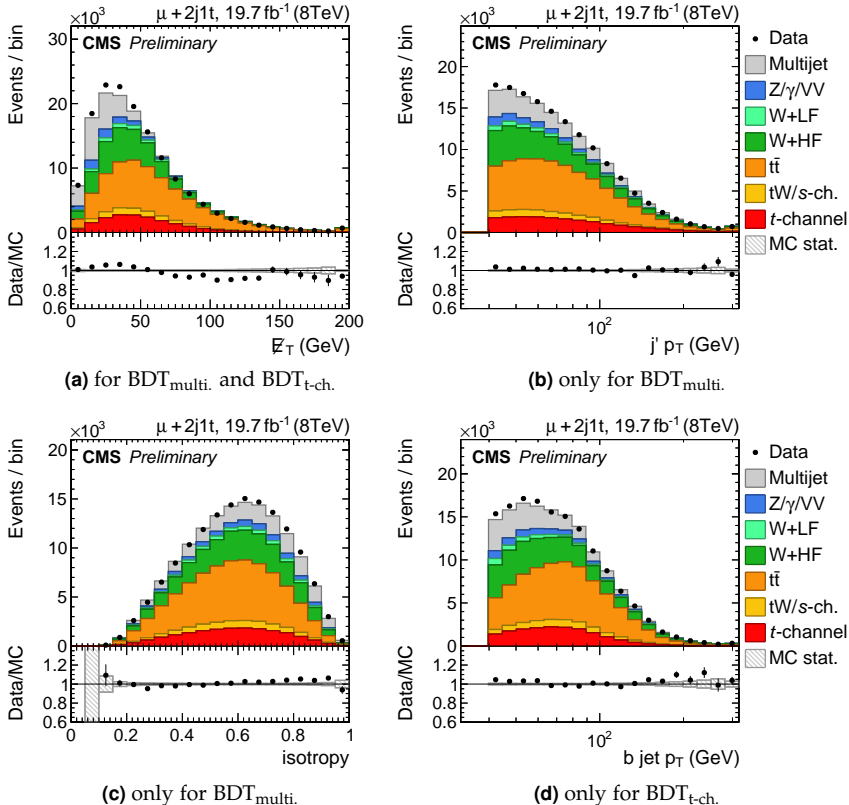


Figure 6.4. | Distributions of some input observables of the $\text{BDT}_{\text{multi.}}$ and $\text{BDT}_{\text{t-ch.}}$ discriminants as indicated in 2j1t muon channel: (a) missing transverse energy; (b) transverse momentum of untagged spectator jet; (c) event isotropy; (d) transverse momentum of b tagged jet.

In a preliminary version of this analysis events with $m_T(W) > 50 \text{ GeV}$ or $\cancel{E}_T > 45 \text{ GeV}$ are selected in muon and electron channel respectively to reject multijet events [189]. To allow a fair comparison the working points of the $\text{BDT}_{\text{multi.}}$ discriminant have been chosen such that a similar signal selection efficiency is obtained per channel. The performance of the working points and a comparison with the preliminary analysis are presented in Tab. 6.2. The $\text{BDT}_{\text{multi.}}$ discriminant allows to reject about twice as many multijet events with respect to $m_T(W)$, \cancel{E}_T for the chosen working points while retaining approximately the same amount of signal events.

The second BDT, $\text{BDT}_{\text{t-ch.}}$, is trained to separate signal events from $W+\text{jets}$ and $t\bar{t}$ production which are the major background processes after applying the multijet rejection selection. It is configured as follows. The GradientBoost method is employed

Table 6.2. Selection efficiencies of multijet and signal events using $\text{BDT}_{\text{multi.}}$, $m_{\text{T}}(\text{W})$, and \cancel{E}_{T} working points. The latter two observables and corresponding working points have been utilized in a preliminary version of the analysis to reject multijet events [189].

Process	Muon channel		Electron channel	
	$m_{\text{T}}(\text{W}) > 50 \text{ GeV}$	$\text{BDT}_{\text{multi.}} > -0.15$	$\cancel{E}_{\text{T}} > 45 \text{ GeV}$	$\text{BDT}_{\text{multi.}} > 0.15$
Multijet	15%	7.7%	7.6%	4.4%
Signal	70%	71%	51%	52%

with a shrinkage of 40%. In total, 200 shallow single decision trees with a maximum depth of two are trained. The minimum node size is set to 100 events and the number of scanned working points per node is set to 50. To mitigate a potential lack in the training statistics of the background samples, additional simulated $\text{W}+\text{jets}$ and $\text{t}\bar{\text{t}}$ events from the 2j0t and 3j2t control regions are added to the training, respectively. In particular, this increases the statistics of simulated events with $\text{W}+\text{light-quark-flavored jets}$ which is relatively low in the 2j1t region but may be larger in data due to mistagging.

The following ten observables have been chosen as input:

- the reconstructed invariant mass of the top quark candidate;
- the missing transverse energy, \cancel{E}_{T} ;
- the transverse mass of the W boson candidate before solving for the unknown neutrino p_z component, $m_{\text{T}}(\text{W})$;
- the transverse momentum of the lepton;
- the transverse momentum of the b-tagged jet;
- the invariant mass of the b-tagged jet from the summed momenta of the clustered PF candidates;
- the absolute pseudorapidity of the untagged spectator jet (j');
- the absolute pseudorapidity of the b-tagged jet;
- the invariant mass of the top quark and spectator jet system, $\sqrt{\hat{s}} = |\vec{p}_{\text{top}} + \vec{p}_{j'}|$;
- the transverse momentum of the hadronic final-state system (HFS), $(\vec{p}_{j'} + \vec{p}_{\text{b}})_{\text{T}}$.

These observables have been chosen for the training because they exhibit only a low correlation with the polarization angle. A bias may otherwise occur since the BDT is trained with a sample of simulated signal events in which a SM coupling structure is assumed. In the worst case, a BDT may select events in such a way that it artificially reproduces the SM shape of the polarization angle in data. Choosing uncorrelated observables makes the BDT training blind to the actual distribution of the polarization angle instead. The distributions of some input observables are shown in Fig. 6.5 after selecting events with $\text{BDT}_{\text{multi.}} > -0.15$ in 2j1t muon channel. The other input observables are presented in Figs. 6.2, 6.3, and 6.4 above. The distributions of the resulting discriminant are shown in Figs. 6.6c and 6.6d in the electron and muon channel respectively. Overall, a good description of data by the simulated samples is observed. The trained $\text{BDT}_{\text{t-ch.}}$ discriminant yields an AUC of 29% for separating signal from $\text{W}+\text{jets}$ and $\text{t}\bar{\text{t}}$ events in both channels.

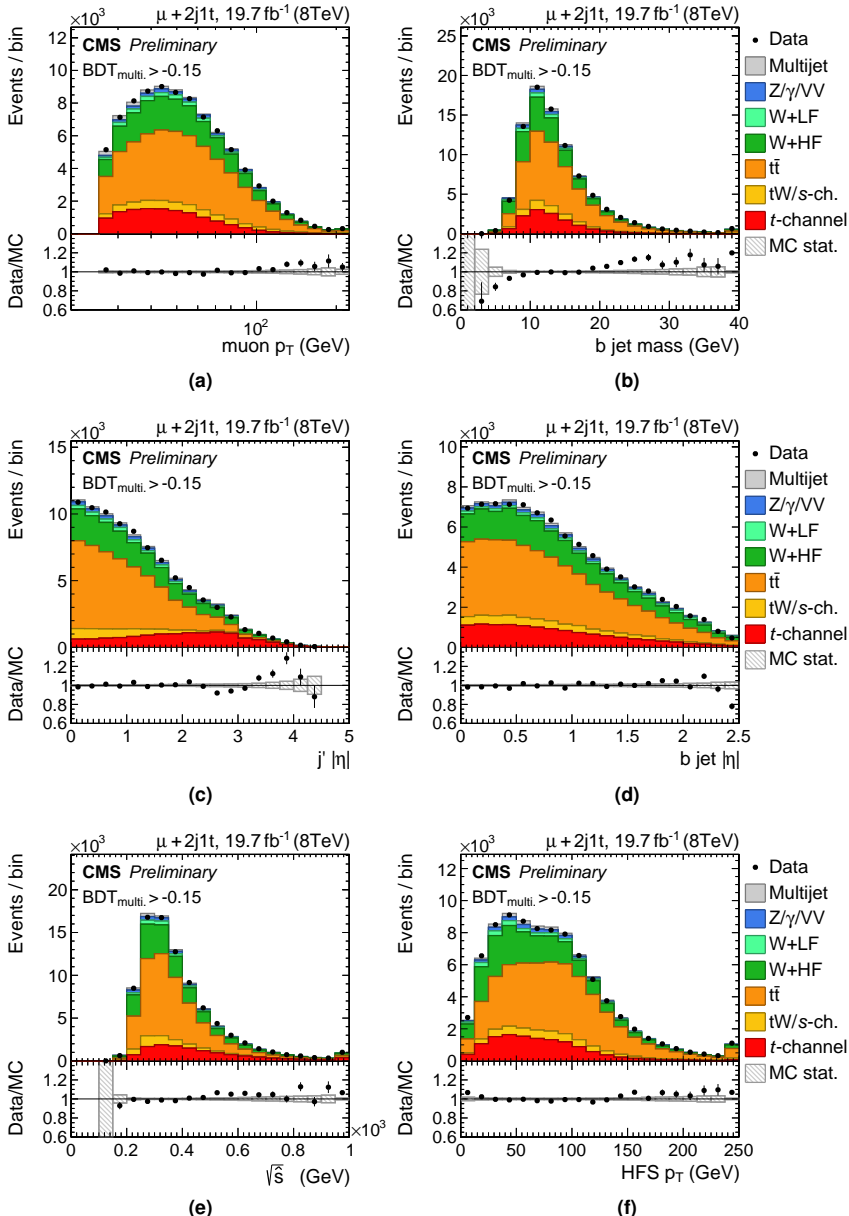


Figure 6.5. Distributions of some input observables to the $BDT_{t\text{-ch.}}$ discriminant in $2j1t$ muon channel: (a) transverse momentum of the muon; (b) invariant mass of the b-tagged jet; (c,d) absolute value of the untagged and b-tagged jet pseudorapidities; (e) invariant mass of the top quark and spectator jet system; (f) p_T of the hadronic final state system.

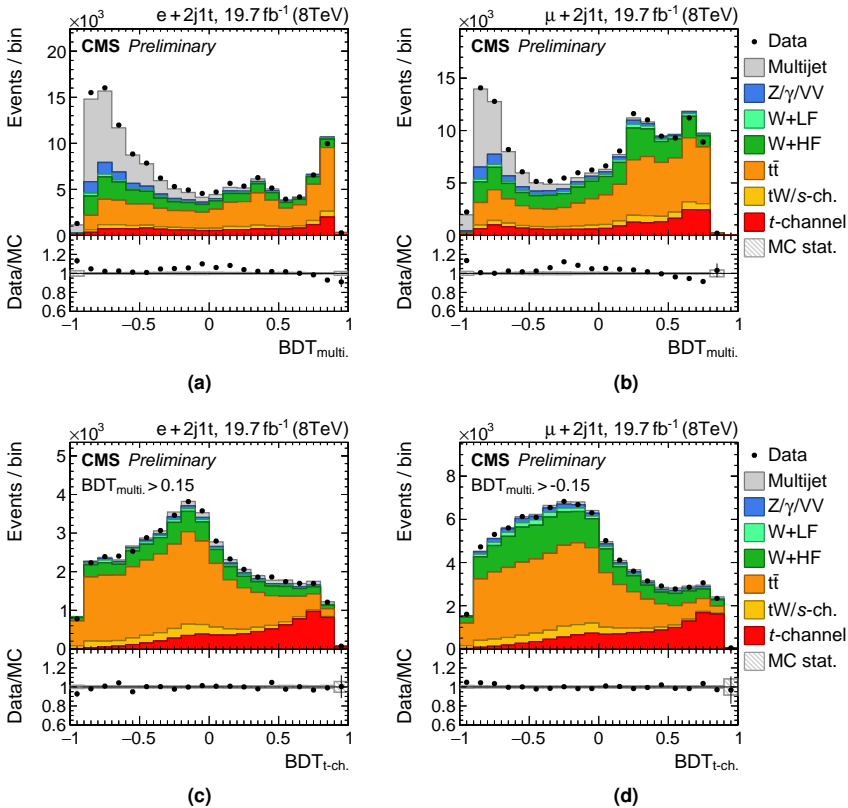


Figure 6.6. | Distributions of the BDT discriminants in 2j1t (left column) electron and (right column) muon channel.

6.4. Background modeling

The modeling of the $W+jets$ and $t\bar{t}$ backgrounds is studied in control regions before performing the measurement. In the 2j0t control region, two mismodeled observables are found which can be attributed to the $W+jets$ background, after applying the $BDT_{multi.}$ selection to reject the multijet background.

The first mismodeled observable is the transverse momentum of the W boson, shown in Fig. 6.7a, which exhibits a softer spectrum in data compared to simulation. This effect can be explained as an insufficient modeling of the hadronic recoil in such events. The recoil momentum is typically defined for Z/γ^*+jets and $W+jets$ events as the net momentum which balances the momentum of the vector boson in the transverse plane. Primarily, it encapsulates the hard jet momenta but additional soft components can contribute to the recoil momentum as well. Such soft contributions can stem from the underlying event, from photons from bremsstrahlung, or from pileup which may not be accurately modeled in simulated samples. Thus, sophisticated methods for correcting the recoil momentum can be found in literature, e.g. Ref. [190]. However, since $W+jets$ events are only a background in this analysis, a simple reweighting in

bins of the W boson p_T is applied instead to for correcting the observed deviation. The derived scale factors in the 2j0t control region are applied in the 2j1t and 3j2t regions. In the statistical evaluation, the shape difference between applying and not applying this reweighting is considered a systematic uncertainty.

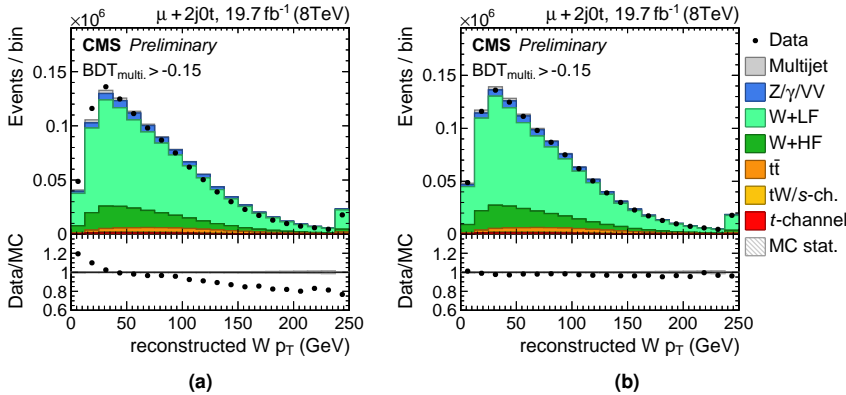


Figure 6.7. | Distributions of the reconstructed W boson p_T in 2j0t control region: (a) before and (b) after applying the W+jets corrections.

Another mismodeling of the W+jets background in 2j0t is observed for the polarization angle itself whose distribution is presented in Fig. 6.8a. This is a peculiar mismodeling since the value of $\cos\theta_\mu^*$ does not reflect any physically meaningful observable for W+jets events. A similar deviation has been observed in measurements at 7 TeV as well (e.g. Ref. [183]) which suggests that the deviation might be attributed to the modeling of W+jets events by the employed MadGraph generator. Therefore, an alternative W+jets sample simulated with the Sherpa generator is used to cross check its modeling. The sample was however simulated with only massless quarks. Hence, the ratio of light, charm, and bottom-quark flavored jets is predicted wrongly. This is corrected by reweighting the flavor ratios to the ones predicted by the default MadGraph sample. The distributions before and after reweighting the flavor fractions are presented in Fig. 6.9. An improved modeling of $\cos\theta_\mu^*$ with the reweighted Sherpa sample is obtained that displays however a slightly opposite trend between data and prediction compared to Fig. 6.8. For the measurement, the predicted shape of $\cos\theta_\mu^*$ in simulated W+jets events by MadGraph is reweighted using MadGraph-to-Sherpa scale factors per jet flavor pair combination that are derived in the 2j0t control region and applied in the 2j1t and 3j2t regions. The resulting distribution in 2j0t is shown in Fig. 6.8b where a fair description of data is achieved. Two additional systematic uncertainties are considered in the measurement which account for the difference between the two $\cos\theta_\mu^*$ shapes and for the jet flavor composition of the W+jets sample.

After applying the described W+jets corrections an improved modeling can also be observed in the distributions of other observables. For example, the distribution of E_T benefits from these corrections which is demonstrated in Fig. 6.10 where it is shown before and after the reweighting in the 2j0t region of the muon channel.

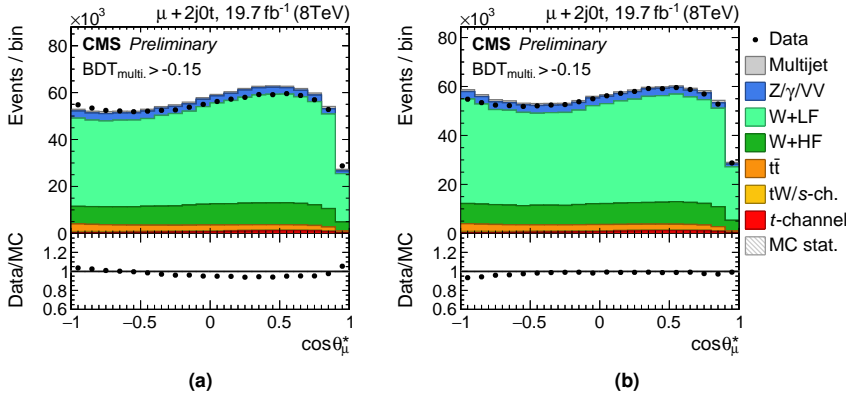


Figure 6.8. | Distributions of the polarization angle in 2j0t control region: (a) before and (b) after applying the W+jets corrections.

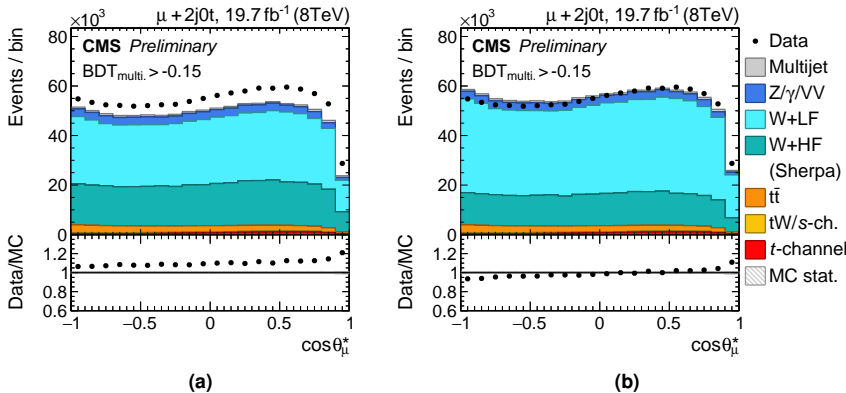


Figure 6.9. | Distributions of the polarization angle in 2j0t control region using an alternative W+jets sample simulated with Sherpa: (a) before and (b) after reweighting the jet flavor fractions to the predictions by MadGraph.

In measurements at 13 TeV (Ch. 7) an improved modeling of the W+jets background is achieved by simulating it at NLO instead using the MadGraph5_aMC@NLO generator. In retrospect, the insufficient modeling at 8 TeV may therefore be attributed to the LO accuracy of the utilized MadGraph W+jets sample.

Another deviation is observed in the t \bar{t} control region. Here, the reconstructed top quark p_T displays a softer spectrum in data than it is predicted by simulation as presented in Fig 6.11a. Similar deviations are also observed in dedicated t \bar{t} cross section measurements [191,192]. To mitigate this, an ad-hoc reweighting of t \bar{t} events is performed where the weight

$$w = \sqrt{\text{SF}(p_T(t)) \cdot \text{SF}(p_T(\bar{t}))} \quad (6.1.)$$

depends on the transverse top quark and antiquark momenta at parton level. The scale

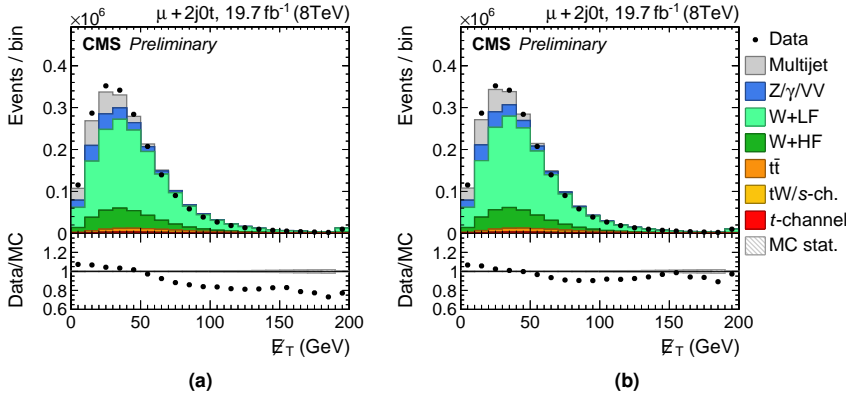


Figure 6.10. Distribution of \not{E}_T in mon channel 2j0t control region for (a) before and (b) after applying the $W + \text{jets}$ corrections.

factor $SF(p_T)$ has been estimated by fitting an exponential function to the measured differential $t\bar{t}$ cross sections. Figure 6.11b demonstrates that an improved description of data is achieved after this reweighting is applied. However, other distributions become distorted by its application. In particular, the recipe leads to a slight slope in the ratio between data and the prediction for the reconstructed top quark mass distribution which is why it has not been applied for the distributions presented in Fig. 6.3 above. Since the reweighting mitigates the observed deviation for the top quark p_T spectrum but introduces new ones, it is treated as an additional systematic uncertainty in the measurement. The influence of the reweighting on the shape of the polarization angle is found to be small as shown in Figs. 6.11c and 6.11d.

An explanation of the deviation between the observed top quark p_T spectrum in data and the predictions by event generators was found through new differential NNLO calculations of $t\bar{t}$ production [193]. It is demonstrated that by including higher order corrections the predicted p_T spectrum becomes softer as well and thus yields an improved description of the measured differential $t\bar{t}$ cross sections.

6.5. Background estimation

A precise determination of the amount of background contributions in the signal region is a crucial ingredient for measuring differential cross sections since those need to be subtracted from data prior to unfolding. In this analysis, the background contributions are estimated through two consecutive template-based ML fits to the trained BDT discriminants.

The first fit uses the distribution of the BDT_{multi} discriminant where only the contamination of multijet events in signal and control regions are estimated through a two-component fit. As described in Sec. 6.2, the shape of multijet events is modeled by a template obtained from data in a sideband region with inverted lepton isolation. To assess the stability of the estimated amount of multijet events, the fit is repeated while extracting the template from different isolation regions. In the fit the multijet template is taken to be unconstrained. The other signal and background templates are

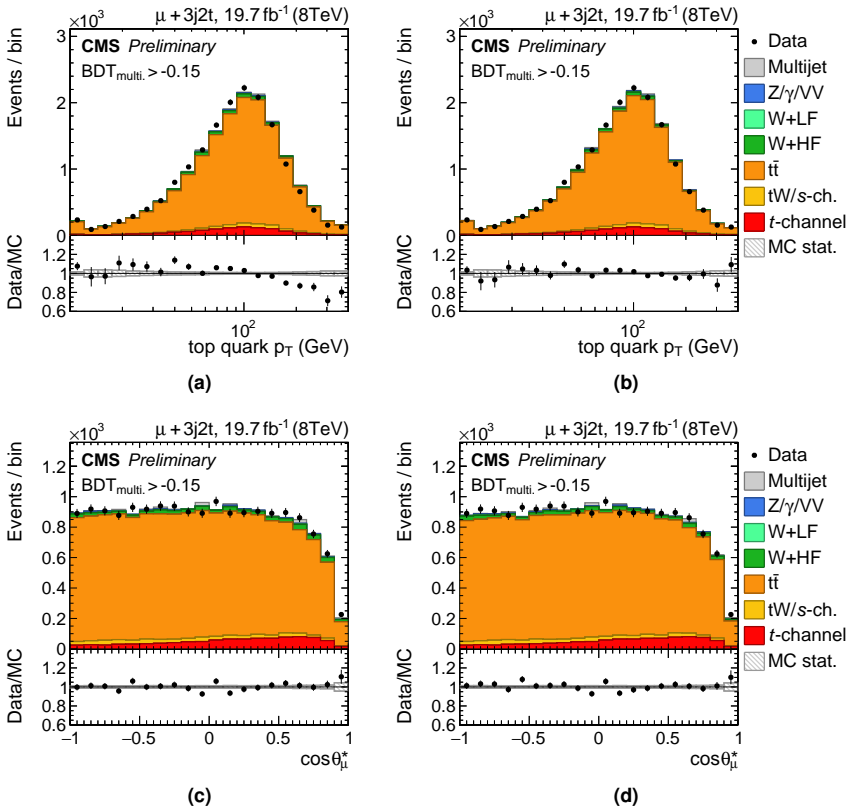


Figure 6.11. || Distributions of (top row) the transverse momentum of the reconstructed top quark and (bottom row) the polarization angle in muon channel 3j2t control region (left column) before and (right column) after applying the top quark p_T reweighting.

summed and fitted as a second component with a log-normal constraint of $\pm 20\%$ on their total yield. The fits are performed per channel using data in the regions below the individual working points of the $BDT_{multi.}$ discriminant for multijet rejection. The resulting event yields in muon and electron channel, extrapolated into the regions above the working points, are listed in Tabs. 6.3 and 6.4 for the 2j1t region respectively. Similar fits for estimating the contamination by multijet events are performed in the W+jets and t \bar{t} control regions as well.

The stability of the estimated amount of multijet events after extrapolating it into the signal region has also been studied when varying the jet energy corrections and jet energy resolution within uncertainties. To account for the induced residual differences in the estimated yield, a conservative systematic uncertainty of 50% is assumed on the multijet yield. An additional systematic uncertainty is considered to account for shape differences in the data-driven multijet template when the lepton isolation in the sideband region is varied.

The individual yields of the signal and background processes which are treated as a

Table 6.3. || Multijet event yields for $\text{BDT}_{\text{multi.}} > -0.15$ in 2j1t muon channel.

Sideband	Event yields	
	Multijet	Others
$0.2 < I_{\text{rel.}}^{\mu} < 0.5$	1607 ± 31	90028 ± 811
$0.2 < I_{\text{rel.}}^{\mu} < 0.3$	1761 ± 40	91374 ± 985
$0.3 < I_{\text{rel.}}^{\mu} < 0.5$	1765 ± 41	88854 ± 1007

Table 6.4. || Multijet event yields for $\text{BDT}_{\text{multi.}} > 0.15$ in 2j1t electron channel.

Sideband	Event yields	
	Multijet	Others
$0.15 < I_{\text{rel.}}^e < 0.5$	1467 ± 27	45620 ± 470
$0.15 < I_{\text{rel.}}^e < 0.25$	1506 ± 28	46283 ± 464
$0.25 < I_{\text{rel.}}^e < 0.5$	1512 ± 36	44916 ± 598

single component in the first fit are estimated in a second ML fit to the distribution of the $\text{BDT}_{\text{t-ch.}}$ discriminant. In this fit, similar background processes are grouped together and the following constraints are applied:

Signal The t -channel single-top-quark template is taken as unconstrained.

Top quark background The background processes which contain genuine top quarks ($t\bar{t}$, tW , s channel) are grouped together. Their summed yield is constrained to the SM prediction though a log-normal prior with an uncertainty of $\pm 20\%$.

Electroweak background The electroweak processes ($W+\text{jets}$, $Z/\gamma^*+\text{jets}$, diboson) are summed together. A log-normal constraint with an uncertainty of $\pm 50\%$ on their SM prediction is applied. The relatively larger uncertainty compared to the top quark background is chosen here because the production rates of $W+\text{heavy-quark-flavored jets}$ are predicted less precisely in the analysis phase space by the employed $W+\text{jets}$ LO MadGraph sample.

Multijet The multijet background yield is kept fixed to the result of the previous fit and varied only as a systematic uncertainty.

To account for the relative fractions of the individual subprocesses within the components, additional systematic uncertainties are considered in the measurement.

In test fits to pseudo-data using the $\text{BDT}_{\text{t-ch.}}$ distribution in the 2j1t region only, a large anticorrelation of about -90% between the estimated yields of the top quark and electroweak backgrounds has been obtained. This is due to the fact that their $\text{BDT}_{\text{t-ch.}}$ shapes are fairly similar compared to the other fit-components as presented in Fig. 6.12. To reduce the large anticorrelation the $\text{BDT}_{\text{t-ch.}}$ distribution is simultaneously fitted in the 3j2t control region as well for the measurement. By including this region the likelihood is supplied with independent information on the $t\bar{t}$ production rate which reduces the anticorrelation to about -75% . It has also been studied if it is beneficial to add the 2j0t control region as well to the fit for constraining the $W+\text{jets}$ yield further. However, including the 2j0t region does not provide significant information on the

$W + \text{heavy-quark-flavored jet}$ production rate, which is the dominant $W + \text{jets}$ fraction in the 2j1t signal region, since this control region is mostly enriched by $W + \text{light-quark-flavored jets}$ instead (see e.g. Fig. 6.3 for comparison). The ML fit is therefore performed simultaneously in the 2j1t and 3j2t region only without including the 2j0t region.

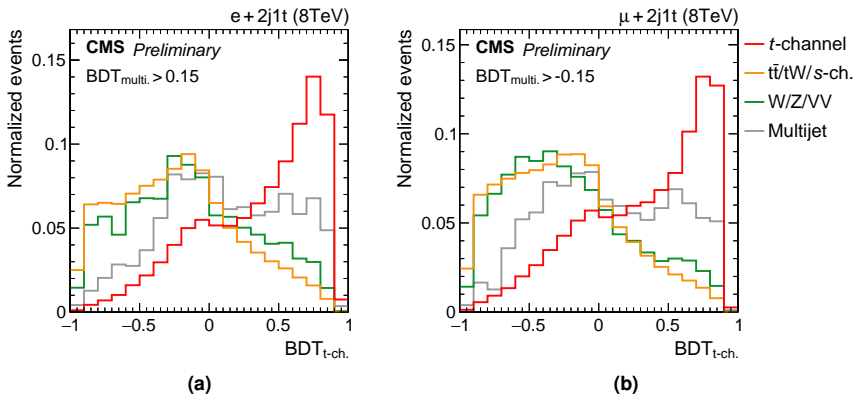


Figure 6.12. | Shape comparison of the components considered in the fit to the $BDT_{t\text{-ch.}}$ discriminant in 2j1t for (a) electron and (b) muon channel.

The obtained fit results per channel are listed in Tab. 6.5. After the event selection, a S/B of about 13% (11%) is obtained in the muon (electron) channel which increases to 90% (88%) in a signal-enriched region, defined by applying an additional selection on both BDT discriminants as detailed in Sec. 6.7 below.

6.6. Validation

The final distributions are validated after applying the additional corrections to the $W + \text{jets}$ and $t\bar{t}$ events (Sec. 6.4) and scaling the signal and background templates to the result of the ML fits (Sec. 6.5) before unblinding the analysis. This revealed an insufficient modeling of multijet events through the data-driven template in the electron channel. The actual problem is multilayered and outlined in the following. A stability test of the data-driven multijet shape has been conducted where separate fits to the $BDT_{\text{multi.}}$ discriminant in bins of the $BDT_{t\text{-ch.}}$ discriminant are performed. The resulting scale factors in muon and electron channel are compared in Fig. 6.13. The estimated scale factors in the muon channel appear to be stable, i.e. without a visible trend, and in agreement with the inclusive fit result within uncertainties. However, in the electron channel the estimated scale factors display an instability. The result shows that the extracted multijet template is scaled differently depending on the interval of the $BDT_{t\text{-ch.}}$ discriminant in which the template is extracted and the fit is carried out.

Further investigations of the modeling of multijet events in the electron channel revealed that the distribution of the difference between the ϕ angles of the lepton and the missing transverse momentum is mismodeled. Figure 6.14 shows the corresponding distributions in electron and muon channel. The $\Delta\phi$ distribution in the muon channel is instead well modeled by the multijet template.

Table 6.5. Estimated event yields in 2j1t after the event selection and in a signal-enriched phase space defined by $\text{BDT}_{\text{multi.}} > -0.15$ in the muon channel, $\text{BDT}_{\text{multi.}} > 0.15$ in the electron channel, and additionally $\text{BDT}_{\text{t-ch.}} > 0.45$ in both channels. The uncertainties reflect the limited MC statistics and the ML fit uncertainties.

Process	Muon channel		Electron channel	
	Selection	Signal-enriched	Selection	Signal-enriched
t̄t	58539±629	3118±34	48208±518	2182±26
tW	6518±76	311±12	5370±64	215±6
s channel	1059±20	72±4	808±17	44±3
W+heavy flavor	30472±1520	2101±113	20707±1034	836±48
W+light flavor	3824±202	252±21	2720±145	94±11
Z/γ*+jets	10284±561	371±32	10696±572	175±27
Diboson	1108±56	33±2	792±40	16±1
Multijet	21416±10707	427±214	33961±16979	423±212
Signal	17796±604	6049±136	13313±452	3502±119
Total expected	151015±3126	12733±271	136576±2826	7488±173
Data	147749±384	12504±112	134472±367	7322±86

From these findings it is concluded that in the electron channel the multijet template extracted from the sideband region provides an insufficient modeling of multijet events. The measurement of the top quark spin asymmetry is therefore continued only with the muon channel. This decision is further motivated by the outcome of a blind measurement using pseudo-data which showed that a combination of both channels will only result in an improvement of less than 5% in precision compared to the result from the muon channel alone since the measurements are mainly limited by systematic uncertainties.

Since the muon channel is validated successfully the analysis is unblinded. In Fig. 6.15a the distribution of the polarization angle is shown in a signal-enriched region. A slight slope is observed between the expected distribution and data. The background modeling is shown in a signal-depleted region in Fig. 6.15b as well, where the distribution of data is well modeled by the simulation.

6.7. Signal-enriched region

After subtracting the remaining background contributions from data in Fig. 6.15a the reconstructed $\cos\theta_\mu^*$ shape is unfolded to parton level and the spin asymmetry is extracted from the differential cross section. The working point of the $\text{BDT}_{\text{t-ch.}}$ discriminant which defines the signal-enriched region can be optimized such that the measured spin asymmetry has a minimum of uncertainty. A scan of the expected uncertainty using pseudo-data as a function of the $\text{BDT}_{\text{t-ch.}}$ working point is shown in Fig. 6.16. Only some representative systematic uncertainties are evaluated which have a major impact on the result. If the working point is chosen too low larger amounts of background contributions have to be subtracted from data leading to an increased systematic uncertainty originating from the background processes. On the

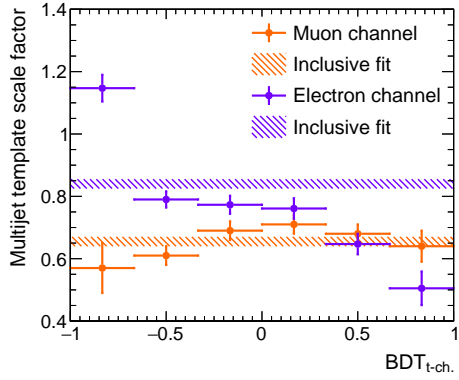


Figure 6.13. | Resulting scale factors for the multijet template by fitting the $\text{BDT}_{\text{multi}}$ discriminant inclusively and separately in bins of $\text{BDT}_{\text{t-ch.}}$.

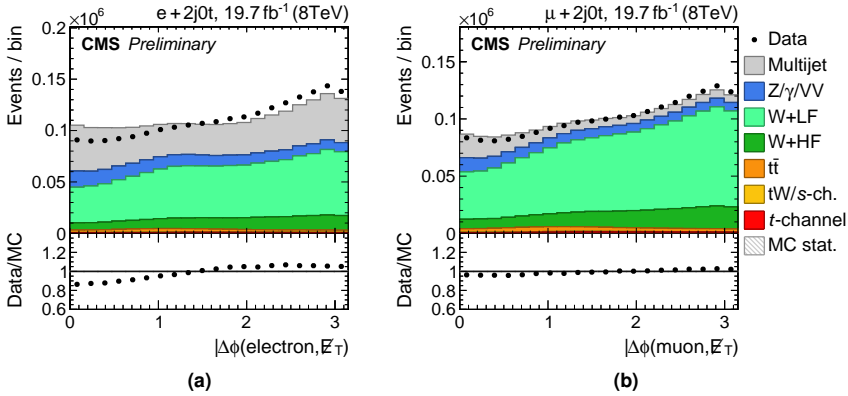


Figure 6.14. | Distributions of the ϕ angle in the transverse plane between the missing transverse momentum and the (a) muon, (b) electron.

other hand, the total uncertainty increases as well towards higher working points due to the decreasing signal selection efficiency which controls the statistical uncertainty. A broad region is observed between both extremes where a measurement with minimal uncertainty can be achieved. For the measurement a working point of $\text{BDT}_{\text{t-ch.}} > 0.45$ is chosen.

6.8. Unfolding and asymmetry estimation

Unfolding to parton level is performed with the TUnfold method [182]. To stabilize the χ^2 minimization inside the method twice as many bins are considered at reconstruction level compared to parton level. The parton level is extended to include also $t \rightarrow b\tau\nu$ decays since about 6% of the selected muons stem from intermediate tau decays which has been studied in simulation (see Sec. 5.5). In such events the polarization angle at parton level is defined between the spectator quark and the tau lepton instead which yields a similar shape compared to events where the W boson decays directly into

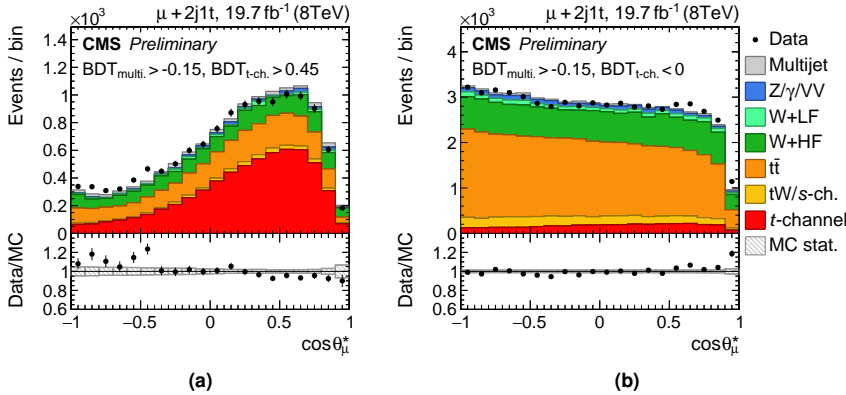


Figure 6.15. | Distributions of the polarization angle in (a) signal-enriched and (b) signal-depleted region in 2j1t muon channel.

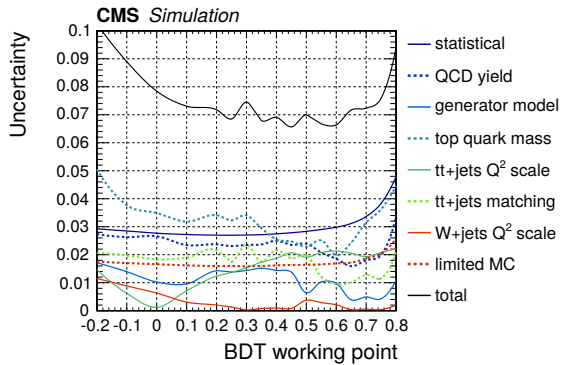


Figure 6.16. | Scan of the total uncertainty on the measured spin asymmetry as a function of the $\text{BDT}_{t\text{-ch.}}$ working point using pseudo-data. Only some representative systematic uncertainties have been evaluated here.

muons. The resulting response matrix is presented in Fig. 6.17. The angle is smeared through manifold effects such as imperfections in the top quark reconstruction and b-tagging where the latter also influences how the spectator jet is chosen.

After unfolding, the top quark spin asymmetry is extracted from the normalized $\cos\theta_\mu^*$ spectrum through a linear χ^2 -fit as

$$\chi^2 = \sum_i \sum_j \left(w \cdot \frac{1}{2} (1 + 2 \cdot A \cos \theta_i) - u_i \right) \mathcal{V}_{ij}^{-1} \left(w \cdot \frac{1}{2} (1 + 2 \cdot A \cos \theta_j) - u_j \right), \quad (6.2.)$$

where w denotes the bin width, u_i the measured cross section in bin i , and \mathcal{V}_{ij} the covariance between bins i and j . The fit allows to properly account for the induced bin-by-bin correlations through the regularized unfolding. To cross check the estimated asymmetry an alternative unfolding is performed based on pure analytical expressions. For this, only two bins are considered which does not allow to apply a curvature-

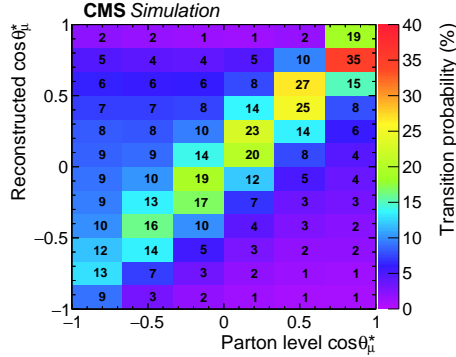


Figure 6.17. | Response matrix from simulated t -channel single-top-quark events in 2j1t muon channel after requiring events with $\text{BDT}_{\text{multi.}} > -0.15$ and $\text{BDT}_{\text{t-ch.}} > 0.45$.

based regularization scheme. Therefore, only an inversion of the response matrix \mathcal{R} is performed and the asymmetry is obtained as

$$A = \frac{u_2 - u_1}{u_1 + u_2}, \quad \vec{u} = \mathcal{R}^{-1} \cdot \vec{d}, \quad (6.3a.)$$

$$\sigma_A^2 = 4 \frac{u_1^2 \mathcal{V}_{22}^{(u)} + u_2^2 \mathcal{V}_{11}^{(u)} - 2 \cdot u_1 u_2 \mathcal{V}_{12}^{(u)}}{(u_1 + u_2)^4}, \quad \mathcal{V}^{(u)} = \mathcal{R}^{-1} \mathcal{V}^{(d)} (\mathcal{R}^{-1})^T, \quad (6.3b.)$$

where \vec{d} denote the distribution of data after the remaining background contributions have been subtracted and $\mathcal{V}^{(d)}$ its corresponding covariance matrix.

A closure test is conducted to validate the overall analysis strategy. Simulated t -channel single-top-quark events with anomalous Wtb couplings are injected into the analysis as pseudo-data. Various couplings scenarios can be realized by applying a special reweighting technique as used in Ref. [194] and explained in the following. It is based on the idea that the single-top-quark cross section can be decomposed as

$$\sigma_{t-\text{ch.}} = V_L^4 \cdot A_{Wb \rightarrow t} A_{t \rightarrow Wb} \quad (6.4a.)$$

$$+ V_L^2 V_R^2 \cdot (A_{Wb \rightarrow t} B_{t \rightarrow Wb} + B_{Wb \rightarrow t} A_{t \rightarrow Wb}) \quad (6.4b.)$$

$$+ V_R^4 \cdot B_{Wb \rightarrow t} B_{t \rightarrow Wb} \quad (6.4c.)$$

if only one anomalous coupling is present while the others vanish, where A and B denote some kinematic function for the production and decay. The vector-like right-handed coupling V_R is taken to be non-zero besides V_L while the tensor-like left- and right-handed couplings are assumed to vanish. An explanation of these couplings is given in Sec. 2.6. Three individual signal samples have been generated using the CompHEP program which correspond to the individual contributions of Eqs. 6.4a, 6.4b, and 6.4c to the total cross section. By multiplying each sample with a coupling-dependent weight arbitrary coupling scenarios in the (V_L, V_R) plane can be realized leading to various top quark spin asymmetries. The analysis strategy is tested by

performing the event selection, the ML fits, the evaluation of the two BDTs, the unfolding, and the estimation of the asymmetry from the differential cross section with pseudo-data generated from the SM background samples and these anomalous coupling samples. Various spin asymmetries are generated by varying the right-handed coupling while keeping the left-handed coupling fixed at 1. The result of this scan is presented in Fig. 6.18 in the form of a Neyman construction [195].

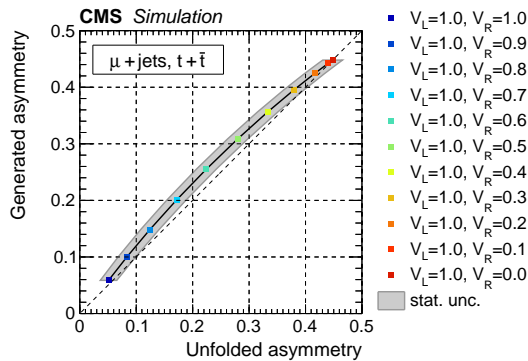


Figure 6.18. | Neyman construction generated by injecting samples with anomalous Wtb couplings as pseudo-data into the measurement for scanning the top quark spin asymmetry.

A bias on the order of the expected statistical uncertainty is observed for some coupling cases. In the statistical evaluation a conservative systematic uncertainty is assumed on the measured asymmetry to cover for such biases. It should be noted that the observed bias cannot be corrected through an ad-hoc transformation of the asymmetry since only a very specific coupling scenarios has been tested here. In the EFT framework the spin asymmetry depends however on multiple anomalous couplings in a complex way.

6.9. Statistical evaluation

The differential cross section and the related extraction of the top quark spin asymmetry from its shape are affected by several sources of systematic uncertainties. Many of them have already been introduced throughout this chapter and in Ch. 4. They are evaluated by using modified templates and response matrices during the ML fits and in the unfolding. The maximal induced shift per source with respect to the nominal asymmetry is listed in Tab. 6.6. Details about sources of systematic uncertainties which have not yet been discussed are given in the following, while for others a reference to their description is provided.

Limited MC statistics This uncertainty is taken into account when subtracting the remaining background contributions from data prior to unfolding and in the unfolding itself since it can influence the transition probabilities within the response matrices. Additionally, this uncertainty is also accounted for when estimating the impact by other sources of systematic uncertainties and thus may result into an overestimation in some cases.

Table 6.6. The considered sources of systematic uncertainties and their impact on the measured asymmetry for events with top quarks, top antiquarks and their combination.

		$\delta A_\mu(t) \cdot 10^2$	$\delta A_\mu(\bar{t}) \cdot 10^2$	$\delta A_\mu(t + \bar{t}) \cdot 10^2$
Signal/background estimation	Statistical	3.2	4.6	2.6
	Limited MC statistics	2.1	3.2	1.8
	ML-fit uncertainty	0.7	1.2	0.6
	Diboson fraction	< 0.1	< 0.1	< 0.1
	$Z/\gamma^* + \text{jets}$ fraction	< 0.1	< 0.1	< 0.1
	s channel fraction	0.3	0.2	0.2
	tW fraction	0.1	0.7	0.2
	Multijet shape	0.5	0.7	0.5
	Multijet yield	1.9	1.2	1.7
Analysis objects	b-tagging	0.7	1.2	0.9
	Mistagging	< 0.1	0.1	< 0.1
	Jet energy resolution	2.7	1.8	2.0
	Jet energy correction	1.3	2.6	1.1
	Unclustered \cancel{E}_T	1.1	3.3	1.3
	Pileup	0.3	0.2	0.2
	Muon identification efficiency	< 0.1	< 0.1	< 0.1
	Muon isolation efficiency	< 0.1	< 0.1	< 0.1
	Trigger efficiency	< 0.1	< 0.1	< 0.1
Modeling	$t\bar{t}$ top quark p_T reweighting	0.3	0.3	0.3
	W+jets W boson p_T reweighting	0.1	0.1	0.1
	W+jets heavy quark flavor fraction	4.7	6.2	5.3
	W+jets light quark flavor fraction	< 0.1	< 0.1	0.1
	W+jets shape reweighting	2.9	3.4	3.1
	Unfolding bias	2.5	4.2	3.1
Theoretical	Generator model	1.6	3.5	0.3
	Top quark mass	1.9	2.9	1.8
	t channel fact./renorm. scale	0.2	0.2	0.2
	$t\bar{t}$ fact./renorm. scale	2.2	3.4	2.7
	$t\bar{t}$ matching	2.2	0.5	1.6
	W+jets fact./renorm. scale	3.7	4.6	4.0
	W+jets matching	3.8	3.0	3.4
	Parton distribution function	0.9	1.6	1.2
Total uncertainty		10.5	13.8	10.5

ML fit uncertainty This uncertainty accounts for the estimated normalization of the backgrounds through the fit (Sec. 6.5).

Other background fractions The yield of each minor process which is grouped into either the electroweak or the top quark background component for fitting is varied conservatively by $\pm 50\%$.

Shape and yield of multijet events A conservative yield uncertainty of $\pm 50\%$ is assumed on the estimated multijet event yield. An additional shape uncertainty is taken into account which is obtained by varying the muon isolation in the sideband region for the template extraction.

Analysis objects A summary of the considered sources of systematic uncertainties related to the reconstruction and selection of analysis objects is provided in Sec. 4.10. This includes uncertainties on the jet energy scale and resolution, the unclustered energy, b-tagging and mistagging efficiencies, the muon trigger, identification, and isolation efficiencies, and the pileup reweighting.

W+jets and $t\bar{t}$ reweighting The applied reweighting of $t\bar{t}$ and W+jets events and its associated uncertainties are motivated in Sec. 6.4.

Unfolding bias The unfolding bias covers for a potential shift in the measured asymmetry which has been observed when injecting pseudo-data with anomalous Wtb couplings (Sec. 6.8).

Generator model The default t -channel single-top-quark sample which is generated with POWHEG and interfaced with Pythia 6 is exchanged by a signal sample generated with aMC@NLO and interfaced with Pythia 8 to assess the dependence of the generator and PS model on the measurement.

Top quark mass An uncertainty on the top quark mass is propagated to the final result by using dedicated $t\bar{t}$ and t -channel single-top-quark samples for which the top quark mass of 172.5 GeV in the default simulation has been conservatively varied by ± 3 GeV.

Factorization and renormalization scales The dependence on the scale is assessed by generating new $t\bar{t}$ and W+jets samples in which the nominally chosen scale per event for the hard interaction, the PDF, and for the PS simulation is either doubled or halved. For signal events, the scale variation is approximated through a reweighting of nominal events as

$$w_{\mu \rightarrow \mu'}(x_1, f_1, x_2, f_2) = \frac{\text{PDF}(x_1, f_1, \mu') \cdot \text{PDF}(x_2, f_2, \mu')}{\text{PDF}(x_1, f_1, \mu) \cdot \text{PDF}(x_2, f_2, \mu)}, \quad (6.5.)$$

where x_i denotes the momentum fraction of the incoming parton and f_i its flavor. It should be noted here that the weight does not depend on the renormalization scale via $\alpha_s(\mu_R)$ since t -channel single-top-quark production in 5 FS occurs only through electroweak interactions at LO. The performed reweighting yields however only an approximation of a proper scale variation because the scale dependence of the PS simulation is neglected. The validity of the approximation is verified through dedicated scale-varied samples. These samples are however limited in their statistics after selecting events in the signal-enriched phase space which is why the approximation is preferred over their usage.

ME-to-PS matching threshold The impact of the MLM matching threshold on the

measurement is investigated for $t\bar{t}$ and $W+jets$ events by producing dedicated samples for which the nominally chosen thresholds are either doubled or halved.

Parton distribution functions The LHAPDF library [36] is used to reweight simulated events to each of the 52 eigenvectors of the CT10 PDF set [196] and to additional eigenvectors which are associated to a variation of α_s . Additionally, the differences with respect to the central PDFs of the MSTW2008CPdeut [197] and NNPDF23 [198] sets are taken into account.

6.10. Results

The measured normalized differential cross sections of t -channel single-top-quark production at 8 TeV as a function of the polarization angle are presented in Figs. 6.19 and 6.20 for top quark events, top antiquark events, and their combination respectively. The measured differential cross sections are compared to the expectations by POWHEG, aMC@NLO, and CompHEP. Uncertainties on the predictions through a variation of the factorization/renormalization scales and the PDF are found to be negligible.

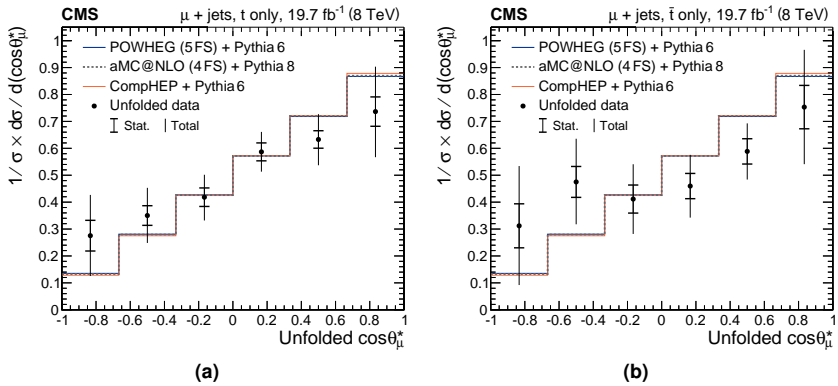


Figure 6.19. | The measured normalized differential cross section as a function of the polarization angle for (a) top quark and (b) top antiquark events. The figures are taken from Ref. [61].

The top quark spin asymmetries are extracted from the shapes through a χ^2 -based linear fit (Sec. 6.8) and measured as

$$A_\mu(t) = 0.29 \pm 0.03 \text{ (stat)} \pm 0.10 \text{ (syst)} = 0.29 \pm 0.11, \quad (6.6a.)$$

$$A_\mu(\bar{t}) = 0.21 \pm 0.05 \text{ (stat)} \pm 0.13 \text{ (syst)} = 0.21 \pm 0.14, \quad (6.6b.)$$

$$A_\mu(t+\bar{t}) = 0.26 \pm 0.03 \text{ (stat)} \pm 0.10 \text{ (syst)} = 0.26 \pm 0.11. \quad (6.6c.)$$

In Fig. 6.21 these results are compared with the obtained asymmetries from the analytical cross check for which only two bins in $\cos\theta_\mu^*$ are used and the unfolding is performed unregularized (Sec. 6.8). A good agreement between the results from the two methods is observed where however the two-bin cross check seems to be more perceptible to statistical fluctuations leading to slightly larger uncertainties.

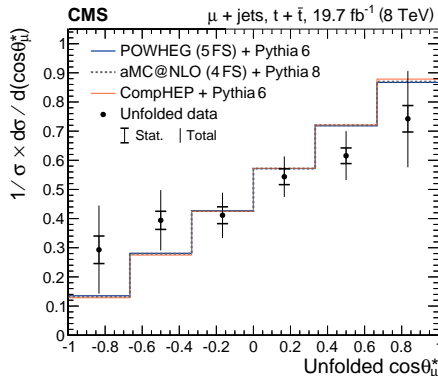


Figure 6.20. | The measured normalized differential cross section as a function of the polarization angle for top quark and antiquark events. The figure is taken from Ref. [61].

The measured $A_\mu(t+\bar{t})$ value from the differential cross section is compatible with a p-value of 4.6% with the SM expectation of 0.44 as predicted by POWHEG which corresponds to 2.0 standard deviations. The compatibility with the hypothetical case of $A_\mu=0$ yields a lower p-value of 0.7% which corresponds to 2.7 standard deviations.

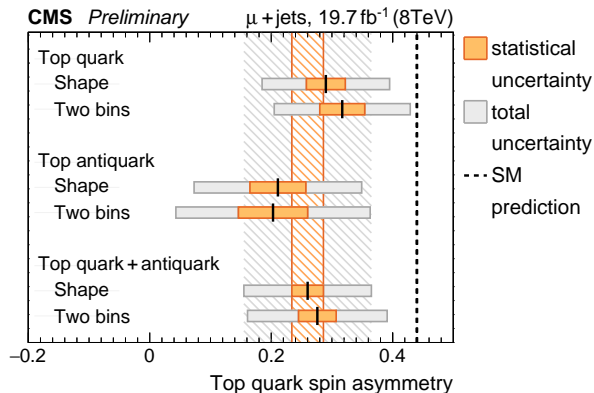


Figure 6.21. | Comparison of the extracted top quark spin asymmetries as obtained through a linear fit to the shape of the differential cross sections or through the analytical two-bin cross check.

6.11. Limits on anomalous couplings

The TopFit program [49, 184] is employed to illustrate the derivation of limits on anomalous electroweak top quark couplings arising from dimension-six effective operators (see Sec. 2.6) using the result of the presented measurement. In addition to the top quark spin asymmetry, the measured single-top-quark cross section in t channel at 8 TeV [167] and the measured W boson helicity fractions in $t\bar{t}$ events at 8 TeV [199] are included in the limit estimation as well. Potential correlations between the results of these measurements are ignored. The limits are derived in the hyperplane spanned

by the anomalous couplings V_L , V_R , g_L , g_R , and the single-top-quark polarization, P_t , in t channel. The couplings are assumed to be real and the polarization is restricted to $P_t > 0$. Since the polarization can additionally be influenced by 4-fermion contact-interactions in production, two versions of limits are set. In the first version the polarization is kept independent from the anomalous couplings. Thus, limits on the polarization are only propagated through the top quark spin asymmetry via the relation

$$A = \frac{1}{2} \cdot P_t \cdot \alpha_\ell(V_L, V_R, g_L, g_R), \quad (6.7.)$$

where α_ℓ denotes the spin-analyzing power of the lepton. For the second version of limits potential extra couplings beyond the ones affecting the Wtb vertex in t -channel production are ignored. Thus, the polarization is a fixed function of the anomalous couplings.

The resulting limits are presented in Fig. 6.22 where two-dimensional projections of the five-dimensional (anomalous couplings, polarization)-hyperspace are shown. For the first version of limits, where the polarization is kept free, the presented spin asymmetry measurement is not yet precise enough to constrain the polarization at an exclusion limit (CL) of 95%. If the polarization is on the other hand fixed to the anomalous couplings, the derived limits become more stringent. In particular, a large region in the (P_t, V_R) -plane can be excluded.

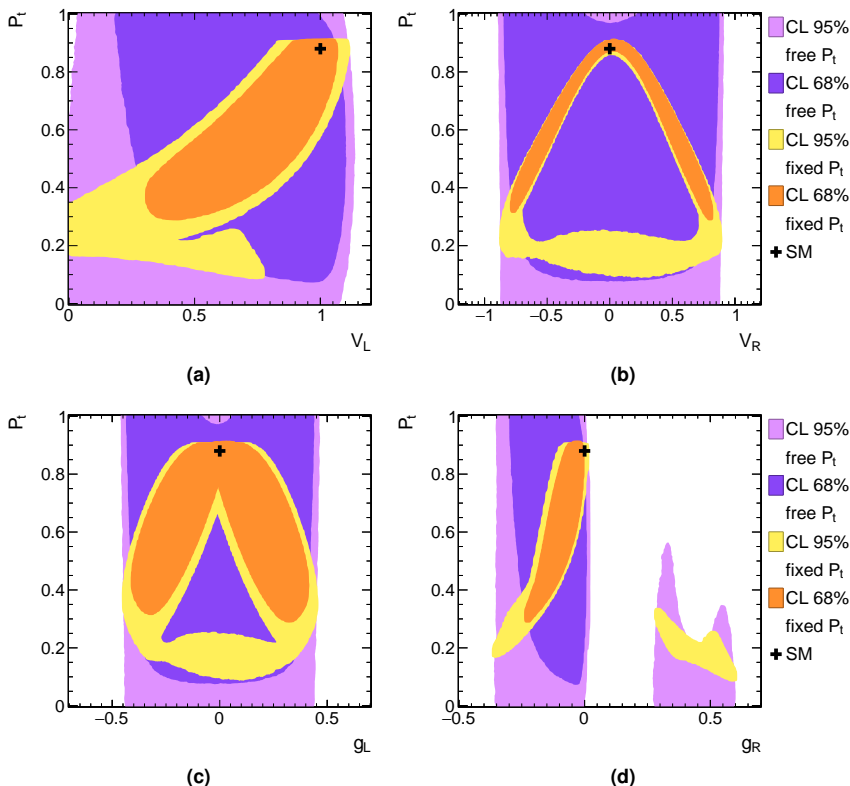


Figure 6.22. | Projections of limits on anomalous couplings and the top quark polarization for cases with free-floating polarization (violet) or when fixing the polarization to the anomalous couplings (orange): (a) left-handed vector couplings against polarization; (b) right-handed vector coupling against polarization; (c) left-handed tensor coupling against polarization; (d) right-handed tensor coupling against polarization.

7.

Chapter

Measurement of differential single-top-quark cross sections at 13 TeV

An early measurement of the normalized differential single-top-quark cross sections in t channel as a function of the top quark transverse momentum and rapidity at a center-of-mass energy of 13 TeV is presented. Proton-proton collision data corresponding to 2.3 fb^{-1} are analyzed which were recorded in 2015 with the CMS experiment. Events containing one isolated muon and two or three jets are selected and a boosted decision tree is trained for separating signal from background events further. The amount of signal events as a function of the top quark transverse momentum and rapidity is estimated by performing multiple maximum-likelihood fits. The results are unfolded to parton level and compared to predictions by various Monte-Carlo generators. No significant deviations are observed. The measurement detailed in this chapter has been published in Ref. [200].

7.1. Outline of analysis strategy

Proton-proton collision data are analyzed corresponding to an integrated luminosity of 2.3 fb^{-1} . Events containing one isolated muon and two or three jets are selected. A BDT is trained to obtain a powerful discriminant for separating signal from background events. The individual amounts of signal and background events in data are estimated by performing a template-based ML fit to the distributions of the transverse W boson mass and the BDT discriminant in the signal and in two $t\bar{t}$ -dominated control regions simultaneously. The contamination by multijet events is estimated by using a data-driven template to model its shape. The template is obtained from a sideband region for which the muon isolation is inverted. Multiple ML fits are performed in separate intervals of the top quark transverse momentum and rapidity in addition. By passing these fit results directly to the unfolding procedure the differential cross section as a function of the top quark p_T and rapidity is inferred. The impact of sources of systematic uncertainties on the differential cross section is evaluated by repeating the measurement with correspondingly modified templates. The resulting differential cross sections are compared to predictions by various event generators.

The outlined strategy has multiple benefits compared to the one chosen for the polarization measurement (Ch. 6). First, it is not necessary to define a signal-enriched region where the remaining backgrounds are subtracted from data prior to unfolding. Instead, the signal yields in intervals of the top quark p_T and rapidity are taken from the fit results directly. Secondly, since no signal-enriched region is defined an optimization of its selection is also not required. The measurement is carried out with no explicit selection to reject multijet events or on the BDT discriminant to reject W+jets/ $t\bar{t}$ events

except for validation purposes. Lastly, residual differences in the estimated background yields between unfolding bins are profiled per bin of the top quark p_T or rapidity spectrum. This reduces the impact of potential shortcomings in their modeling and can also mitigate a potential bias that may occur through correlations of the BDT discriminant with the top quark p_T and rapidity distributions.

7.2. Event selection and simulated samples

The measurement is based on pp collision data corresponding to 2.3 fb^{-1} which were recorded with the CMS experiment in 2015 at a center-of-mass energy of 13 TeV. During this data taking period the instantaneous luminosity was kept relatively low with a maximum of about 5.1 Hz/nb leading to only 14 pileup interactions on average [78].

A muon trigger is employed which requires the presence of an isolated muon candidate with a transverse momentum of at least 20 GeV within $|\eta| < 2.4$. Offline, the muon candidate is required to have $p_T > 22 \text{ GeV}$ within $|\eta| < 2.4$ and it has to fulfill tight identification requirements as well. Furthermore, the muon candidate is required to be isolated with a relative $\Delta\beta$ -based isolation of $I_{\text{rel.}}^{\mu} < 6\%$, calculated from the transverse energy deposits of charged and neutral hadrons, photons, and from tracks associated to pileup interactions within a cone of $\Delta R < 0.4$ around the candidate (see Sec. 4.4). The isolation is explicitly chosen tighter here compared to single-top-quark measurements at 8 TeV (e.g. Ch. 6, Ref. [167]) in which an isolation of $I_{\text{rel.}}^{\mu} < 12\%$ is required instead. The distribution of the relative muon isolation after applying the complete event selection with the exception of the isolation requirement is presented in Fig. 7.1. The multijet template is taken exceptionally from simulation and scaled such that it fits approximately to the bulk of the data distribution within uncertainties. The deviation at high isolation values can be attributed to differences in the trigger isolation efficiencies between data and its emulation in simulation. The tighter isolation working point is motivated by the observed larger background contamination stemming from multijet production. Selection efficiencies for various working points, estimated from simulation, are listed in Tab. 7.1. Compared to $I_{\text{rel.}}^{\mu} < 12\%$, the contamination by multijet events is about halved at the new working point of $I_{\text{rel.}}^{\mu} < 6\%$ whereas only 12% of signal and other background events are rejected.

Table 7.1. Selection efficiencies for various isolation working points estimated from simulation.

Process	Selection efficiency			
	$I_{\text{rel.}}^{\mu} < 12\%$	$I_{\text{rel.}}^{\mu} < 8\%$	$I_{\text{rel.}}^{\mu} < 6\%$	$I_{\text{rel.}}^{\mu} < 4\%$
t channel	94%	88%	83%	73%
Multijet (simulation)	33%	21%	16%	10%
Other backgrounds	93%	87%	82%	72%

For the measurement, contributions from processes with a $\mu\mu$ +jets or a μe +jets final state such as dileptonic $t\bar{t}$ or Z/γ^* +jets production are suppressed by vetoing events containing additional muon ($p_T > 10 \text{ GeV}$, $|\eta| < 2.5$) or electron candidates ($p_T > 20 \text{ GeV}$, $|\eta| < 2.5$). Additional muon candidates are required to be isolated ($I_{\text{rel.}}^{\mu} < 20\%$) and to

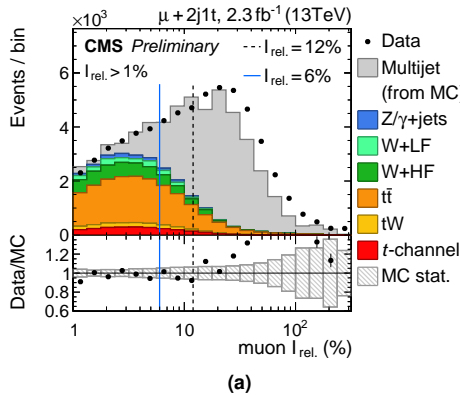


Figure 7.1. | Distribution of the relative $\Delta\beta$ -based muon isolation in 2j1t. The multijet template is taken from simulation.

fulfill loose identification criteria. Electrons candidates on the other hand have to pass identification criteria which are specifically designed for vetoing events containing additional electrons.

Jets are clustered from PF candidates using the anti- k_T algorithm with a distance parameter of $R = 0.4$ while mitigating the influence of pileup through the CHS technique [124]. The reconstructed jet energy is corrected in data and simulation using dedicated scale factors. Additionally, the jet energy is smeared in simulation to match the resolution observed in data. Events containing two or three jets with a corrected transverse momentum of at least 40 GeV that fall within $|\eta| < 4.7$ and fulfill loose identification requirements are selected for analysis. Potential overlaps between selected jets and the single muon candidate are avoided by ignoring jets that are reconstructed within a cone of $\Delta R < 0.3$ around the muon. The CSV algorithm (version 2) is employed for b-tagging [129]. At its tight working point an efficiency of about 50% is achieved for tagging true b jets whereas the fraction of mistagged jets originating from g, u, d, s quarks amounts to only 0.1%. To match the observed b-tagging efficiency in data, simulated events are reweighted using dedicated scale factors.

For validation purposes, events with a transverse W boson mass of $m_T(W) > 50$ GeV are selected to reject multijet events. However, the region $m_T(W) < 50$ GeV is explicitly kept in the measurement since it provides sensitivity to estimate the amount of multijet events as detailed in Sec. 7.5.

The following samples of simulated events are employed in the measurement. The MadGraph5_aMC@NLO generator interfaced with Pythia8 is used to generate the default signal sample of t -channel single-top-quark production in 4 FS. Alternative samples are generated for comparison using the MadGraph5_aMC@NLO generator interfaced with Pythia8 in 5 FS, MadGraph5_aMC@NLO interfaced with Herwig in 4 FS, and POWHEG interfaced with Pythia in 4 FS. Single-top-quark production via tW and tt production are simulated using the POWHEG generator interfaced with Pythia8. Samples of $W+jets$ and Z/γ^*+jets events are generated using MadGraph5_aMC@NLO interfaced with Pythia8 as well. The calculated SM cross sections for normalizing these samples are listed

in Tab. 7.2. The contributions by single-top-quark production in s channel and by diboson production have been found negligible at 13 TeV after the event selection. Thus corresponding samples are not used in the measurement. Special care is taken for normalizing the samples produced with the MadGraph5_aMC@NLO generator because the MC@NLO matching scheme leads to a significant fraction of negatively weighted events. In the employed samples the fractions are found to be about 40% for t -channel, 25% for Z/γ^* +jets, and 15% for W+jets events.

Table 7.2. || Theoretical SM cross sections at 13 TeV used to normalize the simulated samples.

Process	Cross section	Accuracy
t -channel top quark	$136.0^{+5.4}_{-4.6}$ pb	NLO (using HATHOR 2.1 [58])
t -channel top antiquark	$81.0^{+4.1}_{-3.6}$ pb	NLO (using HATHOR 2.1 [58])
tW channel	71.7 ± 3.8 pb	NLO (using HATHOR 2.1 [58])
$t\bar{t}$	832^{+20}_{-29} pb	NNLO (using Top++ 2.0 [52])
$W \rightarrow \ell\nu + \text{jets}$	20509^{+788}_{-776} pb	NNLO (using FEWZ 3.1 [201])
$Z/\gamma^* \rightarrow \ell^+\ell^-, m_{\ell\ell} > 50$ GeV	2008^{+76}_{-75} pb	NNLO (using FEWZ 3.1 [201])

Following a similar procedure as in the top quark polarization measurement (Ch. 6), the shape of multijet events is modeled by a data-driven template from a sideband region for which the muon isolation is inverted as $I_{\text{rel}}^\mu > 20\%$ in the event selection. A systematic uncertainty on the shape of the multijet template is taken into account by extracting the template from an isolation subrange of either $I_{\text{rel}}^\mu \in [20\%, 40\%]$ or $I_{\text{rel}}^\mu \in [40\%, \infty)$ instead. These intervals have been chosen such that they contain approximately equal amounts of data events in order not to increase the . The resulting shape variations after scaling each template to its individual ML fit result are shown in Fig. 7.2a as a function of the transverse W boson mass. In Fig. 7.2b the shape uncertainty as a function of a BDT discriminant (Sec. 7.4) is shown in a multijet-depleted region defined by $m_T(W) > 50$ GeV. In this region the uncertainty on the extrapolated multijet yield amounts to about $\pm 20\%$ on average. In the distributions throughout this chapter, the extracted multijet template as well as other background and signal templates are scaled to the result of a ML fit to data as described in Sec. 7.5 unless explicitly stated otherwise.

After the event selection signal and control regions are defined based on the number of selected jets and the subset of jets which are also b-tagged. The same notation as in the top quark polarization measurement is employed as detailed in Sec. 6.2. In control regions the assignment of jets to the top quark decay and to the spectator quark is performed as follows. First, b-tagged jets are sorted by p_T and non-tagged jets by $|\eta|$. Then, the most forward jet is taken as the spectator jets because in t -channel single-top-quark production it is expected to be scattered into the forward detector region by recoiling against the W boson. In the 2j0t control region the remaining jet is then associated to the top quark decay. In control regions containing multiple b-tagged jets the top quark is reconstructed using the hardest b-tagged jet. This choice is motivated by the fact that an additional b quark in t -channel single-top-quark

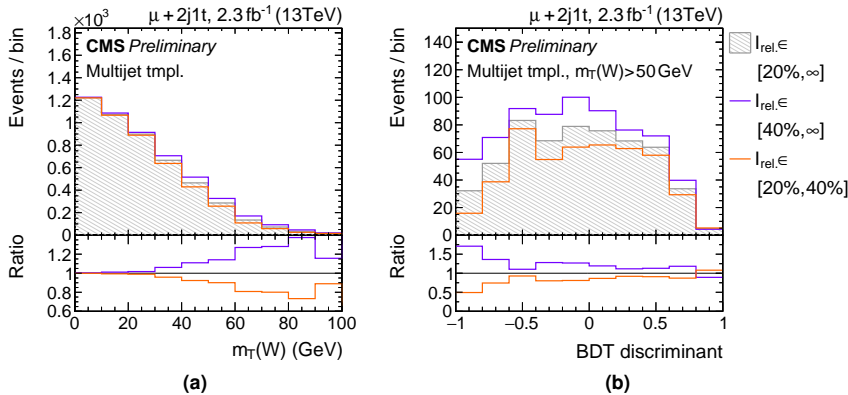


Figure 7.2. | Extracted multijet templates from three sideband regions with different muon isolation ranges in 2j1t region: (a) distribution of the transverse W boson mass; (b) distribution of a BDT discriminant for events with $m_T(W) > 50$ GeV. The individual templates are scaled to the results of corresponding ML fits to data (Sec. 7.5).

production originates from initial state gluon splitting for which a softer spectrum is expected.

Distributions of the reconstructed top quark mass in signal and control regions are presented in Fig. 7.3. Since the 3j2t region contains a relatively low number of events, the 3j1t region is considered as an additional $t\bar{t}$ control region in this analysis for fitting. The shown distributions of data are well described by the simulated signal and background samples, and the extracted multijet templates.

7.3. Background modeling

The modeling of the simulated samples and the applied corrections are assessed. In Fig. 7.4 distributions of the number of jets and the number of b-tagged jets are presented. These allow to validate whether if the applied jet energy corrections and the b-tagging efficiency scale factors correct properly for any residual differences between data and simulation. Good agreement is observed for the number of b-tagged jets and also for the number of jets at low multiplicities ($N \leq 4$) relevant for this analysis. At higher jet multiplicities, the number of jets is overestimated by simulation to which the measurement is however not sensitive. Dedicated $t\bar{t}$ measurements revealed that a refining of generator parameters controlling the radiation of addition partons results in a good description of data at high jet multiplicities as well [202].

The modeling of the data-driven multijet template is validated in Fig. 7.5 where the distributions of the missing transverse energy and the difference in ϕ angles between the muon and the transverse momentum is presented in the 2j0t W+jets and 2j1t signal regions. Both distributions demonstrate a good description of data by the multijet templates and the simulated samples.

Lastly, the W+jets modeling is assessed. Figure 7.6 shows the distributions of the transverse W boson mass and the polarization angle using the default W+jets sample generated with MadGraph5_aMC@NLO at NLO. For comparison, the predicted shape by

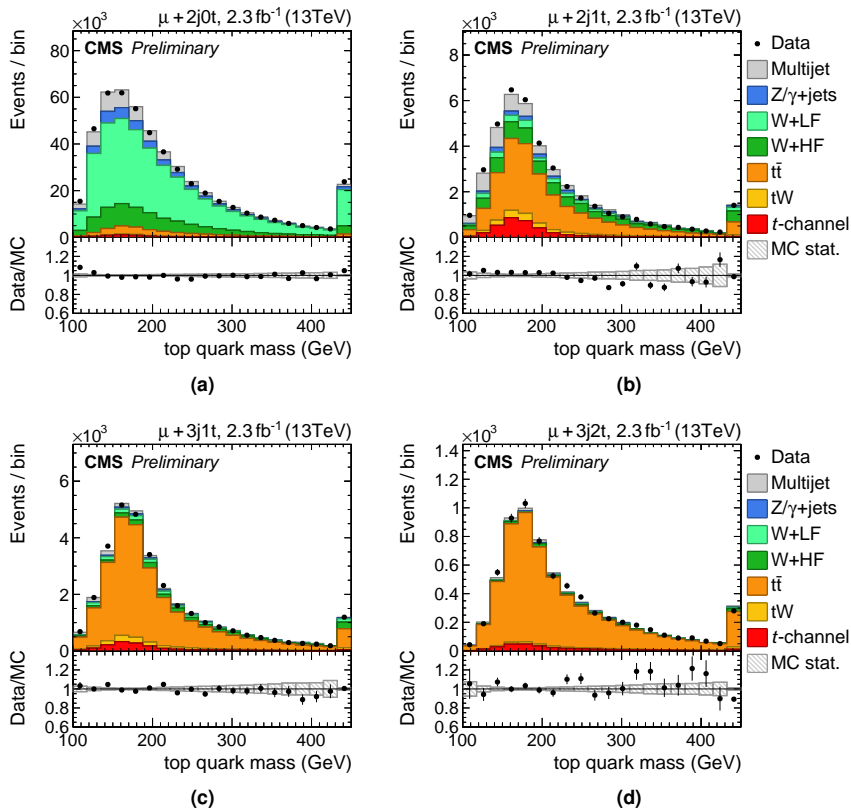


Figure 7.3. | Distributions of the reconstructed top quark mass: (a) W+jets control region; (b) signal region; (c+d) $t\bar{t}$ control regions.

an alternative W+jets sample generated MadGraph at LO is also presented. The sample produced with the new MadGraph5_aMC@NLO generator displays a superior modeling of both observables whereas the MadGraph W+jets sample exhibits some mismodeling. The trend in the ratios is somewhat different here compared to the observations in the top quark polarization measurement at 8 TeV (Sec. 6.4). This may be related to differences in the Pythia tunes^(*) which was however not studied further.

^(*) 8 TeV: Pythia6 Z2* tune [203]; 13 TeV: Pythia8 CUETP8M1 tune [204].

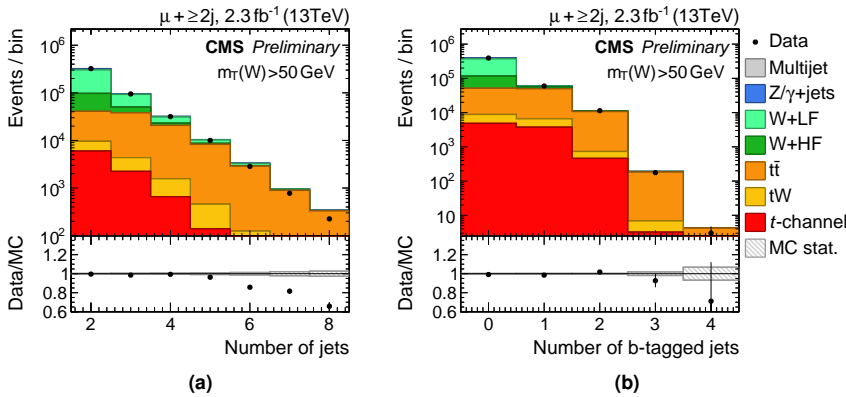


Figure 7.4. | Distributions of the number of selected jets and b-tagged jets for events with at least two selected jets and $m_T(W) > 50 \text{ GeV}$.

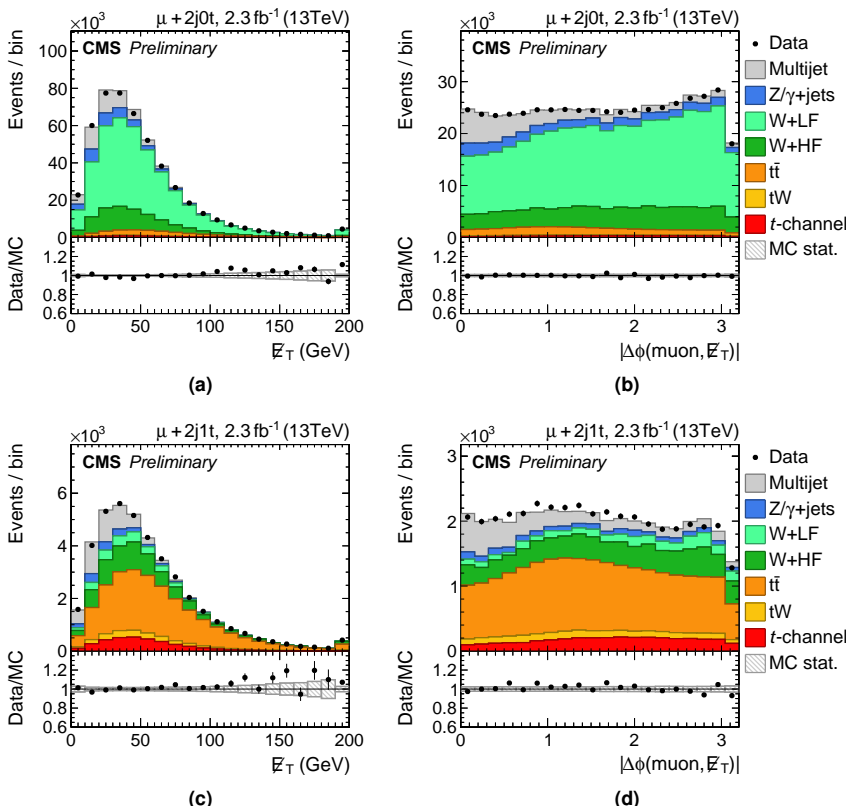


Figure 7.5. | Validation of the data-driven multijet template in (top row) 2j0t $W + \text{jets}$ control region and (bottom row) 2j1t signal region: (left column) distribution of the missing transverse energy; (right column) distribution of the difference of the ϕ angles of the muon and missing transverse momentum.

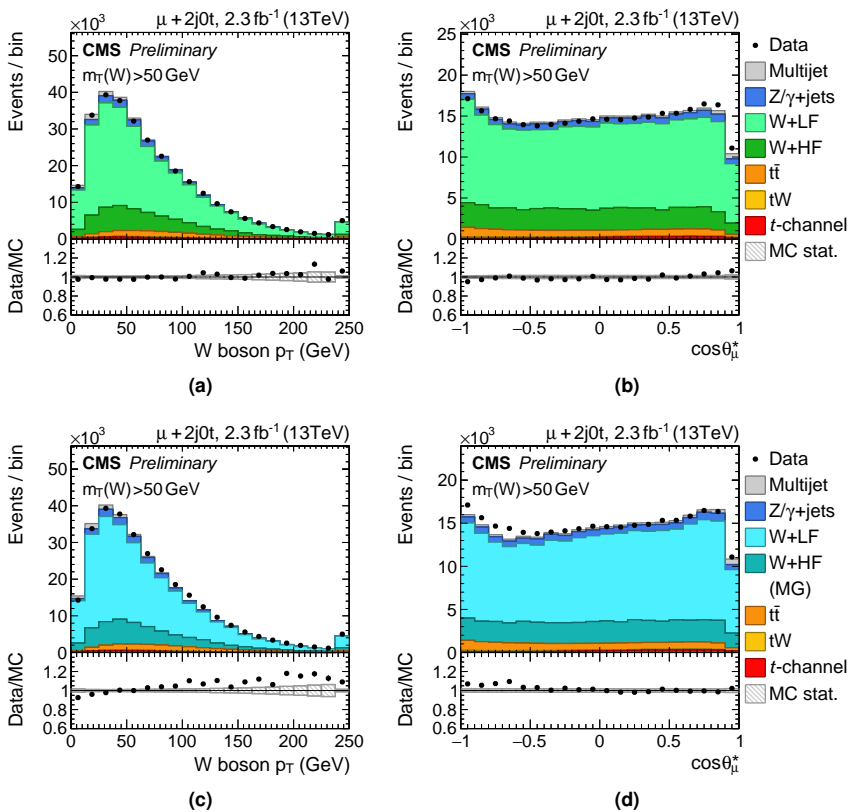


Figure 7.6. W+jets modeling in 2j0t control region by (top row) MadGraph5_aMC@NLO at NLO or by (bottom row) MadGraph at LO accuracy: (left column) distribution of the p_T of the reconstructed W boson candidate; (right column) distribution of the polarization angle.

7.4. BDT training

A BDT is trained for separating t -channel single-top-quark events from $W+jets$ and $t\bar{t}$ background events. It is configured as follows. The AdaBoost algorithm with a learning rate of 40% is chosen. In total, 1 000 decision trees with a maximum depth of three are trained. The number of tested working points per observables is set to 40. Negatively weighted events generated by MadGraph5_aMC@NLO are also included in the training for which the boosting weight is automatically inverted inside TMVA. A potential overtraining through the large fraction of negatively weighted events is mitigated by adding alternative t -channel and $W+jets$ events generated with POWHEG and MadGraph to the training respectively whose events weights are all positive. For validation purposes an alternative BDT is trained as well using the GradientBoost algorithm with a shrinkage of 40% while keeping the other settings identical. In the case significant differences in the performances between both BDTs are obtained, this may reveal potential problems with the chosen setup hinting to e.g. overtraining or improper handling of the negatively weighted events.

In addition to the $W+jets$ and $t\bar{t}$ events a sample of simulated multijet events is added to the training as background as well. The motivation for this is to prevent that multijet events become accidentally clustered at high values of the final BDT discriminant. The exact amount of mixed-in multijet events has to be however carefully chosen since if it is too large the BDT might separate multijet from signal events predominantly while mostly ignoring $W+jets$ and $t\bar{t}$ events.

Various input observables have been investigated for their individual discrimination power per process-pair as listed in Tab. 7.3. The following five observables have been chosen which provide individually already a high discrimination power while exhibiting low correlations with the reconstructed top quark p_T and rapidity:

- the absolute value of the pseudorapidity of the untagged spectator jet (j');
- the invariant mass of the reconstructed top quark candidate;
- the ΔR distance between the two selected jets;
- the difference in pseudorapidity between the muon and the selected b-tagged jet;
- the transverse W boson mass, $m_T(W)$, before solving for the unknown neutrino p_z component in the top quark reconstruction.

Although $m_T(W)$ provides little discrimination power for separating t -channel from $W+jets$ and $t\bar{t}$ events it is included for its discrimination power against multijet events. The event shape variables C and sphericity yield a high discrimination power as well for separating signal from $t\bar{t}$ events as indicated in Tab. 7.3. They are calculated as

$$S^{ab} = \frac{\sum_i^{\text{jets}, \mu, \vec{p}_T} p_i^a \cdot p_i^b}{\sum_i^{\text{jets}, \mu, \vec{p}_T} |\vec{p}_i|^2}, \quad \Rightarrow \quad S = \frac{3}{2}(\lambda_2 + \lambda_3), \quad C = 3(\lambda_1\lambda_2 + \lambda_1\lambda_3 + \lambda_2\lambda_3), \quad (7.1.)$$

where $\lambda_1 + \lambda_2 + \lambda_3 = 1$ are the decreasingly-ordered eigenvalues of the momentum tensor S^{ab} . Their distributions are shown in Fig. 7.7 for which also a good modeling of

Table 7.3. Discrimination power of event observables and the trained BDTs in 2j1t region for various combinations of signal (t -channel) and background ($t\bar{t}$, $W+jets$, multijet) processes. Highlighted are a few of the most discriminating observables per process-pair.

	Observable	Area under ROC curve (AUC)			
		$t\bar{t}$ /signal	$W+jets$ /signal	Multijet/signal	$t\bar{t}/W+jets$
BDT inputs	Spectator jet $ \eta(j') $	26%	21%	10%	6%
	$ m_{top} - 172.5 \text{ GeV} $	13%	24%	14%	11%
	$\Delta R(\text{b jet}, j')$	26%	13%	5%	15%
	$ \Delta\eta(\text{b jet}, \text{muon}) $	5%	20%	5%	16%
	$m_T(W)$	4%	2%	36%	3%
Others	E_T	9%	4%	28%	12%
	Muon p_T	11%	10%	27%	1%
	Spectator jet p_T	1%	4%	9%	4%
	$ \Delta\phi(\text{muon}, E_T) $	6%	3%	19%	4%
	b jet mass	5%	3%	8%	5%
	Dijet p_T	12%	4%	6%	8%
	Dijet mass	23%	14%	11%	10%
	$\sqrt{\hat{s}} = \vec{p}_{top} + \vec{p}_{j'} $	15%	7%	11%	8%
	$(\vec{p}_{top} + \vec{p}_{j'})_T$	16%	1%	1%	17%
	Isotropy	2%	4%	8%	6%
	Sphericity	25%	18%	7%	10%
	Event shape C	25%	17%	7%	10%
	$\cos\theta_\mu^*$ (polarization)	14%	7%	9%	7%
	$\cos\theta_W^*$ (helicity)	1%	11%	10%	10%
	BDT (AdaBoost)	31%	32%	27%	3%
	BDT (GradientBoost)	31%	31%	29%	2%

data by the simulated samples is observed. However, when adding these observables to the BDT training no further improvement in discrimination power was obtained. Thus they have been omitted from the BDT training for the measurement.

The trained BDT discriminant yields an AUC of 31% and 32% for separating t -channel single-top-quark events from $t\bar{t}$ and $W+jets$ events, respectively. The obtained performance is confirmed by the alternative BDT which is trained with the GradientBoost method instead. The BDT discrimination power against multijet events of 27% is not as high as what could be obtained with the transverse W boson mass alone (36%). This is a result of the reduced amount of multijet events added to the training such that the BDT does not discriminates against them predominantly but mostly against $t\bar{t}$ and $W+jets$ events instead.

Distributions of the chosen input observables in the 2j1t region are shown in Fig. 7.8 which the exception of the top quark mass which has already been presented in Fig. 7.3. The distribution of the resulting BDT discriminant is shown in Fig. 7.8e. Since its shape is used later in an ML fit an ad-hoc transformation

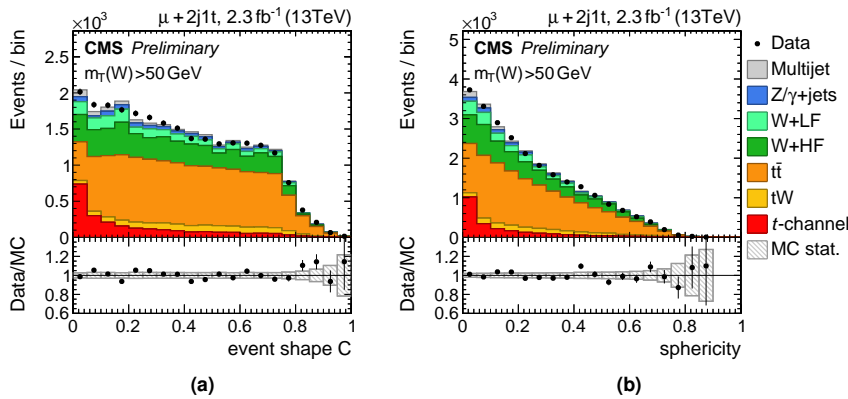


Figure 7.7. | Event shape observables in 2j1t region: (a) event shape C; (b) sphericity. Details on their calculation are given in the text.

$$\text{BDT} \mapsto \text{BDT}' = \tanh(3.2 \cdot (\text{BDT} - 0.12)) \quad (7.2.)$$

is applied to the BDT value per event such that the distribution has an improved spread over the full range of $\text{BDT} \in [-1; 1]$ for fitting. The exact transformation is chosen such that multiple bins with varying signal fractions are obtained which yields a higher sensitivity to the signal yield in the fit.

The correlations between the top quark p_T , rapidity, and the BDT input observables for t -channel single-top-quark events are presented in Fig. 7.9. In general, the correlations with the top quark p_T and rapidity are found to be relatively low. For the top quark rapidity the largest correlation amounts to 8% with the transverse W boson mass while for the top quark p_T a correlation of -14% is observed with the pseudorapidity of the spectator jet.

7.5. Signal extraction

In past single-top-quark measurements (e.g. Refs. [61, 167, 168]), the contamination by multijet events is estimated following a common procedure in which an extra ML fit to data is performed using the $m_T(W)$ or \cancel{E}_T distribution while keeping all other processes grouped together. The amount of signal events is then estimated by performing a second ML fit using a discriminating observables such as the pseudorapidity of the spectator jet or an MVA discriminant while fixing the multijet yield to the first fit result. The reason behind this two-staged fitting procedure is that the $m_T(W)$ or \cancel{E}_T shape is very sensitive to the multijet yield whereas another observable is required to provide sufficient sensitivity to break down the contributions by the signal and the other background processes (see also Tab. 7.3). In this measurement a novel fitting strategy, outlined in the following, has been developed which allows to simultaneously estimated the amount of signal, the contamination by multijet events, and the contributions by the other backgrounds processes by performing only a single ML fit. The log-likelihood of the fit can be written as

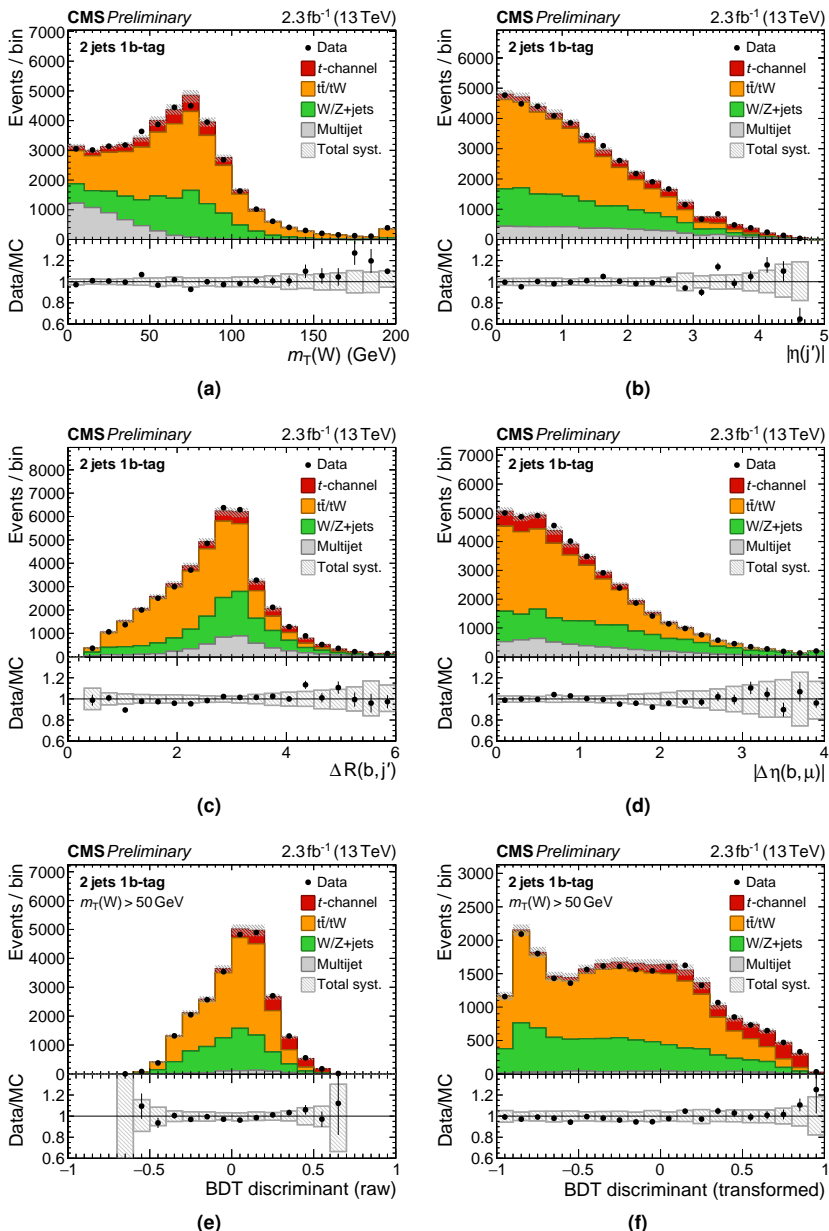


Figure 7.8. Distributions of some input observables for the BDT training in 2j1t signal region and the final discriminant: (a) the transverse W boson mass; (b) pseudorapidity of the spectator jet (j'); (c) ΔR difference between the two jets; (d) difference in pseudorapidities between the muon and b-tagged jet; (e+f) the raw and transformed discriminant. The hatched band reflects the total systematic uncertainties. The figures are taken from Ref. [200].

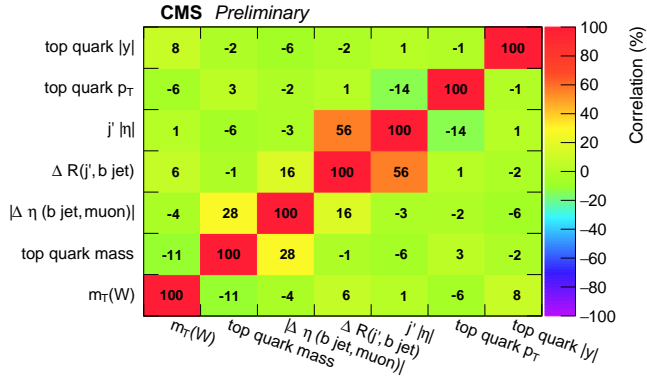


Figure 7.9. | Pearson correlation coefficients between the BDT input observables and the top quark p_T and rapidity for t -channel single-top-quark events.

$$\ln(L_{\text{total}}) = \ln(L_{\text{Poi.}}^{2j1t}) + \ln(L_{\text{Poi.}}^{3j1t}) + \ln(L_{\text{Poi.}}^{3j2t}) + \text{constraints}. \quad (7.3.)$$

in which the Poisson terms per region $X = (2j1t, 3j1t, 3j2t)$ are given by

$$\ln(L_{\text{Poi.}}^X(\vec{d}^X | \vec{p}^X)) = \sum_i^{\text{bins}} (d_i^X \ln p_i^X - p_i^X) + \text{const.}, \quad (7.4.)$$

where d_i denotes the amount of data events and p_i the prediction per bin i . The predictions per region can be expressed as

$$\vec{p}^X = \beta_{t\text{-channel}} \cdot \vec{T}_{t\text{-channel}}^X \quad (7.5a.)$$

$$+ \beta_{\text{top bkg.}} \cdot (\vec{T}_{t\bar{t}}^X + \vec{T}_{tW}^X) \quad (7.5b.)$$

$$+ \beta_{W/Z+\text{jets}} \cdot (\vec{T}_{W+\text{jets}}^X + \vec{T}_{Z/\gamma^*+\text{jets}}^X) \quad (7.5c.)$$

$$+ \beta_{\text{multijet}}^X \cdot \vec{T}_{\text{multijet}}^X, \quad (7.5d.)$$

where \vec{T}_j denotes a template of a process whose normalization is modified by a corresponding scale factor β_j . In this fit, background processes containing genuine top quarks ($t\bar{t}$, tW) have been grouped together as well as the electroweak processes ($W+\text{jets}$, $Z/\gamma^*+\text{jets}$). A log-normal prior with an uncertainty of $\pm 10\%$ is used to constrain the normalization of the top quark background. For the $W/Z+\text{jet}$ background a conservative larger prior with a width of $\pm 30\%$ is assumed. The normalization of the multijet templates are kept almost unconstrained using independent scale factors per region with an uncertainty of $\pm 100\%$ on their yield. No constraint on the signal scale factor is applied.

A compound distribution is utilized for fitting using the transverse W boson mass distribution for events with $m_T(W) < 50$ GeV and the distribution of the trained BDT discriminant otherwise. A comparison of the different template shapes for both

distributions in the 2j1t region is presented in Fig. 7.10. Only five bins are used for the $m_T(W)$ distribution and 15 for the BDT distribution to reduce the impact by the limited simulation statistics on the result. The two $t\bar{t}$ control regions (3j1t, 3j2t) are fitted simultaneously as well which provides an additional handle on the $t\bar{t}$ yield.

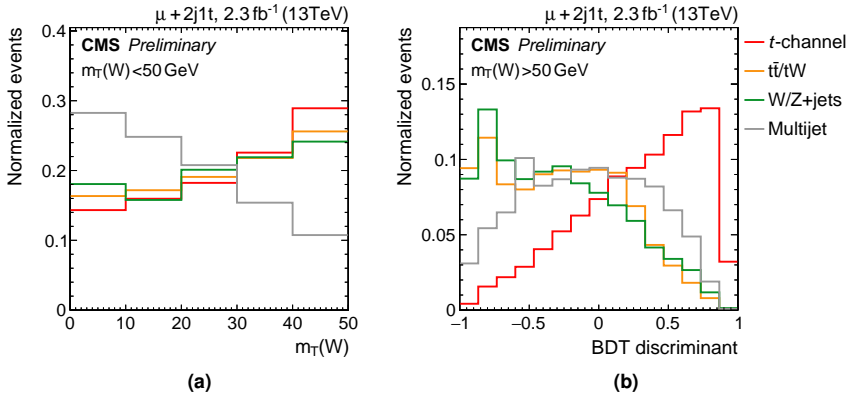


Figure 7.10. | Shapes of the ML fit templates in 2j1t region.

The estimated yields per process in the 2j1t region after the event selection are listed in Tab. 7.4. Extrapolated yields are also given in a multijet-depleted region and in a signal-enriched region for reference, where in the latter a S/B of about 1 is obtained. The correlations between the estimated scale factors are presented in Fig. 7.11. Overall the absolute value of the correlation does not exceed 34% with the exception of the 3j2t multijet scale factor for which the corresponding template contributes however only 2% of events in the 3j2t region in total compared to the other processes. In particular the anticorrelation between the W+jets and $t\bar{t}$ yields amounts to only -33% through the new fitting strategy which marks a significant reduction compared to the fit result in the top quark polarization measurement where an anticorrelation of -75% has been obtained (Sec. 6.5).

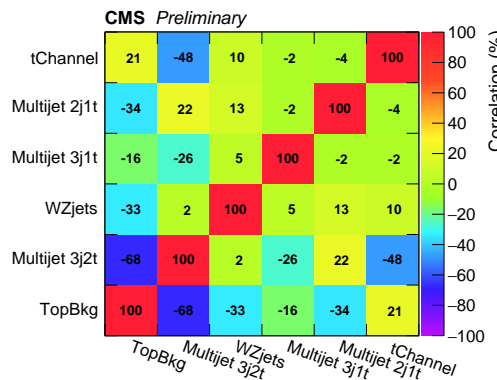


Figure 7.11. | Correlations between the estimated scale factors.

Table 7.4. Estimated event yields in the 2j1t region: after the event selection; for events with $m_T(W) > 50$ GeV; in a signal-enriched phase space defined by $m_T(W) > 50$ GeV and $BDT > 0.6$.

Process	Event yields		
	Selection	$m_T(W) > 50$ GeV	Signal-enriched
tW	2001±14	1343±12	32±2
t̄t	19037±22	12960±18	353±3
W+heavy quark flavor	6825±57	4807±49	189±11
W+light quark flavor	2395±40	1684±34	71±7
Z/ γ^* +jets	1534±24	664±16	23±3
Multijet	4881±18	561±3	38±1
Signal	3385±5	2351±4	700±2
Total expected	40057±80	24369±66	1407±13
Data	40432±201	24417±156	1482±38

Besides the inclusive ML fit, multiple fits are performed in addition using the same strategy while being however restricted to events within a certain interval of the reconstructed top quark p_T or rapidity. Estimating separate scale factors in these intervals results in several advantages for the measurement as listed in the following.

- The estimated scale factors allow to calculate the yield of the signal as a function of the top quark p_T and rapidity directly. Thus, contributions from background processes do not have to be explicitly subtracted from data prior to the unfolding. This new approach mitigates also the impact of the limited simulation statistics on the result since the corresponding uncertainty is profiled in the fit by the Barlow-Beeston method as detailed in Sec. 5.4.
- In the top quark polarization measurement a lengthy procedure was required to obtain an optimal signal-enriched region during which the working point of a trained BDT was scanned while evaluating the impact of the systematic uncertainties on the result using pseudo-data (Sec. 6.7). In this measurement, the estimated scale factors reflect directly the amount of signal and background events after the event selection. Thus, performing an optimization for finding a signal-enriched region is not required.
- Residual differences in the background shapes may still be present in the signal region although their modeling has been validated extensively in control regions. Furthermore, the BDT itself may introduce a bias towards the SM prediction because only a sample of SM t -channel single-top-quark events is used for its training. In the multi-fit approach potential differences and biases are however profiled per bin of the measurement which thus mitigates their impact. On the other hand, problems in the modeling of a background process can be directly identified if a trend in its normalization is obtained as e.g. observed in the polarization measurement for the multijet yield in the electron channel (Sec. 6.6).

The results of the separate ML fits in bins of the top quark p_T and rapidity are presented in Fig. 7.12. The depicted binning scheme for both observables is introduced in Sec. 7.7

below. Overall, the estimated scale factors per process agree with each other within the shown statistical uncertainties of the fit. The only exception is the first top quark p_T bin where an undershoot of signal is observed with respect to the SM expectation.

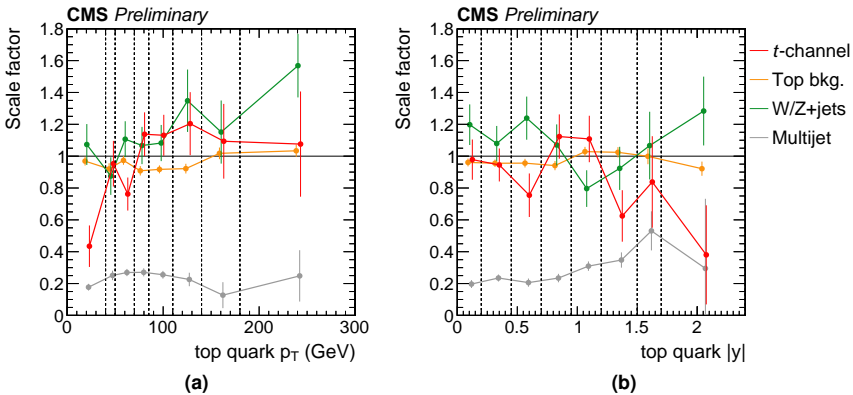


Figure 7.12. | Scale factors of the process yields with respect to their SM expectations as a function of the top quark (a) transverse momentum and (b) rapidity. The vertical bars denote the statistical uncertainties on the yields. For multijet events only the scale factors with respect to the normalization from the sideband region in the 2j1t region are shown. The dashed vertical lines mark the bin edges.

7.6. Validation

Before the unfolding is carried out the distributions of the top quark p_T and rapidity are validated. Figure 7.13 shows the corresponding distributions in a signal-depleted and in a signal-enriched phase space. These are defined by selecting events with either $\text{BDT} < 0$ or $\text{BDT} > 0.6$ respectively while in addition requiring only events with $m_{\text{T}}(\text{W}) > 50$ GeV to suppress contributions from multijet production. A good agreement is observed in the signal-depleted phase space for both observables within uncertainties. For the top quark rapidity distribution a good description of data by the templates is also observed in the signal-enriched region. The top quark p_T distribution in data displays however a somewhat harder spectrum compared to the expectation. In particular the prediction in the first p_T bin overestimates the observed amount of events in data which also confirms the result obtained from the separate ML fits presented in Fig. 7.12.

To cross check the background modeling further, the top quark p_T and rapidity distributions in the 3j1t $t\bar{t}$ control region are shown in Fig. 7.14. Good agreement between data and simulation is observed for both distributions. Since no significant deviations are observed for the background modeling, the unfolding is performed to infer the differential cross sections at parton level.

7.7. Unfolding

The results obtained from the ML fits are used to unfold the estimated distribution of t -channel single-top-quark events as a function of the top quark p_T and rapidity

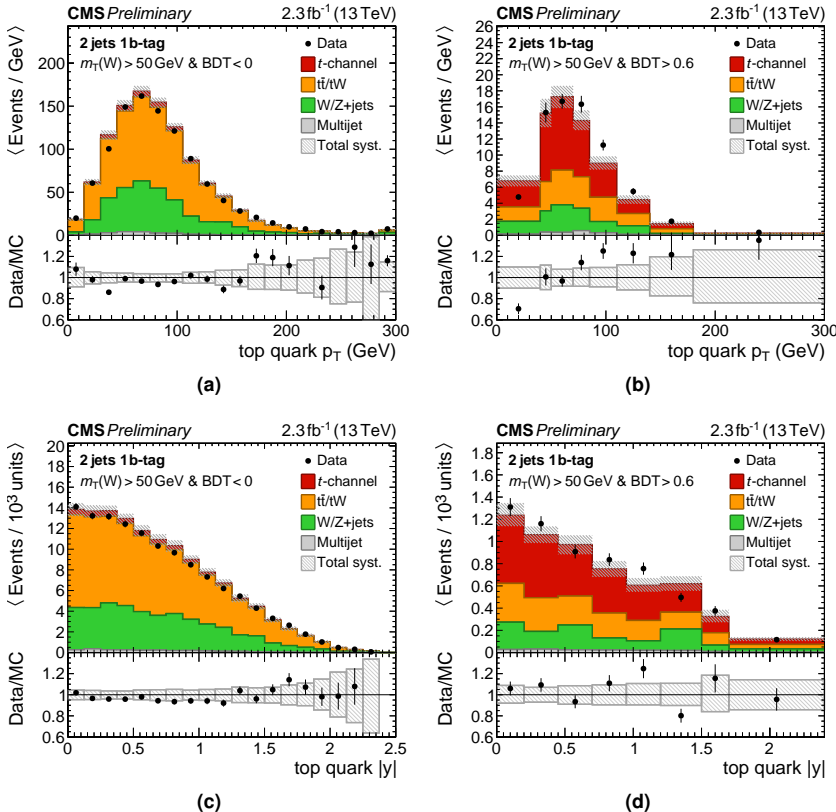


Figure 7.13. || Distributions of the (top row) top quark p_T and (bottom row) rapidity in (left column) a signal-depleted and (right-column) a signal-enriched phase space defined by $BDT < 0$ and $BDT > 0.6$ respectively after requiring only events with $m_T(W) > 50$ GeV to suppress contributions from multijet production. The hatched bands reflect the total systematic uncertainties. The figures are taken from Ref. [200].

to parton level using the TUnfold package. At reconstruction level the top quark p_T and rapidity are calculated from the summed 4-momenta of the selected b-tagged jet, muon and the reconstructed neutrino candidate. In particular the rapidity is calculated as $y = \frac{1}{2} \ln((E + p_z)/(E - p_z))$ without utilizing knowledge about the top quark mass from other measurements. At parton level the top quark is defined to be on-shell while its momentum is also affected by boosts of the event induced by the simulation of QCD/QED radiations and by an intrinsic k_T of the initial-state partons.

The migration of events between bins at reconstruction and parton level is studied to find the optimal binning scheme for the unfolding. For this the stability, S , and purity, P , defined as

$$S_i = \frac{\mathcal{R}_{ii}}{\sum_j \mathcal{R}_{ij}}, \quad P_j = \frac{\mathcal{R}_{jj}}{\sum_i \mathcal{R}_{ij}}, \quad (7.6.)$$

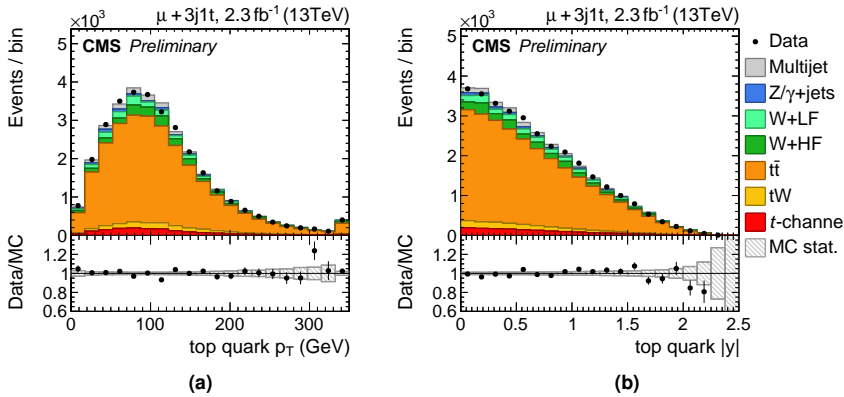


Figure 7.14. Distributions of the (a) top quark p_T and (b) rapidity in the 3j1t control region.

are calculated from the response matrix \mathcal{R} for various test-schemes. The stability denotes the amount of events generated in bin i which do not migrate into other bins at reconstruction level. The purity on the other hand denotes the amount of events which have been reconstructed in bin j but do not migrate into other bins at parton level. By choosing a suitable binning scheme for which both quantities are large (i.e. the migrations are low), less regularization has to be applied in the unfolding procedure. Hence, the procedure of finding such an optimized binning scheme is commonly considered as the first step for regularizing the ill-posed unfolding problem.

The final binning schemes chosen for the top quark p_T and rapidity at parton level are presented in Tab. 7.5 together with the calculated stabilities and purities per bin. Overall, both quantities are found to be above 50% with the exception of the purity in the last rapidity bin which amounts to only 41%. The corresponding response matrices are presented in Fig. 7.15. To stabilize the minimization procedure inside the TUnfold method, eight bins are chosen at reconstruction level whereas only four bins are considered at parton level.

Table 7.5. Stabilities and purities per bin of the top quark p_T and rapidity distributions at parton level.

Top quark p_T range	0–50 GeV	50–85 GeV	85–140 GeV	140–300 GeV
Stability	59%	61%	64%	75%
Purity	63%	62%	63%	64%
Top quark $ y $ range	0–0.45	0.45–0.95	0.95–1.50	1.50–2.40
Stability	63%	54%	61%	86%
Purity	84%	57%	51%	41%

The selection efficiencies for t -channel single-top-quark events at reconstruction level with respect to parton level for the chosen binning schemes are also studied. They are presented in Fig. 7.16 after certain event selection steps as indicated. The efficiencies in

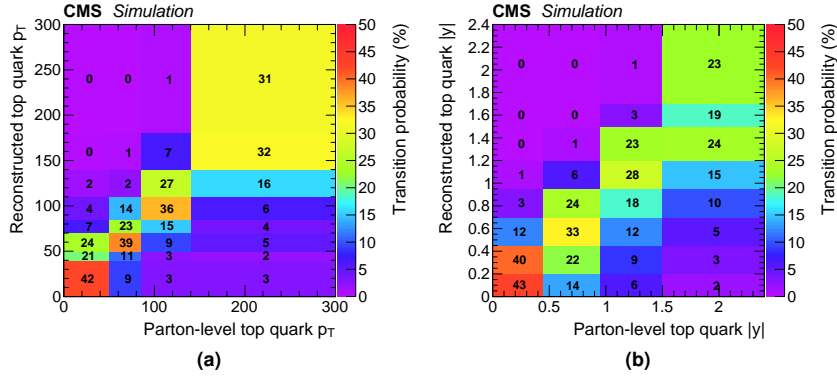


Figure 7.15. Response matrices for the top-quark (a) transverse momentum and (b) rapidity.

the first top quark p_T bin and in the last rapidity bin are found to be relatively small ($\approx 1\%$) compared to all other bins after selecting events in the 2j1t region that pass also $m_T(W) > 50$ GeV. Further optimization of the binning scheme at this stage would however degrade the obtained stability and purity and is therefore not envisaged.

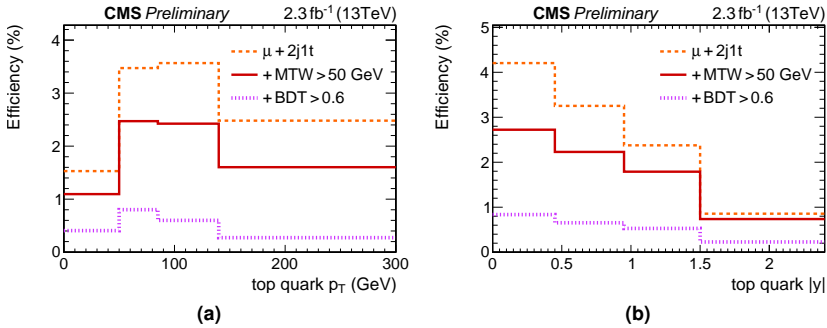


Figure 7.16. Selection efficiencies for the top-quark (a) transverse momentum and (b) rapidity after certain event selection steps.

7.8. Statistical evaluation

The measurement is affected by various sources of systematic uncertainties. For each source new templates are derived which reflect a systematic variation by one standard deviation. Those are then propagated through the fitting procedure, the BDT evaluation, and the unfolding. Special care is taken in the unfolding step since not only the templates can change under a systematic variation but also the response matrices themselves. To calculate the resulting differential cross section pseudo experiments are performed by dicing normal distributions per uncertainty source around the nominal spectrum. The resulting yields y_i^{total} per bin i can be expressed as

$$y_i^{\text{total}} = y_i^{\text{nominal}} + N(0, \mathcal{V}^{\text{stat.}})_i + \sum_j^{\text{sources}} N(0, \Delta_i^{\pm \text{syst.} j}), \quad (7.7.)$$

where N denotes the normal distribution, $\mathcal{V}^{\text{stat}}$ the covariance matrix of the statistical uncertainty, and $\Delta_i^{\pm \text{syst},j}$ the differences in yields between the shifted and nominal templates per systematic source j . From the distribution of the yields over many pseudo experiments, the central value of the differential cross section is taken to be the median and its uncertainty is quoted as the quantile corresponding to one standard deviation. In the following the considered sources of systematic uncertainties are briefly described.

Background composition In the ML fits the Z/γ^* +jets and tW templates are grouped together with the larger W +jets and $t\bar{t}$ templates respectively. To assess the impact of the assumed ratios on the measurement, their contributions to the fit templates are varied conservatively by $\pm 20\%$ independently.

Multijet template An uncertainty on the extract multijet template is taken into account by assessing the impact on the measurement when using two alternative templates derived from subregions in the muon isolation of either $[20\%; 40\%]$ or $[40\%; \infty]$ instead as detailed in Sec. 7.2.

Analysis objects A summary of the considered sources of systematic uncertainties related to the reconstruction and selection of analysis objects is provided in Sec. 4.10. This includes uncertainties on the jet energy scale and resolution, b-tagging and mistagging efficiencies, muon trigger, identification, and isolation efficiencies, and the pileup reweighting.

Signal and hadronization modeling The modeling of signal events generated with `MadGraph5_aMC@NLO` is assessed by comparing to the result obtained when using a sample generated with `POWHEG` instead. Additionally, a sample generated with `MadGraph5_aMC@NLO` interfaced with `Herwig` is used to assess the dependence of the result on the hadronization model.

Top quark mass Dedicated samples of t -channel, tW , and $t\bar{t}$ events are generated to account for a conservative uncertainty of 172.5 ± 1.0 GeV on the top quark mass.

Parton distribution function The uncertainty on the PDF is assessed by reweighting the simulated samples according to the 102 variations of the NNPDF3.0 set [37].

Renormalization and factorization scales The uncertainty on the renormalization scale is propagated to the result by performing a reweighting procedure of simulated $t\bar{t}$, tW , W +jets, and t -channel events according to the scale dependence of the corresponding matrix elements. Additionally, the factorization scale is varied by using dedicated samples. The final uncertainty is taken to be the envelope of varying both scales independently by a factor of two or one-half with respect to the nominal scale choice with the exception of extreme up/down combinations.

$t\bar{t}$ p_T reweighting The $t\bar{t}$ p_T reweighting has been applied by default in this measurement since it improves the agreement of the prediction with data at 13 TeV similar to Sec. 6.4. A corresponding uncertainty is assessed by rederiving the result without applying the reweighting.

The relative impact by some of the major sources of systematic uncertainties on the measurement are shown in Figs. 7.17a and 7.17b per top quark p_T and rapidity bin. The largest ones are the data statistics ($\approx 10\text{--}25\%$), the renormalization and factorization scale choice ($\approx 10\text{--}15\%$), the top quark mass ($\approx 5\text{--}20\%$), and the jet energy scale and

resolution ($\approx 5\text{--}15\%$). Especially the first top quark p_T bin is affected heavily by most uncertainties which is also related to the low acceptance of signal events in this particular bin as presented in Fig. 7.16a. Additionally, a large uncertainty in this bin is also expected from theory originating from differences between the predictions in the 4 or 5 FS as discussed in Sec. 2.5.

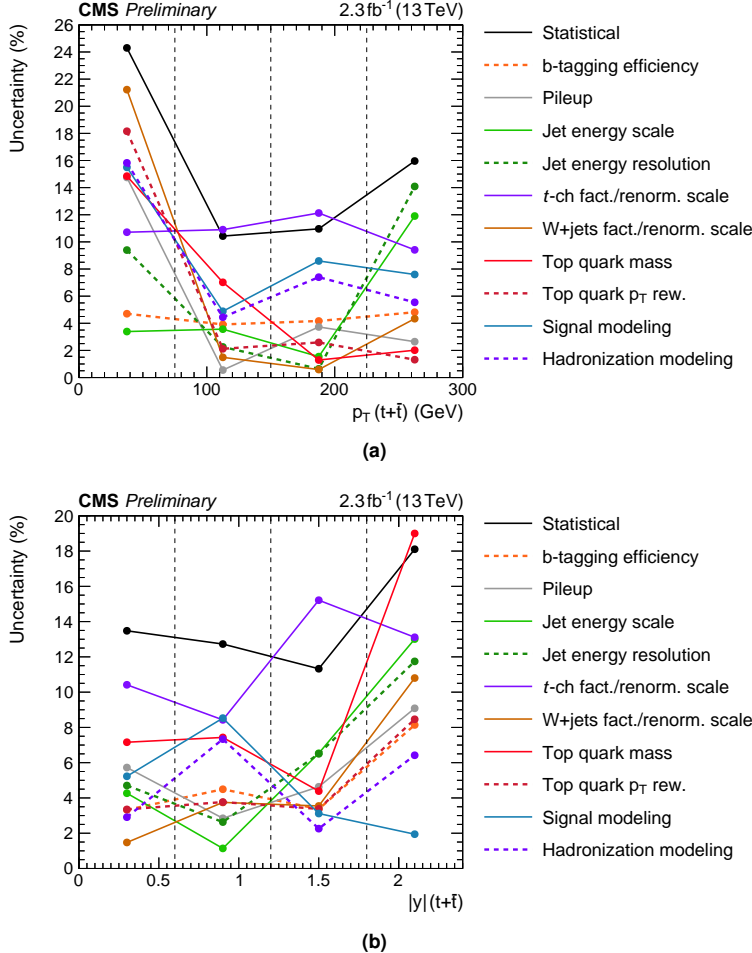


Figure 7.17. Relative impact on the yield for some of the largest systematic uncertainties on the measured (a) top quark p_T and (b) rapidity spectra. The dashed vertical lines mark the bin edges.

7.9. Results

The measured normalized differential cross sections as a function of the top quark p_T and rapidity are presented in Fig. 7.18. The spectra are compared to the SM predictions by MadGraph5_aMC@NLO interfaced with Pythia in 4 FS, POWHEG interfaced with Pythia in 4 FS, MadGraph5_aMC@NLO interfaced with Pythia in 5 FS, and MadGraph5_aMC@NLO

interfaced with Herwig in 4 FS. Overall the results agree with the predictions within uncertainties. In particular, the first top quark p_T bin is found to be affected by uncertainties at large leading to a total relative uncertainty of about $\pm 50\%$ which renders the observed deviation with respect to the predictions not very significant.

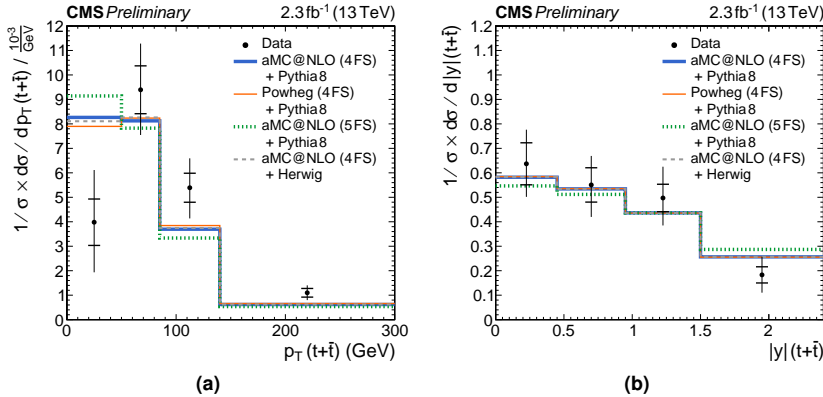


Figure 7.18. The measured normalized differential cross section of t -channel single-top-quark production as a function of the top quark (a) p_T and (b) rapidity. The statistical uncertainties are indicated by horizontal ticks on the error bars. The figures are taken from Ref. [200].

To cross check the result of the top quark p_T spectrum, the measurement has been repeated by fitting the distribution of the pseudorapidity of the spectator jet (Fig. 7.8b) instead of the BDT distribution. The resulting differential cross section is presented in Fig. 7.19. It confirms the obtained result within however larger uncertainties.

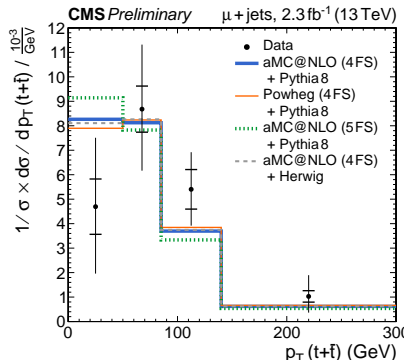


Figure 7.19. Cross check of the top quark p_T differential cross section result by fitting the pseudorapidity distribution of the spectator jet instead of the BDT discriminant. The statistical uncertainties are indicated by horizontal ticks on the error bars.

8.

Chapter

Prospects for differential t -channel measurements at 13 TeV

Improvements for future measurements of differential cross sections are investigated. These are showcased for an envisaged measurement of differential cross sections as a function of the top quark transverse momentum, rapidity, and polarization angle using 36 fb^{-1} of pp collision data recorded with the CMS experiment in 2016. First, the training of a new BDT discriminant for separating W+jets from $t\bar{t}$ events in the signal region is motivated. It enhances the sensitivity to the heavy-quark-flavor component of the W+jet background in the ML fit for which a control region can not easily be defined otherwise. Secondly, the requirements for measuring differential cross sections at particle level in addition to the parton level are discussed. Observables at particle level have the benefits of being closer to their reconstruction level counterparts resulting in lesser migrations and a higher acceptance compared to the parton level. A technical study of the most appropriate selection of event at particle level is detailed which has also been published in Ref. [205]. The chapter is concluded by presenting projections obtained with pseudo-data since the proposed measurement is currently being developed and thus data in the signal-enriched region has been blinded.

8.1. Setup

Prospects for measuring differential single-top-quark cross sections as a function of the top quark p_T , rapidity, and the polarization angle at parton and particle level are investigated in the following. The chosen analysis strategy is an extension of the one developed in the context of the measurement of differential cross section of single-top-quark-production in t channel at 13 TeV (Ch. 7). The setup of this study is briefly outlined in the following.

The data statistics for this study is increased compared to the first differential measurement at 13 TeV by using pp collision data recorded in 2016 with the CMS detector corresponding to 36 fb^{-1} . Events containing an isolated muon candidate and two or three jets are selected using mostly the same criteria as in Sec. 7.2, with a few exceptions as highlighted below. The threshold of the employed single muon trigger has been raised to 24 GeV because of the higher instantaneous luminosity, which peaked at 15.3 Hz/nb [78] in the 2016 data-taking period. Consequently, muon candidates with a higher threshold of $p_T > 26 \text{ GeV}$ are required offline. All other muon selection criteria are kept the same. The analysis of events containing single electrons and two or three jets is also explored. Corresponding data events are recorded with an electron trigger that requires an electron candidate with a transverse momentum of at least 32 GeV within $|\eta| < 2.1$. Offline, an electron candidate has to fulfill tight identification criteria [113]. Events must contain a corresponding tight electron candidate with

$p_T > 35$ GeV within the ECAL barrel region of $|\eta| < 1.479$.

For b-tagging a new algorithm, the so-called cMVA-tagger (combined MVA) [129], is employed which includes amongst other inputs the output of the previously used CSV algorithm in its training. At their corresponding tight working points both algorithms have a mistagging rate of only 0.1% for light-flavored jets originating from u,d,s quarks and gluons while an efficiency of about 55% is obtained for tagging true b jets with the cMVA-tagger, which is approximately 10% higher than the b-tagging efficiency of the CSV algorithm.

The remainder of the event selection is kept identical to Sec. 7.2 which includes the veto of events containing additional electrons or muons, the jet clustering, and the categorization of events into signal and control regions based on the number of selected jets and on the subset of jets which are also b-tagged.

The following samples of simulated events are used for this study. A sample of single-top-quark t -channel events has been generated with the POWHEG generator interfaced with Pythia8 and MadSpin. The POWHEG generator interfaced with Pythia8 is also used to generate events of tW single-top-quark and t \bar{t} production. Samples of W+jets and Z/ γ^* +jets events are generated with the MadGraph5_aMC@NLO generator interfaced with Pythia8. Exclusive W+jets samples with zero, one, or at least two extra partons are generated and merged with the FxFx procedure [150]. The cross sections for normalizing the employed samples are identical to the ones used in Ch. 7 and can be found in Tab. 7.2 with the exception of the exclusive W+jets cross sections which are listed in Tab. 8.1.

Table 8.1. || Theoretical SM cross sections at 13 TeV used to normalize the exclusive W+jets samples. The cross sections have been calculated at NLO with the MadGraph5_aMC@NLO generator.

Sample	Cross section
W $\rightarrow \ell\nu + 0$ partons	49670 pb
W $\rightarrow \ell\nu + 1$ parton	8264 pb
W $\rightarrow \ell\nu + \geq 2$ partons	2544 pb

The contamination by multijet events is estimated in muon and electron channel through templates extracted from data in a sideband region. In the muon channel the sideband region is defined by inverting the relative isolation as: $I_{\text{rel}}^\mu > 20\%$. In the electron channel the isolation requirement is part of the tight identification criteria. Thus a sideband region is defined in the electron channel by inverting loose electron identification criteria [113]. The resulting description of data by the multijet templates is validated in the 2j0t control region. In Fig. 8.1 the \cancel{E}_T distribution and the distribution of the difference in ϕ angles between the lepton and the transverse momentum vector are presented for both channels after scaling the templates to the result of a ML fit as detailed in Sec. 8.3. Both distributions display a good agreement between data and the predictions in the electron and muon channel respectively.

Distributions of the reconstructed top quark mass in the 2j1t signal region and in the 2j0t W+jets and 3j1t t \bar{t} control regions are presented in Fig. 8.2 for the muon and electron channel. A fair modeling is observed in both channels.

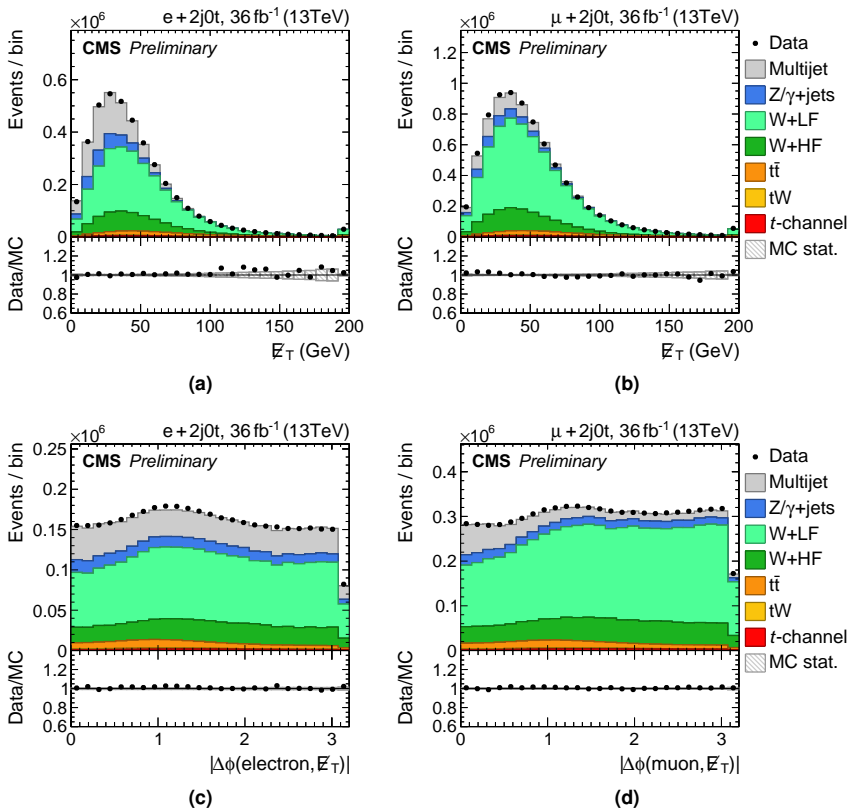


Figure 8.1. | Distributions of (top row) the transverse missing energy and (bottom row) the difference in ϕ angle between the lepton and the missing transverse energy in the 2j0t control region for (a) electron and (b) muon events.

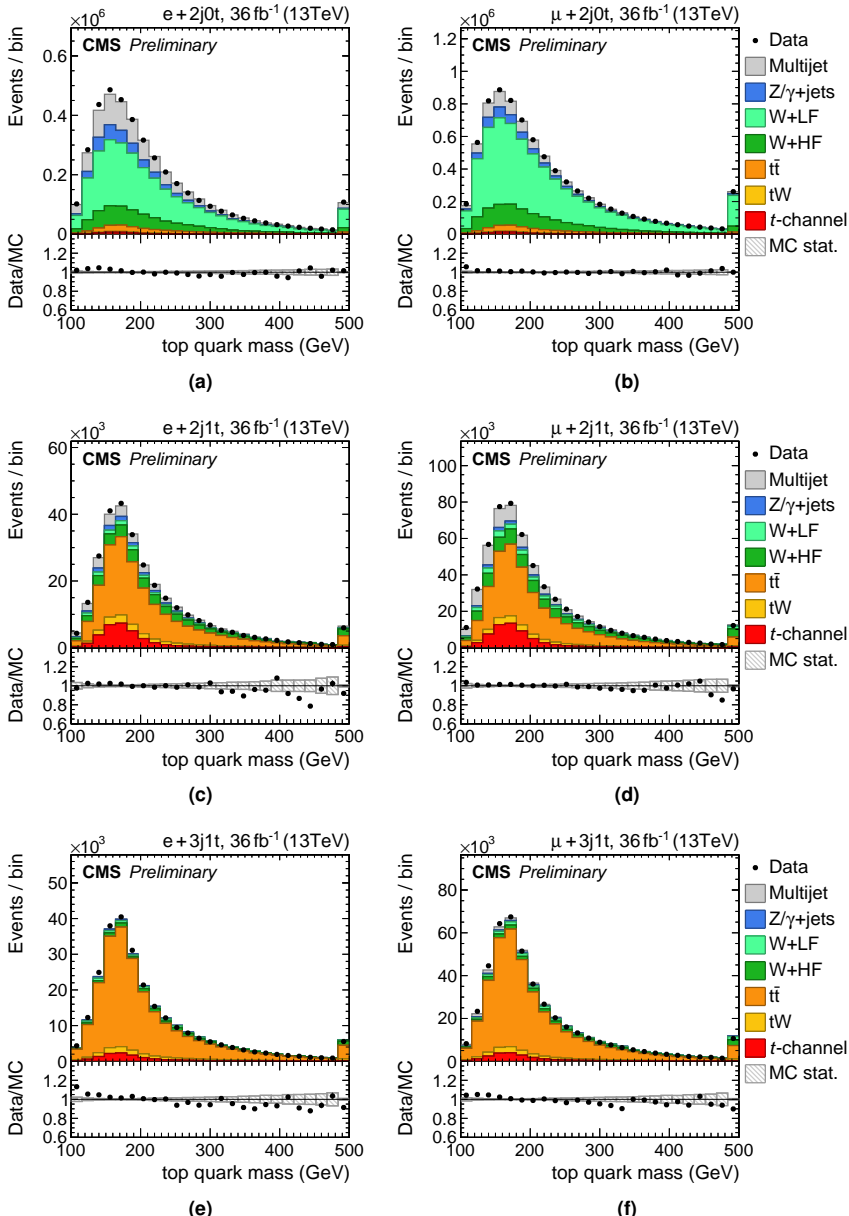


Figure 8.2. | Distributions of the reconstructed top quark mass for (left column) electron and (right column) muon channel: (top row) $W + \text{jets}$ control region; (middle row) signal region; (bottom row) $t\bar{t}$ control region.

8.2. New BDT discriminant

A shortcoming in the previous measurements within this thesis was the lack of a W+jets control region enriched by heavy-quark-flavored jets. Such a region would allow to validate the W+jets modeling in greater detail. Furthermore, including such a region in the ML fit may reduce the correlations between the estimated signal and background yields further. An approach to achieve this is to train an additional BDT, referenced BDT_{t̄t/W} in the following, for separating W+jets from t̄t events. Even observables which are correlated to the unfolding variables can be used safely in its training if the resulting discriminant is not used in a signal-enriched region for the measurement. The following observables have been chosen as input for the training:

- the invariant mass of the reconstructed top quark candidate;
- the missing transverse energy, \cancel{E}_T ;
- the transverse momentum of the dijet system, $(\vec{p}_b + \vec{p}_{j'})_T$;
- the event shape C (introduced in Sec. 7.4);
- the ΔR distance between the two jets;
- the ΔR distance between the b-tagged jet and the lepton;
- the invariant mass of the center-of-mass system; $\sqrt{s} = |p_{top} + p_{j'}|$;
- the W boson helicity angle, $\cos\theta_W^*$, defined between the top quark and lepton momentum in the W boson rest frame (see Sec. 2.1 for details);

The distribution of the W boson helicity angle is shown in Fig. 8.3. A good agreement between data and the prediction is observed in the muon and electron channel. The angle is reconstructed under the *t*-channel single-top-quark hypothesis but it might often overlap here with the proper angle for t̄t events in cases where the selected b-tagged jet and lepton originate from the decay of the same top quark in t̄t events. For W+jets events on the other hand this angle has no physical meaning. Hence its distribution provides separation power for discriminating t̄t against W+jets events in the BDT training.

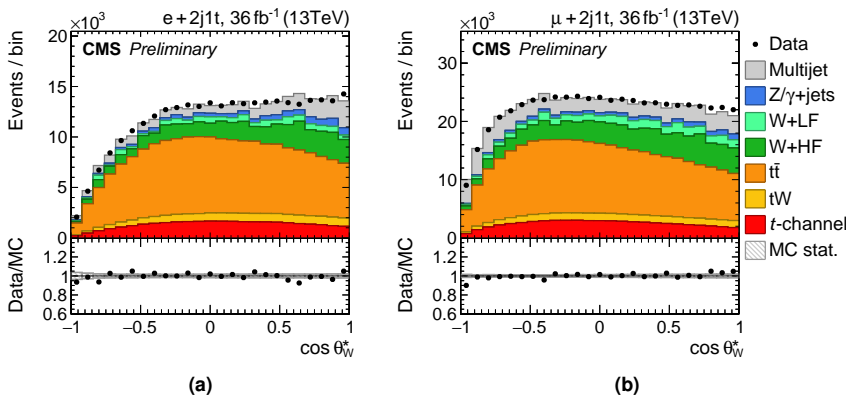


Figure 8.3. | Distributions of the W boson helicity angle in 2j1t region: (a) electron and (b) muon channel.

The new BDT is trained as follows. The AdaBoost algorithm is used with a learning rate of 0.2. The number of tested working points for node-splitting is set to 50. It has been found out that the discrimination power increases when allowing for a maximum tree depth of up to 5, compared to shallower trees for this particular classification problem. In total 1 000 trees have been trained. No sign of overtraining has been observed by checking the compatibility between the discriminant distributions from the training and testing samples.

The resulting $\text{BDT}_{\bar{t}t/W}$ discriminant is presented in Fig. 8.4 in a signal-depleted region. A fair description of data by the prediction is observed. An AUC of about 25% is obtained in both channels for separating $\bar{t}t$ from $W+\text{jets}$ events. Its distribution can be exploited to improve the sensitivity to the $W+\text{jets}$ yield in the ML fit.

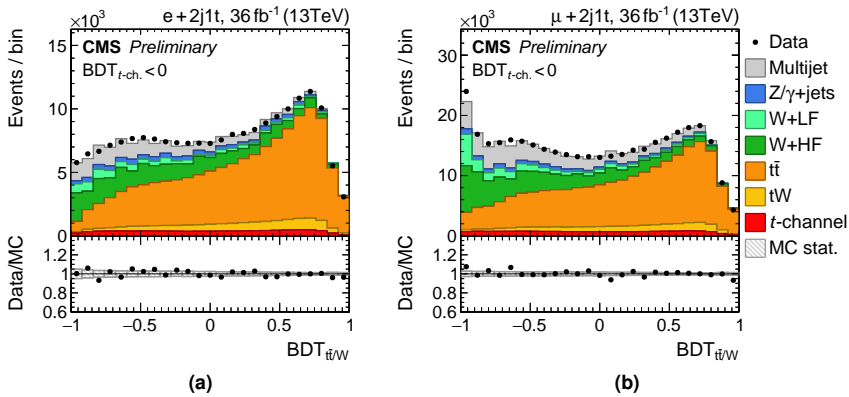


Figure 8.4. | Distributions of the $\text{BDT}_{\bar{t}t/W}$ discriminant, trained for separating $\bar{t}t$ from $W+\text{jets}$ events, in 2j1t (a) electron and (b) muon channel.

The signal-depleted region is defined by selecting events with $\text{BDT}_{t\text{-ch.}} < 0$ using the discriminant of a second BDT trained for separating signal from $W+\text{jets}$ and $\bar{t}t$ events. This second BDT, $\text{BDT}_{t\text{-ch.}}$, has been trained similar to the one used in Sec. 7.4. The distribution of its discriminant is shown in Fig. 8.5 for which a good agreement between data and simulation is obtained as well.

8.3. Signal extraction

The amount of signal is estimated by performing a template-based ML fit to data. The distributions of the transverse W boson mass and the two BDT discriminants are used to construct a compound template as follows. The $m_T(W)$ distribution as shown in Fig. 8.6a is used for events with $m_T(W) < 50$ GeV which provides sensitivity to the multijet event yield. The remaining events are split in two additional regions based on the $\text{BDT}_{t\text{-ch.}}$ discriminant. For event with $\text{BDT}_{t\text{-ch.}} < 0$ the $\text{BDT}_{\bar{t}t/W}$ distribution is fitted as presented in Fig. 8.6b which is sensitive to the $W+\text{jets}$ and $\bar{t}t$ yields while the amount of signal events is negligible in this region as shown in Fig. 8.4. Lastly, the $\text{BDT}_{t\text{-ch.}}$ distribution is used for the remainder of events that fall in the region defined by $\text{BDT}_{t\text{-ch.}} > 0$ and $m_T(W) > 50$ GeV. This region provides sensitivity to the amount of signal events which can be seen in Figs. 8.5 and 8.6c.

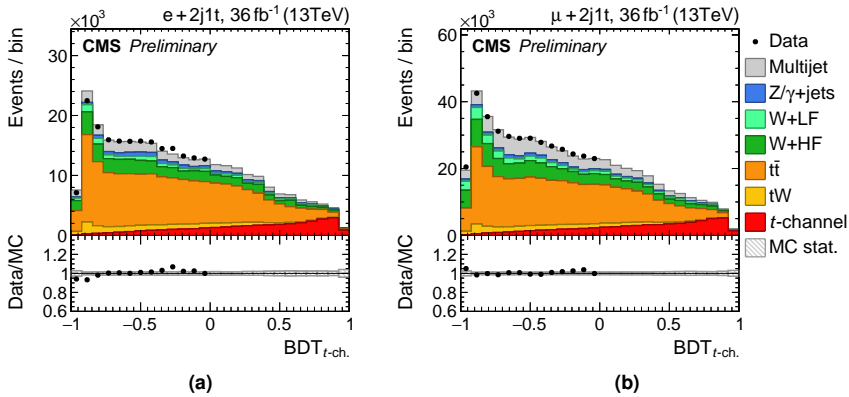


Figure 8.5. | Distributions of the $BDT_{t\text{-ch.}}$ discriminant, trained for separating signal from $t\bar{t}$ and W +jets events, in $2j1t$ (a) electron and (b) muon channel. The distribution of data has been blinded in the signal-enriched region defined by $BDT_{t\text{-ch.}} > 0$.

In addition to the $2j1t$ region, the two $t\bar{t}$ control region ($3j1t, 3j2t$) are fitted simultaneously as well. Similar to the strategy described in Sec. 7.5, multiple ML fits are performed to estimate the amount of signal events as a function of the top quark p_T , rapidity, and the polarization angle.

8.4. Particle level selection

Measuring differential cross sections at particle level has various benefits compared to the parton level as discussed in Sec. 5.5. In this section a technical study of the reconstruction and selection of analysis objects at particle level for t -channel single-top-quark production is described, which is also in Ref. [205].

In the following, comparisons of the shape, acceptance and the overlap between the parton and particle level with respect to the reconstruction level for simulated t -channel single-top-quark events are presented. The distribution of the transverse momentum of the muon at reconstruction level is shown in Fig. 8.7 after selecting events with one muon without any requirements on the number of jets. At particle level single-top-quark events are selected containing a dressed muon candidate with a transverse momentum of at least 26 GeV within $|\eta| < 2.4$ which follows the kinematic selection at reconstruction level. At parton level, events are only required to possess a muon from a top quark decay without applying any kinematic constraints. In the top panel of Fig. 8.7 the overlap of common events selected at parton or particle level which are also selected at reconstruction level is shown. The bottom panel displays the corresponding acceptance of selecting parton/particle-level events at reconstruction level. A large overlap ($> 99\%$) between all three distributions is observed which demonstrates that nearly all events that are selected at reconstruction level can also be found at the particle and parton level. It should be noted that if muons from intermediate prompt tau leptons are excluded from the dressed lepton definition this overlap reduces to about 94% instead. One can observe that the acceptance increases towards higher muon momenta, which is a consequence of the muon isolation and identification

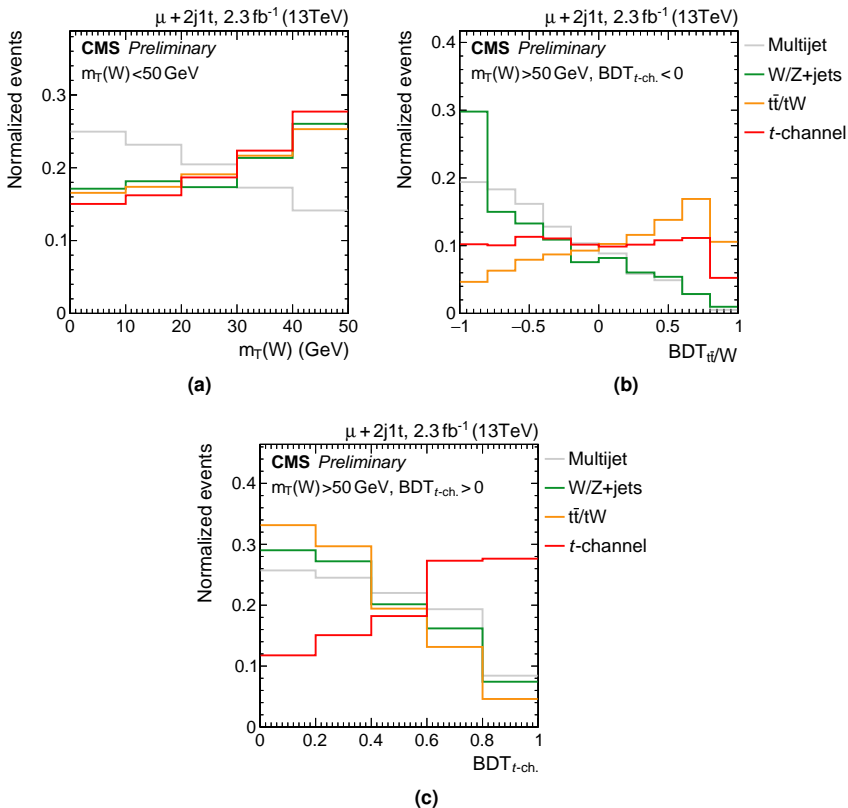


Figure 8.6. | Shape comparison of the fit components in 2j0t: (a) transverse W boson mass; (b) $BDT_{t\bar{t}/W}$ discriminant trained to separate $t\bar{t}$ from $W+jets$ events; (c) $BDT_{t\text{-ch.}}$ discriminant trained to separate signal from $t\bar{t}$ and $W+jets$ events.

requirements at reconstruction level that become less stringent.

Jets at particle level are clustered from stable particles excluding neutrinos and the prompt leptons and photons used in the dressed lepton reconstruction. Resulting jets with a transverse momentum of at least 40 GeV within $|\eta| < 4.7$ are selected. The amount of selected jets for events passing the muon selection step is shown in Fig. 8.8a. At reconstruction level, events with at least two jets are shown while no requirement on the number of jets is made at particle level. When selecting events with exactly two jets at reconstruction and particle level simultaneously, the amount of events at reconstruction level overlapping with the selected events at particle level reduces to about 80%. The remaining 20% of events at reconstruction level have not been selected at particle level due to the broad jet energy resolution leading to a migration of events into either the first or the third jet bin at particle level.

The number of b-tagged jets is shown in Fig. 8.8a after requiring exactly two jets in the event at particle and reconstruction level. At the particle level, the number of b-tagged jets is counted with the ghost-B-hadron method [179]. The distribution reveals that a

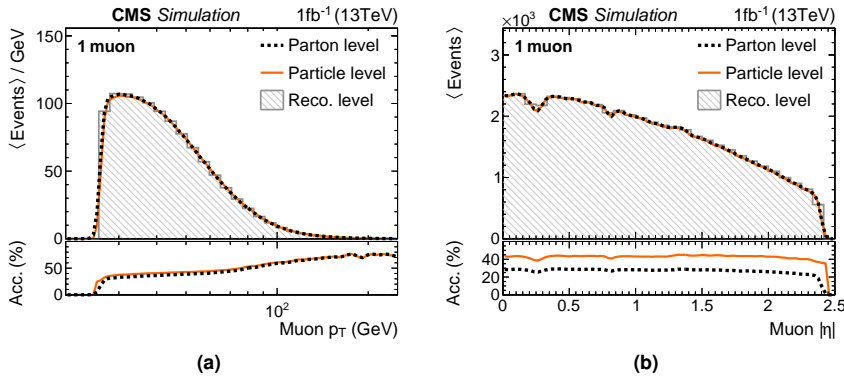


Figure 8.7. | Distributions of the transverse muon momentum after requiring events with one muon at reconstruction, particle, or parton level. No requirement on the number of jets is made. Top panel: common events selected at reconstruction level; bottom panel: acceptance of reconstruction level selection. The figures are taken from Ref. [205].

certain fraction of events has two ghost-b-tagged jets although events with only one b-tagged jet are selected at reconstruction level. This is a consequence of the ghost-B-hadron method which has a relatively high efficiency for tagging true b jets compared to the employed cMVA algorithm at reconstruction level. Selecting events with only one b-tagged jet at the particle level results in a degradation in the overlap to about 70% which is considered a non-negligible loss. Thus, in this study no requirement on the number of b-tagged jets is imposed. This simplification leads to a jet assignment problem for the pseudo-top-quark definition which is solved by associating the jet that yields an invariant pseudo-top-quark mass (together with the muon and neutrino candidate) which is closest to 172.5 GeV.

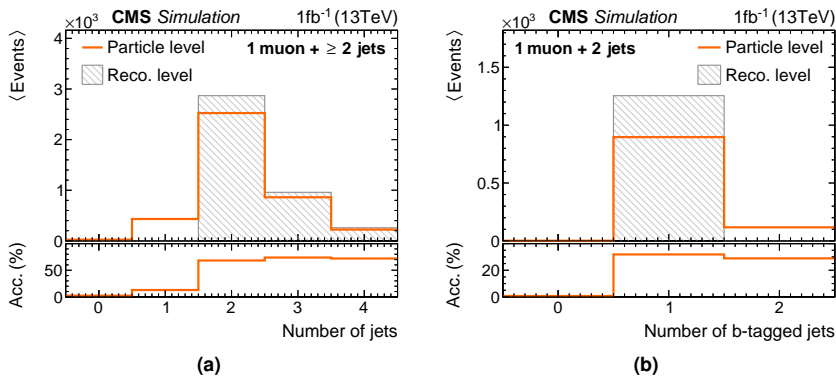


Figure 8.8. | Distributions of the number of jets (left) for events with at least two selected jets at reconstruction level and number of b-tagged jets (right) for events with two selected jets at reconstruction and particle level. Top panels: common events selected at reconstruction level; bottom panels: acceptance of reconstruction level selection. The figures are taken from Ref. [205].

The distributions of the p_T and pseudorapidity of the (un-tagged) jet originating from

the spectator quark are shown in Fig. 8.9. At particle level, it is the jet which is not associated to the pseudo-top-quark decay by the invariant mass criterion. The observed turn-on in the p_T distribution confirms that the drop in the overlap between reconstruction and particle level from > 99% after the muon selection step down to 80% after requiring also two jets in the events is attributed to the jet energy resolution. The overlap can be increased by lowering the transverse momentum threshold of jets at particle level which has however not been studied further in the context of this study.

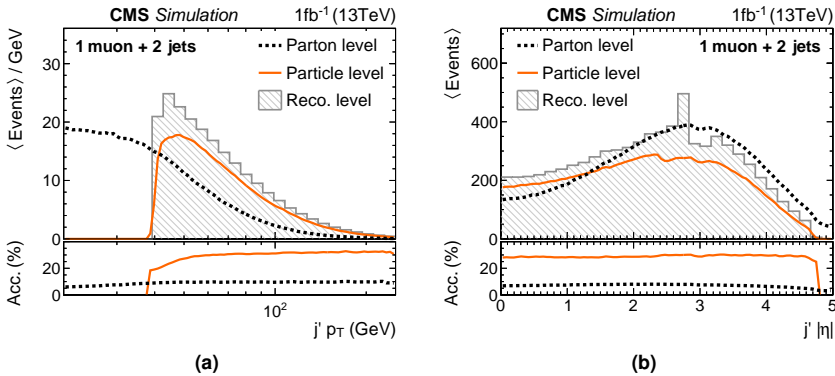


Figure 8.9. | Distributions of the spectator jet: (left) transverse momentum; (right) absolute value of the pseudorapidity. Top panels: common events selected at reconstruction level; bottom panels: acceptance of reconstruction level selection. The figures are taken from Ref. [205].

Lastly, the distribution of the top quark polarization angle is shown in Fig. 8.10. Its definition requires the full reconstruction and assignment of analysis objects to the t -channel single-top-quark signature. It is calculated as the angle between the lepton and the spectator jet in the top quark rest-frame. The drop at $\cos\theta_\ell^* \rightarrow 1$ occurs mainly due to the applied p_T threshold on the selected lepton as detailed in Sec. 5.5. The drop vanishes in the inclusive phase space at parton level. Hence, measuring the polarization angle at the particle level would particularly benefit from the reduced extrapolation to the fiducial phase space.

8.5. Unfolding and results

The unfolding to particle and parton level is demonstrated for pseudo-data only since the analysis has been blinded. The concept of blinding had been applied in the polarization measurement as well and is described in Sec. 6.2.

Distributions of pseudo-data for the $m_T(W)$, and the $BDT_{t\bar{t}/W}$ and $BDT_{t\text{-ch}}$ discriminants are generated from the simulated samples and the multijet template. In addition a random Poisson fluctuation corresponding to the expected number of data events is applied per bin. The distributions are obtained in six independent intervals per top quark p_T , rapidity, or polarization angle. The fitting procedure of Sec. 7.5 is applied, and the estimated signal scale factors are passed to the unfolding procedure. Response matrices for unfolding to parton or particle level are constructed from simulated t -channel single-top-quark events. The obtained matrices in the muon channel

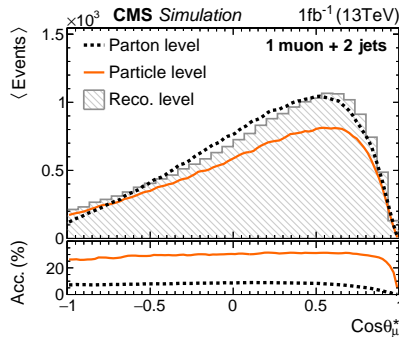


Figure 8.10. | Distribution of the top quark polarization angle. Top panel: common events selected at reconstruction level; bottom panel: acceptance of reconstruction level selection. The figure is taken from Ref. [205].

are presented in Fig. 8.11. The migrations between bins are significantly reduced when unfolding to particle level compared to parton level as particularly visible for the polarization angle.

The resulting unfolded spectra in muon channel for the generated and fitted pseudo-data are presented in Fig. 8.12. The indicated vertical bars reflect the expected statistical uncertainty on the estimated signal scale factor which has been propagated through the unfolding. Comparing the spectra obtained at particle and parton level side-by-side, one can observe that the uncertainties in certain bins are largely increased at parton level compared to particle level as a result of a low selection efficiency in those bins. This is very significant in particular for the first and last bin in the distribution of the top quark polarization angle. Thus, measuring differential cross sections at particle level as a function of these observables is clearly beneficial compared to parton level in terms of precision.

8.6. Summary of improvements

Potential extensions of the employed analysis strategies in this thesis for future differential single-top-quark cross section measurements and their benefits are summarized in the following.

An additional BDT has been proposed to separate between the two main backgrounds, $W+jets$ and $t\bar{t}$, in the 2j1t signal region. Since it is evaluated in a signal-depleted region only, observables correlated to the unfolding variables can be safely used in its training without introducing a potential bias on signal events. The resulting discriminant with an AUC of about 25% provides additional sensitivity to the $W+heavy-quark-flavor$ yield in the ML fit.

The technical requirements for unfolding to particle level have been investigated as well. A suitable selection of events by requiring one dressed lepton and two jets without employing b-tagging at particle level has been devised which yields an overlap of about 80% with the reconstruction level. The missing 20% of events can be attributed to the jet energy resolution. Unfolding of pseudo-data showed that the reduced migration and higher acceptance of events results in an enhanced precision at particle level.

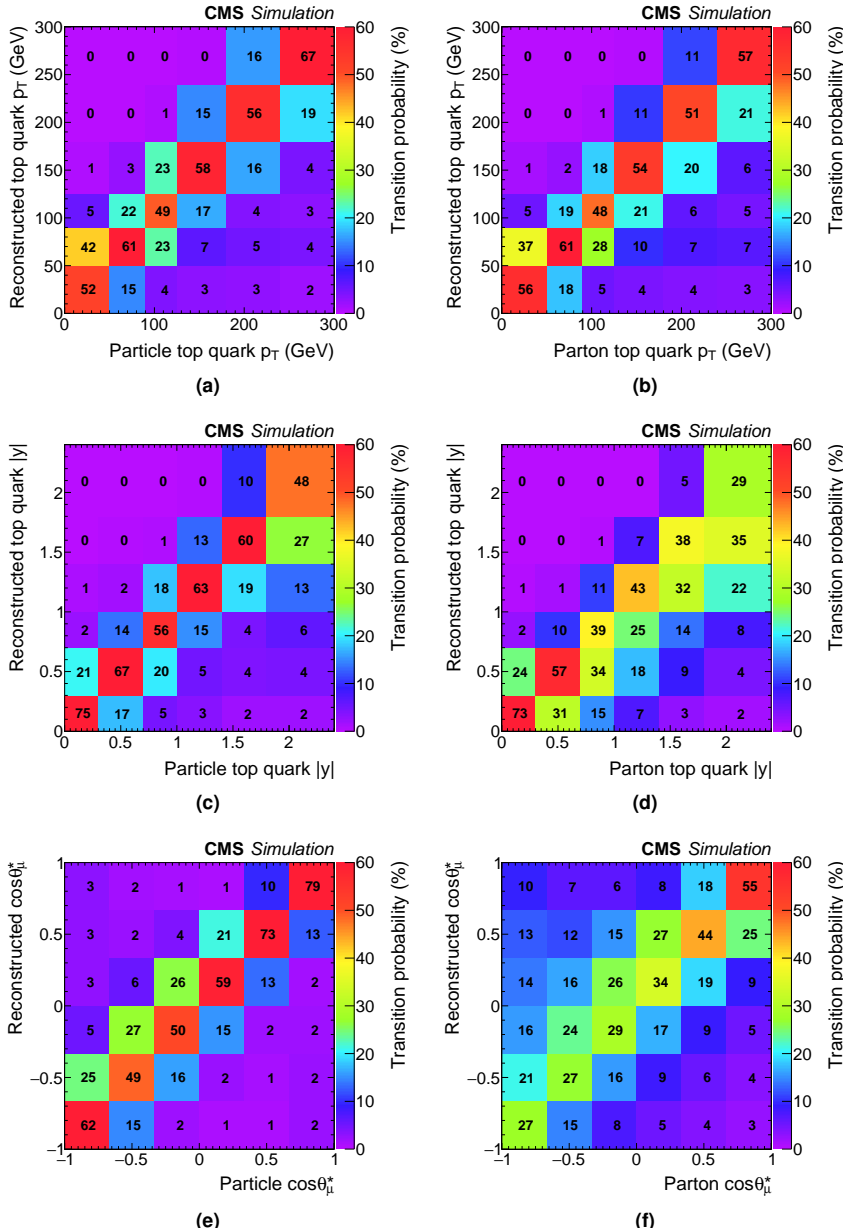


Figure 8.11. Response matrices in muon channel for (left column) particle level and (right column) parton level: (top row) top quark p_T ; (middle row) top quark rapidity; (bottom row) top quark polarization angle.

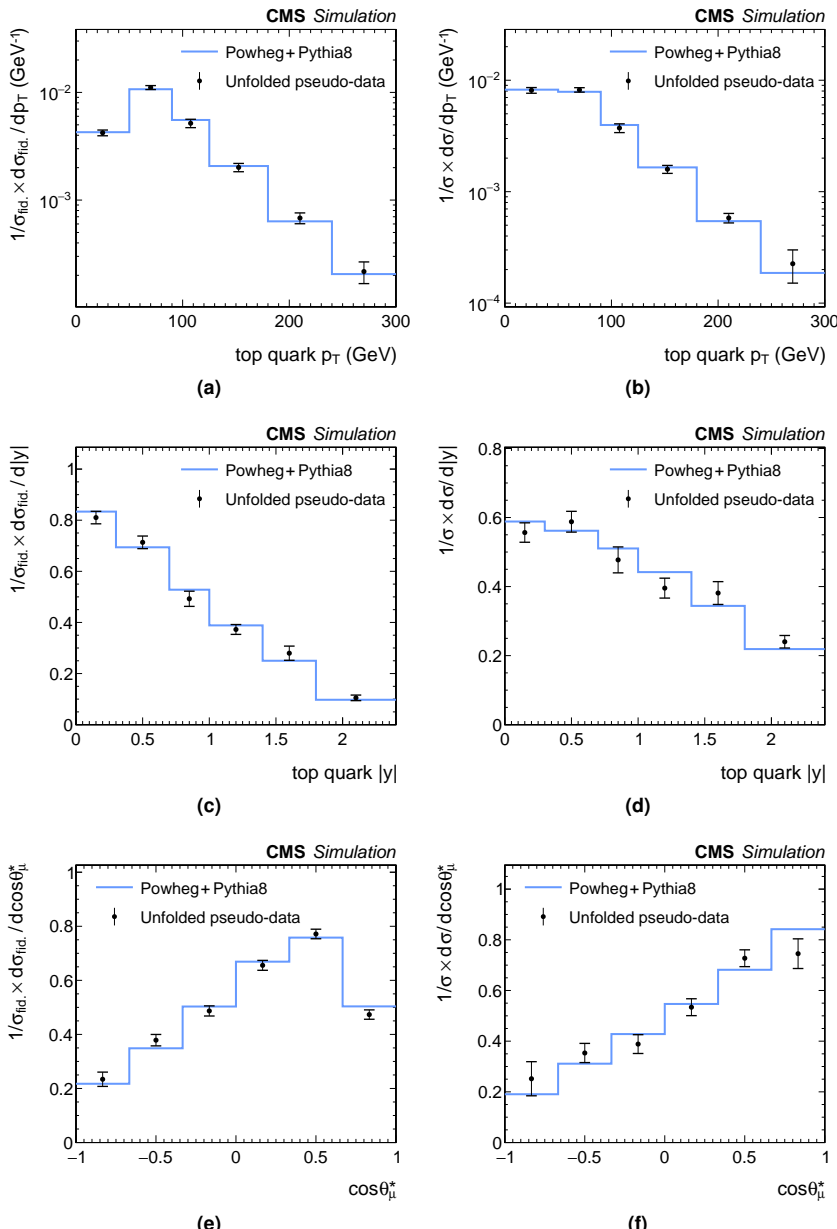


Figure 8.12. Unfolded distributions using pseudo-data in muon channel for (left column) particle level and (right column) parton level: (top row) top quark p_T ; (middle row) top quark rapidity; (bottom row) top quark polarization angle. The vertical bar indicates the expected statistical uncertainty as propagated from the ML fits.

Conclusion

In this thesis, measurements of differential single-top-quark cross sections have been presented based on proton-proton collision data recorded with the CMS experiment at center-of-mass energies of 8 and 13 TeV.

In t -channel single-top-quark production the electroweak V-A coupling structure predicts the production of highly polarized top quarks. The degree of polarization is studied for the first time by measuring the cross section as a function of the polarization angle, defined as the angle between the charged lepton from the top quark decay and a spectator quark which is produced in association with the single top quark. The measurement is based on 8 TeV collision data corresponding to 19.7 fb^{-1} . Events with an isolated muon and two or three jets have been selected for the measurement while events containing single electrons have been studied as a cross check. The large contamination by events stemming from background processes necessitated the usage of two boosted decision trees. Their discriminants are used to estimate the amount of background events from data and to select data events in a signal-enriched phase space. The differential cross section is inferred at parton level through a regularized unfolding procedure from the distribution of the polarization angle in data after the remaining background contributions have been subtracted. The top quark spin asymmetry, a quantity related to the polarization, is extracted from the differential cross section through a linear fit. It is measured to be 0.26 ± 0.11 which is compatible within 2.0 standard deviation with the expected SM spin asymmetry of 0.44 at NLO. The measurement has been published in Ref. [61]. In a further step, the derivation of limits on anomalous couplings and the top quark polarization has been illustrated using the measured asymmetry and related results from the literature.

The first measurement of differential single-top-quark cross sections at 13 TeV as a function of the top quark transverse momentum and rapidity has been performed as well. Events containing an isolated muon candidate and two or three jets have been selected from the first data recorded in 2015 at the new center-of-mass energy corresponding to 2.3 fb^{-1} . A novel fitting strategy has been developed which allows to extract the amount of signal events as a function of the unfolding observables by performing multiple fits to the distributions of the transverse W boson mass and a BDT discriminant. The procedure does not require a signal-enriched region and neither is a subtraction of background contributions from the data distributions necessary before unfolding. The differential cross sections at parton level are instead inferred from the estimated signal yields through unfolding directly. The results are compared to the predictions by various event generator programs. No significant deviation has been observed. The measurement has been published in Ref. [200].

Lastly, various improvements for further measurements of differential single-top-quark cross sections at 13 TeV have been studied using 36 fb^{-1} of data recorded in 2016. In

particular, the benefits for measuring differential cross sections at particle level have been investigated for which reduced migrations and a larger acceptance compared to the parton level are obtained which allows to achieve results with enhanced precision in the future. A related study has been published in Ref. [205].

Acknowledgments

I like to thank all the people with whom I had the pleasure of interacting with during my PhD at CP3, CERN, or on conferences.

A big thanks goes to Andrea Giammanco for his scientific guidance, availability, constructive feedbacks, and his open and friendly attitude. In particular I enjoyed the given freedom to peruse my interests and ideas in single-top-quark physics. I like to thank also my PhD committee members, Freya Blekman, Vincent Lemaitre, Fabio Maltoni, and Andreas Meyer for agreeing to be in my jury and for their friendly input and suggestions.

Furthermore, I like to say thanks to my colleagues, the “The Offbeat Physicists” team, Georgios Krintiras, Hamed Bakhshiansohi, Abideh “Nadjieh” Jafari, Pieter David, and Andrey Popov with whom I had a lot of fun discussing about physics and life during my PhD.

For the successful collaboration on the top quark polarization measurement I like to thank Andres Tiko and Joosep Pata for all the hard work which condensed into the published paper.

I also like to express by gratitude to the CMS (single) top conveners, Rebeca Gonzalez Suarez, Alberto Orso Maria Iorio, Abideh “Nadjieh” Jafari, Jeremy Andrea, Thorsten Chwalek, Andreas Meyer, Andrea Giammanco, and Pedro da Silva. It was a pleasure contributing to the single-top-quark efforts of CMS in the friendly and welcoming atmosphere you created.

I like to give my thanks also to Sezen Sekmen and Lukas Vanelderen for the great collaboration and fun we had while developing the CMS “Fast Simulation” package.

At CP3 I thank Carinne Mertens and Ginette Tabordon for their support when dealing with bureaucracy and travel reimbursements. I like to thank also Jérôme de Favereau and Pavel Demin for their constant efforts to keep the IT infrastructure working and who always helped in fixing my grid/cluster/storage problems.

During my PhD studies I was a recipient of the FRIA scholarship by Fonds de la Recherche Scientifique, Belgium. I am grateful to the committee for awarding me the scholarship.

Finally, I like to thank my parents, sister, and friends in Germany for supporting me from far away.

Acronyms

- 2HDM** Two Higgs doublet model 33
- AdaBoost** A boosting procedure for BDTs 76, 123, 124, 142
- ALICE** A Large Ion Collider Experiment; particle detector at the LHC 43, 44
- aMC@NLO** An event generator 70, 89, 109, 110
- APD** Avalanche photodetector 48
- A_{eff}^ρ** Particle isolation based on effective areas 60, 61, 88
- ATLAS** General purpose particle detector at the LHC 10, 16, 37, 42, 43, 44
- AUC** Area under (ROC) curve 76, 77, 94, 124, 142, 147
- Barlow-Beeston** Barlow-Beeston (method); a procedure to account for limited simulation statistics in ML fits 78, 129
- BCMS** Batch compression merging and splitting scheme; bunch forming scheme for the LHC 43
- BDT** Boosted decision tree 69, 74, 76, 77, 87, 89–91, 93–96, 99–107, 115, 116, 118, 119, 123–131, 133, 136, 137, 141–144, 146, 147, 151, 155, 156
- BPX** Barrel pixel modules of CMS 46
- BSM** Beyond the standard model 9, 23, 26, 28, 29, 33–35
- BU** Builder unit; assembles an event from multiple RUs 52
- c.m.** Center-of-mass 7, 8, 26–30, 36, 37, 41, 42, 63, 87, 115, 116, 141, 151
- CDF** Former particle detector at the Tevatron, Fermilab, USA 7, 23
- CERN** European Organization for Nuclear Research at Geneva; Switzerland 7, 13, 18, 41, 42, 44, 51, 52
- CHS** Charged hadron subtraction (method); a pileup mitigation procedure for jets 61, 88, 117
- CKM** Cabibbo-Kobayashi-Maskawa (matrix); quark mixing matrix of the SM 7, 17, 23, 24, 29, 35, 36, 38
- CL** Exclusion limit 9, 10, 36, 112
- CMS** Compact Muon Solenoid; general purpose particle detector at the LHC 7, 8, 10, 16, 28, 36, 37, 41, 42, 43, 44, 45, 47, 49–53, 56, 57, 64–67, 69, 88, 115, 116, 137, 151, 155, 156, 158, 159
- CMSSW** CMS software; framework and software package for CMS 52
- cMVA** Combined MVA; b-tagging algorithm 65, 138, 145
- CompHEP** An event generator 71, 89, 106, 110
- CP** Charge-parity; usually in the context of invariance or violation under this transformation 26, 31, 44
- CSC** Cathode strip chamber; part of the muon system of CMS 50, 51, 52, 55, 56
- CSV** Combined secondary vertex; b-tagging algorithm 65, 88, 90, 117, 138
- CTF** Combinatorial track finder 55
- DØ** Former particle detector at the Tevatron, Fermilab, USA 7, 23
- DA** Deterministic annealing; an optimization algorithm 57

$\Delta\beta$	Particle isolation based on delta-beta correction	59, 88, 116, 117
DR	Diagram removal; a scheme to define tW single-top-quark production at NLO	28
DS	Diagram subtraction; a scheme to define tW single-top-quark production at NLO	28
DT	Drift tube; part of the muon system of CMS	50, 51, 52, 55, 56, 59
ECAL	Electromagnetic calorimeter of CMS	47, 48, 52, 56–58, 60, 61, 88, 138
EFT	Effective field theory	23, 34, 107, 158
EM	Electromagnetic	59, 60, 62, 71
ES	Electromagnetic preshower of CMS	48, 58
EWK	Electroweak (theory)	14
FED	Front end driver; reads out the frontend detector electronics of CMS	52, 158
FEWZ	A program for calculating cross sections for fully exclusive W and Z boson production	90, 118
FPGA	Field-programmable gate array	51
FPX	Forward pixel modules of CMS	46
FS	Flavor scheme; the number of considered quark flavors in the proton PDF	32, 33, 34, 79, 80, 89, 109, 117, 135, 136
FSR	Final state radiation	30, 70, 81
FU	Filter unit; runs the HLTrigger algorithms	52
FxFx	A matching/merging procedure for simulated event samples	71, 138
GCT	Global calorimeter trigger	52
Geant	A toolkit for simulating interactions of particles with matter	69
GMT	Global muon trigger	52
GradientBoost	A boosting procedure for BDIs	76, 91, 93, 123, 124
GSF	Gaussian sum filter; a special tracking algorithm for electrons	56, 58, 60
GT	Global trigger	52
h.c.	Hermitian conjugate	
HATHOR	A program for calculating top quark production cross sections	29, 118
HB	Hadron barrel calorimeter of CMS	48, 49, 50
HCAL	Hadron calorimeter of CMS	48, 49, 52, 57–59, 159
HE	Hadron endcap calorimeter of CMS	48, 49, 50
HEP	High energy physics	
Herwig	An event generator and parton shower simulation program	71, 117, 134, 136
HF	Hadron forward calorimeter of CMS	49, 50, 58, 67
HFS	Hadronic final-state system	94
HLT	High level trigger	51, 52, 156
HO	Hadron outer calorimeter of CMS	49
HPD	Hybrid photodiode	48
IP	Interaction point	41, 42–45, 47, 49
ISR	Initial state radiation	30, 70, 80
JEC	Jet energy correction	62, 63, 66, 88, 100, 108
JER	Jet energy resolution	62, 63, 88, 100, 108
KEK	High Energy Accelerator Research Organization in Tsukuba; Ibaraki; Japan	18
KF	Kalman filter	55, 56
L1	Level 1 trigger	51, 52
LEP	Large Electron-Positron Collider	41

- LHAPDF** A library for interfacing with various PDF sets **19, 110**
- LHC** Large Hadron Collider **7, 8, 18, 24, 26, 39, 41, 42–44, 50, 51, 67, 155, 157, 158**
- LHCb** Large Hadron Collider beauty; particle detector at the LHC **18, 43, 44**
- LHCf** Large Hadron Collider forward; particle detector at the LHC **44**
- LO** Leading order **21, 25–33, 70, 71, 98, 101, 109, 120, 122**
- LS1** First long shutdown of the LHC (2013–2014) **42**
- MadGraph** An event generator **70, 89, 97, 98, 101, 120, 122, 123**
- MadGraph5_aMC@NLO** An event generator **70, 71, 75, 98, 117–120, 122, 123, 134, 135, 138**
- MadSpin** A program for simulating the decay of narrow resonances **71, 79–81, 138**
- MC** Monte-Carlo **69, 78, 103, 107, 108, 115**
- MCFM** A program for calculating cross sections at hadron colliders **90**
- MC@NLO** A matching/merging procedure for simulated event samples **70, 118**
- ME** Matrix element **20, 69–71, 89, 109, 134**
- Minuit** A minimization algorithm **79**
- ML** Maximum-likelihood (fit) **69, 77, 87, 89–91, 99, 101–103, 107–109, 115, 118, 119, 124, 125, 128–130, 134, 137, 138, 141–143, 147, 149, 155, 158**
- MLM** A matching/merging procedure for simulated event samples **70, 71, 89, 109**
- MoEDAL** Particle detector at the LHC **44**
- MS** Modified minimal subtraction scheme; a renormalization scheme commonly used to define the quark masses **10**
- MSSM** Minimal super symmetric standard model **33**
- MVA** Multivariate analysis (technique) **65, 74, 88, 125, 155**
- NbTi** Niobium-titanium; a superconducting alloy **41, 45**
- ndof** Number of degrees of freedom **55, 59**
- NLO** Next-to-leading order **21, 26, 28–34, 36, 70, 71, 80, 90, 98, 118, 119, 122, 138, 151**
- NNLL** Next-to-next-to-leading logarithmic order **36**
- NNLO** Next-to-next-to-leading order **19, 21, 25, 27, 36, 90, 99, 118**
- OPE** Operator product expansion **34**
- PDF** Parton distribution function; probability densities describing the content of a proton **18, 19, 20, 26–29, 32, 33, 108–110, 134, 156, 157**
- PF** Particle flow; a global event reconstruction algorithm **53, 57, 58, 60–62, 66, 68, 88, 94, 117**
- Photos** A program for accounting for QED corrections in Z/W boson decays **71**
- PMT** Photomultiplier tube **49**
- POWHEG** An event generator **71, 79–81, 89, 109–111, 117, 123, 134, 135, 138**
- pp** Proton-proton (collisions) **41–44, 53, 56–60, 67, 68, 87, 115, 116, 137, 151**
- PS** Proton Synchrotron **43**
- PS** Parton shower **69, 70, 71, 109**
- PSB** Proton Synchrotron Booster **43**

- PU** Pileup; number of additional interactions per bunch crossing **42**, **59**, **60**, **66**, **68**
- Pythia** An event generator and parton shower simulation program **71**, **79–81**, **89**, **109**, **117**, **120**, **135**, **138**
- QCD** Quantum chromodynamics **17**, **18**, **19**, **29**, **79–81**, **131**
- QED** Quantum electrodynamics **12**, **71**, **79–81**, **131**, **157**
- QFT** Quantum field theory **9**, **11**
- RCT** Regional calorimeter trigger **52**
- ROC** Receiver operating characteristic (curve) **76**, **77**, **124**, **155**
- RPC** Resistive plate chamber; part of the muon system of CMS **50**, **51**, **52**, **55**, **56**
- RU** Readout unit; collects event fragments from the FEDs **52**, **155**
- Run 1** Run 1 of the LHC (2010–2012) **42**, **50**, **51**
- Run 2** Run 2 of the LHC (since 2015) **42**
- S-matrix** Scattering matrix **20**, **21**
- S/B** Signal-over-background (yield ratio) **74**, **87**, **102**, **128**
- Sherpa** An event generator **89**, **97**, **98**
- SI** International system of units **8**
- SM** Standard model of particle physics **7**, **9**, **10–13**, **16**, **17**, **21**, **23**, **25**, **26**, **29**, **33–36**, **39**, **43**, **50**, **78**, **87**, **89**, **94**, **101**, **107**, **111**, **117**, **118**, **129**, **130**, **135**, **138**, **151**, **155**
- SPS** Super Proton Synchrotron **13**, **43**
- SUSY** Super symmetry **43**
- SVD** Singular value decomposition **83**, **84**
- Tauola** A program for simulating tau decays **71**, **89**
- TEC** Tracker outer endcap strip modules of CMS **46**
- theta** A program for template-based ML fitting **77**, **79**
- TIB** Tracker inner barrel strip modules of CMS **46**, **54**
- TID** Tracker inner disk strip modules of CMS **46**
- TMVA** Toolkit for Multivariate Data Analysis **74**, **75**, **123**
- TOB** Tracker outer barrel strip modules of CMS **46**, **54**
- Top++** A program for calculating the top-quark-pair cross section at hadron colliders **90**, **118**
- TopFit** A program to estimate limits on anomalous Wtb couplings **88**, **111**
- TopFitter** A program to estimate limits on operators in top quark EFT **39**
- TOTEM** Particle detector at the LHC **44**
- TUnfold** A program for performing regularized unfolding **84**, **86**, **104**, **131**, **132**
- UV** Ultraviolet **21**, **33**, **34**
- V-A** A special coupling structure transforming as a "vector – axialvector" **7**, **17**, **24–26**, **29**, **34**
- VdM** Van der Meer (scan) **67**
- VEGAS** An importance sampling algorithm for numerical integration **69**
- VEV** Vacuum expectation value **14**, **16**
- VPT** Vacuum phototriode **48**
- W+HF** W+jets events with at least one heavy-quark flavored jet **89**
- W+LF** W+jets events with only light-quark flavored jet **89**
- WLS** Wavelength shifting (fibers); used in the CMS HCAL **48**

References

- [1] Particle Data Group, “Review of particle physics”, *Chin. Phys.* **C40** (2016), no. 10, 100001. doi:[10.1088/1674-1137/40/10/100001](https://doi.org/10.1088/1674-1137/40/10/100001).
- [2] Super-Kamiokande Collaboration, “Evidence for oscillation of atmospheric neutrinos”, *Phys. Rev. Lett.* **81** (1998) 1562–1567. doi:[10.1103/PhysRevLett.81.1562](https://doi.org/10.1103/PhysRevLett.81.1562), arXiv:[hep-ex/9807003](https://arxiv.org/abs/hep-ex/9807003).
- [3] CMS Collaboration, “Measurement of the top quark mass using proton-proton data at $\sqrt{s} = 7$ and 8 TeV”, *Phys. Rev.* **D93** (2016), no. 7, 072004. doi:[10.1103/PhysRevD.93.072004](https://doi.org/10.1103/PhysRevD.93.072004), arXiv:[1509.04044](https://arxiv.org/abs/1509.04044).
- [4] ATLAS Collaboration, “Observation of a new particle in the search for the Standard Model Higgs boson with the ATLAS detector at the LHC”, *Phys. Lett.* **B716** (2012) 1–29. doi:[10.1016/j.physletb.2012.08.020](https://doi.org/10.1016/j.physletb.2012.08.020), arXiv:[1207.7214](https://arxiv.org/abs/1207.7214).
- [5] CMS Collaboration, “Observation of a new boson at a mass of 125 GeV with the CMS experiment at the LHC”, *Phys. Lett.* **B716** (2012) 30–61. doi:[10.1016/j.physletb.2012.08.021](https://doi.org/10.1016/j.physletb.2012.08.021), arXiv:[1207.7235](https://arxiv.org/abs/1207.7235).
- [6] ATLAS, CMS Collaboration, “Measurements of the Higgs boson production and decay rates and constraints on its couplings from a combined ATLAS and CMS analysis of the LHC pp collision data at $\sqrt{s} = 7$ and 8 TeV”, *JHEP* **08** (2016) 045. doi:[10.1007/JHEP08\(2016\)045](https://doi.org/10.1007/JHEP08(2016)045), arXiv:[1606.02266](https://arxiv.org/abs/1606.02266).
- [7] ATLAS, CMS Collaboration, “Combined measurement of the Higgs boson mass in pp collisions at $\sqrt{s} = 7$ and 8 TeV with the ATLAS and CMS experiments”, *Phys. Rev. Lett.* **114** (2015) 191803. doi:[10.1103/PhysRevLett.114.191803](https://doi.org/10.1103/PhysRevLett.114.191803), arXiv:[1503.07589](https://arxiv.org/abs/1503.07589).
- [8] E. Majorana, “A symmetric theory of electrons and positrons”, *Nuovo Cimento* **14** (1937) 171.
- [9] S. Dell’Oro et al., “Neutrinoless double beta decay: 2015 review”, *Adv. High Energy Phys.* **2016** (2016) 2162659. doi:[10.1155/2016/2162659](https://doi.org/10.1155/2016/2162659), arXiv:[1601.07512](https://arxiv.org/abs/1601.07512).
- [10] UA1 Collaboration, “Experimental observation of isolated large transverse energy electrons with associated missing energy at $\sqrt{s} = 540$ GeV”, *Phys. Lett.* **B122** (1983) 103–116. doi:[10.1016/0370-2693\(83\)91177-2](https://doi.org/10.1016/0370-2693(83)91177-2).
- [11] UA2 Collaboration, “Observation of single isolated electrons of high transverse momentum in events with missing transverse energy at the CERN anti-p p collider”, *Phys. Lett.* **B122** (1983) 476–485. doi:[10.1016/0370-2693\(83\)91605-2](https://doi.org/10.1016/0370-2693(83)91605-2).
- [12] UA1 Collaboration, “Experimental observation of lepton pairs of invariant mass around 95 GeV/c² at the CERN SPS collider”, *Phys. Lett.* **B126** (1983) 398–410. doi:[10.1016/0370-2693\(83\)90188-0](https://doi.org/10.1016/0370-2693(83)90188-0).
- [13] UA2 Collaboration, “Evidence for $Z \rightarrow e^+e^-$ at the CERN anti-p p collider”, *Phys. Lett.* **B129** (1983) 130–140. doi:[10.1016/0370-2693\(83\)90744-X](https://doi.org/10.1016/0370-2693(83)90744-X).

- [14] Gargamelle Neutrino Collaboration, "Observation of neutrino-like interactions without muon or electron in the Gargamelle neutrino experiment", *Phys. Lett.* **B46** (1973) 138–140. doi:[10.1016/0370-2693\(73\)90499-1](https://doi.org/10.1016/0370-2693(73)90499-1).
- [15] C. S. Wu et al., "Experimental test of parity conservation in beta decay", *Phys. Rev.* **105** (1957) 1413–1415. doi:[10.1103/PhysRev.105.1413](https://doi.org/10.1103/PhysRev.105.1413).
- [16] A. Salam et al., "Electromagnetic and weak interactions", *Phys. Lett.* **13** (1964) 168–171. doi:[10.1016/0031-9163\(64\)90711-5](https://doi.org/10.1016/0031-9163(64)90711-5).
- [17] S. Weinberg, "A model of leptons", *Phys. Rev. Lett.* **19** (1967) 1264–1266. doi:[10.1103/PhysRevLett.19.1264](https://doi.org/10.1103/PhysRevLett.19.1264).
- [18] S. L. Glashow, "Partial symmetries of weak interactions", *Nucl. Phys.* **22** (1961) 579–588. doi:[10.1016/0029-5582\(61\)90469-2](https://doi.org/10.1016/0029-5582(61)90469-2).
- [19] P. Higgs, "Broken symmetries, massless particles and gauge fields", *Phys. Lett.* **12** (1964), no. 2, 132–133. doi:[10.1016/0031-9163\(64\)91136-9](https://doi.org/10.1016/0031-9163(64)91136-9).
- [20] P. W. Higgs, "Broken symmetries and the masses of gauge bosons", *Phys. Rev. Lett.* **13** (1964) 508–509. doi:[10.1103/PhysRevLett.13.508](https://doi.org/10.1103/PhysRevLett.13.508).
- [21] F. Englert et al., "Broken symmetry and the mass of gauge vector mesons", *Phys. Rev. Lett.* **13** (1964) 321–323. doi:[10.1103/PhysRevLett.13.321](https://doi.org/10.1103/PhysRevLett.13.321).
- [22] G. S. Guralnik et al., "Global conservation laws and massless particles", *Phys. Rev. Lett.* **13** (1964) 585–587. doi:[10.1103/PhysRevLett.13.585](https://doi.org/10.1103/PhysRevLett.13.585).
- [23] MuLan Collaboration, "Measurement of the positive muon lifetime and determination of the Fermi constant to part-per-million precision", *Phys. Rev. Lett.* **106** (2011) 041803. doi:[10.1103/PhysRevLett.106.041803](https://doi.org/10.1103/PhysRevLett.106.041803).
- [24] Y. Sumino, "QCD potential as a "Coulomb-plus-linear" potential", *Phys. Lett.* **B571** (2003), no. 3-4, 173–183. doi:[10.1016/j.physletb.2003.05.010](https://doi.org/10.1016/j.physletb.2003.05.010).
- [25] Belle Collaboration, "Observation of a narrow charmoniumlike state in exclusive $B^\pm \rightarrow K^\pm \pi^+ \pi^- J/\psi$ decays", *Phys. Rev. Lett.* **91** (2003) 262001. doi:[10.1103/PhysRevLett.91.262001](https://doi.org/10.1103/PhysRevLett.91.262001).
- [26] LHCb Collaboration, "Determination of the X(3872) meson quantum numbers", *Phys. Rev. Lett.* **110** (2013) 222001. doi:[10.1103/PhysRevLett.110.222001](https://doi.org/10.1103/PhysRevLett.110.222001), arXiv:[1302.6269](https://arxiv.org/abs/1302.6269).
- [27] LHCb Collaboration, "Observation of the resonant character of the Z(4430)⁻ state", *Phys. Rev. Lett.* **112** (2014), no. 22, 222002. doi:[10.1103/PhysRevLett.112.222002](https://doi.org/10.1103/PhysRevLett.112.222002), arXiv:[1404.1903](https://arxiv.org/abs/1404.1903).
- [28] LHCb Collaboration, "Observation of $J/\psi \phi$ structures consistent with exotic states from amplitude analysis of $B^+ \rightarrow J/\psi \phi K^+$ decays", *Phys. Rev. Lett.* **118** (2017), no. 2, 022003. doi:[10.1103/PhysRevLett.118.022003](https://doi.org/10.1103/PhysRevLett.118.022003), arXiv:[1606.07895](https://arxiv.org/abs/1606.07895).
- [29] LHCb Collaboration, "Observation of $J/\psi p$ resonances consistent with pentaquark states in $\Lambda_b^0 \rightarrow J/\psi K^- p$ decays", *Phys. Rev. Lett.* **115** (2015) 072001. doi:[10.1103/PhysRevLett.115.072001](https://doi.org/10.1103/PhysRevLett.115.072001), arXiv:[1507.03414](https://arxiv.org/abs/1507.03414).
- [30] R. P. Feynman, "The behavior of hadron collisions at extreme energies", *Conf. Proc.* **C690905** (1969) 237–258.
- [31] J. D. Bjorken, "Current algebra at small distances", *Conf. Proc.* **C670717** (1967) 55–81.

- [32] Y. L. Dokshitzer, "Calculation of the structure functions for deep inelastic scattering and e^+e^- annihilation by perturbation theory in quantum chromodynamics.", *Sov. Phys. JETP* **46** (1977) 641–653. [*Zh. Eksp. Teor. Fiz.* **73** (1977) 1216].
- [33] V. N. Gribov et al., "Deep inelastic e p scattering in perturbation theory", *Sov. J. Nucl. Phys.* **15** (1972) 438–450. [*Yad. Fiz.* **15** (1972) 781].
- [34] G. Altarelli et al., "Asymptotic freedom in parton language", *Nucl. Phys.* **B126** (1977) 298–318. doi:[10.1016/0550-3213\(77\)90384-4](https://doi.org/10.1016/0550-3213(77)90384-4).
- [35] A. Accardi et al., "A critical appraisal and evaluation of modern PDFs", *Eur. Phys. J.* **C76** (2016), no. 8, 471. doi:[10.1140/epjc/s10052-016-4285-4](https://doi.org/10.1140/epjc/s10052-016-4285-4).
- [36] A. Buckley et al., "LHAPDF6: parton density access in the LHC precision era", *Eur. Phys. J.* **C75** (2015) 132. doi:[10.1140/epjc/s10052-015-3318-8](https://doi.org/10.1140/epjc/s10052-015-3318-8), arXiv:[1412.7420](https://arxiv.org/abs/1412.7420).
- [37] NNPDF Collaboration, "Parton distributions for the LHC Run II", *JHEP* **04** (2015) 040. doi:[10.1007/JHEP04\(2015\)040](https://doi.org/10.1007/JHEP04(2015)040), arXiv:[1410.8849](https://arxiv.org/abs/1410.8849).
- [38] S. Durr et al., "Ab-initio determination of light hadron masses", *Science* **322** (2008) 1224–1227. doi:[10.1126/science.1163233](https://doi.org/10.1126/science.1163233), arXiv:[0906.3599](https://arxiv.org/abs/0906.3599).
- [39] E. Boos et al., "Interference between W' and W in single-top quark production processes", *Phys. Lett.* **B655** (2007) 245–250. doi:[10.1016/j.physletb.2007.03.064](https://doi.org/10.1016/j.physletb.2007.03.064), arXiv:[hep-ph/0610080](https://arxiv.org/abs/hep-ph/0610080).
- [40] CDF Collaboration, "Observation of top quark production in $\bar{p}p$ collisions", *Phys. Rev. Lett.* **74** (1995) 2626–2631. doi:[10.1103/PhysRevLett.74.2626](https://doi.org/10.1103/PhysRevLett.74.2626), arXiv:[hep-ex/9503002](https://arxiv.org/abs/hep-ex/9503002).
- [41] D0 Collaboration, "Search for high mass top quark production in $p\bar{p}$ collisions at $\sqrt{s} = 1.8$ TeV", *Phys. Rev. Lett.* **74** (1995) 2422–2426. doi:[10.1103/PhysRevLett.74.2422](https://doi.org/10.1103/PhysRevLett.74.2422), arXiv:[hep-ex/9411001](https://arxiv.org/abs/hep-ex/9411001).
- [42] M. Kobayashi et al., "CP-violation in the renormalizable theory of weak interaction", *Prog. Theor. Phys.* **49** (1973), no. 2, 652–657. doi:[10.1143/PTP.49.652](https://doi.org/10.1143/PTP.49.652).
- [43] J. E. Augustin et al., "Total cross-section for hadron production by electron-positron annihilation between 2.4 GeV and 5.0 GeV center-of-mass energy", *Phys. Rev. Lett.* **34** (1975) 764. doi:[10.1103/PhysRevLett.34.764](https://doi.org/10.1103/PhysRevLett.34.764).
- [44] S. W. Herb et al., "Observation of a dimuon resonance at 9.5 GeV in 400-GeV proton-nucleus collisions", *Phys. Rev. Lett.* **39** (1977) 252–255. doi:[10.1103/PhysRevLett.39.252](https://doi.org/10.1103/PhysRevLett.39.252).
- [45] CDF Collaboration, "Observation of electroweak single top-quark production", *Phys. Rev. Lett.* **103** (2009) 092002. doi:[10.1103/PhysRevLett.103.092002](https://doi.org/10.1103/PhysRevLett.103.092002).
- [46] D0 Collaboration, "Observation of single top-quark production", *Phys. Rev. Lett.* **103** (2009) 092001. doi:[10.1103/PhysRevLett.103.092001](https://doi.org/10.1103/PhysRevLett.103.092001).
- [47] J. Mitrevski, "Measurement of single top quark production at D0 using a matrix element method", PhD thesis, Columbia University, New York, USA, *ProQuest Dissertations Publishing* 3285137, 2007.
- [48] I. Bigi et al., "Production and decay properties of ultra-heavy quarks", *Phys. Lett.* **B181** (1986), no. 1, 157–163. doi:[10.1016/0370-2693\(86\)91275-X](https://doi.org/10.1016/0370-2693(86)91275-X).

- [49] J. A. Aguilar-Saavedra et al., “W polarisation beyond helicity fractions in top quark decays”, *Nucl. Phys.* **B840** (2010) 349–378. doi:[10.1016/j.nuclphysb.2010.07.012](https://doi.org/10.1016/j.nuclphysb.2010.07.012), arXiv:1005.5382.
- [50] W. Bernreuther, “Top quark physics at the LHC”, *J. Phys.* **G35** (2008) 083001. doi:[10.1088/0954-3899/35/8/083001](https://doi.org/10.1088/0954-3899/35/8/083001), arXiv:0805.1333.
- [51] A. Czarnecki et al., “Helicity fractions of W bosons from top quark decays at NNLO in QCD”, *Phys. Rev.* **D81** (2010) 111503. doi:[10.1103/PhysRevD.81.111503](https://doi.org/10.1103/PhysRevD.81.111503), arXiv:1005.2625.
- [52] M. Czakon et al., “Top++: A program for the calculation of the top-pair cross-section at hadron colliders”, *Comput. Phys. Commun.* **185** (2014) 2930. doi:[10.1016/j.cpc.2014.06.021](https://doi.org/10.1016/j.cpc.2014.06.021), arXiv:1112.5675.
- [53] M. Czakon et al., “Total top-quark-pair production cross section at hadron colliders through $O(a_s^4)$ ”, *Phys. Rev. Lett.* **110** (2013) 252004. doi:[10.1103/PhysRevLett.110.252004](https://doi.org/10.1103/PhysRevLett.110.252004), arXiv:1303.6254.
- [54] T. M. P. Tait, “The tW^- mode of single top production”, *Phys. Rev.* **D61** (1999) 034001. doi:[10.1103/PhysRevD.61.034001](https://doi.org/10.1103/PhysRevD.61.034001), arXiv:hep-ph/9909352.
- [55] C. D. White et al., “Isolating Wt production at the LHC”, *JHEP* **11** (2009) 074. doi:[10.1088/1126-6708/2009/11/074](https://doi.org/10.1088/1126-6708/2009/11/074), arXiv:0908.0631.
- [56] F. Cascioli et al., “A unified NLO description of top-pair and associated Wt production”, *Eur. Phys. J.* **C74** (2014), no. 3, 2783. doi:[10.1140/epjc/s10052-014-2783-9](https://doi.org/10.1140/epjc/s10052-014-2783-9), arXiv:1312.0546.
- [57] T. Jezo et al., “An NLO+PS generator for $t\bar{t}$ and tW production and decay including non-resonant and interference effects”, *Eur. Phys. J.* **C76** (2016), no. 12, 691. doi:[10.1140/epjc/s10052-016-4538-2](https://doi.org/10.1140/epjc/s10052-016-4538-2), arXiv:1607.04538.
- [58] M. Aliev et al., “HATHOR: HAdronic Top and Heavy quarks crOss section calculatoR”, *Comput. Phys. Commun.* **182** (2011) 1034–1046. doi:[10.1016/j.cpc.2010.12.040](https://doi.org/10.1016/j.cpc.2010.12.040), arXiv:1007.1327.
- [59] P. Kant et al., “Hathor for single top-quark production: Updated predictions and uncertainty estimates for single top-quark production in hadronic collisions”, *Comput. Phys. Commun.* **191** (2015) 74–89. doi:[10.1016/j.cpc.2015.02.001](https://doi.org/10.1016/j.cpc.2015.02.001), arXiv:1406.4403.
- [60] R. Schwienhorst et al., “Single top quark production and decay in the t -channel at next-to-leading order at the LHC”, *Phys. Rev.* **D83** (2011) 034019. doi:[10.1103/PhysRevD.83.034019](https://doi.org/10.1103/PhysRevD.83.034019), arXiv:1012.5132.
- [61] CMS Collaboration, “Measurement of top quark polarisation in t -channel single top quark production”, *JHEP* **04** (2016) 073. doi:[10.1007/JHEP04\(2016\)073](https://doi.org/10.1007/JHEP04(2016)073), arXiv:1511.02138.
- [62] F. Maltoni et al., “b-initiated processes at the LHC: a reappraisal”, *JHEP* **07** (2012) 022. doi:[10.1007/JHEP07\(2012\)022](https://doi.org/10.1007/JHEP07(2012)022), arXiv:1203.6393. [Erratum: *JHEP* **04** (2013) 095].
- [63] J. M. Campbell et al., “Next-to-leading-order predictions for t -channel single-top production at hadron colliders”, *Phys. Rev. Lett.* **102** (2009) 182003. doi:[10.1103/PhysRevLett.102.182003](https://doi.org/10.1103/PhysRevLett.102.182003), arXiv:0903.0005.

- [64] C. Csaki, “The minimal supersymmetric standard model (MSSM)”, *Mod. Phys. Lett.* **A11** (1996) 599. doi:10.1142/S021773239600062X, arXiv:hep-ph/9606414.
- [65] G. C. Branco et al., “Theory and phenomenology of two-Higgs-doublet models”, *Phys. Rept.* **516** (2012) 1–102. doi:10.1016/j.physrep.2012.02.002, arXiv:1106.0034.
- [66] LHCb, CMS Collaboration, “Observation of the rare $B_s^0 \rightarrow \mu^+ \mu^-$ decay from the combined analysis of CMS and LHCb data”, *Nature* **522** (2015) 68–72. doi:10.1038/nature14474, arXiv:1411.4413.
- [67] K. G. Wilson et al., “Operator product expansions and composite field operators in the general framework of quantum field theory”, *Commun. Math. Phys.* **24** (1972) 87–106. doi:10.1007/BF01878448.
- [68] B. Grzadkowski et al., “Dimension-six terms in the Standard Model Lagrangian”, *JHEP* **10** (2010) 085. doi:10.1007/JHEP10(2010)085, arXiv:1008.4884.
- [69] J. A. Aguilar-Saavedra, “A minimal set of top anomalous couplings”, *Nucl. Phys. B* **812** (2009) 181–204. doi:10.1016/j.nuclphysb.2008.12.012, arXiv:0811.3842.
- [70] F. Bach et al., “Anomalous top couplings at hadron colliders revisited”, *Phys. Rev.* **D86** (2012) 114026. doi:10.1103/PhysRevD.86.114026, arXiv:1209.4564.
- [71] J. A. Aguilar-Saavedra et al., “New directions for top quark polarization in the t -channel process”, *Phys. Rev.* **D89** (2014), no. 11, 114009. doi:10.1103/PhysRevD.89.114009, arXiv:1404.1585.
- [72] W. Bernreuther et al., “A set of top quark spin correlation and polarization observables for the LHC: Standard Model predictions and new physics contributions”, *JHEP* **12** (2015) 026. doi:10.1007/JHEP12(2015)026, arXiv:1508.05271.
- [73] ATLAS, CMS Collaboration, “LHC Top Working Group Summary Plots”. <https://twiki.cern.ch/twiki/bin/view/LHCTopWGSummaryPlots>. Accessed: 24th May, 2017.
- [74] CMS Collaboration, “Measurement of the W boson helicity in events with a single reconstructed top quark in pp collisions at $\sqrt{s} = 8$ TeV”, *JHEP* **01** (2015) 053. doi:10.1007/JHEP01(2015)053, arXiv:1410.1154.
- [75] A. Buckley et al., “Constraining top quark effective theory in the LHC Run II era”, *JHEP* **04** (2016) 015. doi:10.1007/JHEP04(2016)015, arXiv:1512.03360.
- [76] L. Evans et al., “LHC Machine”, *JINST* **3** (2008) S08001. doi:10.1088/1748-0221/3/08/S08001.
- [77] LHC team, “End of 2016 proton-proton operation”, LHC report, 2016. <http://cds.cern.ch/record/2229040>.
- [78] CMS Collaboration, “CMS luminosity—public results”. <https://twiki.cern.ch/twiki/bin/view/CMSPublic/LumiPublicResults>. Accessed: 15th Aug., 2017.
- [79] E. A. Mobs, “The CERN accelerator complex”, General Photo OPEN-PHO-ACCEL-2016-013, 2016. <https://cds.cern.ch/record/2225847>.
- [80] K. Hanke, “Past and present operation of the CERN PS Booster”, *Int. J. Mod. Phys. A* **28** (2013), no. 13, 1330019. doi:10.1142/S0217751X13300196.
- [81] M. Benedikt et al., “Performance of the LHC Pre-Injectors”, Technical Report CERN-PS-2001-011-DR, 2001. <https://cds.cern.ch/record/494746>.

- [82] P. Freyermuth, “LHC Report: Imaginative injectors”, *CERN Bulletin* (July, 2016). <https://cds.cern.ch/journal/CERNBulletin/2016/30/News%20Articles/2201549>.
- [83] ATLAS Collaboration, “The ATLAS Experiment at the CERN Large Hadron Collider”, *JINST* **3** (2008) S08003. doi:[10.1088/1748-0221/3/08/S08003](https://doi.org/10.1088/1748-0221/3/08/S08003).
- [84] CMS Collaboration, “The CMS Experiment at the CERN LHC”, *JINST* **3** (2008) S08004. doi:[10.1088/1748-0221/3/08/S08004](https://doi.org/10.1088/1748-0221/3/08/S08004).
- [85] ALICE Collaboration, “The ALICE experiment at the CERN LHC”, *JINST* **3** (2008) S08002. doi:[10.1088/1748-0221/3/08/S08002](https://doi.org/10.1088/1748-0221/3/08/S08002).
- [86] LHCb Collaboration, “The LHCb Detector at the LHC”, *JINST* **3** (2008) S08005. doi:[10.1088/1748-0221/3/08/S08005](https://doi.org/10.1088/1748-0221/3/08/S08005).
- [87] F. Follin et al., “Implementation and experience with luminosity levelling with offset beam”, *Proceedings, ICFA Mini-Workshop on Beam-Beam Effects in Hadron Colliders (BB 2013), Geneva, Switzerland* (2014) 183–187. doi:[10.5170/CERN-2014-004.183](https://doi.org/10.5170/CERN-2014-004.183), arXiv:[1410.3667](https://arxiv.org/abs/1410.3667).
- [88] LHCf Collaboration, “The LHCf detector at the CERN Large Hadron Collider”, *JINST* **3** (2008) S08006. doi:[10.1088/1748-0221/3/08/S08006](https://doi.org/10.1088/1748-0221/3/08/S08006).
- [89] TOTEM Collaboration, “The TOTEM experiment at the CERN Large Hadron Collider”, *JINST* **3** (2008) S08007. doi:[10.1088/1748-0221/3/08/S08007](https://doi.org/10.1088/1748-0221/3/08/S08007).
- [90] MoEDAL Collaboration, “Technical design report of the MoEDAL experiment”, Technical Report CERN-LHCC-2009-006, MoEDAL-TDR-001, 2009. <https://cds.cern.ch/record/1181486>.
- [91] CMS Collaboration, “CMS physics: Technical design report volume 1: Detector performance and software”, Technical Report CERN-LHCC-2006-001, CMS-TDR-8-1, 2006. <http://cds.cern.ch/record/922757>.
- [92] CMS Collaboration, “CMS, the magnet project: Technical design report”, Technical Report CERN-LHCC-97-10, 1997. <https://cds.cern.ch/record/331056>.
- [93] CMS Collaboration, “Precise mapping of the magnetic field in the CMS barrel yoke using cosmic rays”, *JINST* **5** (2010) T03021. doi:[10.1088/1748-0221/5/03/T03021](https://doi.org/10.1088/1748-0221/5/03/T03021), arXiv:[0910.5530](https://arxiv.org/abs/0910.5530).
- [94] CMS Collaboration, “Description and performance of track and primary-vertex reconstruction with the CMS tracker”, *JINST* **9** (2014), no. 10, P10009. doi:[10.1088/1748-0221/9/10/P10009](https://doi.org/10.1088/1748-0221/9/10/P10009), arXiv:[1405.6569](https://arxiv.org/abs/1405.6569).
- [95] P. Adzic et al., “Energy resolution of the barrel of the CMS electromagnetic calorimeter”, *JINST* **2** (2007) P04004. doi:[10.1088/1748-0221/2/04/P04004](https://doi.org/10.1088/1748-0221/2/04/P04004).
- [96] CMS HCAL Collaboration, “Design, performance, and calibration of CMS hadron-barrel calorimeter wedges”, Technical Report CMS-NOTE-2006-138, 2007. [http://cds.cern.ch/record/1049915](https://cds.cern.ch/record/1049915).
- [97] G. Bayatian et al., “Design, performance and calibration of the CMS forward calorimeter wedges”, *Eur. Phys. J.* **C53** (2008) 139–166. doi:[10.1140/epjc/s10052-007-0459-4](https://doi.org/10.1140/epjc/s10052-007-0459-4).
- [98] CMS Collaboration, “The performance of the CMS muon detector in proton-proton collisions at $\sqrt{s} = 7$ TeV at the LHC”, *JINST* **8** (2013) P11002. doi:[10.1088/1748-0221/8/11/P11002](https://doi.org/10.1088/1748-0221/8/11/P11002), arXiv:[1306.6905](https://arxiv.org/abs/1306.6905).

- [99] H. W. Wulsin, “Performance of the cathode strip chamber endcap muon detectors in Run 2”, *Proceedings, Meeting of the APS Division of Particles and Fields, Ann Arbor, Michigan, USA* (2015). arXiv:1510.08908.
- [100] M. Tytgat et al., “The upgrade of the CMS RPC system during the first LHC long shutdown”, *PoS RPC2012* (2012) 063. doi:10.1088/1748-0221/8/02/T02002, arXiv:1209.1979.
- [101] CMS Collaboration, “CMS The TriDAS project: Technical design report, volume 2: Data acquisition and high-level trigger. CMS trigger and data-acquisition project”, Technical Report CERN-LHCC-2002-026, CMS-TDR-6, 2002. <http://cds.cern.ch/record/578006>.
- [102] T. Bawej et al., “The new CMS DAQ system for Run-2 of the LHC”, *IEEE Trans. Nucl. Sci.* **62** (2015), no. 3, 1099–1103. doi:10.1109/TNS.2015.2426216.
- [103] CMS Collaboration, “Reconstruction and identification of τ lepton decays to hadrons and ν_τ at CMS”, *JINST* **11** (2016), no. 01, P01019. doi:10.1088/1748-0221/11/01/P01019, arXiv:1510.07488.
- [104] CMS Collaboration, “Performance of photon reconstruction and identification with the CMS detector in proton-proton collisions at $\sqrt{s} = 8$ TeV”, *JINST* **10** (2015), no. 08, P08010. doi:10.1088/1748-0221/10/08/P08010, arXiv:1502.02702.
- [105] M. Swartz et al., “A new technique for the reconstruction, validation, and simulation of hits in the CMS pixel detector”, *PoS Vertex2007* (2007) 035.
- [106] CMS Collaboration, “CMS tracking POG performance plots 2014”. <https://twiki.cern.ch/twiki/bin/view/CMS/TrackingPOGPlots2014>. Accessed: 4th, Feb., 2017.
- [107] R. Fröhwirth, “Application of Kalman filtering to track and vertex fitting”, *Nucl. Instrum. Meth.* **A262** (1987) 444–450. doi:10.1016/0168-9002(87)90887-4.
- [108] P. Billoir, “Progressive track recognition with a Kalman like fitting procedure”, *Comput. Phys. Commun.* **57** (1989) 390–394. doi:10.1016/0010-4655(89)90249-X.
- [109] P. Billoir et al., “Simultaneous pattern recognition and track fitting by the Kalman filtering method”, *Nucl. Instrum. Meth.* **A294** (1990), no. 1, 219–228. doi:10.1016/0168-9002(90)91835-Y.
- [110] W. Adam et al., “Reconstruction of electrons with the Gaussian-sum filter in the CMS tracker at the LHC”, *J. Phys. G: Nucl. Partic.* **31** (2005), no. 9, N9. doi:10.1088/0954-3899/31/9/N01.
- [111] CMS Collaboration, “Particle-flow commissioning with muons and electrons from J/ Ψ and W events at 7 TeV”, CMS Physics Analysis Summary CMS-PAS-PFT-10-003, 2010. <https://cds.cern.ch/record/1279347>.
- [112] CMS Collaboration, “Performance of electron reconstruction and selection with the CMS detector in proton-proton collisions at $\sqrt{s} = 8$ TeV”, *JINST* **10** (2015), no. 06, P06005. doi:10.1088/1748-0221/10/06/P06005, arXiv:1502.02701.
- [113] CMS Collaboration, “Electron and photon performance in CMS with the full 2016 data sample.”, CMS Detector Performance Summary CMS-DP-2017-004, 2017. <http://cds.cern.ch/record/2255497>.

- [114] K. Rose, "Deterministic annealing for clustering, compression, classification, regression, and related optimization problems", *Proceedings of the IEEE* **86** (1998), no. 11, 2210–2239. doi:[10.1109/5.726788](https://doi.org/10.1109/5.726788).
- [115] W. Waltenberger et al., "Adaptive vertex fitting", *J. Phys. G: Nucl. Partic.* **34** (2007), no. 12, N343.
- [116] CMS Collaboration, "Primary vertex resolution in 2016", CMS Detector Performance Summary CMS-DP-2016-041, 2016. <https://cds.cern.ch/record/2202968>.
- [117] CMS Collaboration, "Particle-flow reconstruction and global event description with the CMS detector", *submitted to JINST* (2017) CMS-PRF-14-001. arXiv:[1706.04965](https://arxiv.org/abs/1706.04965).
- [118] CMS Collaboration, "Particle-flow event reconstruction in CMS and performance for jets, taus, and \cancel{E}_T ", CMS Physics Analysis Summary CMS-PAS-PFT-09-001, 2009. <https://cds.cern.ch/record/1194487>.
- [119] CMS Collaboration, "Performance of CMS muon reconstruction in pp collision events at $\sqrt{s} = 7$ TeV", *JINST* **7** (2012) P10002. doi:[10.1088/1748-0221/7/10/P10002](https://doi.org/10.1088/1748-0221/7/10/P10002), arXiv:[1206.4071](https://arxiv.org/abs/1206.4071).
- [120] CMS Collaboration, "Single muon efficiencies in 2012 data", CMS Detector Performance Summary CMS-DP-2013-009, 2013. <https://cds.cern.ch/record/1536406>.
- [121] CMS Collaboration, "Muon identification and isolation efficiency on full 2016 dataset", CMS Detector Performance Summary CMS-DP-2017-007, 2017. <http://cds.cern.ch/record/2257968>.
- [122] CMS Collaboration, "Electron performance with 19.6 fb^{-1} of data collected at $\sqrt{s} = 8$ TeV with the CMS detector.", CMS Detector Performance Summary CMS-DP-2013-003, 2013. <https://cds.cern.ch/record/1523273>.
- [123] M. Cacciari et al., "Pileup subtraction using jet areas", *Phys. Lett.* **B659** (2008) 119–126. doi:[10.1016/j.physletb.2007.09.077](https://doi.org/10.1016/j.physletb.2007.09.077), arXiv:[0707.1378](https://arxiv.org/abs/0707.1378).
- [124] CMS Collaboration, "Pileup removal algorithms", CMS Physics Analysis Summary CMS-PAS-JME-14-001, 2014. <http://cds.cern.ch/record/1751454>.
- [125] M. Cacciari et al., "The anti- k_T jet clustering algorithm", *JHEP* **04** (2008) 063. doi:[10.1088/1126-6708/2008/04/063](https://doi.org/10.1088/1126-6708/2008/04/063), arXiv:[0802.1189](https://arxiv.org/abs/0802.1189).
- [126] CMS Collaboration, "Jet energy scale and resolution in the CMS experiment in pp collisions at 8 TeV", *JINST* **12** (2017), no. 02, P02014. doi:[10.1088/1748-0221/12/02/P02014](https://doi.org/10.1088/1748-0221/12/02/P02014), arXiv:[1607.03663](https://arxiv.org/abs/1607.03663).
- [127] CMS Collaboration, "Jet energy scale and resolution performances with 13 TeV data", CMS Detector Performance Summary CMS-DP-2016-020, 2016. <http://cds.cern.ch/record/2160347>.
- [128] CMS Collaboration, "Identification of b-quark jets with the CMS experiment", *JINST* **8** (2013) P04013. doi:[10.1088/1748-0221/8/04/P04013](https://doi.org/10.1088/1748-0221/8/04/P04013), arXiv:[1211.4462](https://arxiv.org/abs/1211.4462).
- [129] CMS Collaboration, "Identification of b quark jets at the CMS experiment in the LHC Run 2", CMS Physics Analysis Summary CMS-PAS-BTV-15-001, 2016. <http://cds.cern.ch/record/2138504>.

- [130] CMS Collaboration, “Performance of b tagging at $\sqrt{s} = 8$ TeV in multijet, $t\bar{t}$ and boosted topology events”, CMS Physics Analysis Summary CMS-PAS-BTV-13-001, 2013. <http://cds.cern.ch/record/1581306>.
- [131] CMS Collaboration, “ \cancel{E}_T performance in 8 TeV data”, CMS Physics Analysis Summary CMS-PAS-JME-12-002, 2013. <http://cds.cern.ch/record/1543527>.
- [132] CMS Collaboration, “The CMS pixel luminosity telescope”, CMS Conference Report CMS-CR-2015-121, 2015. <https://cds.cern.ch/record/2039978>.
- [133] CMS Collaboration, “CMS luminosity based on pixel cluster counting—summer 2013 update”, CMS Physics Analysis Summary CMS-PAS-LUM-13-001, 2013. <http://cds.cern.ch/record/1598864>.
- [134] CMS Collaboration, “CMS luminosity measurement for the 2015 data-taking period”, CMS Physics Analysis Summary CMS-PAS-LUM-15-001, 2017. <http://cds.cern.ch/record/2138682>.
- [135] CMS Collaboration, “CMS luminosity measurements for the 2016 data taking period”, CMS Physics Analysis Summary CMS-PAS-LUM-17-001, 2017. <http://cds.cern.ch/record/2257069>.
- [136] CMS Collaboration, “Measurement of the inelastic proton-proton cross section at $\sqrt{s} = 13$ TeV”, CMS Physics Analysis Summary CMS-PAS-FSQ-15-005, 2016. <https://cds.cern.ch/record/2145896>.
- [137] S. Banerjee, “CMS simulation software”, *J. Phys. Conf. Ser.* **396** (2012), no. 2, 022003. doi:[10.1088/1742-6596/396/2/022003](https://doi.org/10.1088/1742-6596/396/2/022003).
- [138] M. Hildreth et al., “CMS Full simulation for Run 2”, *J. Phys. Conf. Ser.* **664** (2015), no. 7, 072022. doi:[10.1088/1742-6596/664/7/072022](https://doi.org/10.1088/1742-6596/664/7/072022).
- [139] S. Agostinelli et al., “Geant4—a simulation toolkit”, *Nucl. Instr. Meth. Phys. A* **506** (2003), no. 3, 250–303. doi:[10.1016/S0168-9002\(03\)01368-8](https://doi.org/10.1016/S0168-9002(03)01368-8).
- [140] R. Rahmat et al., “The Fast simulation of the CMS experiment”, *J. Phys. Conf. Ser.* **396** (2012), no. 6, 062016.
- [141] A. Giannanco, “The Fast Simulation of the CMS Experiment”, *J. Phys. Conf. Ser.* **513** (2014), no. 2, 022012.
- [142] T. Ohl, “Vegas revisited: Adaptive Monte Carlo integration beyond factorization”, *Comput. Phys. Commun.* **120** (1999), no. 1, 13–19. doi:[10.1016/S0010-4655\(99\)00209-X](https://doi.org/10.1016/S0010-4655(99)00209-X).
- [143] S. Höche, “Introduction to parton-shower event generators”, *Proceedings, Amplitudes for Colliders (TASI 2014) Boulder, Colorado* (2014). arXiv:1411.4085.
- [144] J. Alwall et al., “Comparative study of various algorithms for the merging of parton showers and matrix elements in hadronic collisions”, *Eur. Phys. J.* **C53** (2008) 473–500. doi:[10.1140/epjc/s10052-007-0490-5](https://doi.org/10.1140/epjc/s10052-007-0490-5), arXiv:0706.2569.
- [145] J. Alwall et al., “The automated computation of tree-level and next-to-leading order differential cross sections, and their matching to parton shower simulations”, *JHEP* **07** (2014) 079. doi:[10.1007/JHEP07\(2014\)079](https://doi.org/10.1007/JHEP07(2014)079), arXiv:1405.0301.
- [146] J. Alwall et al., “MadGraph 5: Going beyond”, *JHEP* **06** (2011) 128. doi:[10.1007/JHEP06\(2011\)128](https://doi.org/10.1007/JHEP06(2011)128), arXiv:1106.0522.

- [147] R. Frederix et al., “Scalar and pseudoscalar Higgs production in association with a top-antitop pair”, *Phys. Lett.* **B701** (2011) 427–433. doi:[10.1016/j.physletb.2011.06.012](https://doi.org/10.1016/j.physletb.2011.06.012), arXiv:1104.5613.
- [148] M. L. Mangano et al., “Matching matrix elements and shower evolution for top-quark production in hadronic collisions”, *JHEP* **01** (2007) 013. doi:[10.1088/1126-6708/2007/01/013](https://doi.org/10.1088/1126-6708/2007/01/013), arXiv:hep-ph/0611129.
- [149] S. Frixione et al., “Matching NLO QCD computations and parton shower simulations”, *JHEP* **06** (2002) 029. doi:[10.1088/1126-6708/2002/06/029](https://doi.org/10.1088/1126-6708/2002/06/029), arXiv:hep-ph/0204244.
- [150] R. Frederix et al., “Merging meets matching in MC@NLO”, *JHEP* **12** (2012) 061. doi:[10.1007/JHEP12\(2012\)061](https://doi.org/10.1007/JHEP12(2012)061), arXiv:1209.6215.
- [151] S. Alioli et al., “A general framework for implementing NLO calculations in shower Monte Carlo programs: The POWHEG BOX”, *JHEP* **06** (2010) 043. doi:[10.1007/JHEP06\(2010\)043](https://doi.org/10.1007/JHEP06(2010)043), arXiv:1002.2581.
- [152] S. Alioli et al., “NLO single-top production matched with shower in POWHEG: s - and t -channel contributions”, *JHEP* **09** (2009) 111. doi:[10.1088/1126-6708/2009/09/111](https://doi.org/10.1088/1126-6708/2009/09/111), arXiv:0907.4076. [Erratum: *JHEP* **02** (2010) 011].
- [153] S. Frixione et al., “Matching NLO QCD computations with parton shower simulations: The POWHEG method”, *JHEP* **11** (2007) 070. doi:[10.1088/1126-6708/2007/11/070](https://doi.org/10.1088/1126-6708/2007/11/070), arXiv:0709.2092.
- [154] CompHEP Collaboration, “CompHEP 4.4: Automatic computations from Lagrangians to events”, *Nucl. Instrum. Meth.* **A534** (2004) 250–259. doi:[10.1016/j.nima.2004.07.096](https://doi.org/10.1016/j.nima.2004.07.096), arXiv:hep-ph/0403113.
- [155] E. E. Boos et al., “Method for simulating electroweak top-quark production events in the NLO approximation: SingleTop event generator”, *Phys. Atom. Nucl.* **69** (2006) 1317–1329. doi:[10.1134/S1063778806080084](https://doi.org/10.1134/S1063778806080084). [*Yad. Fiz.* **69** (2006) 1352].
- [156] S. Jadach et al., “The tau decay library TAUOLA: Version 2.4”, *Comput. Phys. Commun.* **76** (1993) 361–380. doi:[10.1016/0010-4655\(93\)90061-G](https://doi.org/10.1016/0010-4655(93)90061-G).
- [157] N. Davidson et al., “Universal interface of TAUOLA: Technical and physics documentation”, *Comput. Phys. Commun.* **183** (2012) 821–843. doi:[10.1016/j.cpc.2011.12.009](https://doi.org/10.1016/j.cpc.2011.12.009), arXiv:1002.0543.
- [158] P. Golonka et al., “PHOTOS Monte Carlo: A precision tool for QED corrections in Z and W decays”, *Eur. Phys. J.* **C45** (2006) 97–107. doi:[10.1140/epjc/s2005-02396-4](https://doi.org/10.1140/epjc/s2005-02396-4), arXiv:hep-ph/0506026.
- [159] P. Artoisenet et al., “Automatic spin-entangled decays of heavy resonances in Monte Carlo simulations”, *JHEP* **03** (2013) 015. doi:[10.1007/JHEP03\(2013\)015](https://doi.org/10.1007/JHEP03(2013)015), arXiv:1212.3460.
- [160] T. Sjöstrand et al., “PYTHIA 6.4 physics and manual”, *JHEP* **05** (2006) 026. doi:[10.1088/1126-6708/2006/05/026](https://doi.org/10.1088/1126-6708/2006/05/026), arXiv:hep-ph/0603175.
- [161] T. Sjöstrand et al., “An introduction to PYTHIA 8.2”, *Comput. Phys. Commun.* **191** (2015) 159–177. doi:[10.1016/j.cpc.2015.01.024](https://doi.org/10.1016/j.cpc.2015.01.024), arXiv:1410.3012.

- [162] M. Bahr et al., “Herwig++ physics and manual”, *Eur. Phys. J.* **C58** (2008) 639–707. doi:[10.1140/epjc/s10052-008-0798-9](https://doi.org/10.1140/epjc/s10052-008-0798-9), arXiv:[0803.0883](https://arxiv.org/abs/0803.0883).
- [163] J. Bellm et al., “Herwig 7.0/Herwig++ 3.0 release note”, *Eur. Phys. J.* **C76** (2016), no. 4, 196. doi:[10.1140/epjc/s10052-016-4018-8](https://doi.org/10.1140/epjc/s10052-016-4018-8), arXiv:[1512.01178](https://arxiv.org/abs/1512.01178).
- [164] B. R. Webber, “A QCD model for jet fragmentation including soft gluon interference”, *Nucl. Phys.* **B238** (1984) 492–528. doi:[10.1016/0550-3213\(84\)90333-X](https://doi.org/10.1016/0550-3213(84)90333-X).
- [165] D. Amati et al., “Preconfinement as a property of perturbative QCD”, *Phys. Lett.* **B83** (1979) 87–92. doi:[10.1016/0370-2693\(79\)90896-7](https://doi.org/10.1016/0370-2693(79)90896-7).
- [166] T. Chwalek, “Measurement of W boson helicity fractions in top quark decays with the CDF II experiment and prospects for an early $t\bar{t}$ cross-section measurement with the CMS experiment”, PhD thesis, Karlsruhe University, Karlsruhe, Germany CERN-THESIS-2010-255, 2010. <https://cds.cern.ch/record/1416031>.
- [167] CMS Collaboration, “Measurement of the t -channel single-top-quark production cross section and of the $|V_{tb}|$ CKM matrix element in pp collisions at $\sqrt{s} = 8$ TeV”, *JHEP* **06** (2014) 090. doi:[10.1007/JHEP06\(2014\)090](https://doi.org/10.1007/JHEP06(2014)090), arXiv:[1403.7366](https://arxiv.org/abs/1403.7366).
- [168] CMS Collaboration, “Cross section measurement of t -channel single-top-quark production in pp collisions at $\sqrt{s} = 13$ TeV”, *Accepted by Phys. Lett. B* (2016) CMS-TOP-16-003. doi:[10.1016/j.physletb.2017.07.047](https://doi.org/10.1016/j.physletb.2017.07.047), arXiv:[1610.00678](https://arxiv.org/abs/1610.00678).
- [169] A. Hoecker et al., “TMVA: Toolkit for multivariate data analysis”, *PoS ACAT2007* (2007) 040. arXiv:[physics/0703039](https://arxiv.org/abs/physics/0703039).
- [170] C. Gini, “Concentration and dependency ratios (1909, in Italian)”, English translation in *Rivista di Politica Economica* **87** (1997) 769–789.
- [171] R. E. Schapire, “The strength of weak learnability”, *Machine Learning* **5** (1990), no. 2, 197–227. doi:[10.1007/BF00116037](https://doi.org/10.1007/BF00116037).
- [172] Y. Freund, “Boosting a weak learning algorithm by majority”, *Inform. Comput.* **121** (1995), no. 2, 256–285. doi:<http://dx.doi.org/10.1006/inco.1995.1136>.
- [173] Y. Freund et al., “A decision-theoretic generalization of online learning and an application to boosting”, *JCSS* **55** (1997), no. 1, 119–139. doi:<http://dx.doi.org/10.1006/jcss.1997.1504>.
- [174] J. H. Friedman, “Greedy function approximation: A gradient boosting machine”, *Ann. Stat.* **29** (2000) 1189–1232. doi:[10.1214/aos/1013203451](https://doi.org/10.1214/aos/1013203451).
- [175] J. Ott et al., “THETA—a framework for template-based statistical modeling and inference”, Preprint IEKP-KA-CMS/2012-1, 2012. <http://www-ekp.physik.uni-karlsruhe.de/~ott/theta/theta-auto/>.
- [176] R. J. Barlow et al., “Fitting using finite Monte Carlo samples”, *Comput. Phys. Commun.* **77** (1993) 219–228. doi:[10.1016/0010-4655\(93\)90005-W](https://doi.org/10.1016/0010-4655(93)90005-W).
- [177] J. S. Conway, “Incorporating nuisance parameters in likelihoods for multisource spectra”, *Proceedings, PHYSTAT 2011, CERN, Switzerland* (2011) 115–120. doi:[10.5170/CERN-2011-006.115](https://doi.org/10.5170/CERN-2011-006.115), arXiv:[1103.0354](https://arxiv.org/abs/1103.0354).
- [178] F. James et al., “Minuit: A system for function minimization and analysis of the parameter errors and correlations”, *Comput. Phys. Commun.* **10** (1975) 343–367. doi:[10.1016/0010-4655\(75\)90039-9](https://doi.org/10.1016/0010-4655(75)90039-9).

- [179] M. Cacciari et al., “The catchment area of jets”, *JHEP* **04** (2008) 005. doi:10.1088/1126-6708/2008/04/005, arXiv:0802.1188.
- [180] A. Höcker et al., “SVD approach to data unfolding”, *Nucl. Instrum. Meth.* **A372** (1996) 469–481. doi:10.1016/0168-9002(95)01478-0, arXiv:hep-ph/9509307.
- [181] A. N. Tikhonov, “On the stability of inverse problems”, *Doklady Akademii Nauk SSSR* **39** (1943) 195–198.
- [182] S. Schmitt, “TUnfold, an algorithm for correcting migration effects in high energy physics”, *JINST* **7** (2012), no. 10, T10003.
- [183] M. Komm, “Measurement of top-quark spin asymmetries in t -channel single-top-quark production at 7 TeV with the CMS experiment”, Master’s thesis, RWTH Aachen University, Aachen, Germany 2012.
- [184] J. A. Aguilar-Saavedra, “TopFit—a program to fit the Wtb vertex”. <http://jaguilar.web.cern.ch/jaguilar/topfit/>. Accessed: 6th May, 2017.
- [185] S. Höche et al., “W+ n -jet predictions at the Large Hadron Collider at next-to-leading order matched with a parton shower”, *Phys. Rev. Lett.* **110** (2013), no. 5, 052001. doi:10.1103/PhysRevLett.110.052001, arXiv:1201.5882.
- [186] N. Kidonakis, “Differential and total cross sections for top pair and single top production”, *Proceedings, 20th International Workshop on Deep-Inelastic Scattering and Related Subjects (DIS 2012), Bonn, Germany* (2012) 831–834. doi:10.3204/DESY-PROC-2012-02/251, arXiv:1205.3453.
- [187] R. Gavin et al., “FEWZ 2.0: A code for hadronic Z production at next-to-next-to-leading order”, *Comput. Phys. Commun.* **182** (2011) 2388–2403. doi:10.1016/j.cpc.2011.06.008, arXiv:1011.3540.
- [188] J. M. Campbell et al., “MCFM for the Tevatron and the LHC”, *Nucl. Phys. Proc. Suppl.* **205-206** (2010) 10–15. doi:10.1016/j.nuclphysbps.2010.08.011, arXiv:1007.3492.
- [189] CMS Collaboration, “Measurement of top quark polarization in t -channel single-top production”, CMS Physics Analysis Summary CMS-PAS-TOP-13-001, 2013. <https://cds.cern.ch/record/1601800>.
- [190] D0 Collaboration, “A Novel method for modeling the recoil in W boson events at hadron collider”, *Nucl. Instrum. Meth.* **A609** (2009) 250–262. doi:10.1016/j.nima.2009.08.056, arXiv:0907.3713.
- [191] CMS Collaboration, “Measurement of differential top-quark pair production cross sections in pp colisions at $\sqrt{s} = 7$ TeV”, *Eur. Phys. J.* **C73** (2013), no. 3, 2339. doi:10.1140/epjc/s10052-013-2339-4, arXiv:1211.2220.
- [192] CMS Collaboration, “Measurement of the differential cross section for top quark pair production in pp collisions at $\sqrt{s} = 8$ TeV”, *Eur. Phys. J.* **C75** (2015), no. 11, 542. doi:10.1140/epjc/s10052-015-3709-x, arXiv:1505.04480.
- [193] M. Czakon et al., “High-precision differential predictions for top-quark pairs at the LHC”, *Phys. Rev. Lett.* **116** (2016), no. 8, 082003. doi:10.1103/PhysRevLett.116.082003, arXiv:1511.00549.

- [194] CMS Collaboration, “Search for anomalous Wtb couplings and flavour-changing neutral currents in t -channel single top quark production in pp collisions at $\sqrt{s} = 7$ and 8 TeV”, *JHEP* **02** (2017) 028. doi:10.1007/JHEP02(2017)028, arXiv:1610.03545.
- [195] J. Neyman, “On the problem of confidence intervals”, *Ann. Math. Statist.* **6** (1935), no. 3, 111–116. doi:10.1214/aoms/1177732585.
- [196] H.-L. Lai et al., “New parton distributions for collider physics”, *Phys. Rev.* **D82** (2010) 074024. doi:10.1103/PhysRevD.82.074024, arXiv:1007.2241.
- [197] A. D. Martin et al., “Extended parameterisations for MSTW PDFs and their effect on lepton charge asymmetry from W decays”, *Eur. Phys. J.* **C73** (2013), no. 2, 2318. doi:10.1140/epjc/s10052-013-2318-9, arXiv:1211.1215.
- [198] R. D. Ball et al., “Parton distributions with LHC data”, *Nucl. Phys.* **B867** (2013) 244–289. doi:10.1016/j.nuclphysb.2012.10.003, arXiv:1207.1303.
- [199] CMS Collaboration, “Measurement of the W boson helicity fractions in the decays of top quark pairs to lepton+jets final states produced in pp collisions at $\sqrt{s} = 8$ TeV”, *Phys. Lett.* **B762** (2016) 512–534. doi:10.1016/j.physletb.2016.10.007, arXiv:1605.09047.
- [200] CMS Collaboration, “Measurement of the differential cross section for t -channel single-top-quark production at $\sqrt{s} = 13$ TeV”, CMS Physics Analysis Summary CMS-PAS-TOP-16-004, 2016. <https://cds.cern.ch/record/2151074>.
- [201] Y. Li et al., “Combining QCD and electroweak corrections to dilepton production in FEWZ”, *Phys. Rev.* **D86** (2012) 094034. doi:10.1103/PhysRevD.86.094034, arXiv:1208.5967.
- [202] CMS Collaboration, “Investigations of the impact of the parton shower tuning in Pythia8 in the modelling of $t\bar{t}$ at $\sqrt{s} = 8$ and 13 TeV”, CMS Physics Analysis Summary CMS-PAS-TOP-16-021, 2016. <http://cds.cern.ch/record/2235192>.
- [203] CMS Collaboration, “Measurement of the underlying event activity at the LHC with $\sqrt{s} = 7$ TeV and comparison with $\sqrt{s} = 0.9$ TeV”, *JHEP* **09** (2011) 109. doi:10.1007/JHEP09(2011)109, arXiv:1107.0330.
- [204] CMS Collaboration, “Event generator tunes obtained from underlying event and multiparton scattering measurements”, *Eur. Phys. J.* **C76** (2016), no. 3, 155. doi:10.1140/epjc/s10052-016-3988-x, arXiv:1512.00815.
- [205] CMS Collaboration, “Object definitions for top quark analyses at the particle level”, CMS-NOTE-2017-004, 2017. <https://cds.cern.ch/record/2267573>.